DIGITALCOMMONS
@WAYNESTATE

Wayne State University

Wayne State University Dissertations

1-1-2016

Design Of First-Row Transition Metal Bis(alkoxide) Complexes And Their Reactivity Toward Nitrene And Carbene Transfer

James Bellow
Wayne State University,

Follow this and additional works at: http://digitalcommons.wayne.edu/oa_dissertations


Part of the Inorganic Chemistry Commons

Recommended Citation
Bellow, James, "Design Of First-Row Transition Metal Bis(alkoxide) Complexes And Their Reactivity Toward Nitrene And Carbene Transfer" (2016). *Wayne State University Dissertations.* Paper 1517.

This Open Access Dissertation is brought to you for free and open access by DigitalCommons@WayneState. It has been accepted for inclusion in Wayne State University Dissertations by an authorized administrator of DigitalCommons@WayneState.

DESIGN OF FIRST-ROW TRANSITION METAL BIS(ALKOXIDE) COMPLEXES AND THEIR REACTIVITY TOWARD NITRENE AND CARBENE TRANSFER

by

JAMES A. BELLOW

DISSERTATION

Submitted to the Graduate School

of Wayne State University,

Detroit, Michigan

in partial fulfillment of the requirements

for the degree of

DOCTOR OF PHILOSOPHY

2016

MAJOR: INORGANIC CHEMISTRY

Approved By:

_____

Advisor Date

_____

_____

_____

© COPYRIGHT BY

JAMES A. BELLOW

2016

All Rights Reserved

ACKNOWLEDGEMENTS

First and foremost, I would like to express my sincere gratitude to my advisor, Professor Stanislav Groysman, for his mentorship and guidance throughout my journey through graduate school. I have learned a great deal about chemistry from him, and it was an absolute privilege to be among the first graduate students in his lab and to witness the growth of his own career firsthand.

I would like to thank my committee members, Professor Charles H. Winter, Professor Jeremy Kodanko, and Professor Pavel Nagorny for their valued input on both this thesis, as well as my research in general.

I am extremely grateful to all members of the Groysman group, past and present, for their friendship and support throughout the years. Specifically, I thank Amanda Grass for her willingness to take over this project upon my graduation: I know that her dedication will lead to exciting new developments! I want to thank Ryan Hollingsworth for his friendship, insightful research suggestions, and organic chemistry expertise, all of which have helped me tremendously! I thank Thilie Poramba Liyanage for her good nature, her kind words, and her superb organizational skills, all of which have contributed to our lab's general well-being. I want to thank Jeff Beattie and Blake Reed for embarking on this graduate school journey with me, and for their support, friendship, and valued constructive criticism. I thank our postdoc, Dr. Amarnath Bheemaraju, who has since returned home to India and started a professorship, for teaching me various synthetic techniques, for helping to get the Groysman lab up and running, and for the numerous insightful conversations about chemistry and life in general. I have also had the pleasure of mentoring five exceptional undergraduate students: Monika Toton, Natalija Kovacevic, Asmar Georges, Katlyn Holt, and Shervyn Karthanal. I thank all of them for helping with my research. Finally, I have to thank Maryam Yousif for being the best glovebox companion I could ever ask for: I will never forget her constant support and encouragement, as well as all of our day-to-day conversations!

I would like to thank all of our collaborators (names mentioned in the text of this dissertation), without whom much of this research would not be possible.

I thank the individuals at the Lumigen Instrument Center, whose instruments have provided

valuable structural insight into the new molecules we have synthesized.

I would like to thank the various staff in our department for taking care of the business side of things, keeping our department up and running, and helping to maintain my sanity in the process!

I would also like to thank both Wayne State University and the American Chemical Society Petroleum Research Fund (Grant 54178-DNI3) for the funding that made this research possible. I thank Wayne State specifically for the startup funding, as well as for the Heller Research Fellowship.

Finally, I would like to thank my family and friends, who have always had my back in everything that I do. Your support means everything to me!

TABLE OF CONTENTS

LIST OF TABLES

LIST OF FIGURES

CHAPTER 1: INTRODUCTION

Portions of the text in this chapter were reprinted or adapted with permission from: Bellow, J. A.; Yousif, M.; Groysman, S. *Comments Inorg. Chem.* **2016**, *36*, 92-122. All rights to the work are retained by the authors and any reuse requires permission of the authors.

1.1. Organic Azides and Diazoalkanes: Versatile Molecules for a Variety of Transformations

Organic azides (RN_3) are reactive, often energetic molecules that are easily synthesized and can serve as precursors to a myriad of new nitrogen-containing organic molecules.[1] Most transformations of organic azides take advantage of their overwhelming tendency to extrude dinitrogen gas. This extrusion leads to the formation of the reactive nitrene moiety (RN), which can then conveniently react with a variety of substrates, yielding value-added organic products that can be utilized in many different applications. While nitrenes can be generated via thermal or photochemical decomposition of azides, controlling their subsequent transfer to a substrate can be difficult by these means. As a result of this, to help better facilitate nitrene transfer, transition metal complexes are typically employed.[2] Upon reaction of a complex [M] with an organic azide, a two-electron reduction of the azide by the metal takes place, and dinitrogen is extruded. The resulting nitrene moiety binds to the metal, forming a metal imido complex, [M]=NR (**Figure 1**). Here, the metal serves as a nitrene carrier, stabilizing it so that it can be reacted in a controlled manner. The nitrene may then be transferred to any number of substrates, thus regenerating the starting complex and making the process catalytic.

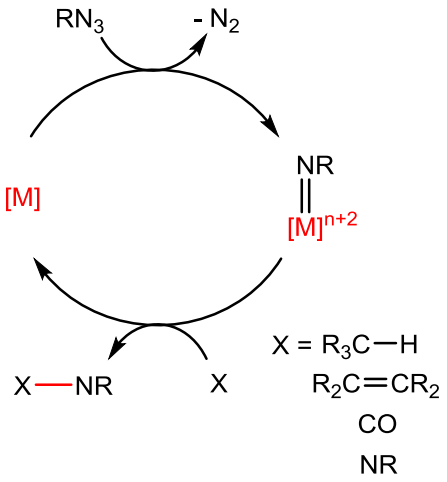

Figure 1. Catalytic nitrene transfer facilitated by a metal complex [M].

As shown in **Figure 1**, a multitude of substrates can react with nitrene to generate new compounds with a variety of applications. Nitrenes can potentially activate C−H bonds in alkanes to yield aminated products, as well as add across the multiple bond of olefins to give aziridines.[3, 4] Synthetically, amines commonly serve as stepping stones toward other useful organic products, and they can also be used as bases in organic reactions. In terms of applications, the amine moiety can be found in pharmaceutical drugs, as well as in certain types of dyes.[1, 3h] Amines can also be used in coatings, as curing agents in the production of epoxy resins, and as gas treating agents, among other uses.[5] Aziridines find uses in organic synthesis and pharmaceutical chemistry and are challenging to synthesize by other means.[3a] In terms of other C−N bond formation reactions, nitrenes can also couple with CO or isocyanides (R'NC) to give isocyanates (RNCO) and carbodiimides (RNCNR'), respectively.[6] Isocyanates are widely used in the production of polyurethanes, which are polymers commonly employed in foam and insulation materials.[7] More rarely, nitrenes can also couple with themselves to form azo compounds (RNNR),[8] highly colored substances which find uses as textile dyes and pigments, as well as chemical indicators.[9] The photoresponsive nature of azo compounds has also loaned its use in the production of liquid crystal displays,[10] molecular switches,[11] optical storage devices,[12] and drug

delivery.[13] A summary of nitrene transfer reactions to the aforementioned substrates can be found in **Figure 2** below.

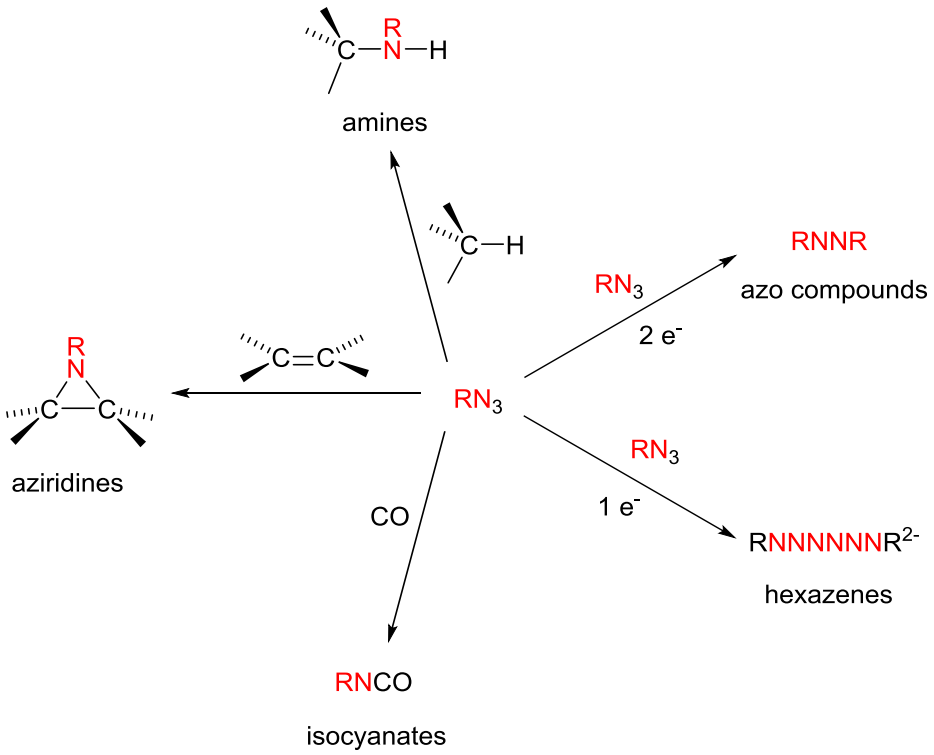

Figure 2. Transformations of organic azides to various substrates.

The previously discussed transformations all involve transfer of nitrene, which entails a two-electron reduction of the organic azide followed by dinitrogen extrusion. One other transformation of organic azide at a transition metal center instead evokes one-electron reduction, forming an azide radical. This radical can then couple with itself to give the hexazene moiety, $RNNNNNNR^{2-}$, which contains a chain of six nitrogens bonded together via the terminal nitrogens of two azides. This rare transformation of an organic azide has only been observed for a few systems.[14] The hexazene molecule chelates between two transition metal centers, which provide stability to what would otherwise be considered a highly reactive molecule. While means to remove or transfer the hexazene molecule from the complex are only beginning to be realized,[15] one can envision a catalytic process to do so. The resulting hexazene salt or hexaazadiene could serve as the basis for a new type of energetic material (**Figure 2**).

Diazoalkanes (R_2CN_2), like organic azides, are reactive precursors that can extrude dinitrogen. However, in this case a reactive carbene (R_2C) is formed instead of a nitrene. Similarly to nitrenes, metal complexes with terminal carbene ligands can be formed, serving as carbene transfer agents in a similar manner.[3c, 16] There are three common transformations employed using metal carbenes: cyclopropanation, C−C bond formation, and olefin metathesis (**Figure 3**). In cyclopropanation, the carbene is added across an olefin to generate a cyclopropane.[16b, 16d, 17] Late transition metal carbenes are typically employed for this process. Cyclopropanes find various uses in organic synthesis, as well as in the synthesis of antibiotics.[18] They are also a major component of pyrethroids, which are used in insect repellants.[19] Similar to azides, C−H bond activation of alkanes can be done using a carbene, providing convenient synthetic access to compounds containing new C−C bonds.[16e, 20] Finally, olefin metathesis[21] using early transition metal alkylidenes can generate new olefins for use in synthesis and in pharmaceuticals, as well as in the industrial preparation of higher olefins and propylene, a raw material used in the production of many industrial chemicals.[22]

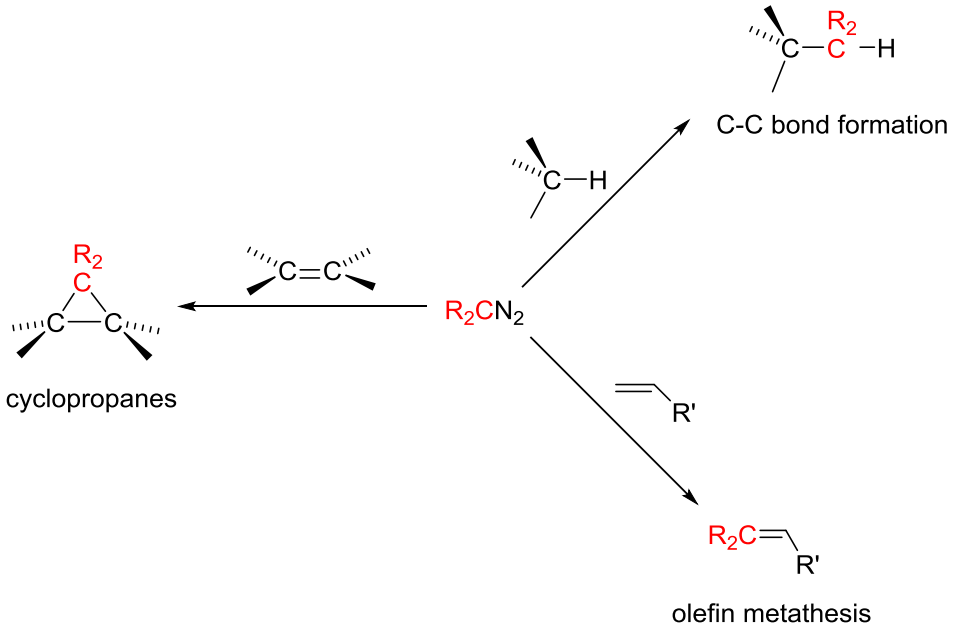

Figure 3. Transformations of diazoalkanes using transition metal complexes.

1.2. Design of Reactive Metal Imido and Metal Carbene Complexes

The reactive nature of metal imido and metal carbene complexes can vary widely depending on the choice of metal and the type of ligand environment used to stabilize that metal. In the case of metal imido complexes, when an early transition metal is used, the imido group tends to be unreactive toward substrates and is instead ancillary in nature. This is because the d-orbitals of the early transition metals are empty, allowing for better π-orbital overlap and thus greater electron donation from multiply-bonded ligands. The textbook example of an ancillary imido complex is the Schrock catalyst, $M(OR)_2(NAr)(CH^tBu)$ (M = Mo, W) (**Figure 4**).[21] This complex, widely known for its high catalytic efficiency toward olefin metathesis, is reactive at the CH^tBu alkylidene, with the imido only serving as an ancillary ligand. A more recent example of an ancillary imido is in the niobium(III) complex $Nb(Nacnac)(C_6H_6)(NR)$ (**Figure 4**).[23] This complex has been shown to catalytically defluorinate aryl fluorides, with the active site generated upon loss of the benzene ligand. Again, the imido here is ancillary in nature.

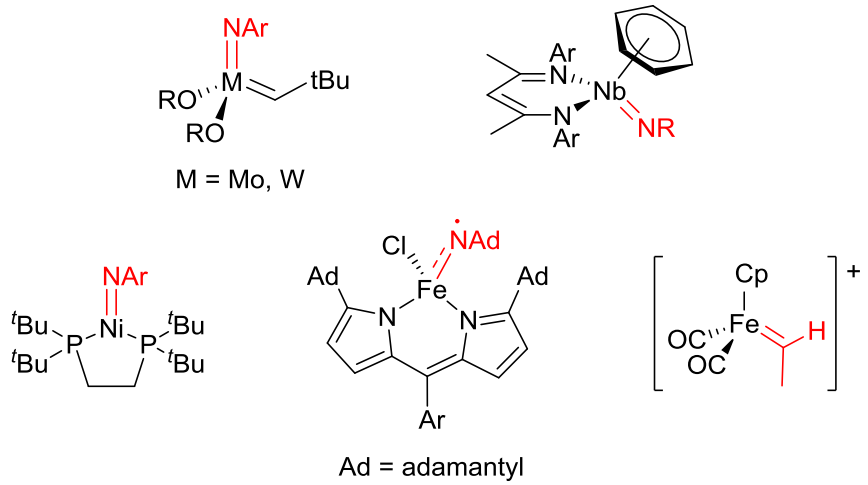

Figure 4. Examples of early (top) and late (bottom) transition metal imido and carbene complexes.

Imido complexes of the later transition metals, particularly of the later first-row transition metals, are far less commonly encountered than their early transition metal counterparts. This is to be expected, as metal-ligand multiple bonds are destabilized for later transition metals due to poor overlap of imido pπ-

orbitals with the metal's filled dπ-orbitals. However, this also means that late transition metal imido complexes are more reactive, making them suitable candidates for nitrene transfer. One recent example of a late transition metal imido complex is the iron(III) radical imido complex synthesized by Betley and coworkers.[4b] It is stabilized by a dipyrromethane ligand (**Figure 4**) and can catalytically aminate C-H bonds via its highly reactive imido radical ligand. In another example, the highly unusual nickel(II) imido phosphine complex synthesized by Hillhouse and coworkers can perform clean aziridination of olefins (**Figure 4**).[24]

Early transition metal carbene complexes typically possess Schrock carbenes (also known as alkylidenes), in which the carbene is treated as a 2- ligand.[3c] In contrast to imido complexes, alkylidene complexes can be more reactive for early transition metals, displaying olefin metathesis capabilities depending on the choice of metal. The molybdenum and tungsten Schrock catalysts (both of which contain a Schrock carbene) are prime examples of reactive early transition metal carbene complexes.[21] Late transition metal carbene complexes possess Fischer carbenes, which behave as neutral ligands. Several carbene complexes of iron, ruthenium, cobalt, rhodium, and copper have been shown to facilitate catalytic cyclopropanation of olefins, as well as C−C bond formation.[25] An example of a cationic iron carbene complex is shown in **Figure 4**.

For late transition metals, imido and carbene complexes are notoriously reactive and can be difficult to isolate. In fact, complexes of this type have really only been isolated and structurally characterized within the past 15 years. As such, ligand design plays a crucial role in stabilizing the imido or carbene. A common trend among isolated and characterized late transition metal imido and carbene complexes is that they are typically stabilized by soft, strong-field ligand platforms. Strong-field σ-donating and/or π-accepting ligands such as phosphines, N-heterocyclic carbenes (NHCs), cyclopentadienyls (Cp), and CO presumably stabilize the metal-ligand multiple bond by allowing for better π-overlap between the metal and the imido or carbene. In addition, good σ-donors stabilize high oxidation states of the late transition metals. Several examples of isolated imido and carbene complexes of the later first-row transition metals are shown in **Figure 5**.[4f, 8e, 26] Nearly all of them display nitrene or

carbene transfer reactivity, and most do so catalytically. Another common trend is that most of them display coordination numbers of four or less. What is noticeably absent from the literature is the exploration of the reactivity of late transition metal imido and carbene complexes in weak-field, anionic π-donating ligand environments. Such a ligand environment would potentially destabilize the metal imido or carbene by forcing the metal-ligand multiple bond to compete with the π-bonding of the ancillary ligands, leading to higher reactivity and ease of imido/carbene transfer. Alkoxides are one such ligand that could be utilized for this purpose.

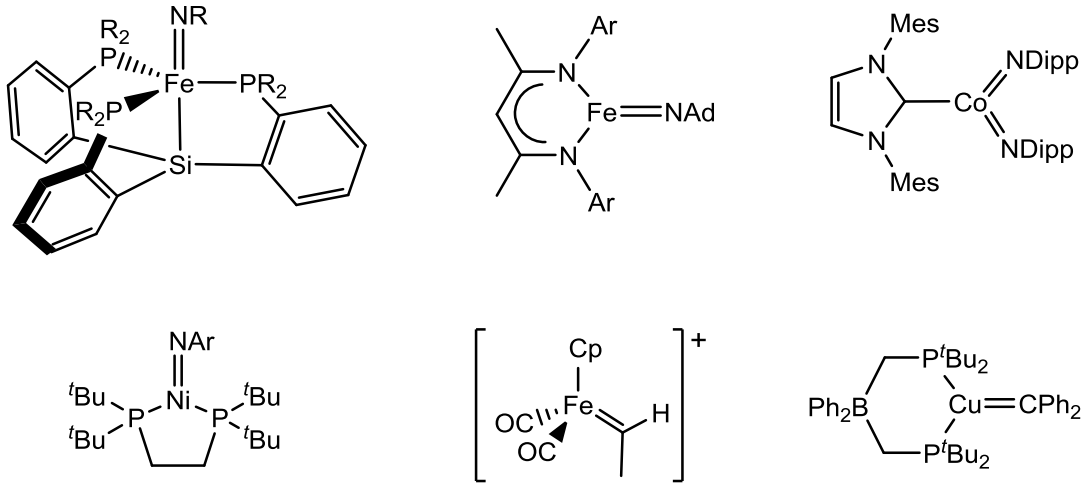

Figure 5. Examples of late transition metal imido and carbene complexes stabilized by soft, strong-field ligands.

1.3. Alkoxides as Ligands

Alkoxides (OR^-) are one of the most commonly utilized ligands in all of coordination chemistry, partly because of their ease of synthesis. As a result of this, alkoxide compounds exist for nearly every element on the periodic table.[27] They are often encountered as ancillary ligands in transition metal chemistry, particularly with the first-row metals, with which they form strong, nearly ionic bonds.[2a, 27b, 28] This ionic nature arises due to the high electronegativity of oxygen. Alkoxides are also poor σ-donating ligands. However, they are excellent π-donating ligands due to the presence of three lone pairs on the binding oxygen. There has been significant interest in the quantification of the π-donation capability of alkoxides.[29] In the late 1980s and early 1990s, the revival of interest in transition metal alkoxide

chemistry stemmed from an orbital analogy proposed by Wolczanski and coworkers that compared an alkoxide ligand to a Cp ligand (**Figure 6**).[29a] The crux of this proposition centers around the comparison of the three linear combination orbitals of Cp—one σ-type and two π-type—to the σ-type and π-type interactions of an alkoxide. This theoretically means that an alkoxide ligand can serve as a six-electron donor, similar to a Cp ligand.

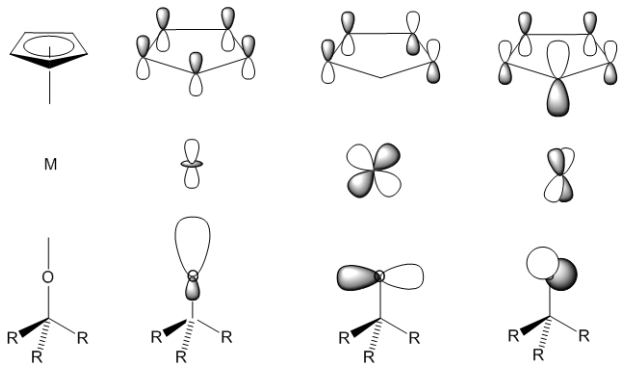

Figure 6. Orbital analogy between a Cp ligand and an alkoxide showing the σ- and π-bonding with the metal.

One commonly encountered issue when working with alkoxide ligands is their overwhelming tendency to bridge between metal centers. This bridging arises primarily due to increased nucleophilicity of the lone pairs on the alkoxide oxygen. Often undesirable, this bridging is commonplace for simple alkoxide complexes of most of the transition metals, giving rise to cluster-type and polymeric complexes, many of which are difficult to characterize due to their lack of solubility in organic solvents.[30] Characterization of those complexes that do dissolve in organic solvents is further complicated by the lability of the alkoxide ligand in solution, which gives rise to a multitude of concentration-dependent solution structures that often differ drastically from their solid-state structures. Unsurprisingly, this makes the isolation of alkoxide complexes with low nuclearities very challenging. Two solutions to remedy this issue have previously been employed: adding fluorine groups to create an electron-deficient alkoxide, and adding steric bulk to the alkoxide to minimize steric crowding at the metal center.

The chemistry of electron-deficient fluorinated alkoxides has recently been explored by Doerrer

and coworkers and will only briefly be mentioned here.[31] Through the use of the highly fluorinated alkoxide ligand [$OC(CF_3)_3$], the nucleophilicity of the alkoxide lone pairs was greatly diminished, allowing for the isolation of monomeric alkoxide complexes of the later first-row transition metals. A consequence of this, however, is the sharp decrease in π-donating capabilities of the alkoxide, as proven by DFT calculations. Thus, while monomeric complexes were able to be isolated, the alkoxide ligands stabilizing them behaved more like halide ligands rather than good π-donating ligands.

1.4. The Chemistry of Bulky Alkoxides

The use of bulky alkoxides to minimize bridging has proven to be a far more widely studied approach toward the synthesis of alkoxide complexes with low nuclearities. The chemistry of bulky alkoxides has primarily been explored by two groups—the Wolczanski group and the Power group—in the late 1980s and early 1990s. Both groups utilized the alkoxide ligand known as "tritox", [OC^tBu_3], to synthesize a wealth of early and late transition metal alkoxide complexes.[29, 32] In nearly all cases the complexes were well-defined mononuclear or dinuclear species that displayed exceptional solubility in organic solvents. The structures of some of the most commonly utilized bulky alkoxide ligands are shown in **Figure 7** below. These include the aforementioned tritox ligand, as well as the phenyl and cyclohexyl derivatives [$OCPh_3$] and [$OCCy_3$], whose chemistry was explored primarily by Power and coworkers.[33] Also shown is the asymmetric alkoxide [OC^tBu_2H] studied by Wilkinson and coworkers, as well as Power and coworkers.[32d, 34] Most recently, the asymmetric [OC^tBu_2Me], or "ditox" ligand, has been explored by Nocera and coworkers.[35]

By far the most thoroughly explored bulky alkoxide chemistry is that of the tritox ligand. The synthesis of this ligand was achieved by simple addition of one equivalent of *tert*-butyl lithium to one equivalent of hexamethylacetone.[32c, 36] Protic workup afforded the alcohol HOC^tBu_3 (**Figure 8**). An alternative synthesis involved addition of two equivalents of *tert*-butyl lithium to methyl pivalate to afford the alcohol, followed by subsequent lithiation with *n*-butyl lithium to give the lithium tritox salt as a dimer.[32c] Other bulky alkoxides mentioned henceforth can be synthesized using similar procedures.

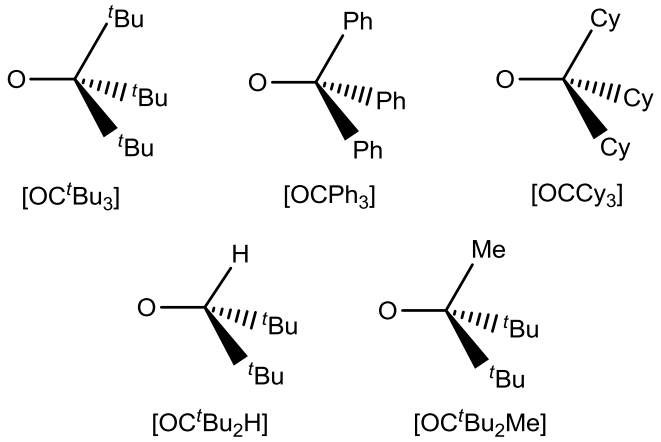

Figure 7. Structures of several bulky alkoxide ligands.

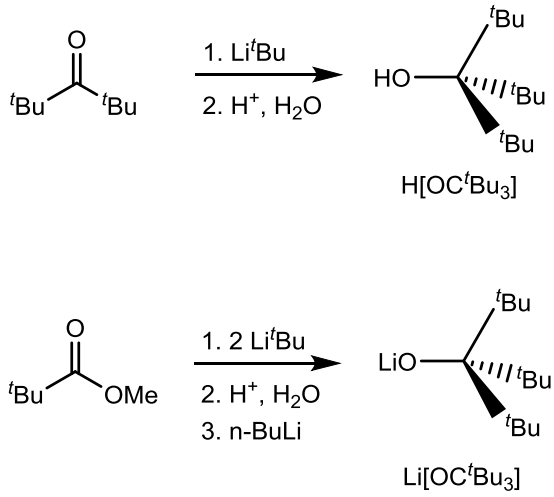

Figure 8. Synthesis of the [OC(^{t}Bu)$_3$] precursor.

The tritox ligand is generally considered to be the bulkiest alkoxide ligand, with a cone angle greater than 120°, as determined by Wolczanski and coworkers. The coordination chemistry of tritox at transition metal centers is dominated by bis(tritox) complexes. While mono(tritox) complexes can be prepared under certain conditions, no tris(tritox) transition metal complexes have been reported. Wolczanski and coworkers have investigated the coordination behavior of tritox in complexes of titanium and zirconium (see **Figure 9** for the chemistry of titanium-tritox complexes).[32c, 32f] Salt metathesis of $TiCl_4$ with one or two equivalents of Li[OC^{t}Bu$_3$] lead to the formation of Ti(OC^{t}Bu$_3$)Cl$_3$ and

$Ti(OC^tBu_3)_2Cl_2$, respectively. Alkylation of $Ti(OC^tBu_3)Cl_3$ and $Ti(OC^tBu_3)_2Cl_2$ with MeMgCl formed $Ti(OC^tBu_3)Me_3$ and $Ti(OC^tBu_3)_2Me_2$, respectively. These species can be considered analogues of the corresponding mono(cyclopentadienyl) and bis(cyclopentadienyl) complexes. Bis(tritox) complexes are significantly more stable than the corresponding mono(tritox) complexes: while $Ti(OC^tBu_3)Me_3$ decomposes at room temperature within several hours, only 10% decomposition is observed for $Ti(OC^tBu_3)_2Me_2$ after two weeks at 100 °C in C_6D_6. Furthermore, the bis(tritox) titanium dimethyl complex is more stable than its bis(cyclopentadienyl) analogue that was reported to decompose upon heating to 97 °C.[37] Both mono(tritox) and bis(tritox) titanium methyl complexes underwent oxygen insertion reactions to give mixed titanium-methoxide products.

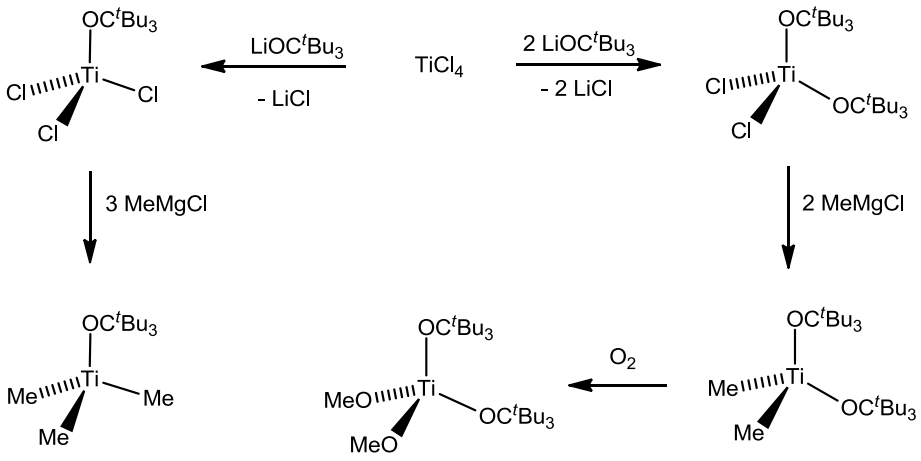

Figure 9. Chemistry of the mono(tritox) and bis(tritox) titanium complexes.

Power and coworkers have investigated the chemistry of chromium, manganese and cobalt with $[OC^tBu_3]$.[32a, 32b, 32d, 32e] The obtained complexes were of $[M(OC^tBu_3)_2X(THF)_n]^-$ or $[M(OC^tBu_3)_2X_2]^{2-}$ form (M = Cr, Mn, Co; X = Cl, Br, $N(SiMe_3)_2$; n = 0-2) in which the transition metal centers featured trigonal planar or tetrahedral geometry. The complexes were generally obtained by salt metathesis reactions, or by protonolysis reactions (see **Figure 10** for selected examples). The precise structure of the resulting compounds was determined by the reaction conditions, emphasizing lability of the alkoxide ligands. In all cases, however, only two $[OC^tBu_3]$ ligands coordinated to a single transition metal center, consistent with the previously described findings in titanium chemistry.

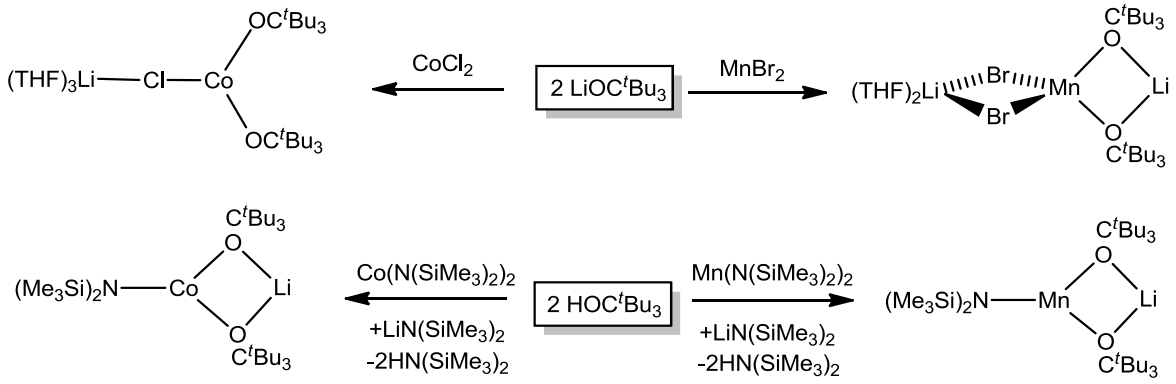

Figure 10. Coordination chemistry of manganese and cobalt with [OC^{t}Bu$_3$].

The related alkoxide ligands [OCPh$_3$] and [OCCy$_3$] manifest similar coordination behavior to that of [OC^{t}Bu$_3$] with 3d metals, generally forming bis(alkoxide) complexes, although stable mono(alkoxide) complexes featuring additional non-alkoxide ligands have also been prepared.[38] Due to the ease of its synthesis and the availability of starting materials, [OCPh$_3$] proved to be somewhat more popular than other bulky alkoxide ligands. Power and coworkers described a series of M(OCPh$_3$)$_2$L$_2$ complexes (M = Mn, Fe, Co; L = THF, pyridine) obtained by the treatment of two equivalents of HOCPh$_3$ with M(N(SiMe$_3$)$_2$)$_2$ in THF or pyridine (**Figure 11**).[33a, 33c] M(OCPh$_3$)$_2$L$_2$ complexes demonstrate highly distorted (towards linearity) tetrahedral geometry featuring very wide RO-M-OR angles in the 140 – 154° range. For cobalt, both Co(OCPh$_3$)$_2$(THF)$_2$ and dinuclear [Co(OCPh$_3$)$_2$]$_2$ were obtained, depending on the choice of the reaction solvent (THF versus toluene, **Figure 11**). Osborn and coworkers reported both bis(triphenylmethoxide) and mono(triphenylmethoxide) chromyl complexes CrO$_2$(Cl)(OCPh$_3$) and CrO$_2$(OCPh$_3$)$_2$, both manifesting tetrahedral geometry at the Cr(VI) center.[33b] Another example of a mono(triphenylmethoxide) complex is Fe$_2$(μ_2-SAr)$_2$(OCPh$_3$)$_2$, which has been reported by Tatsumi and coworkers.[33d] The complex was obtained from the previously synthesized Fe(SAr)(N(SiMe$_3$)$_2$) by a protonolysis reaction. Fe$_2$(μ_2-SAr)$_2$(OCPh$_3$) was further used to prepare an oxygen-containing model of the active site of iron-molybdenum nitrogenase.

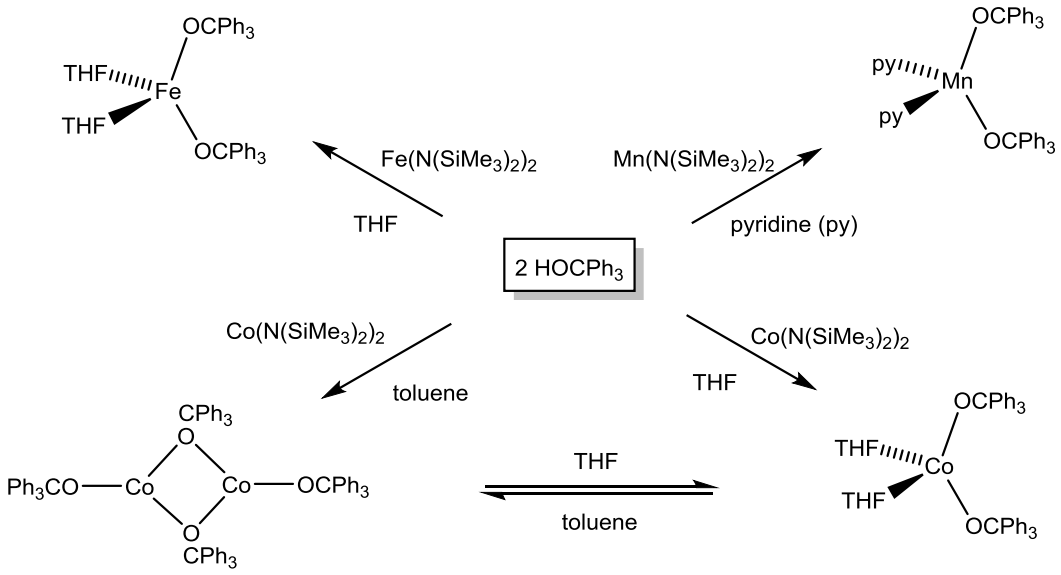

Figure 11. Coordination chemistry of [$OCPh_3$] at 3d metal centers.

Tris(*tert*-butyl)methoxide [OC^tBu_3] and triphenylmethoxide [$OCPh_3$] preferentially form tri- or tetra-coordinate bis(alkoxide) metal complexes $M(OR)_2L_n$, thus enabling steric control of the nuclearity and coordination numbers. The remaining positions (occupied by relatively weakly bound neutral ligands) may provide docking sites for a substrate of interest in the activation of small molecules/catalysis. It is important to note that no mononuclear tris(alkoxide) or tetra(alkoxide) species were observed for these ligands with transition metals. Thus, even though coordination of a monodentate alkoxide may be labile, no thermodynamic "sinks" of $M(OR)_3$ or $M(OR)_4$ composition are expected to form. In sharp contrast to the chemistry of [OC^tBu_3] and [$OCPh_3$], bis(*tert*-butyl)methoxide [OC^tBu_2H] leads to a variety of coordination modes, including tris(alkoxide) and tetrakis(alkoxide) complexes.[32d, 34] **Figure 12** demonstrates the synthesis of several 3d metal complexes which contain coordination of four [OC^tBu_2H] ligands to a single metal center. Formation of $M(OC^tBu_2H)_4$ occurs at even lower than 4:1 ligand-to-metal stoichiometries, emphasizing the importance of the third substituent at the central carbon for the control of the metal-alkoxide coordination sphere.

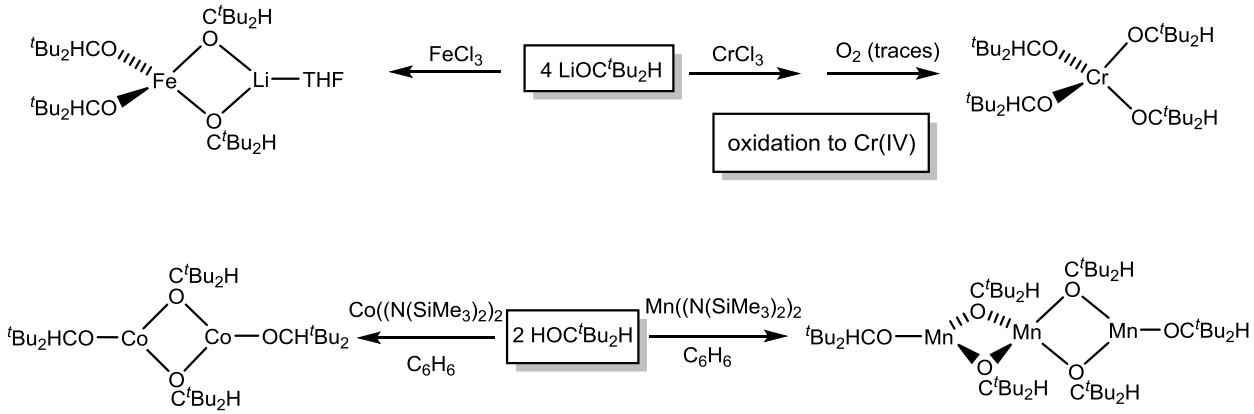

Figure 12. Synthesis of various complexes with [OC^{t}Bu$_2$H].

More recently the asymmetric bulky alkoxide ligand [OC^{t}Bu$_2$Me] has been investigated by the Nocera group. The term "asymmetric", as it is used here, refers to the asymmetry of the conical shape rather than the presence of a chiral center; true asymmetric alkoxides such as [OCMeEt^{i}Pr] have also been explored.[39] In the previous paragraphs, it was demonstrated that while [OC^{t}Bu$_3$] (and [OCPh$_3$]) produce mostly bis(alkoxide) ligand environments, [OC^{t}Bu$_2$H] leads to the formation of tetra(alkoxide) complexes. Nocera and coworkers postulated that the utilization of an R group in [OC^{t}Bu$_2$R] larger than H but smaller than ^{t}Bu may lead preferentially to the formation of tris(alkoxide) complexes. The resulting di-*tert*-butyl(methyl)methoxide ligand [OC^{t}Bu$_2$Me] (or "ditox") has indeed selectively formed three-coordinate (trigonal planar) or four-coordinate (trigonal monopyramidal or tetrahedral) complexes all featuring ligation of three ditox ligands. The reaction of three equivalents of LiOC^{t}Bu$_2$Me with VCl$_3$(THF)$_3$, CrCl$_3$(THF)$_3$ or FeCl$_3$ led to the formation of V(OC^{t}Bu$_2$Me)$_3$(THF), Cr(OC^{t}Bu$_2$Me)$_3$, and Fe(OC^{t}Bu$_2$Me)$_3$(THF), respectively (**Figure 13**).[35] The reaction of LiOC^{t}Bu$_2$Me with FeCl$_2$ formed heterodinuclear Fe(OC^{t}Bu$_2$Me)$_3$Li(THF) in which the Fe center is distorted trigonal planar. The reaction of FeCl$_2$ with KOC^{t}Bu$_2$Me followed by the addition of 12-crown-4 afforded the ion-separated complex [Fe(OC^{t}Bu$_2$Me)$_3$](K(12-crown-4)$_2$) in which the transition metal fragment is mononuclear and nearly perfectly trigonal planar. M(OC^{t}Bu$_2$Me)$_4$-type complexes were not detected even when an excess of ligand was used. Notably, tetrahedral M(OC^{t}Bu$_2$Me)$_3$(O) species demonstrate the aforementioned

preferred orientation of the defective cone in which the smallest substituent (Me) is forced to occupy the most sterically congested position. The resulting "head-to-tail" orientation leads to the nearly C_3-symmetrical structures of $M(OC^tBu_2Me)_3(O)$ complexes (discussed below).

The interesting structural dichotomy between the trigonal monopyramidal complex $V(OC^tBu_2Me)_3(THF)$ and trigonal planar $Cr(OC^tBu_2Me)_3$ prompted the authors to investigate the stability of $V(OC^tBu_2Me)_3(THF)$ in non-coordinating solvents. Several cycles of exposure of $V(OC^tBu_2Me)_3(THF)$ to vacuum followed by dissolution in toluene led to a gradual color change from blue to dark brown. Crystallization of the product from pentane yielded the V(III) dinitrogen complex $V_2(OC^tBu_2Me)_6(\mu_2\text{-}N_2)$ (**Figure 14**).[35b] Although the complex demonstrated a significant elongation of the N-N bond (1.23 Å vs. 1.10 Å in free N_2), the lack of reactivity of $V_2(OC^tBu_2Me)_6(\mu_2\text{-}N_2)$ with reducing agents and the loss of N_2 in solution was consistent with a relatively weak binding/activation of N_2. Nevertheless, it remains a rare example of a dinitrogen complex of any metal in an oxygen-only ligand environment,[40] being potentially relevant to Shilov's chemistry of nitrogen fixation by vanadium and molybdenum hydroxides.[41]

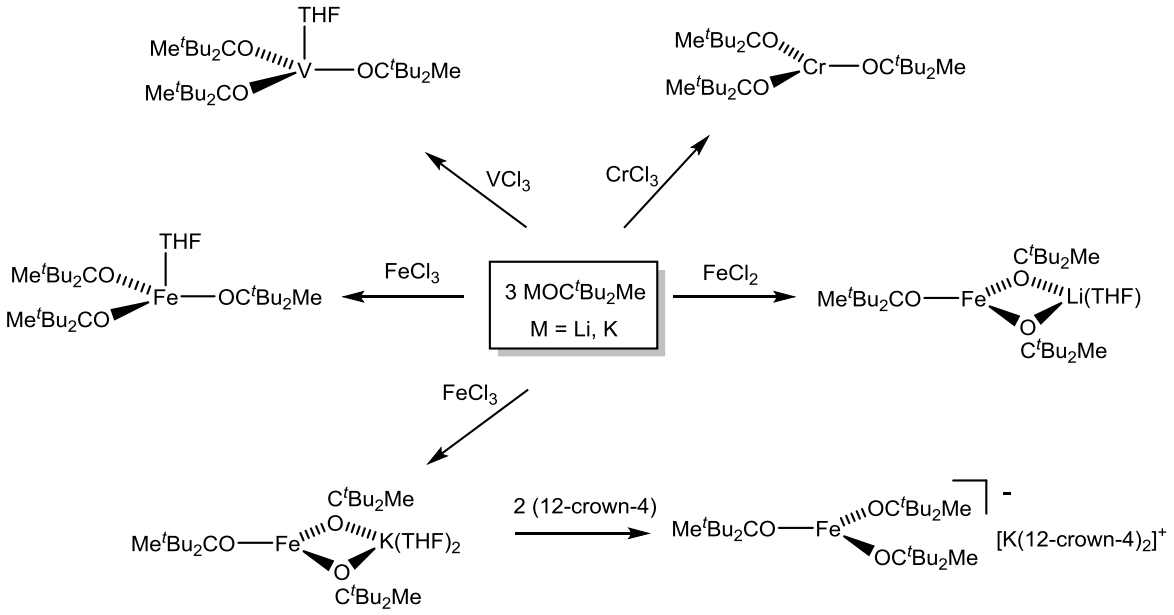

Figure 13. Coordination chemistry of ditox with selected 3d transition metals.

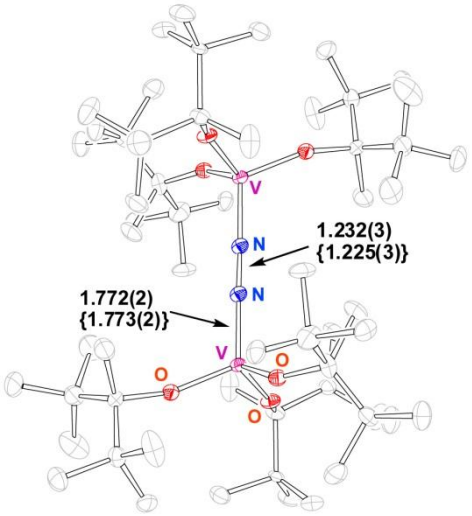

Figure 14. X-ray crystal structure of $V_2(OC^tBu_2Me)_6(\mu_2\text{-}N_2)$. Two independent molecules with slightly different metrics are present in the asymmetric unit.

1.5. Metal-Ligand Multiple Bonding in Alkoxide Ligand Environments: Recent Advances

Recently, Nocera and coworkers also reported on some of the first examples of metal-ligand multiple bonding in alkoxide ligand environments. Specifically, tetrahedral metal-oxo complexes in alkoxide ligand environments (M = V, Cr, Fe) were targeted.[35b, 35c] Unlike other bulky alkoxides, [OC^tBu_2Me] formed tris(alkoxide) complexes exclusively, thus allowing for the formation of a homologous series of pseudotetrahedral metal-oxo complexes of the form $M(OC^tBu_2Me)_3(O)$. The initial study focused on the d^0, d^1 and d^2 complexes $V(OC^tBu_2Me)_3(O)$, $Cr^V(OC^tBu_2Me)_3(O)$, and $[Cr^{IV}(OC^tBu_2Me)_3(O)]$, which were prepared via oxo-transfer from the corresponding $M(OC^tBu_2Me)_3$ complexes (vanadium(V) and chromium(V)), or by the reduction of a corresponding metal(V) complex (chromium(IV)) (**Figure 15**). The complexes were characterized by X-ray crystallography, IR spectroscopy, magnetic measurements, and DFT calculations (**Figure 16**). The study revealed strong dependence of the $M(OR)_3$-oxo functionality on the number of d electrons, with d electrons residing primarily in the metal-oxo antibonding orbitals and thus affecting metal-oxo bond order. As such, a d^0 V(V)-oxo demonstrates a triple bond, a d^1 Cr(V)-oxo features a 2.5 order bond, and a d^2 Cr(IV)-oxo features a double bond. The nature of the Cr(IV)-oxo and the Cr(V)-oxo was also probed by reactivity

studies. Generally, metal-oxo complexes featuring double bonds are nucleophilic (i. e. are easily protonated), whereas metal-oxo complexes featuring triple bonds do not react even with strong acids.[42] The observed nucleophilic reactivity of $[Cr(OC^tBu_2Me)_3(O)]^-$ (**Figure 15**) is consistent with the double-bond formulation: it undergoes an immediate reaction with Me_3SiCl (a proton surrogate) to form $Cr^{IV}(OC^tBu_2Me)_3(OSiMe_3)$. Under the same reaction conditions no reaction between $Cr^V(OC^tBu_2Me)_3(O)$ and Me_3SiCl was observed. This behavior of a pseudotetrahedral metal-oxo stands in contrast to the behavior of tetragonal metal-oxos, in which a d^2 Cr(IV)-oxo features a triple bond and reacts as an electrophile.[43]

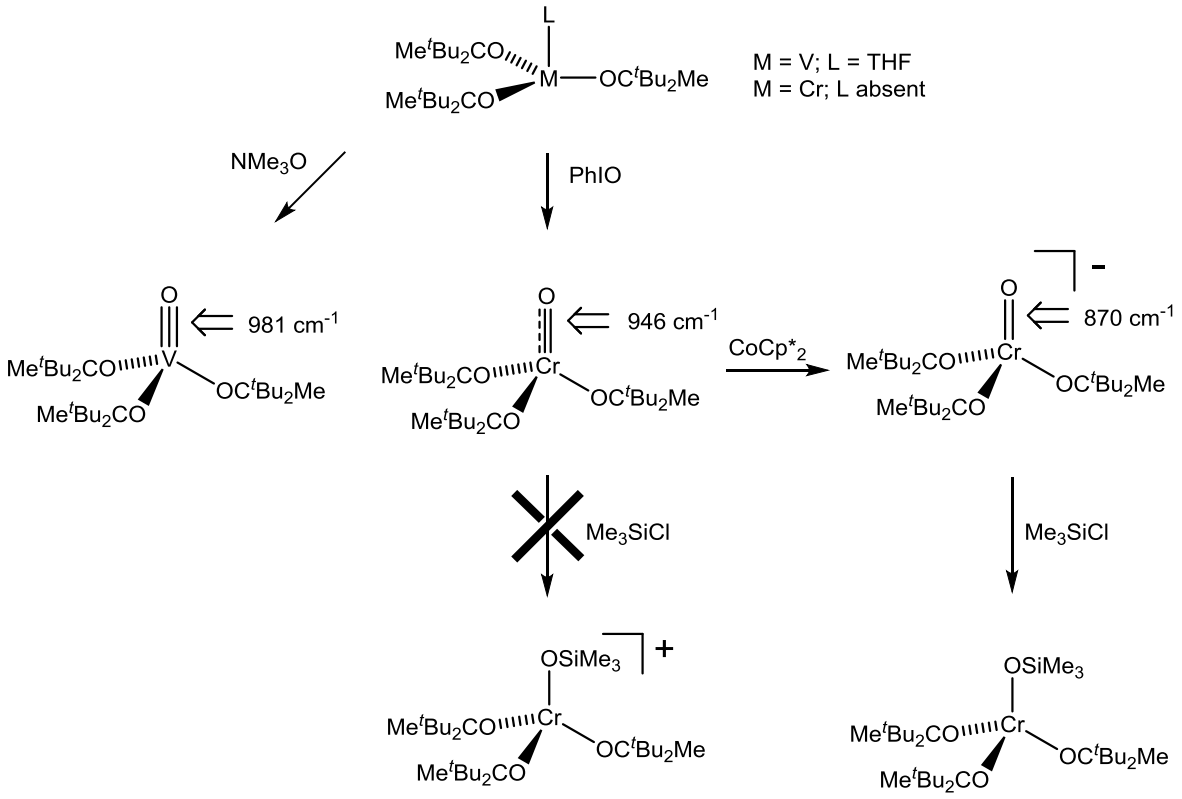

Figure 15. Synthesis of d^0, d^1, and d^2 metal-oxos indicating bond orders, IR stretching frequencies of the corresponding metal-oxo bonds, and reactivity of the Cr(IV) and Cr(V)-oxo with Me_3SiCl.

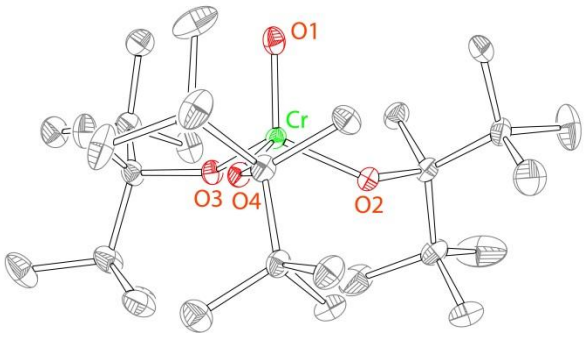

Figure 16. X-ray crystal structure of pseudotetrahedral $Cr(OR)_3(O)$ demonstrating the "head-to-tail" arrangement of the ditox ligands.

Nocera and coworkers have also investigated the d^4 complex $[Fe(OC^tBu_2Me)_3(O)]^-$.[35c] An Fe(IV)-oxo complex was generated via oxo-transfer to $[FeLi(OC^tBu_2Me)_3(THF)]$ or to $[FeK(OC^tBu_2Me)_3(THF)_2]$ using iodosylbenzene (PhIO) (**Figure 17**). As anticipated from the study of Cr(V) and Cr(IV) oxo complexes, Fe(IV) oxo was found to be high-spin (quintet, by DFT calculations) and therefore highly reactive. Generation of the $[Fe^{IV}(OC^tBu_2Me)_3(O)]^-$ in protio solvents (THF, benzene, cyclohexane, pentane) formed Fe(III)-hydroxo complexes, all of which contain a $[Fe^{III}(OC^tBu_2Me)_3(OH)]^-$ core but differ by the coordination environment of the alkali metal ion. The formation of the Fe(III)-hydroxo products is postulated to proceed via an H-atom abstraction by the transient $[Fe^{IV}(OC^tBu_2Me)_3(O)]^-$. This hypothesis is supported by the fact that the reaction in THF leads to the formation of two products, one of which ($[Fe^{III}Li(OC^tBu_2Me)_3(OH)(2,2'\text{-OHBF})]$) features the peculiar C−C coupled 2,2'-octahydrobifuran ligand (2,2'-OHBF) that is likely generated by the coupling of two tetrahydrofuranyl radicals resulting from H-atom abstraction from the THF solvent (**Figure 17** and **Figure 18**). In acetonitrile, the reaction of $[Fe(OC^tBu_2Me)_3](K(12\text{-crown-}4)_2)$ with PhIO yields $[Fe(OC^tBu_2Me)_3(CH_2CN)](K(12\text{-crown-}4)_2)$. It is possible that the "$NCCH_2^-$" ligand similarly results from the H-atom abstraction from $NCCH_3$, followed by recombination of $NCCH_2$ radical with another Fe(II) center. In 1,2-difluorobenzene, transient $[Fe^{IV}(OC^tBu_2Me)_3(O)]^-$ catalyzes oxo-transfer to Ph_3P to form Ph_3PO.

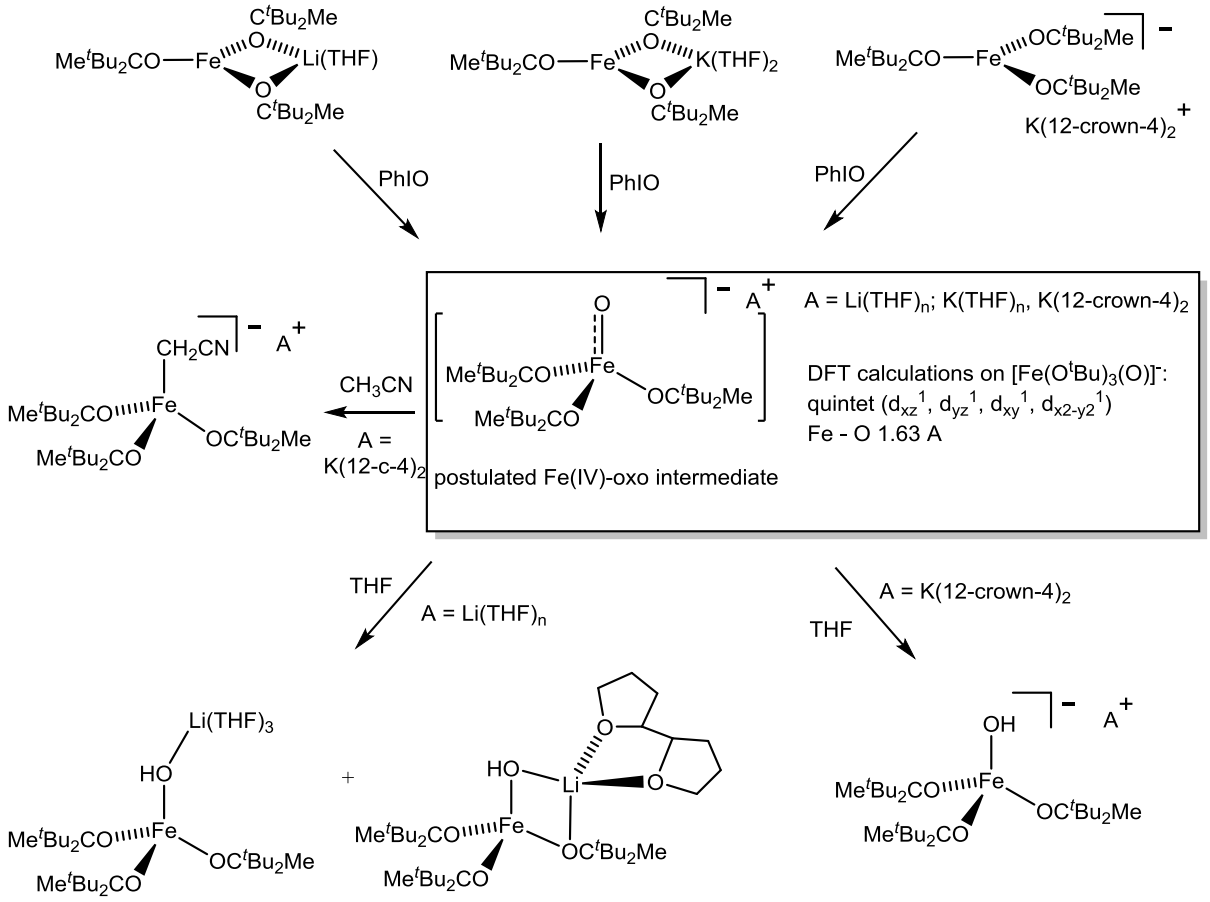

Figure 17. Oxidation reactivity of [Fe(OCMe^{t}Bu$_2$)$_3$] complexes.

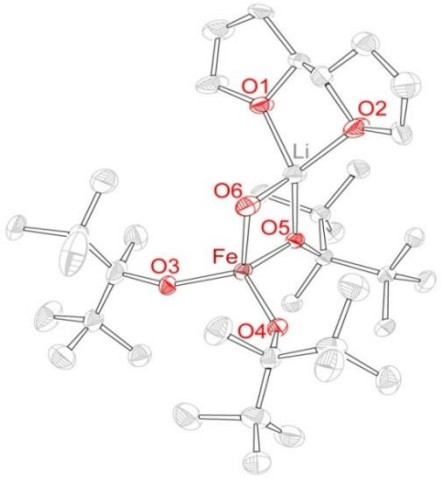

Figure 18. Structure of [Fe^{III}Li(OC^{t}Bu$_2$Me)$_3$(OH)(2,2'-OHBF)], isolated from the reaction of [FeLi(OC^{t}Bu$_2$Me)$_3$(THF) with PhIO in THF.

1.6. Summary and Outlook

Group transfer reactions, including oxo, nitrene, and carbene transfer reactions, continue to be some of the most highly sought after transformations in the chemistry of the transition metals. Recently there has been a great interest in utilizing the cheaper, more readily accessible first-row transition metals to design complexes containing M=X multiple bonds (X = O, NR, CR_2) for catalytic group transfer reactions. Specifically, the later first-row transition metals often lead to reactive metal-imido complexes that could potentially be used for group transfer processes. Both early and late metal carbene complexes can be employed for various C−C bond forming reactions. A common trend among isolated first-row transition metal complexes with metal-ligand multiple bonds is the use of strong-field σ-donating ligands and lower coordination numbers. There has been relatively little investigation of metal-ligand multiple bonds stabilized by weak-field ligands.

Prior to this dissertation, there is little doubt that the chemistry of bulky alkoxides has been thoroughly explored. The groups of Wolczanski, Power, and others have devised synthetic means to create simple mononuclear or dinuclear alkoxide complexes for nearly all of the first-row transition metals. What is noticeably lacking from the literature though is any study of bulky alkoxide complexes toward group transfer and small molecule activation reactions. Only recently through the work of Nocera and coworkers has the synthesis and reactivity of alkoxide complexes containing multiply bonded oxo ligands been explored, as well as the surprising reactivity of a vanadium alkoxide complex with dinitrogen. There is a noticeable absence of these types of reactivity investigations with first-row transition metal alkoxide complexes, as well as with alkoxide complexes in general.

1.7. Research Statement and Objectives

The major focus of this research emphasizes the use of first-row transition metals toward the synthesis of novel alkoxide complexes for catalytic group transfer reactions and small molecule activation. The first-row metals are attractive for this purpose due to their higher abundance and lower overall cost. They also form strong, nearly ionic bonds with alkoxide ligands. However, a major hurdle to overcome in first-row transition metal catalysis is the difficulty in inducing multi-electron chemistry at

the first-row metal, a property synonymous with the second and third row metals. One means to combat this issue is to increase complex reactivity by enforcing lower coordination numbers at the metal through the use of sterically demanding ligands. This creates a more electrophilic, reactive metal center while conversely providing steric protection, allowing only small molecules to penetrate the inner coordination sphere and minimizing ligand lability issues that may arise in solution. The specific metals focused on in this research are the later first-row transition metals (Cr-Cu). With their more populated d-orbitals, the later metals are predicted to form more reactive metal-ligand multiple bonds due to increased π* character of the M=X bond.

The ligand of choice in this research is the asymmetric alkoxide, [OC^{t}Bu$_2$Ph] (**Figure 19**). As discussed previously, alkoxide ligands are hard, π-donating ligands that form strong bonds with first-row transition metals. Similar to previously synthesized bulky alkoxide ligands, [OC^{t}Bu$_2$Ph] (henceforth abbreviated as [OR] for convenience) possesses two *tert*-butyl groups that provide necessary steric bulk while also allowing the alkoxide complexes formed to be soluble in organic solvents of low polarity. The addition of a phenyl group on the ligand maintains the asymmetry of the alkoxide ligand, giving it an overall directionality and allowing for improved crystallinity of its complexes. It also allows for tunability, should additional steric bulk on the ligand be required. The type of precursor envisioned in this research is the bis(alkoxide) framework shown in **Figure 19**. The added phenyl group makes the alkoxide ligand bulkier than the ditox ligand reported by Nocera and coworkers, which may prevent the formation of tris(alkoxide) complexes. Labile solvent ligands L could be coordinated to the complexes formed. Upon reaction with nitrene- or carbene-transfer agents, these weakly bound ligands can be removed, generating reactive three-coordinate complexes of the type M(OR)$_2$(X) (X = NR', CR'$_2$) (**Figure 20**). The presence of the alkoxide ligands in these types of complexes is expected to destabilize the metal-ligand multiple bond by competing for π-donation with the imido or carbene. This in turn should facilitate simple transfer of nitrene or carbene to various substrates.

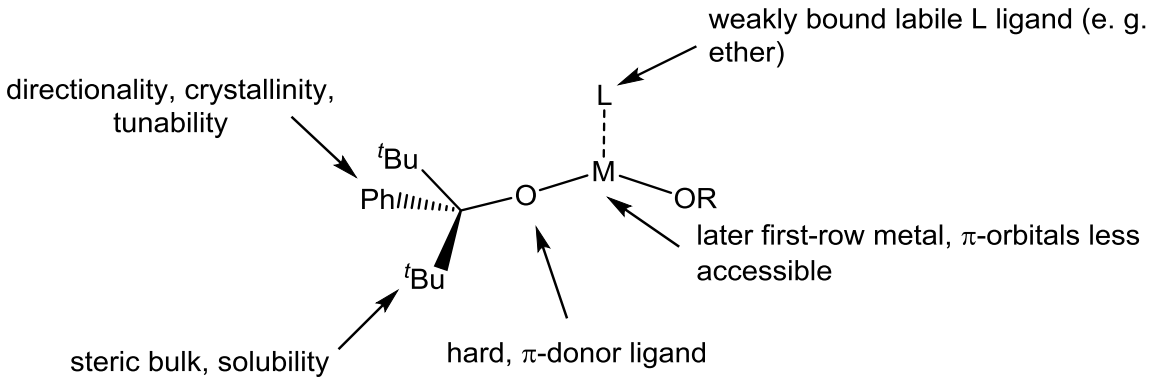

Figure 19. Design of first-row bis(alkoxide) complexes supported by [OC^{t}Bu$_2$Ph].

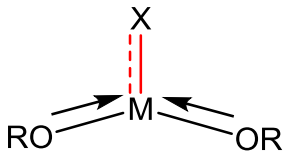

Figure 20. Proposed design of three-coordinate imido or carbene complexes in a bis(alkoxide) ligand environment (X = NR', CR'$_2$).

The overall goal of this research is to explore the synthesis and reactivity of middle to late first-row transition metal imido and carbene complexes in a bis(alkoxide) ligand environment. Three objectives toward the pursuit of this goal are:

1. ***Design and Synthesis of a Bis(alkoxide) System of the Middle and Late First-Row Transition Metals.*** Full synthesis and characterization of the complexes will be performed. This objective is addressed in Chapters 2 and 3.
2. ***Exploration of the Reactivity of Bis(alkoxide) Complexes with Alkyl and Aryl Azides.*** Reactivity of the bis(alkoxide) complexes with azides toward the synthesis of novel imido complexes will be investigated, as well as their potential for nitrene transfer. This objective is addressed in Chapters 4 and 5.

3. ***Exploration of the Reactivity of Bis(alkoxide) Complexes with Diazoalkanes.*** Bis(alkoxide) reactivity with diazoalkanes toward the synthesis of novel carbene complexes will be explored, as well as their potential for carbene transfer. This objective is addressed in Chapter 6.

These topics were developed over the course of the last four years and constitute the body of this dissertation.

CHAPTER 2: REACTIVITY OF THE BULKY ALKOXIDE [OC^{t}Bu$_2$Ph] WITH FIRST-ROW TRANSITION METALS: NOVEL CLUSTER TOPOLOGIES FEATURING RARE SEESAW GEOMETRY AT TRANSITION METAL CENTERS

Portions of the text in this chapter were reprinted or adapted with permission from: (a) Bellow, J. A.; Fang, D.; Kovacevic, N.; Martin, P. D.; Shearer, J.; Cisneros, G. A.; Groysman, S. *Chem. Eur. J.* **2013**, *19*, 12225-12228. (b) Bellow, J. A.; Yousif, M.; Fang, D.; Kratz, E. G.; Cisneros, G. A.; Groysman, S. *Inorg. Chem.* **2015**, *54*, 5624-5633.

2.1. Introduction

As discussed in Chapter 1, there is a noticeable lack of alkoxide complexes being utilized for small molecule activation and group transfer reactions. The objective of this chapter was to synthesize novel bis(alkoxide) precursors using the newly synthesized [OR] ligand. These complexes can then be tested as precursors for nitrene and carbene transfer, which shall be discussed in subsequent chapters. We investigated the reactivity of [OR] with the middle to late transition metals chromium, manganese, iron, cobalt, nickel, and copper, expecting a facile means toward obtainment of bis(alkoxide) complexes of the type $M(OR)_2L_n$ (L = labile solvent ligand, n = 0-2). Isolation and crystallographic characterization of the complexes formed will be discussed first. Characterization of the complexes via a multitude of experimental, spectroscopic, and computational techniques will follow.

2.2. Synthesis and Characterization of the Novel Transition Metal Clusters $M_2(OR)_4Li_2Cl_2$

2.2.1. Synthesis and Structural Characterization

Treatment of one equivalent of hexamethylacetone with one equivalent of phenyllithium followed by workup and crystallization from hexane afforded the lithium salt of [OR] (**1**) as a white, crystalline solid (**Figure 21**). X-ray structure determination reveals that **1** crystallizes as a trimer in the solid state, with two-coordinate geometry featured at the lithium centers (**Figure 22**).

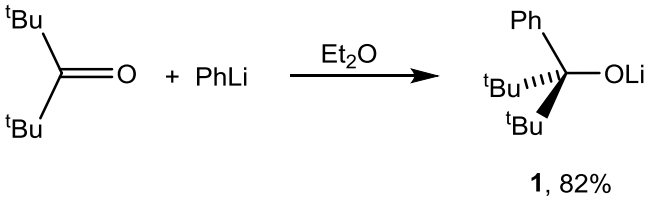

Figure 21. Synthesis of **1**.

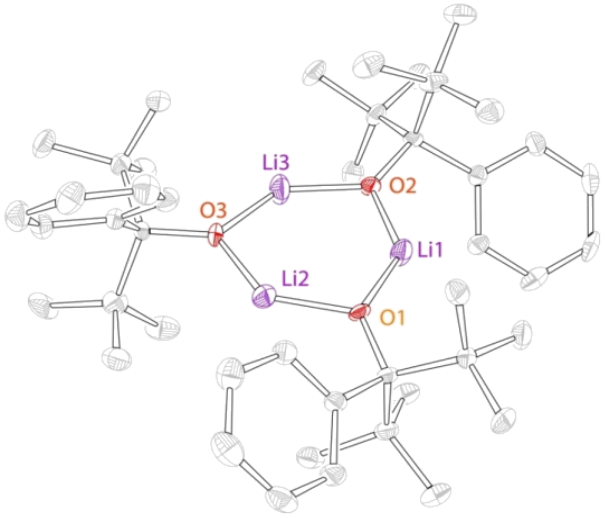

Figure 22. Crystal structure of **1**, 50% probability ellipsoids. H atoms are omitted for clarity.

As an initial test to synthesize the desired bis(alkoxide) complexes, two equivalents of **1** were added to one equivalent of iron(II) chloride in THF. Workup in the presence of small amounts of THF followed by crystallization from hexanes afforded the three-coordinate bis(alkoxide) complex $Fe(OR)_2ClLi(THF)_2$ (**2**, **Figure 23**). Notably, while the bis(alkoxide) moiety had indeed been synthesized, the complex also contained bound chloride and lithium ions. Ion inclusion such as this was commonly observed in the previously discussed alkoxide complex synthesis. Specifically, **2** is structurally similar to the chromium bis(alkoxide) complex synthesized by Power and coworkers using the tritox ligand.[32a] Complex **2** is noticeably unstable, however: upon workup from hexane or by repeated removal of hexane under vacuum, the labile THF ligands of **2** can be removed, followed by dimerization to give the cluster compound $Fe_2(OR)_4Li_2Cl_2$ (**3**, **Figure 23**). Following the same procedure, the isostructural chromium, manganese, and cobalt complexes can be synthesized from the analogous metal(II) chlorides (complexes

4-**6**, **Figure 23**). X-ray quality crystals of all the dimeric complexes could be obtained by crystallization from hexanes.

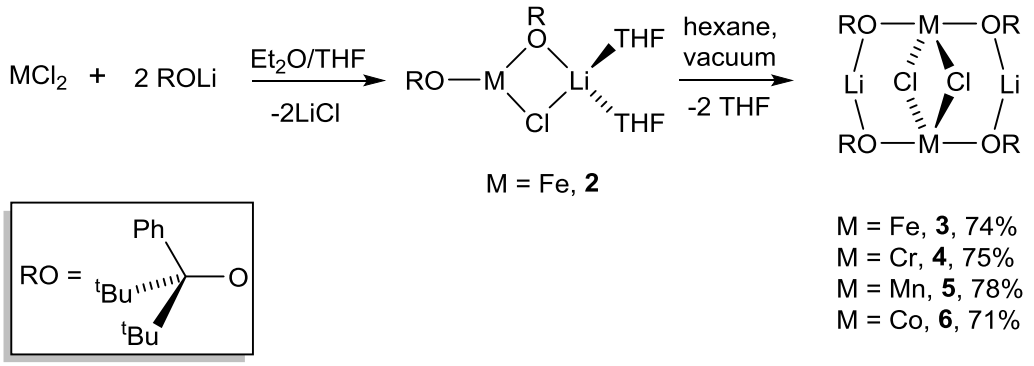

Figure 23. Synthesis of the novel transition metal alkoxide clusters **2**-**6**.

The structures of **2**-**6** were all determined by X-ray crystallography. The structures of **3** and **5** are shown in **Figure 24** below. The analogous structures of **4** and **6**, as well as the structure of **2**, can be found in Appendix B. A table of selected bond lengths and angles for **3**-**6** can be found in **Table 1**. Experimental crystallographic parameters for structures **1**-**6** are listed in **Tables 2** and **3**. Complexes **3**-**6** are all isostructural clusters featuring an $M_2(OR)_4Li_2Cl_2$ core. Each chloride is bridging two transition metals. The lithium centers are two-coordinate as in the structure of **1**, and the transition metals are four-coordinate. A Crystal Structure Database search demonstrates that such a topology is unprecedented.[44] Most significantly, **3**-**6** all possess seesaw geometry at the transition metal centers. The space-filling model of **3** (**Figure 24c**) shows the bulky *tert*-butyl and phenyl groups on the alkoxides forming a tight cage around the complex. We propose that the seesaw geometry arises in part because of the steric bulk of the alkoxide ligands. The immediate coordination environment of the transition metals is presented in **Figure 24d**. The O−M−O angles of the complexes range from 171° to 176°, and the Cl−M−Cl angles are all within the 84°-88° range. The M−Cl distances in each complex are similar to those in related complexes, suggesting that there are actual M−Cl bonds in these structures.[32a, 32e, 45] In addition, the Li−Cl distances range from 2.5-3.0 Å, which are longer than those in related structures.[32a, 32e, 45]

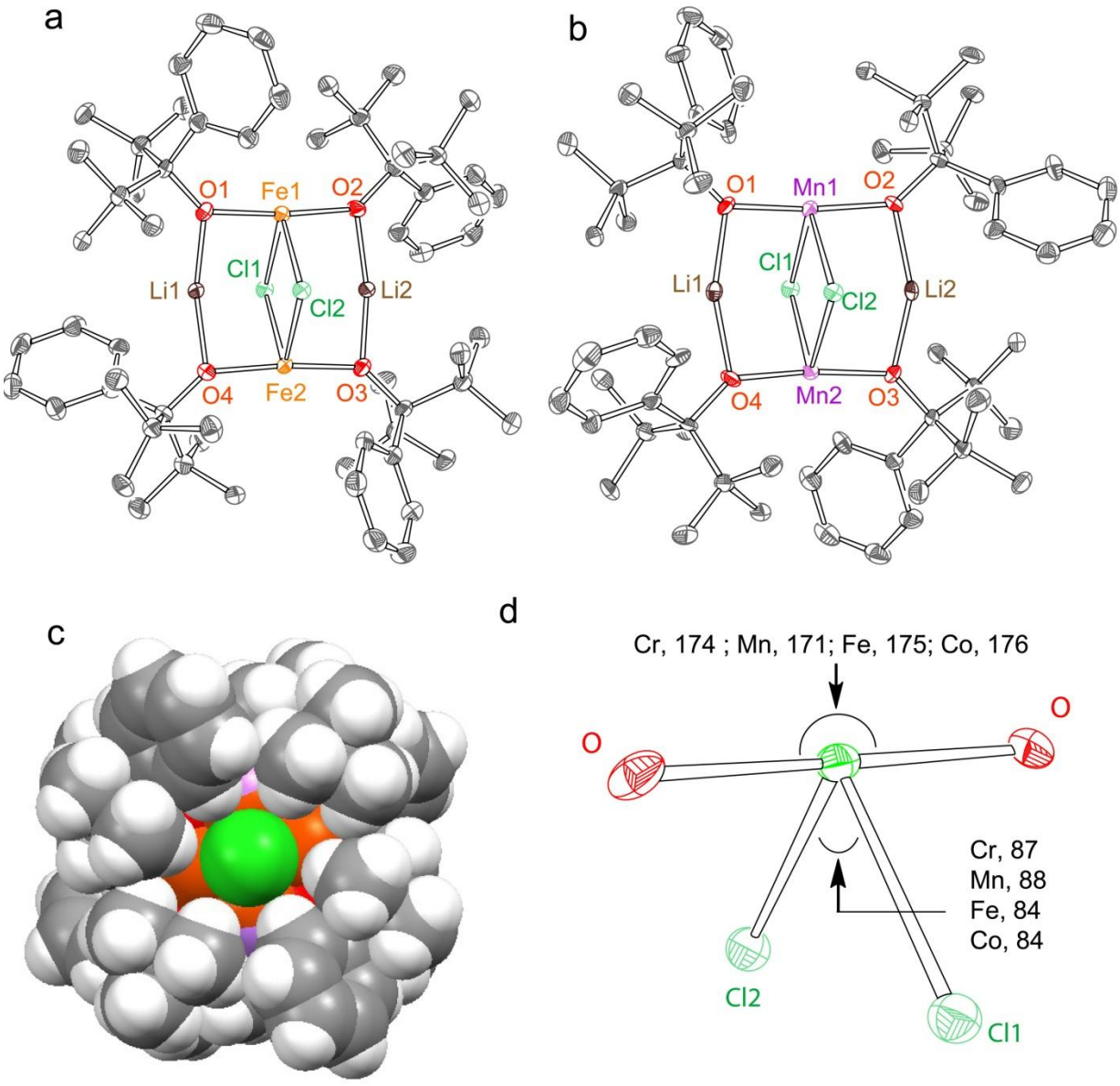

Figure 24. (a) Crystal structure of **3**. (b) Crystal structure of **5**. (c) Space-filling model of **3**. (d) Structure of seesaw core with O−M−O and Cl−M−Cl angles (°). For the crystal structures of **3** and **5**, 50% probability ellipsoids are shown. Hydrogen atoms are omitted for clarity.

Table 1. Selected structural data for **3**-**6**.

Complex	**3 (Fe)**	**4 (Cr)**	**5 (Mn)**	**6 (Co)**
M1−O1	1.904(4)	1.906(2)	1.926(2)	1.893(2)
M1−O2	1.917(4)	1.908(2)	1.915(2)	1.877(2)
M1−Cl1	2.474(2)	2.493(2)	2.455(1)	2.540(3)
M1−Cl2	2.520(2)	2.603(2)	2.600(1)	2.457(3)
O1−M1−O2	173.8(2)	175.2(1)	171.37(9)	175.5(2)
Cl1−M1−Cl2	86.96(8)	84.43(6)	88.07(4)	84.47(7)

Table 2. Experimental crystallographic parameters for **1**-**3**.

complex	**1**	**2**	**3**
formula	$C_{48}H_{76}O_3Li_3$	$C_{38}H_{62}O_4LiClFe$	$C_{72}H_{120}O_4Li_2Cl_2Fe_2$
fw	721.91	681.12	1246.3
crystal system	triclinic	monoclinic	rhombohedral
space group	*P-1*	$P2_1/n$	*R3c*
a (Å)	12.4967(11)	8.6288(9)	23.0159(11)
b (Å)	12.9665(12)	19.0324(17)	23.0159(11)
c (Å)	16.5773(14)	22.834(2)	23.0159(11)
α (deg)	93.467(3)	90.00	90.026(2)
β (deg)	104.742(3)	96.051(6)	90.026(2)
γ (deg)	117.338(3)	90.00	90.026(2)
V (Å^3)	2257.9(3)	3729.1(6)	12192.2(10)
D_c (g cm^{-3})	1.062	1.213	1.036
Z	2	4	6
μ (mm^{-1})	0.062	0.512	0.596
T (K)	100(2)	100(2)	100(2)
R_1 (%)	5.68	15.69	6.14
GOF	1.034	1.167	1.036

Table 3. Experimental crystallographic parameters for **4**-**6**.

complex	**4**	**5**	**6**
formula	$C_{205}H_{276}O_{12}Li_6Cl_6Cr_6$	$C_{60}H_{92}O_4Li_2Cl_2Mn_2$	$C_{60}H_{92}O_4Li_2Cl_2Co_2$
fw	3498.79	1072.03	1079.98
crystal system	rhombohedral	rhombohedral	rhombohedral
space group	*R3c*	*R3c*	*R3c*
a (Å)	32.452(2)	23.0213(3)	22.9432(13)
b (Å)	32.452(2)	23.0213(3)	22.9432(13)
c (Å)	39.787(3)	23.0213(3)	22.9432(13)
α (deg)	90.00	90.02	90.015(4)
β (deg)	90.00	90.02	90.015(4)
γ (deg)	120.00	90.02	90.015(4)
V (Å^3)	36288(4)	12200.8(3)	12077.1(12)
D_c (g cm^{-3})	0.305	1.107	1.188
Z	6	6	6
μ (mm^{-1})	0.166	0.345	0.680
T (K)	100(2)	100(2)	100(2)
R_1 (%)	6.52	4.54	4.99
GOF	1.094	0.923	0.874

2.2.2. Spectroscopic Characterization

To confirm that the structures obtained by single crystal diffraction analysis are representative of the bulk material, **3**, **5**, and **6** were subjected to metal K-edge X-ray absorption spectroscopy (in collaboration with Professor Jason Shearer, University of Nevada, Reno). The XANES region of the X-ray absorption spectra (XAS) all display pre-edge features corresponding to nominal 1s→3d transitions.

The pre-edge feature of **3** has a peak-area of 8.2(1) % eV relative to the edge height (**Figure 25a**). Although the geometry about the iron(II) center is unprecedented, we can think of the iron(II) center as contained in a pseudotrigonal bipyramidal structure. We find that the area under this feature compares well with other five-coordinate iron(II) complexes, and thus is consistent with seesaw geometry.[46]

High resolution (k = 2.0-17.5 Å^{-1}) EXAFS analysis of the XAS is also consistent with the crystallographic structure of **3**. In addition to the two Fe−O (1.89 Å), two Fe−Cl (2.48 Å), and one Fe−Fe (3.60 Å) vectors, there were also a plethora of multiple scattering (MS) pathways that needed to be accounted for to properly solve the EXAFS (**Figure 25b**). These MS pathways are strongly dependent on the O−Fe−O and Cl−Fe−Cl bond angles. A best fit to the data yields an O−Fe−O bond angle of 174° and a Cl−Fe−Cl angle of 86°. Thus, the results are consistent with the crystallographic data. Analysis of the XAS for **5** and **6** yield similar fits to the data (see Appendix B).

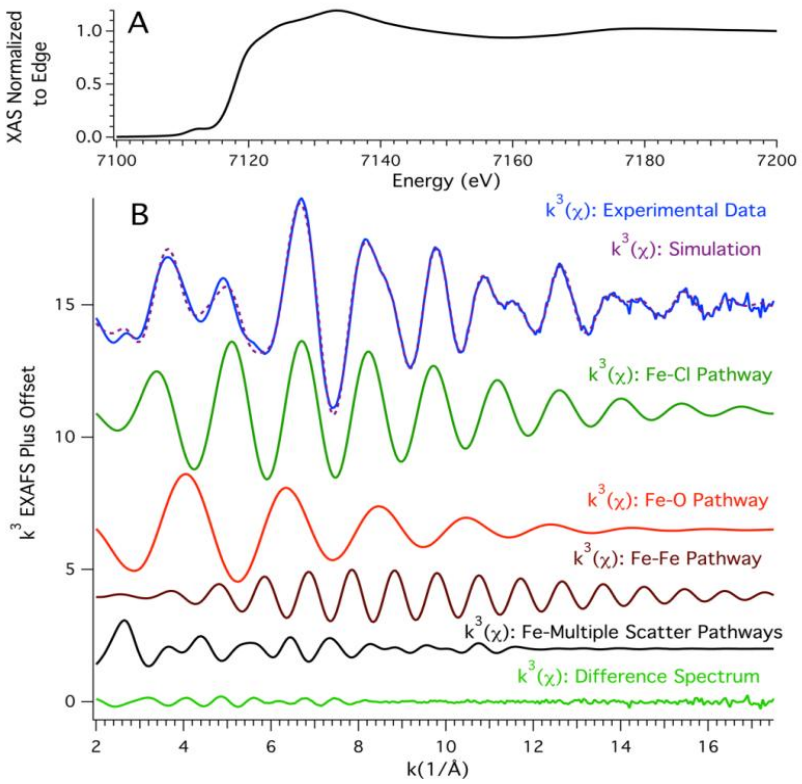

Figure 25. (a) XANES region of the Fe K-edge XAS for **3**. (b) The k^3 (χ) plots of the experimental data, best fit, deconvoluted scattering pathways, and residual for **3**.

Continuous symmetry measurements were also used to evaluate the geometry of the metal center.[47] These are calculated values that provide a numeric respresentation of how close the geometry at a metal center is to the predicted "perfect" geometry. The continuous symmetry values have been calculated using the method detailed by Cicera, Alemany, and Alvarez in the Shape2 software.[48] The continuous symmetry values of the crystal (computationally optimized) structures for **3**-**6** are 2.2 (2.6), 2.1 (2.5), 2.2 (2.4), and 2.0 (2.9), respectively. As the continuous symmetry values range from 0 to 100 (0 means perfect seesaw, whereas 100 means totally distorted), both crystal and computational structures present geometry close to that of a perfect seesaw.

We also carried out a preliminary investigation of the magnetic properties of **3**-**6**. To probe the solution state magnetic moments of **3**-**6**, the Evans method was conducted.[49] The largest effective magnetic moment observed was that of **5**, which was 11.6 μB. The expected spin-only magnetic moment for two uncoupled manganese(II) centers is 11.0 μB. The calculated and observed values were also similar for **3** (8.8 μB, calcd 8.9 μB), **4** (8.4 μB, calcd 8.9 μB), and **6** (7.8 μB, calcd 6.9 μB). We have also conducted SQUID magnetometry on **5** (in collaboration with the Freedman group, Northwestern University), featuring the largest number of unpaired electrons (**Figure 26**). SQUID data are fully consistent with solution measurements. At room temperature, a magnetic moment of 11.6 μB (χT = 16.8 cm^3 $(mol\ K)^{-1}$ is observed, indicating two uncoupled metal centers. At low temperatures, χT values drop to about 0, indicating antiferromagnetic coupling.

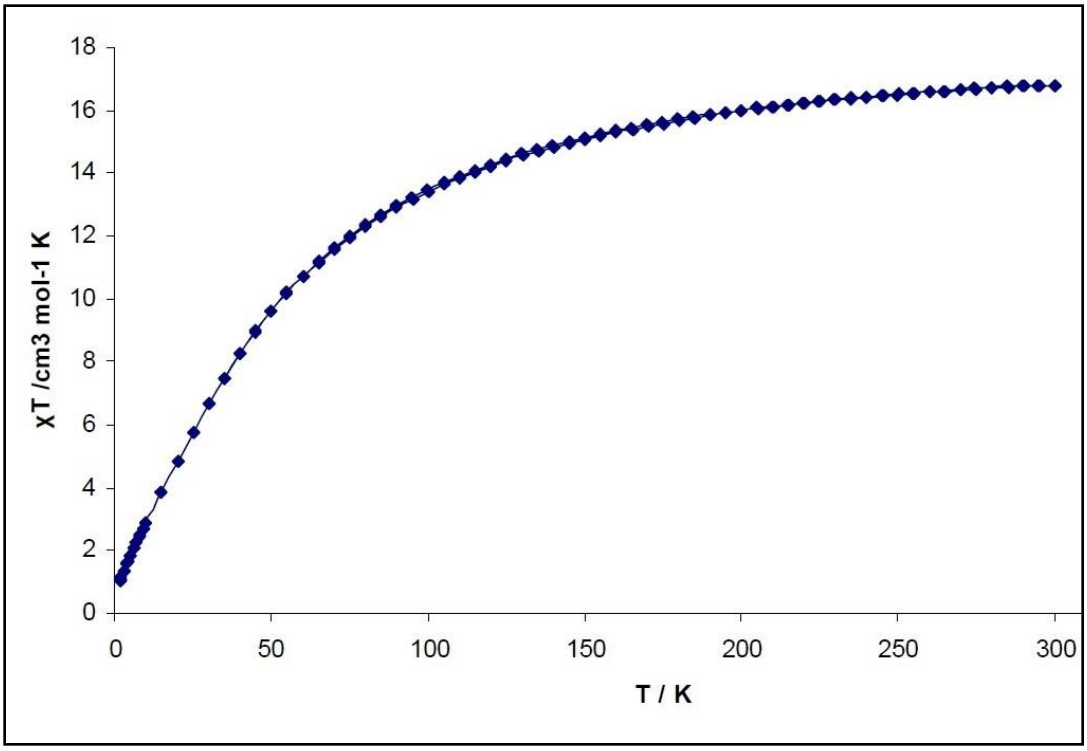

Figure 26. SQUID data for **5** (11.6 μB).

2.2.3. Computational Characterization

To shed light on the bonding and the electronic structure of the unusual seesaw molecules, DFT calculations on the simplified models of **3**-**6** (^{t}Bu groups replaced by Me groups) were performed (in collaboration with the Cisneros group, Wayne State University). The superposition of the calculated and crystal structures shows good agreement between them (See Appendix B). Combined electron localization function (ELF)[50]/noncovalent interaction (NCI)[51] analysis[52] was performed to gain a better understanding of interatomic interactions (See Appendix B for ELF results). NCI describes interatomic interactions by peaks of the reduced electron density gradient at low electron densities. Taking **4** as an example, the strong metal-ligand (Cr−O and Cr−Cl) interaction is evidenced by the blue NCI surfaces in **Figure 27a**. Regarding the chosen arbitrary color code, red surfaces indicate strong repulsion, blue surfaces indicate strong attraction, and green surfaces indicate relatively weak interactions. In addition, the surface for Cr−O (circled in black) has a darker blue color than the surface for Cr−Cl (circled in red),

indicating that the interaction between Cr and Cl is slightly weaker than between Cr and O. Moreover, the interaction between Li and Cl is much weaker than the one between Cr and Cl as demonstrated by the green surfaces (circled in yellow). Next, the alkyl substituents R of the OR groups were replaced by hydrogen atoms to investigate their effect on the stability of the seesaw geometry in the core. Although the optimized chromium complex did not retain the seesaw geometry, the other (Mn-Co) complexes were found to only undergo slight distortion (See Appendix B). These results underscore the importance of lithium-oxygen interactions (circled in blue) in these structures for the stabilization of the seesaw core. To determine the steric effect of the [OR] ligand, we carried out the NCI analysis on the full crystal structure of **4** (unoptimized, **Figure 27b**). Some of the notable interactions include a weak attraction between Cr and *ortho*-H (circled in red), and a weak attraction between Cl and H (^{t}Bu) atoms (circled in blue). Similar interactions are also present in the optimized simplified structures bearing methyl substituents (Appendix B). However, the full structure also demonstrates a weak attraction between the *tert*-butyl groups and the neighboring phenyl group (circled in violet). This interaction may be responsible for the formation of the cage-like structure.

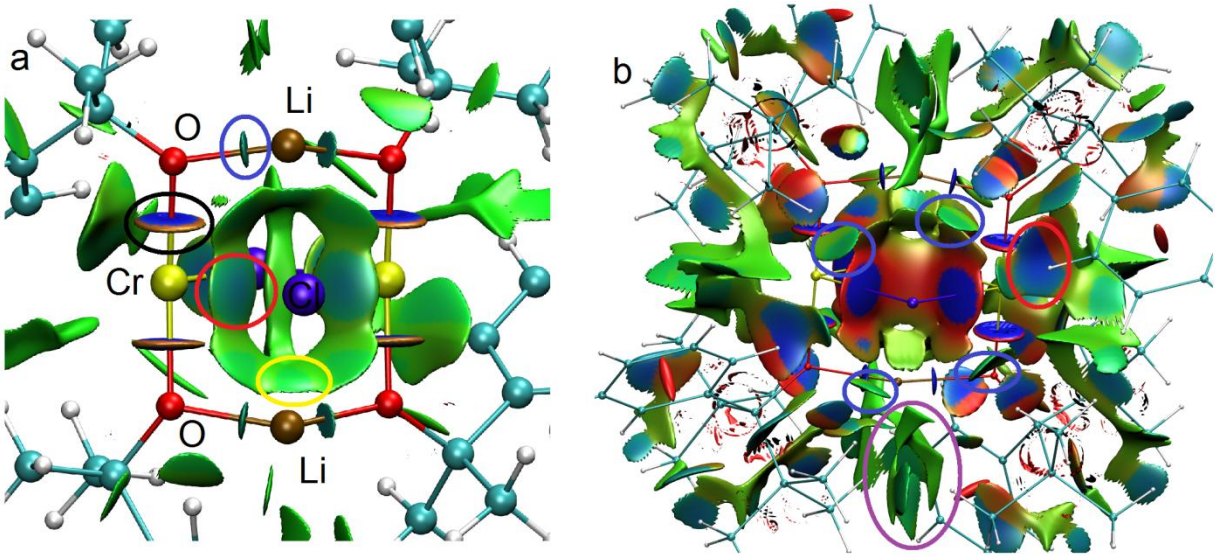

Figure 27. NCI surfaces for **4**. The isovalue is 0.5 (a) The optimized structure with *tert*-butyl was replaced by methyl (only the core is shown), $-0.07<\text{sign}(\lambda_2)\rho<0.07$ a.u. (b) NCI analysis for the complete (unoptimized) crystal structure, $-0.02<\text{sign}(\lambda_2)\rho<0.02$ a.u. Different $\text{sign}(\lambda_2)\rho$ ranges may be used to distinguish the strength of the interactions. Note that one can compare the relative strength of the interactions based on the colors only when using the same $\text{sign}(\lambda_2)\rho$ range.

The observation of seesaw geometry in the dimeric complexes **3**-**6** is certainly unprecedented, but not entirely surprising given the excessive steric bulk of the [OR] ligand. Spectroscopic and computational analyses confirm that it is indeed the steric bulk of the ligand, coupled with the strong lithium-oxygen interactions in the complexes that enforce the seesaw geometry. While novel, **3**-**6** unfortunately do not serve as suitable precursors toward group transfer reactions: as can be seen by the space-filling model in **Figure 24c**, the metal atoms are difficult to access due to the cage-like structure surrounding and protecting them. A likely solution to this is to find a means to remove the lithium and chloride atoms intercalated into the structure to give the desired bis(alkoxide) precursors. This shall be discussed in Chapter 3.

2.3. Synthesis and Characterization of Alkoxide Complexes of Nickel and Copper

2.3.1. Synthesis and Structural Characterization

In contrast to the reactions of chromium, manganese, iron, and cobalt chlorides with **1**, reactions with nickel and copper yielded strikingly different results. Instead of forming a complex similar to the seesaw dimers **3**-**6**, the reaction of $NiCl_2$(dme) (dme = dimethoxyethane) with two equivalents of **1** yields the monomeric complex $NiCl(OR)_2Li(THF)_2$ (**7**, see **Figure 28**). Similarly, the reaction of $NiBr_2$(dme) with **1** yields $NiBr(OR)_2Li(THF)_2$ (**8**, **Figure 28**). Both **7** and **8** are analogous to **2**. In contrast to **2**, however, **7** and **8** are both stable species, likely due to the smaller size of nickel compared to the earlier transition metals. It is likely this smaller size that prevents dimerization from occurring. Treatment of either copper(II) chloride or copper(II) bromide with two equivalents of **1** leads to several color changes before the solution ultimately turns and remains colorless. Crystallization gives colorless crystals confirmed to be the copper(I) cluster $Cu_4(OR)_4$ (**9**, **Figure 28**). Complex **9** can also be obtained via reaction of **1** with CuCl (**Figure 28**). An apparent reduction of copper(II) has taken place, presumably via one of the added alkoxide equivalents.

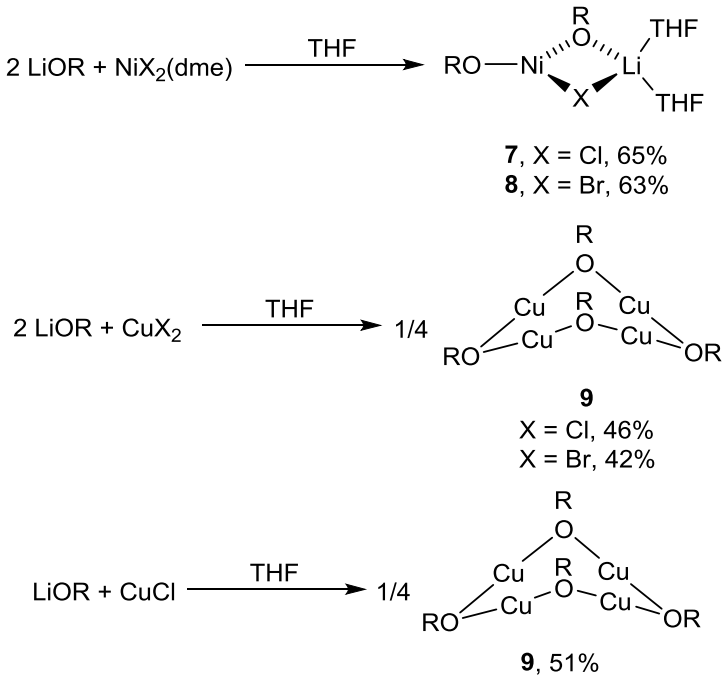

Figure 28. Reactions of nickel and copper precursors with **1**.

The structures of **7**, **8**, and **9** are shown in **Figures 29-31**. Selected structural data for **7-9** can be found in **Table 4**. Experimental crystallographic parameters for structures **7-9** can be found in **Table 5**. Both **7** and **8** display distorted trigonal planar geometry at the nickel centers (sum of angles at nickel 360°). Complex **9** is a tetramer of [CuOR] units featuring nearly linear copper(I) centers each ligated by two alkoxides. The four copper(I) centers form a plane with copper-copper distances ranging from 2.64 to 2.72 Å. The alkoxides coordinate above and below the Cu_4 plane, leading to an overall "butterfly"-type structure. Such a geometry can also be described in terms of two $Cu_2(OR)_3$ planes (i.e. O4Cu4Cu3O1O3 and O2Cu1Cu2O1O3) intersecting at a 115° angle. Several related compounds exist in the literature: namely, $Cu_4(O^tBu)_4$, $Cu_4(OAr)_4$ (Ar = $C_6H_3Ph_2$), and $Cu_4(OCPh_3)_4$.[53] Of the above, $Cu_4(O^tBu)_4$ and $Cu_4(OAr)_4$ are planar, while $Cu_4(OCPh_3)_4$ has a similar butterfly geometry to **9**, but with a wider angle (141°) between the $Cu_2(OR)_3$ planes.

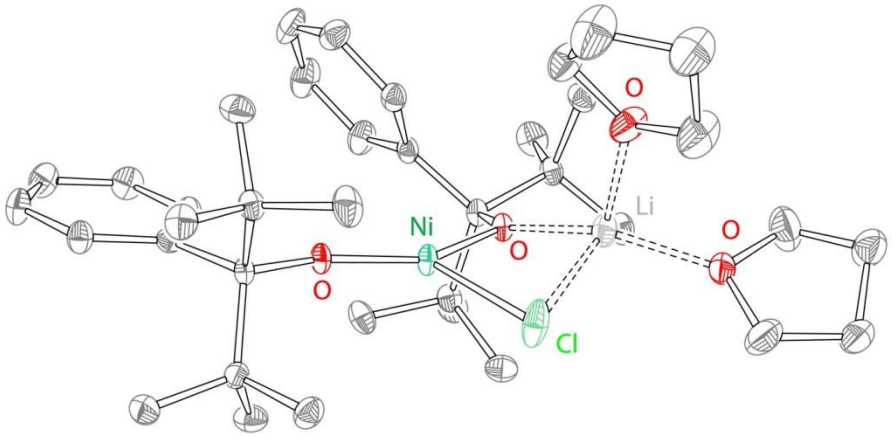

Figure 29. Crystal structure of **7**, 50% probability ellipsoids. H atoms were omitted for clarity. Dashed lines indicate largely ionic interactions with lithium.

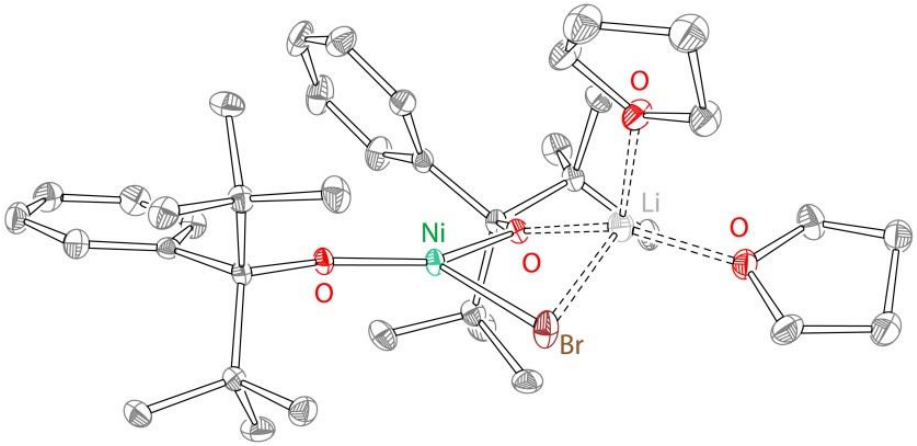

Figure 30. Crystal structure of **8**, 50% probability ellipsoids. H atoms were omitted for clarity. Dashed lines indicate largely ionic interactions with lithium.

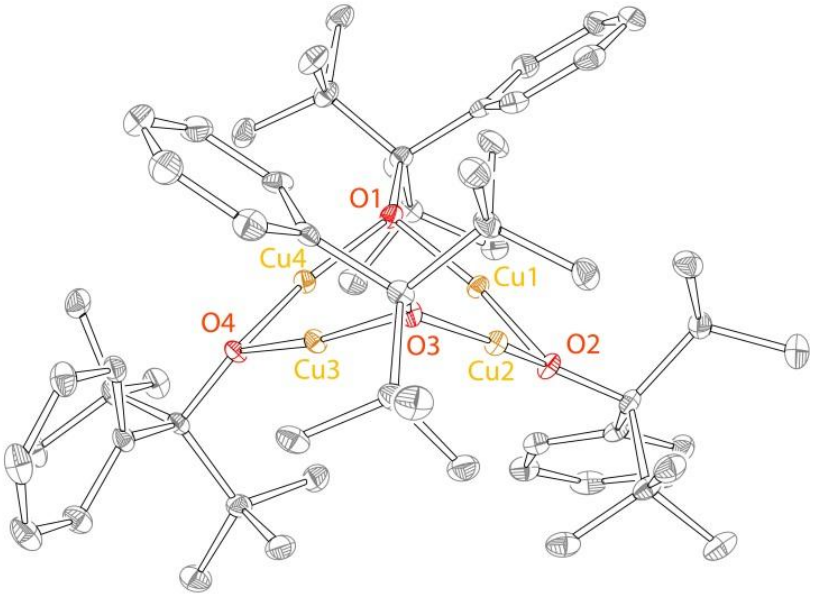

Figure 31. Crystal structure of **9**, 50% probability ellipsoids. H atoms and THF solvent were omitted for clarity.

Table 4. Selected structural data for **7**-**9**.

Complex	M-OR$_{terminal}$ (Å)	M-OR$_{bridging}$ (Å)	OR-M-OR (°)
7	1.748(1)	1.871(1)	147.67(6)[a]
8	1.747(1)	1.872(1)	148.24(5)[a]
9	–	1.85(1)[c]	165(4)[b]

(a) The angle between terminal and bridging alkoxides. (b) Average of four angles. (c) Average of eight bonds.

Table 5. Experimental crystallographic parameters for **7**-**9**.

complex	**7**	**8**	**9**
formula	$C_{38}H_{62}ClLiNiO_4$	$C_{38}H_{62}BrLiNiO_4$	$C_{64}H_{100}Cu_4O_5$
fw	683.99	728.45	1203.60
crystal system	monoclinic	monoclinic	triclinic
space group	*P 21/n*	*P 21/n*	*P-1*
a (Å)	8.6238(3)	8.5787(8)	12.1232(5)
b (Å)	18.9889(7)	19.1206(17)	12.7191(5)
c (Å)	22.8625(8)	22.8759(18)	21.0633(9)
α (deg)	90.00	90.00	91.982(2)
β (deg)	96.585(2)	96.788(4)	103.747(2)
γ (deg)	90.00	90.00	109.308(2)
V (Å^3)	3719.2(2)	3726.0(6)	2954.6(2)
D_c (g cm^{-3})	1.222	1.277	1.353
Z	4	4	2
μ (mm^{-1})	0.630	1.629	1.468
T (K)	100(2)	100(2)	100(2)
R_1 (%)	4.17	2.92	3.39
GOF	1.076	1.033	1.025

2.3.2. Formation of $Cu_4(OR)_4$: Spectroscopic Studies

The reduction of copper(II) to copper(I) in an alkoxide ligand environment is certainly an unusual transformation. Indeed, all of the previously reported $Cu_4(OR)_4$ compounds were obtained from copper(I) rather than copper(II) precursors. It is possible that initially a copper(II) bis(alkoxide) $CuX(OR)_2Li(THF)_2$ is formed. The copper center then undergoes reduction, and because there are no other species present in the reaction besides alkoxide ligands, the second equivalent of alkoxide is the only possible reducing agent present. Upon oxidation, [OR] is expected to form a radical species. The cyclic voltammetry (CV) of the lithium salt of [OR] (**1**) demonstrates an irreversible oxidation at the relatively accessible potential of 0.51 V versus $FeCp_2/FeCp_2^+$ (**Figure 32**). We note that tertiary alkoxides are not commonly observed as reductants.[27b] However, we are aware of one reported example of copper(II) being reduced by a tertiary bulky alkoxide.[39] It is also worth noting that the inability of [OR] to support copper(II) centers stands in sharp contrast to the behavior of the previously discussed fluorinated alkoxides (Doerrer, *et al*) to support even copper(III).[31a, 31c, 31e]

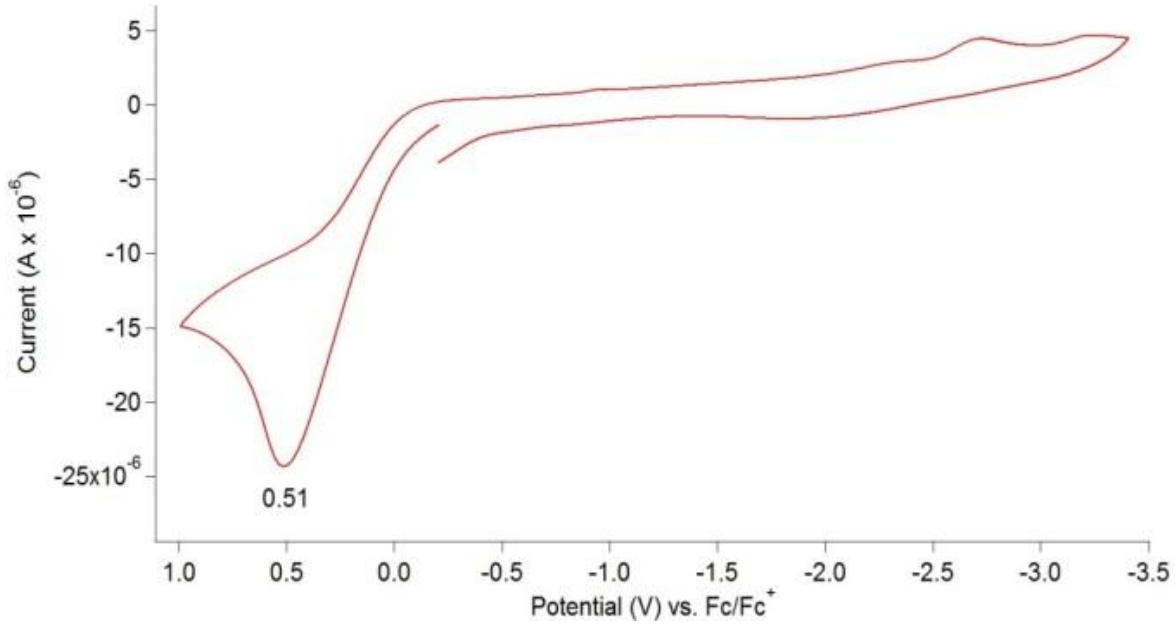

Figure 32. CV of LiOR (**1**) in THF (0.1 M $[NBu_4](PF_6)$, 25°C, platinum working electrode, 100 mV/s scan rate).

In an attempt to observe any possible intermediates along the route to the formation of **9**, a UV-vis experiment was performed. The reaction of $CuBr_2$ with two equivalents of LiOR was monitored over time. The addition of 0.5 mL of a 2.86 M LiOR solution into an orange 0.286 mM solution of $CuBr_2$ (2.5 mL in THF) immediately leads to a color change to colorless. A UV-vis scan performed ca. 10 s after the addition revealed only the final product (See Appendix B). The reaction was next attempted at lower temperatures (0 °C and −78 °C), but the reaction still proceeded too rapidly at 0 °C, and no reaction took place at −78°C. However, batch-wise addition of the LiOR solution at room temperature provided clear evidence for the intermediate (see **Figure 33**). The red trace in **Figure 33** represents the UV-vis spectrum of the starting $CuBr_2$ solution in THF, which is dominated by two signals at 415 and 355 nm, attributed to the $CuBr_2$. The addition of 0.1 mL of the LiOR solution leads to a decline in the intensity of these absorbances and an appearance of a new signal at 660 nm. The spectrum of the final product of the reaction (**9**, $Cu_4(OR)_4$, see black spectrum in **Figure 33** inset) is nearly featureless. Thus, we conclude that the absorbance at 660 nm belongs to a short-lived intermediate of the reaction. The addition of another batch of LiOR (purple trace, next 0.1 mL) causes a further increase in the intensity of the signal at 660 nm, which is accompanied by a decrease in the intensity of the signals at 415 and 355 nm. The next addition (orange trace) leads to a further decrease in the absorbances of the starting material, while the intermediate signal persists. Further additions of LiOR (green and black traces, two equivalents of LiOR total) lead to the disappearance of the 660 nm signal.

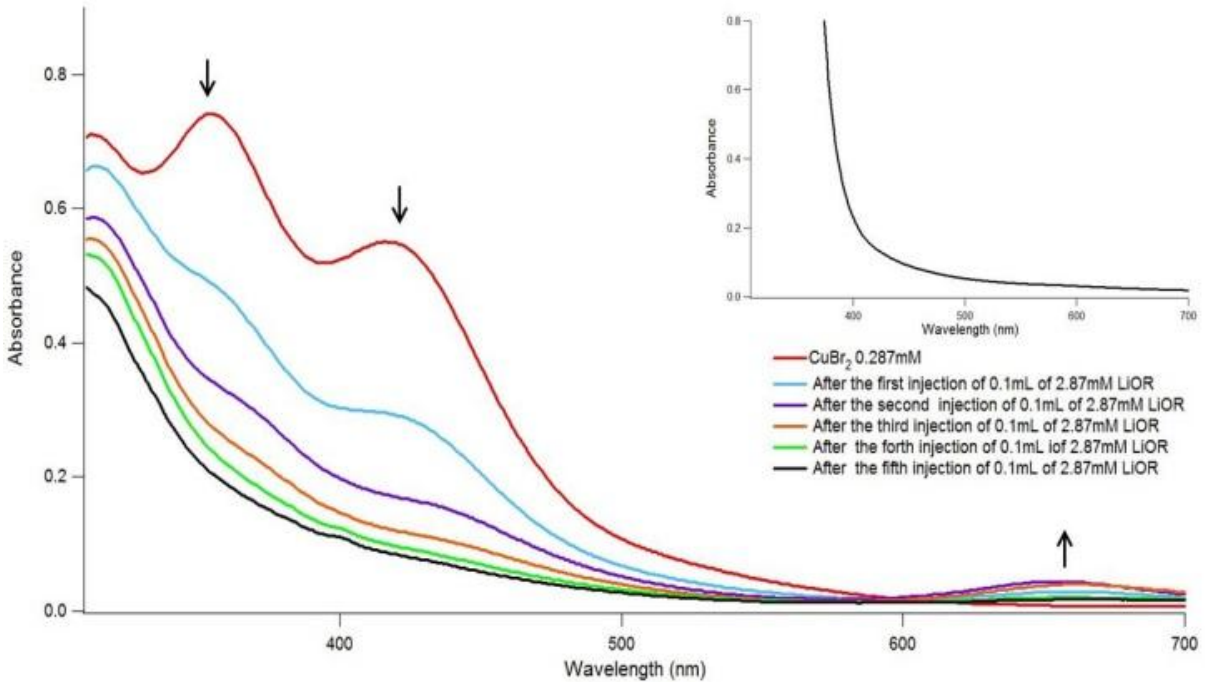

Figure 33. UV-vis spectra following the batch-wise addition of LiOR to a solution of $CuBr_2$. Inset: The spectrum of **9**.

To gain further insight into the reaction mechanism, the reaction was also analyzed by ^{1}H NMR spectroscopy. The reaction of $CuBr_2$ with two equivalents of LiOR in THF in the presence of trimethoxybenzene as an internal standard was allowed to stir for 30 minutes, after which an aliquot was taken, and its ^{1}H NMR spectrum was collected in C_6D_6. **Figure 34** below depicts the aromatic region of the resulting solution (spectrum A). The full spectrum can be found in Appendix B. For comparison, **Figure 34** also presents spectra of clean $Cu_4(OR)_4$ (spectrum B), *tert*-butyl phenyl ketone (spectrum C), and HOR (spectrum D) over the same region. Full spectra of these compounds are given in Appendix B. Spectrum A demonstrates that the crude reaction mixture contains $Cu_4(OR)_4$. In addition, resonances attributed to *tert*-butyl phenyl ketone and HOR are observed as well. Using the internal standard, the overall amount of "[OR]" produced in the reaction was quantified (quantification based off of the *tert*-butyl resonance). We calculated that 0.012 mmol of $Cu_4(OR)_4$ (0.048 mmol "CuOR") formed, along with 0.026 mmol of *tert*-butyl phenyl ketone and 0.022 mmol of HOR. Given that 0.156 mmol of LiOR were used initially, we account for ~62% of the [OR]; it is consistent with the observed yield of $Cu_4(OR)_4$.

Furthermore, these data also suggest that for each equivalent of Cu(OR), about 0.5 equivalents each of the *tert*-butyl phenyl ketone and HOR are being formed.

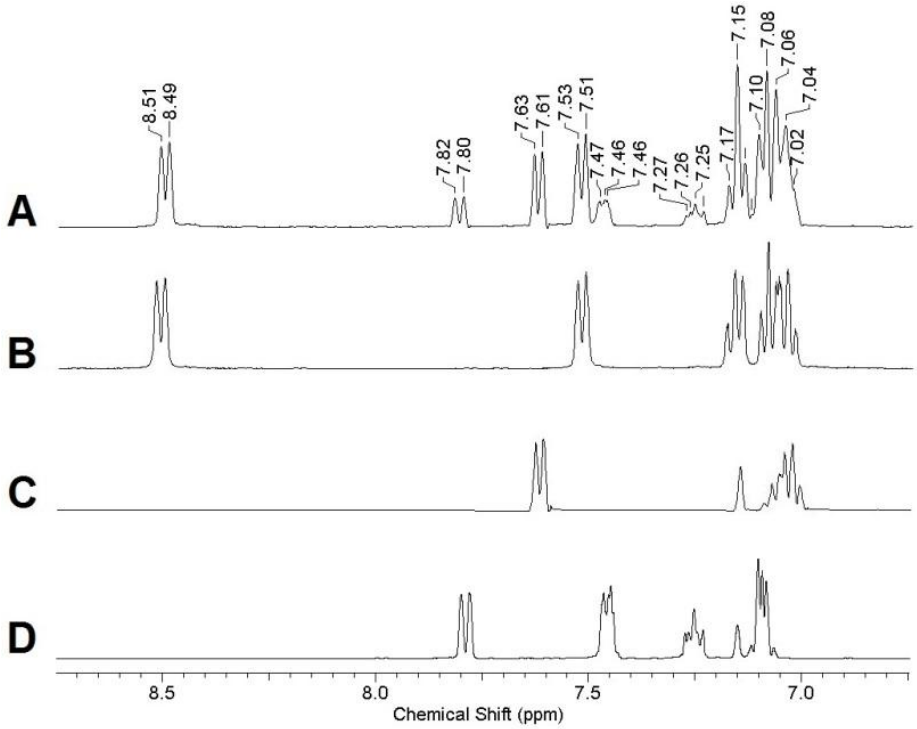

Figure 34. (A) ^{1}H NMR spectrum of an aliquot of the crude reaction mixture displayed at 6.8 to 8.8 ppm. (B) ^{1}H NMR spectrum of $Cu_4(OR)_4$ in the same region. (C) ^{1}H NMR spectrum of *tert*-butyl phenyl ketone (2,2-dimethyl-1-phenylpropan-1-one). (D) ^{1}H NMR spectrum of HOR.

The observation of a colored intermediate by UV-vis spectroscopy coupled with the detection and quantification of various reaction products by NMR spectroscopy provides a key to understanding the reaction mechanism leading to the formation of the copper(I) tetramer **9** (**Figure 35**). We propose that $CuBr(OR)_2Li(THF)_2$ forms first, as observed or proposed for **3**-**8**. Next, the Cu-OR bond undergoes a homolytic cleavage to form "$Cu^{I}(OR)$", which tetramerizes to give **9**. The remaining alkoxy radical then undergoes *β*-scission, which has been previously observed for alkoxy radicals.[54] The *β*-scission produces *tert*-butyl phenyl ketone and a *tert*-butyl radical, which may decompose to give isobutylene and a hydrogen atom. The hydrogen atom can then couple with another equivalent of alkoxy radical to give HOR. The formation of HOR is also possible via H atom abstraction by the alkoxy radical from the

solvent.[54] We did not observe the formation of isobutylene: the reaction takes place in a volatile solvent that must be removed prior to redissolving the reaction mixture in C_6D_6.

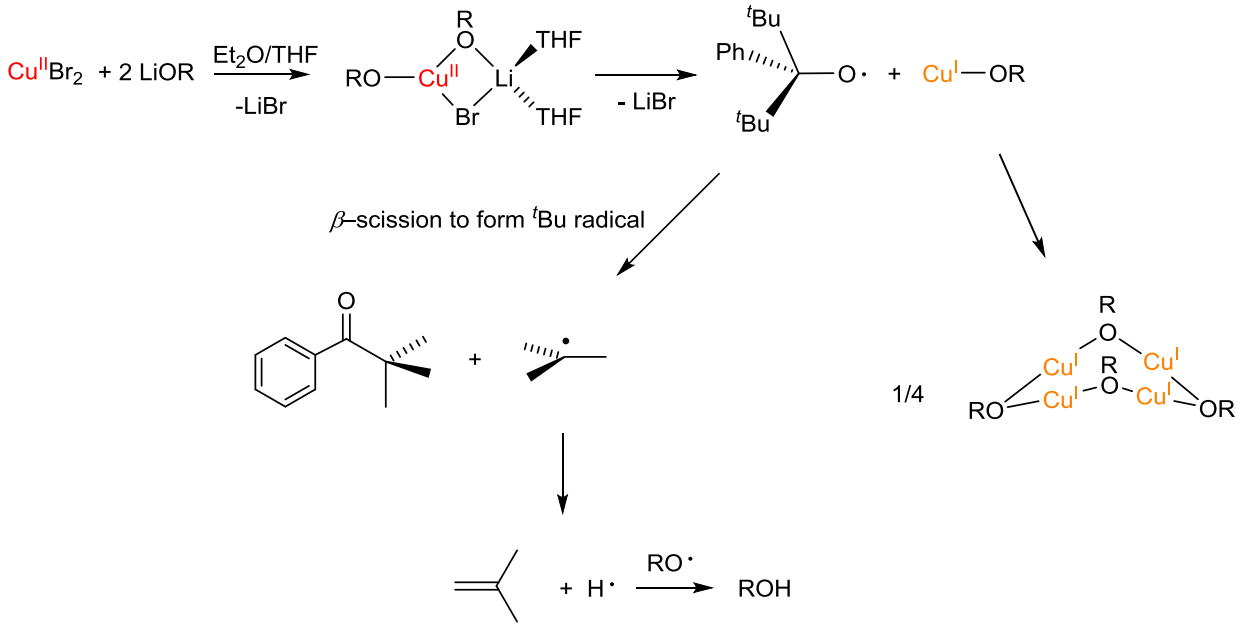

Figure 35. Proposed pathway to the formation of $Cu_4(OR)_4$, *tert*-butyl phenyl ketone, and HOR.

2.3.3. DFT Calculations: Stability of the Seesaw "Dimers" Versus the Trigonal Planar "Monomers"

Intrigued by the stark differences in reactivity between LiOR with chromium, manganese, iron, and cobalt versus nickel and copper, we performed DFT calculations to test the stability of selected $MX(OR')_2Li(THF)_2$ ("monomers") and $M_2(OR')_4Li_2Cl_2$ ("dimers") (in collaboration with the Cisneros group, Wayne State University). The OR' group here is the modified alkoxide ligand [$OCMe_2Ph$]. The energy change during the formation of dimers was calculated both in the gas phase and in a solvent environment (**Figure 36**). The relative change in electronic energy ($\Delta E0$) during the reaction in the gas phase for nickel (39.1 kcal/mol) is indeed larger than the other metals (Cr, 32.6 kcal/mol; Mn, 28.2 kcal/mol; Fe, 34.6 kcal/mol; Co, 31.5 kcal/mol). When solvation effects are included in the calculations, the dimers become more stable; however, this effect is smaller for the nickel complexes than for the other metal complexes. Most of the change in the free energy of reaction is due to the entropic term ($-T\Delta S$), which corresponds to −27.2 and −19.6 kcal/mol for nickel and manganese, respectively, in the gas phase.

In THF (hexane), the contribution for nickel is smaller by comparison at −26.3 (−26.9) kcal/mol. In contrast, the entropic contribution decreases to −29.5 (−29.0) kcal/mol for manganese in THF (hexane). As a result, a relatively large electronic energy change and small stabilization from the solvation effects lead to a positive Δ*G* for nickel (6.9 kcal/mol in hexane, 10.5 kcal/mol in THF) compared to manganese (−5.2 kcal/mol in hexane, −6.0 kcal/mol in THF).

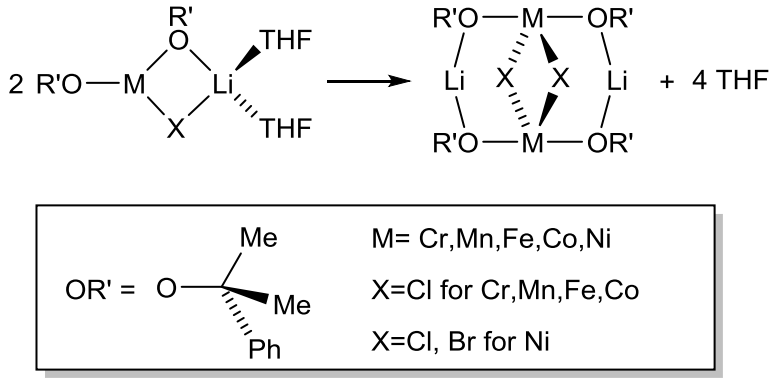

Figure 36. Transformation used to determine the free energy differences (Δ*G*) between monomeric and dimeric alkoxide complexes.

2.4. Summary and Conclusions

A new type of bulky alkoxide ligand, [OR] has been synthesized. The reactivity of [OR] with the first-row transition metals chromium, manganese, iron, cobalt, nickel, and copper has been investigated. For the middle to late metals chromium through cobalt, dimeric complexes displaying seesaw geometry at the metal can be synthesized (**3**-**6**). The excessive steric bulk of the ligand leads to cage-like structures, whereby the phenyl group on the alkoxide crystallizes in a "lock-and-key" orientation between the ligand's *tert*-butyl groups. Unfortunately this leads to complete inaccessibility of the metal center due to excessive steric hindrance, making **3**-**6** unsuitable as precursors for the synthesis of metal-ligand multiple bonds. For nickel, stable monomeric **7** and **8** can be synthesized. Nickel's smaller size in comparison with the earlier metals suggests that dimerization of nickel complexes with [OR] is thermally disfavored. DFT calculations support this finding by indicating positive Δ*G* values for the formation of a seesaw dimer from **7** or **8**. Once again, for steric reasons, **7** and **8** are also unsuitable precursors toward the synthesis of

metal-ligand multiple bonds. Reaction with copper(II) leads to an unprecedented reduction to the copper(I) tetramer **9**. UV-vis and NMR experiments suggest homolytic cleavage of the Cu-OR bond in the copper(II) species giving way to **9**, as well as spectroscopically observable organic byproducts. Because our system does not appear to be capable of supporting copper oxidation states higher than 1+, copper is an unsuitable metal toward oxidative chemistry and will not be considered henceforth.

2.5. Experimental Details

General Methods and Procedures. All reactions involving air-sensitive materials were executed in a nitrogen-filled glovebox. Chromium(II) chloride, iron(II) chloride, copper(II) chloride, copper(II) bromide, and copper(I) chloride were purchased from Strem. 1.8 M phenyllithium solution in dibutyl ether, manganese(II) chloride, cobalt(II) chloride, nickel(II) chloride dimethoxyethane, and nickel(II) bromide dimethoxyethane were purchased from Aldrich. Hexamethylacetone was purchased from Alfa Aesar. All materials were used as purchased. All solvents were purchased from Fisher scientific and were of HPLC grade. The solvents were purified using an MBRAUN solvent purification system and stored over 3-Å molecular sieves. The ligand **1** was characterized by ^{1}H and ^{13}C NMR spectroscopy, IR spectroscopy, and elemental analysis. The dimeric **3**-**6** were characterized using IR spectroscopy, elemental analysis, X-ray absorption spectroscopy, and the Evans method for determination of magnetic moment. Compounds **7**-**9** were characterized by ^{1}H and ^{13}C NMR spectroscopy, IR spectroscopy, UV-vis spectroscopy, solution state magnetic susceptibility, cyclic voltammetry, and elemental analysis. All compounds were characterized by X-ray crystallography. NMR spectra were recorded at the Lumigen Instrument Center (Wayne State University) on a Varian Mercury 400 MHz NMR Spectrometer in C_6D_6, CD_2Cl_2, or C_7D_8 at room temperature. Chemical shifts and coupling constants (*J*) were reported in parts per million (δ) and Hertz respectively. IR spectra were recorded on a Shimadzu IR-Affinity1 FT-IR spectrometer as paratone oil mull suspensions. UV-vis spectra were obtained in a Shimadzu UV-1800 spectrometer. Solution state effective magnetic moments were determined using the Evans method,[49] and diamagnetic corrections were calculated using the Pascal's constants method;[55] three independent measurements were carried out for each sample. Electrochemical properties were determined using cyclic

voltammetry on a BAS Epsilon system in a nitrogen-filled glovebox. Samples were prepared in anhydrous THF with 0.1 M tetrabutylammonium hexafluorophosphate [NBu_4][PF_6] as the supporting electrolyte. Redox potentials were determined with a scan rate of 100 mV/sec at 25 °C by using a platinum disc working electrode (2 mm diameter), a platinum wire counter electrode, and a non-aqueous Ag^+/Ag reference electrode, and referenced to ferrocene/ferrocenium couple. Elemental analyses were performed by Midwest Microlab LLC. Acceptable elemental analysis data could not be obtained for **5** due to its low stability at ambient temperature. Experimental details regarding XAS, SQUID, and DFT, as well as additional spectral data, can be found in Appendix B.

X-ray Crystallographic Details. The structures of **1**-**9** were all confirmed by X-ray analysis. The crystal was mounted on a Siemens Platform three circle goniometer equipped with an APEX detector using Graphite monochromated Mo Kα radiation (λ = 0.71073 Å). The data were processed using the programs SAINT and SADABS supplied by Bruker-AXS. The structure was solved by direct methods with SHELXS and refined by standard difference Fourier techniques with SHELXL (6.10 v., Sheldrick G. M., and Siemens Industrial Automation, 2000). Hydrogen atoms were placed in calculated positions using a standard riding model and refined isotropically; all other atoms were refined anisotropically. The structure of the ligand contained one trimeric molecule per asymmetric unit. The crystal quality of **2** was not sufficient enough to merit publication of bond lengths and angles.

Li[OR] (1). 2.46 mL (0.372 g, 4.43 mmol) of a phenyllithium solution was added dropwise with stirring to 0.761 mL (0.627 g, 4.43 mmol) of hexamethylacetone in a small quantity (~1.0 mL) of diethyl ether. The resulting orange solution was stirred at room temperature for 24h. Solvent was removed in vacuo to give an orange crystalline residue. Repeated recrystallizations from hexane (× 3) afforded the product as a white, crystalline solid (0.821 g, 82%).^{1}H NMR (C_6D_6, 400 MHz) δ 7.97 (d, J = *8.0*, 1H), 7.66 (d, J = *4.0*, 1H), 7.29 (m, 1H), 7.09 (m, 2H), 1.10 (s, 18H); ^{13}C NMR (C_6D_6, 75 MHz) δ 152.39, 130.24, 128.71, 126.52, 125.84, 84.82, 42.48, 31.29. IR (cm^{-1}): 1483 (m), 1387 (m), 1364 (m), 1067 (s), 1015 (s), 947 (m), 910 (m), 893 (m), 800 (m), 748 (s), 714 (s), 656 (m). Anal. Calcd. for $C_{45}H_{69}O_3Li_3$: C, 79.6; H, 10.2. Found: C, 79.6, 10.4.

$Fe_2(OR)_4Li_2Cl_2$ (3). A 5 mL diethyl ether solution of **1** (48.5 mg, 0.214 mmol) was added in one portion to a stirred THF of solution of $FeCl_2$ (13.6 mg, 0.107 mmol). The solution color changed from light brown to yellow. The reaction was stirred for one hour, upon which the solvent was removed. The resulting residue was redissolved in hexane and filtered to give the monomer $Fe(OR)_2LiCl(THF)_2$, **2**, in solution. Hexane was repeatedly added to and removed from the residue four times to yield a pale yellow solid (40.5 mg, 70%). Colorless X-ray quality crystals could be produced via crystallization from hexane at -35°C. IR (cm^{-1}): 1489 (m), 1393 (m), 1368 (m), 1049 (s), 993 (s), 951 (m), 918 (m), 752 (s), 716 (s), 681 (m), 638 (m). μ_{eff} (Evans, CD_2Cl_2, 298 K): 8.8 μ_B (calc. 8.9); Anal. Calcd. for $C_{60}H_{92}O_4Li_2Cl_2Fe_2$: C, 67.1; H, 8.6. Found: C, 67.0; H, 8.9.

$Cr_2(OR)_4Li_2Cl_2$ (4). A 5 mL diethyl ether solution of **1** (61.6 mg, 0.272 mmol) was added in one portion to a stirred THF solution of $CrCl_2$ (16.7 mg, 0.136 mmol). The solution color immediately changed to a light blue-green. The reaction was stirred for one hour, upon which the solvent was removed. The resulting residue was redissolved in hexane and filtered. Hexane was repeatedly added to and removed from the residue four times to yield a pale green solid (51.8 mg, 71%). Pale green X-ray quality crystals could also be produced via crystallization from hexane at -35°C. IR (cm^{-1}): 1489 (m), 1393 (m), 1368 (m), 1053 (s), 999 (s), 949 (m), 918 (m), 752 (s), 718 (s), 681 (m), 638 (m). μ_{eff} (Evans, C_7D_8, 298 K): 8.41 μ_B (calc. 8.9); Anal. Calcd. for $C_{60}H_{92}O_4Li_2Cl_2Cr_2$: C, 67.6; H, 8.7. Found: C, 66.9; H, 8.5.

$Mn_2(OR)_4Li_2Cl_2$ (5). A 5 mL diethyl ether solution of **1** (51.3 mg, 0.227 mmol) was added in one portion to a stirred THF solution of $MnCl_2$ (14.3 mg, 0.113 mmol). The colorless solution was stirred for one hour, upon which the solvent was removed. The resulting residue was redissolved in hexane and filtered. Hexane was repeatedly added to and removed from the residue four times to yield a white solid (43.1 mg, 71%). White X-ray quality crystals could be produced via crystallization from hexane at -35°C. IR (cm^{-1}): 1485 (m), 1391 (m), 1368 (m), 1051 (s), 995 (s), 945 (m), 918 (m), 750 (s), 718 (s), 682 (m), 640 (m). μ_{eff} (Evans, CD_2Cl_2, 298 K): 11.6 μ_B (calc. 11.0); Anal. Calcd. for $C_{60}H_{92}O_4Li_2Cl_2Mn_2$: C, 67.2; H, 8.7. Found: C, 66.1; H, 8.1.

$Co_2(OR)_4Li_2Cl_2$ (6). A 5 mL diethyl ether solution of **1** (45.4 mg, 0.201 mmol) was added in one portion to a stirred THF solution of $CoCl_2$ (13.0, 0.100 mmol). The solution color immediately changed to a deep blue. The reaction was stirred for one hour, upon which the solvent was removed. The resulting residue was redissolved in hexane and filtered. Hexane was repeatedly added to and removed from the residue four times to yield a magenta solid (39.2 mg, 72%). Magenta X-ray quality crystals could also be produced via crystallization from hexane at -35°C. IR (cm^{-1}): 1489 (m), 1393 (m), 1368 (m), 1049 (s), 989 (s), 951 (m), 918 (m), 752 (s), 718 (s), 679 (m), 638 (m). μ_{eff} (Evans, C_7D_8, 298 K): 7.8 μ_B (calc. 6.9); Anal. Calcd. for $C_{60}H_{92}O_4Li_2Cl_2Co_2$: C, 66.7; H, 8.6. Found: C, 66.9; H, 8.7.

$Ni(OR)_2ClLi(THF)_2$ (7). A 5 mL diethyl ether solution of LiOR (47.7 mg, 0.211 mmol) was added in one portion to a stirred THF solution of $NiCl_2$(dme) (23.2 mg, 0.105 mmol). The solution color changed from light orange to deep orange. The reaction was stirred for one hour, upon which the volatiles were removed *in vacuo*. The resulting residue was redissolved in hexane and filtered. Recrystallization from hexane at -35°C afforded the product as orange crystals (46.9 mg, 65%). IR (cm^{-1}): 2972 (m), 2876 (m), 1487 (w), 1391 (w), 1360 (w), 1099 (s), 1072 (m), 1043 (w), 1022 (s), 891 (m), 745 (s), 708 (s), 677(w), 650 (w). μ_{eff} = 3.0 ± 0.2 μ_B (calc. 2.8). ^{1}H NMR (C_6D_6, 400 MHz) δ 14.18, 10.55, 9.74, 7.86, 0.46, 0.02, -0.44, -0.65, -2.81. λ_{max} (ε): 676 (22), 547 (99) M^{-1} cm^{-1}. Anal. Calcd. for $C_{38}H_{62}O_4ClLiNi$: C, 66.7; H, 9.1. Found: C, 66.7, H, 9.0.

$Ni(OR)_2BrLi(THF)_2$ (8). A 5 mL diethyl ether solution of LiOR (49.1 mg, 0.217 mmol) was added in one portion to a stirred THF solution of $NiBr_2$(dme) (33.5 mg, 0.109 mmol). The solution color changed to deep orange. The reaction was stirred for one hour, upon which the volatiles were removed *in vacuo*. The resulting residue was redissolved in hexane and filtered. Recrystallization from hexane at -35°C afforded the product as orange crystals (49.8 mg, 63%). IR (cm^{-1}): 2972 (w), 2876 (w), 1522 (w), 1489 (m), 1393 (m), 1366 (w), 1098 (w), 1072 (m), 1043 (s), 1022 (w), 991 (s), 889 (m), 745 (s), 708 (s), 675 (m). μ_{eff} = 3.1 ± 0.2 μ_B (calc. 2.8). ^{1}H NMR (C_6D_6, 400 MHz) δ 13.79, 10.09, 9.75, 6.88, -1.16, -2.49, -3.28. λ_{max} (ε): 682 (33), 559 (91) M^{-1} cm^{-1}. Anal. Calcd. for $C_{38}H_{62}O_4BrLiNi$: C, 62.7; H, 8.6. Found: C, 61.7, H, 8.0. Our repeated attempts to obtain better elemental analysis for **8** failed. However, **8** is obtained

in an identical fashion to **7** as large orange crystals, and its spectroscopic and magnetic data matches well that of **7**.

$Cu_4(OR)_4$ (9) via $CuCl_2$. A 5 mL diethyl ether solution of LiOR (45.2 mg, 0.200 mmol) was added in one portion to a stirred THF of solution of $CuCl_2$ (13.4 mg, 0.100 mmol). The solution color immediately changed deep red before darkening to brown. The reaction was stirred for one hour, upon which the volatiles were removed in vacuo. The resulting residue was redissolved in hexane and filtered. Recrystallization from hexane at -35°C afforded the product as colorless crystals (26.0 mg, 46%). IR (cm^{-1}): 3001 (w), 2951 (w), 2905 (w), 2878 (w), 1489 (w), 1389 (m), 1362 (w), 1153 (w), 1049 (s), 995 (s), 895 (w), 745 (s), 706 (s). ^{1}H NMR (C_6D_6, 400 MHz) δ 8.52 (d, *J* = 8.0, 4H), 7.53 (d, *J* = 8.0, 4H), 7.17 (t, *J* = 4.0, 4H), 7.06 (m, 8H), 1.39 (s, 72H). ^{13}C NMR (C_6D_6, 75 MHz) δ 149.02, 130.19, 128.50, 127.47, 126.07, 125.13, 86.32, 41.61, 31.22. IR (cm^{-1}): 3001 (w), 2951 (w), 2905 (w), 2878 (w), 1489 (w), 1389 (m), 1362 (w), 1153 (w), 1049 (s), 995 (s), 895 (w), 745 (s), 706 (s). No discernible features in the UV−vis spectrum. Anal. Calcd. for $C_{60}H_{92}O_4Cu_4$: C, 63.7; H, 8.2. Found: C, 63.6, H, 8.0.

$Cu_4(OR)_4$ (9) via $CuBr_2$. A 5 mL diethyl ether solution of LiOR (47.8 mg, 0.211 mmol) was added in one portion to a stirred THF of solution of $CuBr_2$ (23.6 mg, 0.106 mmol). The solution color rapidly changed through red, amber, and light blue before ultimately turning colorless. The volatiles were removed in vacuo. The resulting residue was redissolved in hexane and filtered. Recrystallization from hexane at -35°C afforded the product as colorless crystals (25.2 mg, 42%). ^{1}H NMR spectrum of the product matched that of the product obtained via $CuCl_2$.

$Cu_4(OR)_4$ (9) via CuCl. This procedure is identical to that for the reaction with copper(II) halides. LiOR (49.3 mg, 0.218 mmol) was added to CuCl (21.6 mg, 0.218 mmol) to give a colorless solution. The reaction was stirred for one hour, upon which the volatiles were removed in vacuo. The resulting residue was redissolved in hexane and filtered. Recrystallization from hexane at -35°C afforded the product as colorless crystals (31.4 mg, 51%). ^{1}H NMR matched that of the product obtained via $CuCl_2$.

CHAPTER 3: SYNTHESIS AND CHARACTERIZATION OF THE BIS(ALKOXIDE) COMPLEXES $M(OR)_2(THF)_2$

Portions of the text in this chapter were reprinted or adapted with permission from: (a) Bellow, J. A.; Martin, P. D.; Lord, R. L.; Groysman, S. *Inorg. Chem.* **2013**, *52*, 12335-12337. (b) Bellow, J. A.; Yousif, M.; Fang, D.; Kratz, E. G.; Cisneros, G. A.; Groysman, S. *Inorg. Chem.* **2015**, *54*, 5624-5633.

3.1. Introduction

While the chemistry of [OR] with the first-row transition metals explored in Chapter 2 is no doubt novel and intriguing, the complexes synthesized therein do not serve as suitable precursors toward the synthesis of metal-ligand multiple bonds. The seesaw dimers **3**-**6**, in addition to possessing undesired chloride and lithium ions that would likely interfere with reactivity, are also sterically hindered, as shown by their space-filling models. This makes any attempt to perform additional reactions at the metal challenging. A similar situation arises for the monomeric nickel complexes **7** and **8** due to the presence of chloride and lithium ions. One means to circumvent this issue is by removing the intercalated chloride and lithium ions. Chloride abstraction agents such as silver(I) hexafluorophosphate or thallium(I) hexafluorophosphate could be utilized for this purpose. The objective of this chapter was to perform chloride abstraction on the complexes described in Chapter 2 in order to obtain a suitable bis(alkoxide) ligand platform toward the stabilization of metal-ligand multiple bonds.

3.2. Synthesis and Characterization of the Bis(alkoxide) Complexes $M(OR)_2(THF)_2$

Attempts at chloride abstraction from the iron and cobalt seesaw dimers **3** and **6** using silver(I) hexafluorophosphate were unsuccessful, leading to reduction of the silver (indicated by formation of a gray precipitate) and drastic color changes in both cases. However, by switching to the less oxidizing thallium(I) hexafluorophosphate, immediate formation of a white precipitate was observed upon addition to the iron, manganese, and cobalt seesaw dimers in THF. Subsequent workup and crystallization afforded the desired bis(alkoxide) complexes of the form $M(OR)_2(THF)_2$ (M = Mn, Fe, Co, **10**-**12**) (**Figure 37**). Complexes **10**-**12** are all related to the previously described $M(OCPh_3)_2(THF)_2$ (M = Mn, Fe, Co) complexes,[33a, 33c] as well as recently synthesized manganese aryloxide complexes of the form

$Mn(OAr)_2(THF)_2$.[56] Surprisingly, all attempts to perform chloride abstraction on the chromium seesaw dimer **4** led to the formation of a gray, metallic precipitate, suggesting that the highly reducing chromium(II) is capable of reducing thallium(I) to thallium metal. Additionally, halide abstraction attempts from the nickel complexes **7** and **8** also failed: workup of the reaction mixtures in both cases led to reisolation of the starting materials. Due to the inability to remove chloride, as well as the fact that performing oxidative chemistry on nickel(II) in an alkoxide ligand environment would likely prove difficult (if not impossible), we chose to no longer consider nickel precursors toward the synthesis of metal-ligand multiple bonds.

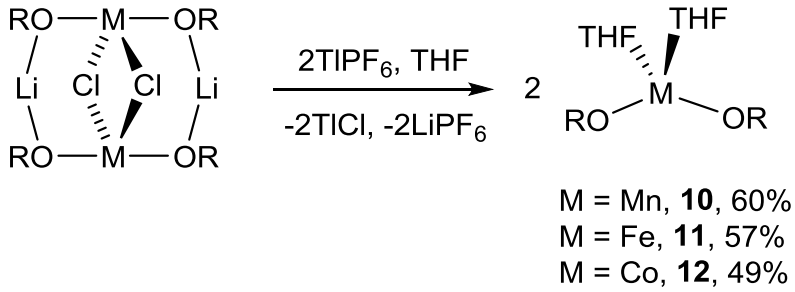

Figure 37. Synthesis of the bis(alkoxides) **10**-**12**.

Complexes **10**-**12** were characterized by IR spectroscopy, ^{1}H NMR spectroscopy, solution magnetic measurements, UV-vis spectroscopy, cyclic voltammetry, and X-ray crystallography. All of them are four-coordinate, distorted tetrahedral complexes containing two labile THF ligands. They all display μ_{eff} values that are consistent with a high-spin metal(II) in a weak-field ligand environment (5.5 μB for **10**, 4.7 μB for **11**, 3.6 μB for **12**). We note that in contrast, two-coordinate bis(aryloxide) complexes of iron and cobalt demonstrate significantly higher μ_{eff} values due to a considerable orbital contribution.[57, 58] The IR spectra of **10**-**12** are, as anticipated, nearly identical, with prominent C-O stretches around 1100 cm^{-1}. The manganese and iron complexes **10** and **11** are both colorless, and as a result their UV-vis spectra are nearly featureless. The violet cobalt complex **12**, however, gives rise to several peaks in the visible region. The most significant peak at 734 nm exhibits an extinction coefficient of 175 M^{-1} cm^{-1}.

Cyclic voltammetry of **10**-**12** are shown in **Figure 38** below. CVs were obtained in THF using $[NBu_4](PF_6)$ as the supporting electrolyte and are reported versus the $FeCp_2/FeCp_2^+$ couple. Only irreversible oxidations are observed, peaking at 0.45 V for $Fe(OR)_2(THF)_2$ (onset at ~0 V), 1.27 V for $Co(OR)_2(THF)_2$ (onset at ~0.5 V), and 1.43 V for $Mn(OR)_2(THF)_2$ (onset at ~0.7 V). The lack of reversible features in the CVs is not uncommon in the electrochemistry of complexes supported by bulky monodentate alkoxides,[31c, 35c, 59] indicating that the complexes undergo rearrangement upon oxidation. No reductions were observed up to −2.0 V. This electrochemical behavior demonstrates that the complexes in their present form are unlikely to reach oxidation states lower than 2+ and that while the oxidation of the iron(II) complex **11** is relatively accessible, oxidative chemistry on the manganese(II) and cobalt(II) complexes **10** and **12** may be less feasible.

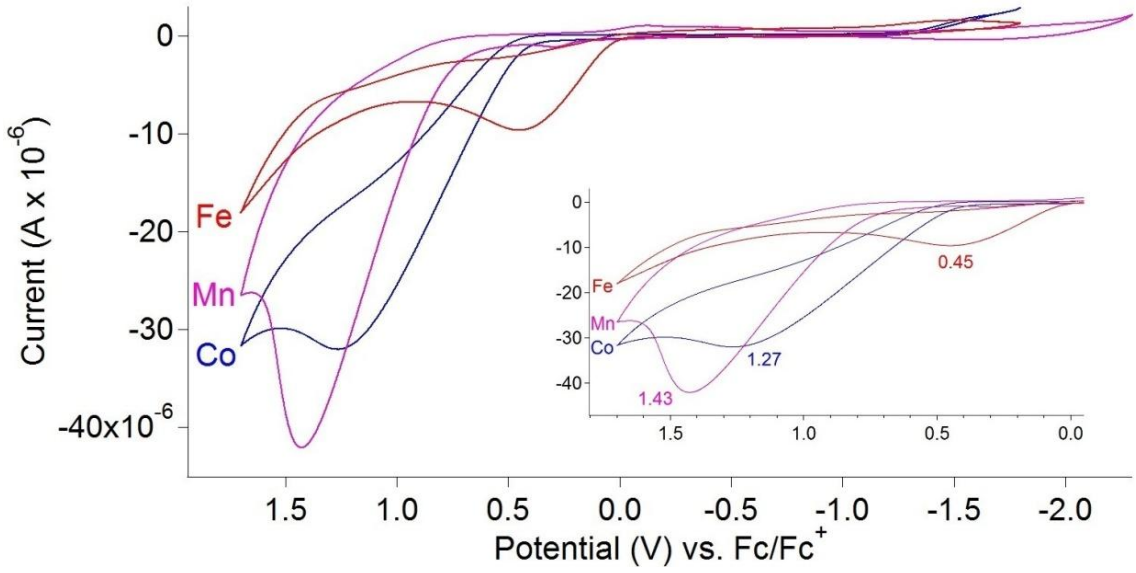

Figure 38. CVs of **10**-**12** in THF, (0.1 M $[NBu_4](PF_6)$, 25 °C, platinum working electrode, 100 mV/s scan rate).

X-ray quality crystals of **10**-**12** were obtained from hexanes at −35 °C. The structures of all three complexes can be seen in **Figures 39**-**41** below. Selected structural data can be found in **Table 6**. Experimental crystallographic parameters can be found in **Table 7**. All three display distorted tetrahedral geometry at the metal center, with wide RO−M−OR angles ranging from 130-139° and narrow

THF−M−THF angles ranging from 83-88°. The related complexes $Fe(OCPh_3)_2(THF)_2$ and $Mn(OAr)_2(THF)_2$ both exhibited comparable RO-M-OR angles of about 140°.[33c, 56] This structure type matches the desired bis(alkoxide) framework we are seeking. The presence of two labile THF ligands indicates that these complexes may be able to support metal-ligand multiple bond functionalities.

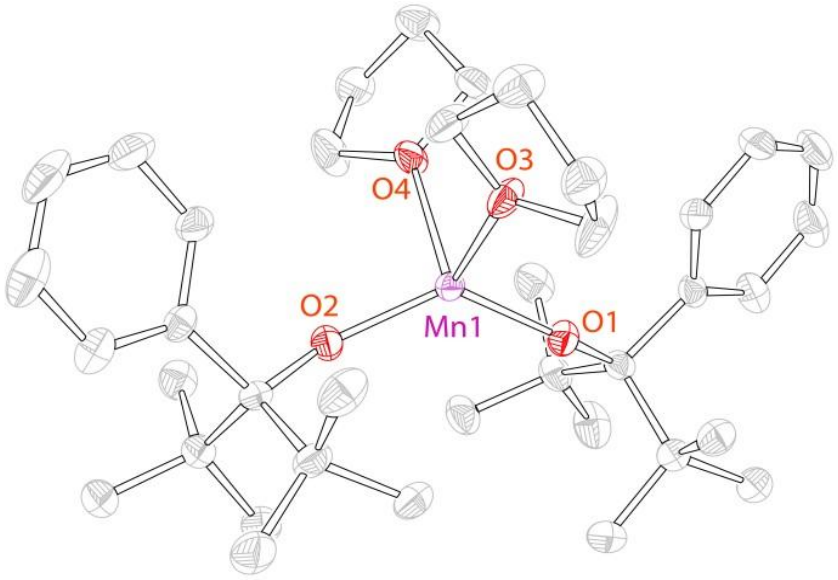

Figure 39. Structure of $Mn(OR)_2(THF)_2$ (**10**), 50% probability ellipsoids. H atoms are omitted for clarity.

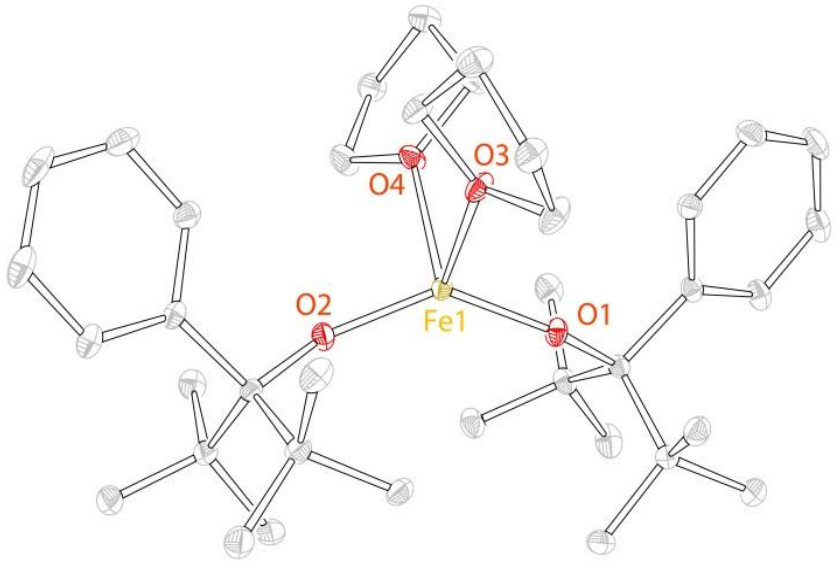

Figure 40. Structure of $Fe(OR)_2(THF)_2$ (**11**), 50% probability ellipsoids. H atoms are omitted for clarity.

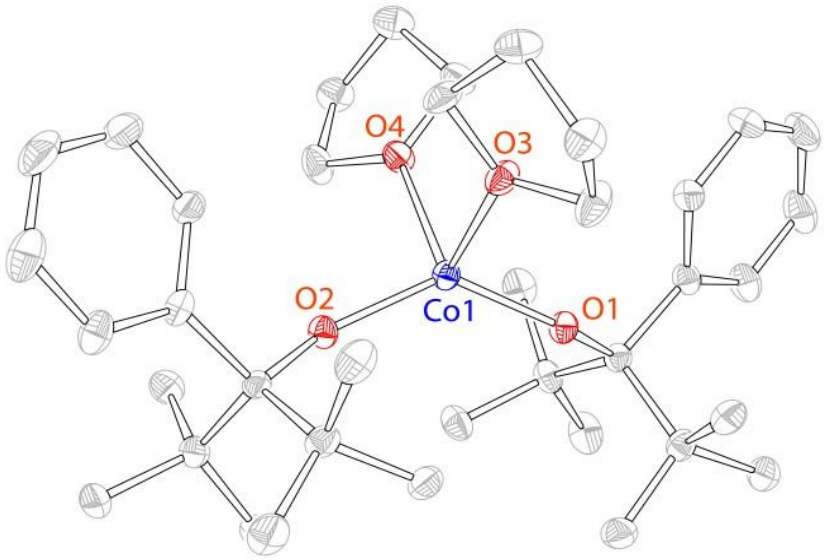

Figure 41. Structure of $Co(OR)_2(THF)_2$ (**12**), 50% probability ellipsoids. H atoms are omitted for clarity.

Table 6. Selected structural data for **10**-**12**.

Complex	M−$OR_{terminal}$ (Å)	OR−M−OR (°)	THF−M−THF (°)
10	1.899(1)	130.0(1)	86
11	1.838(1)	138.7(1)	83
12	1.8491(1)	131.1(1)	88

Table 7. Experimental crystallographic parameters for **10**-**12**.

complex	**10**	**11**	**12**
formula	$C_{38}H_{62}MnO_4$	$C_{38}H_{62}O_4Fe$	$C_{38}H_{62}CoO_4$
fw	637.85	638.73	641.84
crystal system	orthorhombic	monoclinic	orthorhombic
space group	*Fdd2*	*Cc*	*Fdd2*
a (Å)	21.016(3)	9.3154(6)	20.707(4)
b (Å)	37.071(4)	36.698(3)	37.128(6)
c (Å)	9.3300(10)	11.4911(7)	9.2640(17)
α (deg)	90.00	90.00	90.00
β (deg)	90.00	113.894(2)	90.00
γ (deg)	90.00	90.00	90.00
V (Å^3)	7268.8(15)	3591.7(4)	7122.(2)
D_c (g cm^{-3})	1.166	1.181	1.197
Z	16	4	16
μ (mm^{-1})	0.399	0.456	0.518
T (K)	100(2)	100(2)	100(2)
R_1 (%)	2.72	3.56	3.41
GOF	1.046	1.075	0.891

3.3. Summary and Conclusions

Through the use of thallium(I) hexafluorophosphate as a chloride abstracting agent, the bis(alkoxide) complexes **10**-**12** can be isolated in a facile manner. The inability to remove chloride from the chromium seesaw dimer **4**, as well as from the monomeric nickel complexes **7** and **8** ultimately leads to their elimination from further study in this dissertation. While chromium bis(alkoxide) complexes may display intriguing reactivity and shall be investigated in the future, it is unlikely that nickel(II) complexes

would be suitable as a platform for metal-ligand multiple bonds due to the difficulty in oxidizing nickel beyond its 2+ oxidation state. The crystal structures of **10**-**12** all display distorted tetrahedral geometry at the metal center, with large RO−M−OR angles. Our proposed bis(alkoxide) system has been realized: the inclusion of two labile THF ligands in the complexes gives rise to a sort of protected bis(alkoxide) system, whereby THF removal can lead to reactivity at the vacant coordination sites on the metal. Cyclic voltammetry data reveal that **10**-**12** can all be oxidized, indicating that they could potentially support additional multiply-bonded ligands. However, the high oxidation potentials for both the manganese complex **10** and the cobalt complex **12** suggest that oxidative reactivity at these metals may prove challenging.

3.4. Experimental Details

General Methods and Procedures. All reactions involving air-sensitive materials were executed in a nitrogen-filled glovebox. Thallium hexafluorophosphate was purchased from Strem. All materials were used as received. All solvents were purchased from Fisher Scientific and were of HPLC grade. The solvents were purified using an MBRAUN solvent purification system and stored over 3-Å molecular sieves. Compounds **10**-**12** were characterized by ^{1}H and ^{13}C NMR spectroscopy, IR spectroscopy, UV-vis spectroscopy, solution state magnetic susceptibility, X-ray crystallography, cyclic voltammetry, and elemental analysis. NMR spectra were recorded at the Lumigen Instrument Center (Wayne State University) on a Varian Mercury 400 MHz NMR spectrometer in C_6D_6 or $C_6D_5CD_3$ at room temperature. Chemical shifts and coupling constants (*J*) were reported in parts per million (δ) and Hertz respectively. IR spectra were recorded on a Shimadzu IR-Affinity1 FT-IR spectrometer as paratone oil mull suspensions. UV-vis spectra were obtained in a Shimadzu UV-1800 spectrometer. Solution state effective magnetic moments were determined using the Evans method[49] and diamagnetic corrections were calculated using the Pascal's constants method;[55] three independent measurements were carried out for each sample. Electrochemical properties were determined using cyclic voltammetry on a BAS Epsilon system in a nitrogen-filled glovebox. Samples were prepared in anhydrous THF with 0.1 M tetrabutylammonium hexafluorophosphate $[NBu_4][PF_6]$ as the supporting electrolyte. Redox potentials

were determined with a scan rate of 100 mV/sec at 25 °C by using a platinum disc working electrode (2 mm diameter), a platinum wire counter electrode, and a non-aqueous Ag^{+}/Ag reference electrode, and referenced to ferrocene/ferrocenium couple. Elemental analyses were performed by Midwest Microlab LLC. Additional spectral data can be found in Appendix C.

X-ray Crystallographic Details. The structures of **10-12** were confirmed by X-ray analysis. The crystal was mounted on a Siemens Platform three circle goniometer equipped with an APEX detector using Graphite monochromated Mo Kα radiation (λ = 0.71073 Å). The data were processed using the programs SAINT and SADABS supplied by Bruker-AXS. The structure was solved by direct methods with SHELXS and refined by standard difference Fourier techniques with SHELXL (6.10 v., Sheldrick G. M., and Siemens Industrial Automation, 2000). Hydrogen atoms were placed in calculated positions using a standard riding model and refined isotropically; all other atoms were refined anisotropically.

$Mn(OR)_2(THF)_2$ (10). A 5.0 mL THF solution containing 27.8 mg (0.0795 mmol) of thallium(I) hexafluorophosphate was added dropwise to a 5.0 mL THF solution containing 42.6 mg (0.0397 mmol) of the dimeric manganese bis(alkoxide) complex $Mn_2(OR)_4Li_2Cl_2$ (**5**). Immediately a white precipitate formed. The reaction was stirred for one hour, upon which the volatiles were removed in vacuo. About 2.0 mL of hexanes were added to the remaining white cake, and subsequent filtration gave a pale yellow solution. Recrystallization from hexane at -35°C afforded the product as white crystals (30.4 mg, 60%). IR (cm^{-1}): 2988 (m), 2963 (m), 2880 (m), 1377 (w), 1356 (w), 1107 (s), 1067 (m), 1026 (m), 872 (m), 745 (s), 708 (s), 642 (w). $\mu_{eff} = 5.5 \pm 0.3\ \mu_B$ (calc. 5.9). No discernible features in the UV−vis spectrum. Anal. Calcd. for $C_{38}H_{62}O_4Mn$: C, 71.6; H, 9.8. Found: C, 71.3, H, 9.7.

$Fe(OR)_2(THF)_2$ (11). A 5.0 mL THF solution containing 38.9 mg (0.111 mmol) of thallium(I) hexafluorophosphate was added dropwise to a 5.0 mL THF solution containing 59.8 mg (0.0557 mmol) of the dimeric iron bis(alkoxide) complex $Fe_2(OR)_4Li_2Cl_2$ (**3**). Immediately a white precipitate formed. The reaction was stirred for one hour, upon which the volatiles were removed in vacuo. About 2.0 mL of hexanes were added to the remaining white cake, and subsequent filtration gave a pale yellow solution. Recrystallization from hexane afforded the product as white crystalline rods (40.7 mg, 57%). IR (cm^{-1}):

2987 (br), 2880 (m), 1379 (w), 1356 (w), 1101 (s), 1069 (m), 1034 (s), 1022 (s), 905 (w), 874 (m), 746 (s), 708 (s). μ_{eff} (Evans, CD_2Cl_2, 298 K): 4.7 ± 0.3 μ_B (calc. 4.9); Anal. Calcd. for $C_{38}H_{62}O_4Fe$: C, 71.5; H, 9.8. Found: C, 71.0, 9.5.

$Co(OR)_2(THF)_2$ (12). A 5.0 mL THF solution containing 28.1 mg (0.0806 mmol) of thallium(I) hexafluorophosphate was added dropwise to a 5.0 mL THF solution containing 43.5 mg (0.0403 mmol) of the dimeric cobalt bis(alkoxide) complex $Co_2(OR)_4Li_2Cl_2$ (**6**). Immediately a white precipitate formed, and the reaction color changed from blue to violet. The reaction was stirred for one hour, upon which the volatiles were removed in vacuo. About 2.0 mL of hexanes were added to the remaining white cake, and subsequent filtration gave a violet solution. Recrystallization from hexane at -35°C afforded the product as violet crystalline rods (25.3 mg, 49%). IR (cm^{-1}): 2988 (w), 2967 (w), 2895 (w), 2876 (w), 1489 (w), 1381 (w), 1360 (w), 1090 (m), 1063 (m), 1018 (s), 868 (m), 745 (s), 708 (s). ^1H NMR (C_6D_6, 400 MHz) δ 42.81, 24.95, 17.09, 13.05, 9.59, 9.39, 5.34. μ_{eff} = 3.6 ± 0.3 μ_B (calc. 3.9). λ_{max} (ε): 734 (176), 578 (64), 472 (40), 386 (98) M^{-1} cm^{-1}. Anal. Calcd. for $C_{38}H_{62}O_4Co$: C, 71.1; H, 9.7. Found: C, 70.8, H, 9.6.

Reaction of $Ni(OR)_2BrLi(THF)_2$ with $TlPF_6$. The nickel complex **8** (80.7 mg, 0.11 mmol) and $TlPF_6$ (38.7 mg, 0.11 mmol) were dissolved in separate THF solutions. The thallium hexafluorophosphate solution was added dropwise to the nickel solution, leading to the formation of a white precipitate. The reaction was stirred for one hour, upon which the volatiles were removed in vacuo, and the resulting residue was taken up in hexane. After filtering off the insoluble precipitate, the solution was concentrated before crystallization at −35 °C was attempted. Orange crystals were isolated, but they were confirmed to be the starting complex **8** (48.8 mg, 60% recovery).

CHAPTER 4: REACTIVITY OF AN IRON BIS(ALKOXIDE) COMPLEX WITH ADAMANTYL AZIDE: FORMATION OF AN IRON HEXAZENE COMPLEX

Portions of the text in this chapter were reprinted or adapted with permission from: Bellow, J. A.; Martin, P. D.; Lord, R. L.; Groysman, S. *Inorg. Chem.* **2013**, *52*, 12335-12337.

4.1. Introduction

With our desired bis(alkoxide) platform in hand, we next turned our attention toward using this platform for the synthesis of reactive metal-ligand multiple bonds. Specifically we chose to focus on metal imidos (M=NR), as metal-imido complexes in alkoxide-only ligand environments have yet to be investigated, and their increased reactivity could prove crucial toward discovering new catalytic nitrene transfer processes. As discussed in Chapter 1, such complexes could serve as reactive nitrene transfer agents for several different substrates. The most convenient method to prepare transition metal imido complexes is via reaction of a low-valent complex with an organic azide. The organic azide we chose to focus on for initial reactivity studies was adamantyl azide, AdN_3. Adamantyl azide was chosen due to its commercial availability, but also because it is a solid as opposed to many other azides, which are liquids, making its handling more convenient. Finally, its larger molecular weight increases its thermal stability, making it much safer to handle than the volatile lower molecular weight organic azides, which are potentially explosive. The objective of this chapter was to explore the reactivity of our newly designed bis(alkoxide) complexes with adamantyl azide. Spectroscopic and computational studies are also included.

4.2. Synthesis and Structural Characterization of the Iron Hexazene Complex $(RO)_2Fe(\mu\text{-}\kappa^2\text{:}\kappa^2\text{-}AdN_6Ad)Fe(OR)_2$

Because the iron bis(alkoxide) complex **11** looked to be the most easily oxidized according to cyclic voltammetry experiments, **11** was chosen for initial reactivity studies with organic azides. The addition of one equivalent of adamantyl azide to the iron bis(alkoxide) complex **11** in toluene led to a gradual color change to dark orange over the course of a few minutes. Crystallization from hexanes afforded the dark-orange product **13**, confirmed to be the hexazene complex $(RO)_2Fe(\mu\text{-}\kappa^2\text{:}\kappa^2\text{-}$

$AdN_6Ad)Fe(OR)_2$ (**Figure 42**). Rather than two-electron reduction of the azide followed by dinitrogen extrusion, two adamantyl azide molecules have been reduced by only one electron, and both have been reductively coupled through the terminal nitrogens. The irons therefore have been oxidized to iron(III). The crystal structure of **13** reveals that the diiron-hexazene core is essentially planar, with each iron center displaying a distorted tetrahedral geometry (**Figure 43**). Experimental crystallographic parameters are given in **Table 8**. The internal azide bond distances are about 1.29 Å, indicative of bond lengths between single and double bonds and showing that electron delocalization is present in the azide moieties. The distance between the two coupled azides is lengthened by about 0.1 Å and is more akin to an N−N single bond. The Fe−O bond lengths are comparable to those in similar iron(III) alkoxide complexes.[33c, 60] The Fe−O bonds are also noticeably shorter in the hexazene complex as opposed to those in **11**. This further suggests the presence of iron(III). The ^{1}H NMR spectrum of **13** failed to provide any meaningful data toward its characterization, likely due to its paramagnetism. The magnetic moment of **13** in solution (11.2 μB) is consistent with two uncoupled iron(III) centers. It is also worth mentioning here that similar reactions of both the manganese (**10**) and cobalt (**12**) bis(alkoxide) complexes with adamantyl azide were attempted, but no reactivity was observed. This reaffirms the high oxidation potentials observed in the CV shown in Chapter 3 and suggests that these complexes may not react with azides at all.

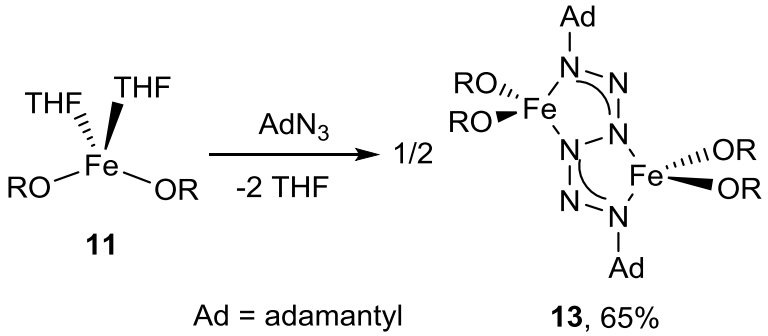

Figure 42. Reaction of the iron bis(alkoxide) **11** with adamantyl azide to form the hexazene complex, **13**.

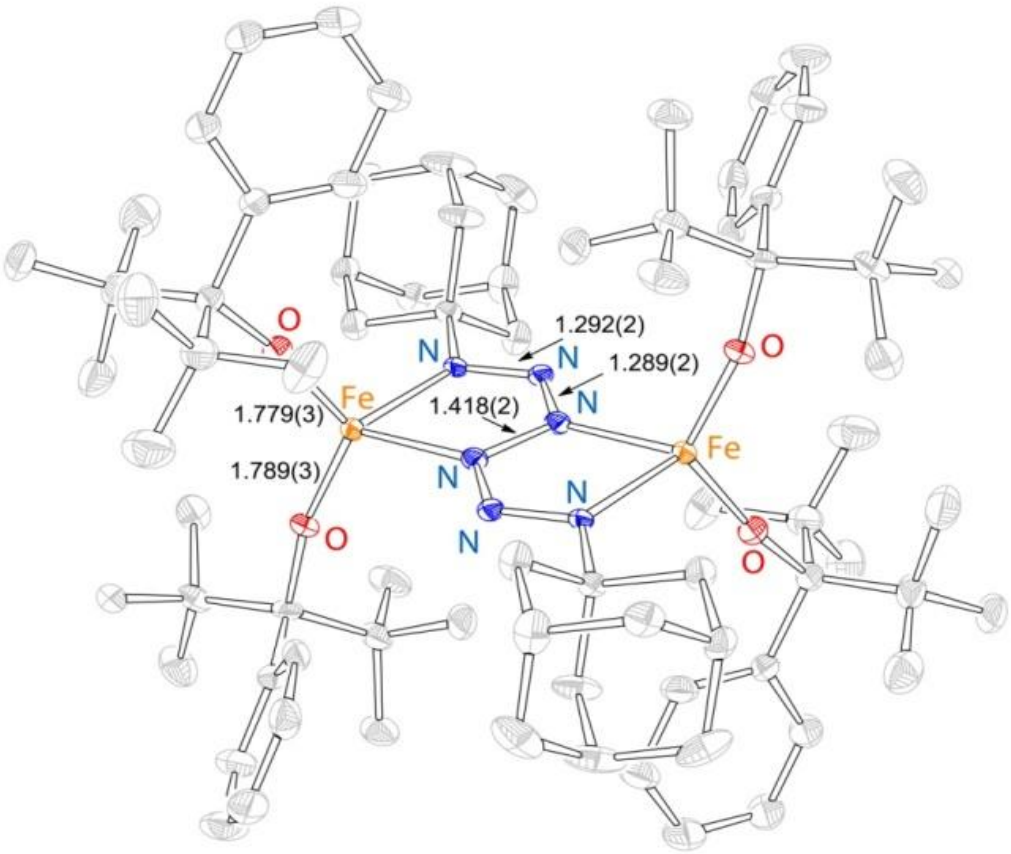

Figure 43. X-ray crystal structure of **13**, 50% probability ellipsoids. H atoms are omitted for clarity.

Table 8. Experimental crystallographic parameters for **13**.

complex	**13**
formula	$C_{80}H_{122}O_4N_6Fe_2$
fw	1343.54
crystal system	triclinic
space group	*P-1*
a (Å)	12.9324(6)
b (Å)	12.9330(6)
c (Å)	14.1689(7)
α (deg)	93.360(2)
β (deg)	93.147(2)
γ (deg)	115.750(2)
V (Å^3)	2122.29(17)
D_c (g cm^{-3})	1.058
Z	2
μ (mm^{-1})	0.388
T (K)	100(2)
R_1 (%)	5.39
GOF	1.042

The one-electron reduction of adamantyl azide and subsequent formation of the hexazene complex **13** is far from unprecedented; however, this type of reactivity is certainly uncommon. Currently in the literature there are only a handful of other reported examples of hexazene formation from organic azides.[14] However, in all reported cases the transformation was only made possible through the use of highly reducing metalloradicals, including iron(I), magnesium(I), and zinc(I), whereas we are able to

reductively couple adamantyl azide using the far less reducing iron(II). As a specific example, when Holland and coworkers reacted their three-coordinate iron(I) complex LFeNNFeL (L = HC[C(CH_3)N(2,6-*i*$Pr_2C_6H_3$)]$_2$) with two equivalents of adamantyl azide, two azides reductively coupled to form a product similar to **13**.[14a] Their complex is the only other reported hexazene complex for iron. Complex **13** is also the first example of a hexazene complex containing bulky alkoxide ligands.

Nitrogen-rich compounds are known to be energetic materials.[61] Therefore, we also assessed the potential of the hexazene complex **13** as a primary explosive. The complex did not detonate when subjected to impact, heat, or electrostatic discharge, confirming its stability toward explosive decomposition and its subsequent safe handling. Holland and coworkers performed similar tests on their hexazene complex, with analogous results.[14a]

4.3. Computational Characterization: Investigation of the Mechanism of Formation

To gain insight into the electronic structure of **13**, we turned to DFT calculations[62-65] on a model system, replacing adamantyl azide with methyl azide and replacing the [OR] ligands with methoxide ligands (in collaboration with Professor Richard Lord and his group, Grand Valley State University). Despite these simplifications, excellent agreement is seen for the hexazene bond lengths (**Figure 44**, left)[66] in the lowest-energy spin state (See Appendix D for the energetics and structures of alternative spin states). This structure had ten unpaired electrons (S = 5) with five singly occupied molecular orbitals on each iron center (See Appendix D), implying high-spin iron(III) ions and a dianionic hexazene ligand. A dianionic hexazene ligand was also observed in the previously reported dimetallic hexazene compounds.[14] One possible mechanism for the formation of **13** involves initial coordination of the azide to the iron bis(alkoxide) **11**. Next, dimerization occurs before the N−N bond is formed to give the hexazene, **13**. What is not clear is at what point the azide gets reduced. Spin density plots shed light on a possible answer to this question (**Figure 45**). No spin density is observed on the azide for the initial azide intermediate, Fe(OMe)$_2$(N_3Me) (**Figure 45**, left), indicating that the azide coordinates as a neutral ligand, and the iron(II) remains unoxidized. This stands in contrast to what Holland and coworkers observe in their system.[14a] However, dimer formation (**Figure 44**, right) results in an S = 4 species that has two high-

spin iron(III) ions antiferromagnetically coupled to the monoreduced bridging azide radicals. Spin density can clearly be observed on the azide radicals in $[Fe(OMe)_2(N_3Me)]_2$ (**Figure 45**, center), further supporting that reduction of the azides has taken place. To our knowledge, such a dimer is unprecedented, even though bimetallic species with bridging azides (N_3^-) are known.[3b] The dimeric structure places the terminal nitrogens of the azides in close proximity for coupling (2.937 Å), whereby the hexazene complex **13** can then be formed (**Figure 45**, right). Our computed thermodynamics for dimer formation are highly dependent on the functional chosen, but both B3LYP and BLYP suggest that dimerization is enthalpically favored.[67-69]

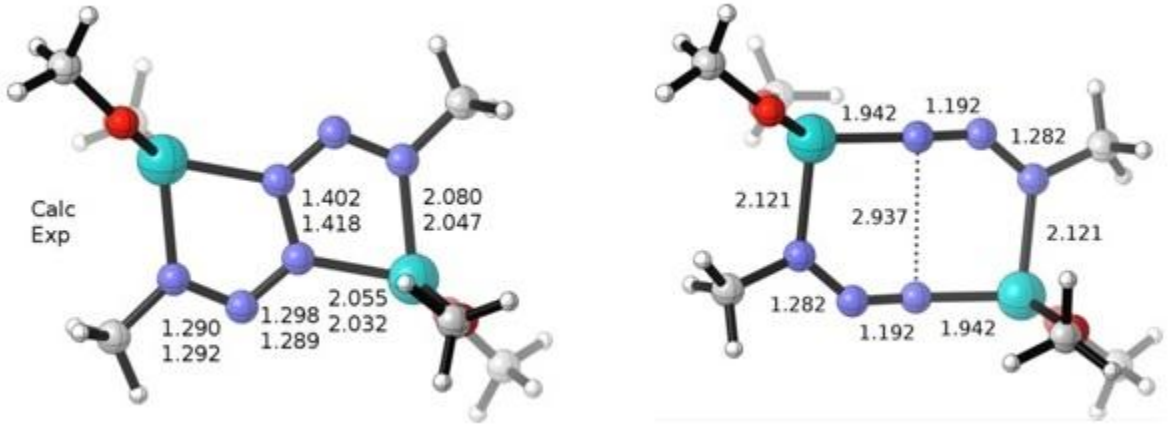

Figure 44. Comparison of computed and experimental bond lengths (Å) for the lowest-energy $S = 5$ state (left) and a putative intermediate prior to reductive coupling (right).

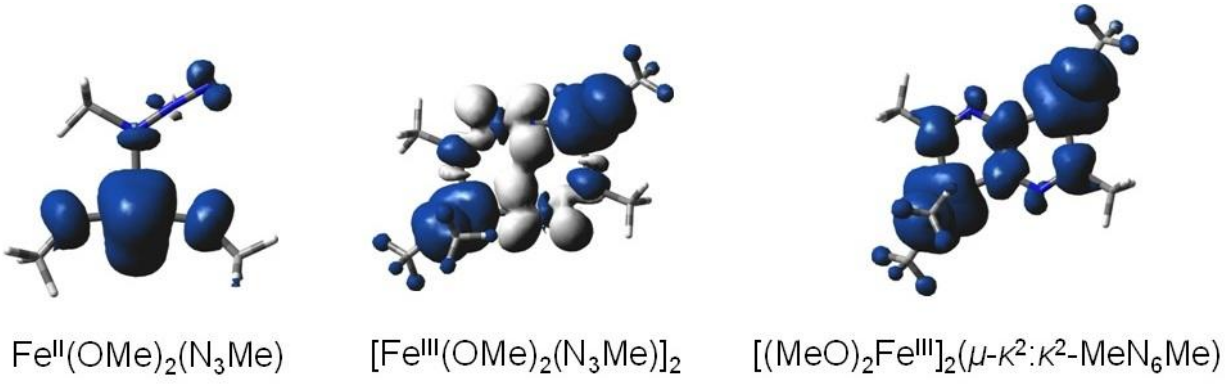

Figure 45. Spin density plots for the initial azide intermediate $Fe(OMe)_2(N_3Me)$ (left), the proposed dimeric intermediate $[Fe(OMe)_2(N_3Me)]_2$ (center), and the final product (right).

4.4. Summary and Conclusions

The iron bis(alkoxide) complex reacts with adamantyl azide to form an unusual hexazene complex: instead of two-electron azide reduction and metal-imido formation though, reductive coupling of monoreduced azides is observed. Complex **13** contains the hexazene moiety $AdNNNNNNAd^{2-}$ and is likely stabilized by the electron delocalization imparted from the iron centers. Coupled with a lack of sensitivity toward explosive decomposition, we can conclude that **13** is an exceptionally stable molecule. It is remarkable that the reducing power of iron(I) or other metalloradicals is not required to facilitate one-electron reduction of an organic azide using our bis(alkoxide) system, unlike other reported systems. This also further supports the higher reactivity of metals in alkoxide ligand systems. We were unable to observe similar reactivity with the manganese and cobalt bis(alkoxide) complexes **10** and **12**, likely due to their high oxidation potentials. Despite the unusual observed reactivity of **11** with adamantyl azide, we were unable to form a metal-imido complex, so we next turned our attention toward reactions with other organic azides to see if differing reactivity is observed.

4.5. Experimental Details

General Methods and Procedures. All reactions involving air-sensitive materials were executed in a nitrogen-filled glovebox. 1-azidoadamantane was purchased from Aldrich. All materials were used as purchased. All solvents were purchased from Fisher scientific and were of HPLC grade. The solvents were purified using an MBRAUN solvent purification system and stored over 3-Å molecular sieves. The complexes were characterized using IR spectroscopy, elemental analysis, and the Evans method. NMR spectra were recorded at the Lumigen Instrument Center (Wayne State University) on a Varian Mercury 400 MHz NMR Spectrometer in C_6D_6 or C_7D_8 at room temperature. IR spectra were recorded on a Shimadzu IR-Affinity1 FT-IR spectrometer as paratone oil mull suspensions. Elemental analyses were performed by Midwest Microlab LLC. Additional spectral data and experimental details regarding DFT can be found in Appendix D.

X-ray Crystallographic Details. The structure of **13** was confirmed by X-ray analysis. The crystals were mounted on a Bruker APEXII/Kappa three circle goniometer platform diffractometer

equipped with an APEX-2 detector. A graphic monochromator was employed for wavelength selection of the Mo Kα radiation (λ = 0.71073 Å). The data were processed and the structure was solved using the APEX-2 software supplied by Bruker-AXS. The structure was refined by standard difference Fourier techniques with SHELXL (6.10 v., Sheldrick G. M., and Siemens Industrial Automation, 2000). Hydrogen atoms were placed in calculated positions using a standard riding model and refined isotropically; all other atoms were refined anisotropically. The structure of **13** contained half of the hexazene complex per asymmetric unit. Structure **13** also contains a disordered hexane molecule that has been modeled in three different conformations.

$(RO)_2Fe(\mu\text{-}\eta^2\text{:}\eta^2\text{-}AdN_6Ad)Fe(OR)_2$ (13). A 5.0 mL toluene solution of 1-azidoadamantane (10.2 mg, 0.0576 mmol) was added dropwise to a 5.0 mL toluene solution of the iron bis(alkoxide) complex **11** (36.8 mg, 0.0576 mmol). Over the course of a few minutes the solution color changed from pale yellow to orange-brown. The reaction was stirred for an hour, upon which the volatiles were removed in vacuo. Recrystallization from hexanes afforded the product as dark orange crystals (25.2 mg, 65%). μ_{eff} = 11.2 μ_B (calc. 11.0) IR (cm^{-1}): 2918 (m), 2853 (m), 1520 (m), 1489 (m), 1456 (m), 1271 (w), 1179 (w), 1121 (m), 1049 (s), 1018 (m), 766 (w), 739 (m). Anal. Calcd. for $C_{80}H_{122}O_4N_6Fe_2$: C, 71.5; H, 9.2; N, 6.3. Found: C, 71.4; H, 9.1; N, 6.2.

CHAPTER 5: REACTIVITY OF AN IRON BIS(ALKOXIDE) COMPLEX WITH ARYL AZIDES: CATALYTIC NITRENE COUPLING TO FORM AZOARENES

Portions of the text in this chapter were reprinted or adapted with permission from: Bellow, J. A.; Yousif, M.; Cabelof, A. C.; Lord, R. L.; Groysman, S. *Organometallics* **2015**, *34*, 2917-2923.

5.1. Introduction

This chapter focuses on the reactivity of aryl azides with $Fe(OR)_2(THF)_2$. Aryl azides may present a different reactivity than alkyl azides. Aryl nitrene formation is as common—if not more common—than alkyl nitrene formation in the literature. As a result of this, the objective of this part of my work was to prepare several different aryl azides and test their reactivity with the iron bis(alkoxide) complex **11**. Our initial hypothesis was that we would observe similar reactivity to adamantyl azide, in that the complex would reductively couple the azides to form a hexazene. Hexazene formation from aryl azides has recently been observed by Schultz and coworkers.[14d, 15] However, our bis(alkoxide) system was found to lead to an entirely different reactivity with aryl azides, as shall be discussed.

5.2. Stoichiometric and Catalytic Nitrene Coupling of Aryl Azides to form Azoarenes

Aryl azides, in contrast to alkyl azides, are actually far easier to synthesize, largely due to a lack of stereochemistry at the carbon adjacent to the azide moiety. The most common method to synthesize aryl azides proceeds via formation of an aryl diazonium intermediate (ArN_2^+). This intermediate can be formed by reacting an aniline precursor with sodium nitrite in the presence of hydrochloric acid. Subsequent reaction with sodium azide generates the desired aryl azide. Our initial studies with aryl azides began with the synthesis of mesityl azide ($MesN_3$). Mesityl azide, along with the other bulky azides discussed herein, were synthesized using reported procedures from their corresponding, commercially available anilines.[70] While the aryl azides considered herein are not reported to explosively decompose under ambient conditions, proper safety precautions, including small-scale syntheses and usage of a blast shield, were observed in all cases.

In a similar manner to the preparation of the hexazene complex **13**, one equivalent of mesityl azide was added to one equivalent of the bis(alkoxide) **11** in toluene. Unlike the reaction to form **13**, gas

evolution was immediately observed, along with a gradual color change to dark orange. The gas evolved here is suspected to be dinitrogen, hinting that nitrene formation may be occurring. Reaction workup and subsequent crystallization afforded two different cocrystallized products (**Figure 46**). The first product, as observed by X-ray diffractometry, was the iron(III) tris(alkoxide) complex $Fe(OR)_3$ (**14**) which is a rare example of iron in a trigonal planar coordination environment.[31c, 35c] The second product, also identified by X-ray crystallography, was azomesitylene, MesN=NMes. An NMR experiment was then performed, running the same reaction in C_6D_6 and taking NMR of the resulting solution in the presence of trimethoxybenzene as an internal standard. Quantitative consumption of the starting azide was confirmed, as well as three new peaks corresponding to a product featuring the mesityl moiety, consistent with the observed crystallization of azomesitylene. Thus, both X-ray crystallography and NMR spectroscopy indicate that rather than reductively coupling mesityl azide to give a hexazene complex, the iron bis(alkoxide) instead induces nitrene formation, followed by coupling of nitrenes via N=N bond formation to give an azoarene. Addition of the internal standard in the NMR confirms that the azoarene forms quantitatively. We were unable to determine the yield of the iron tris(alkoxide) **14** due to its nearly featureless NMR and UV-vis spectra. Complex **14** can be synthesized independently from the reaction of iron(III) chloride with three equivalents of LiOR (**Figure 46**, bottom). Again, it is worth noting that similar reactions of the manganese (**10**) and cobalt (**12**) bis(alkoxide) complexes with mesityl azide were also attempted, but no reactivity was observed, thus eliminating these systems from further study.

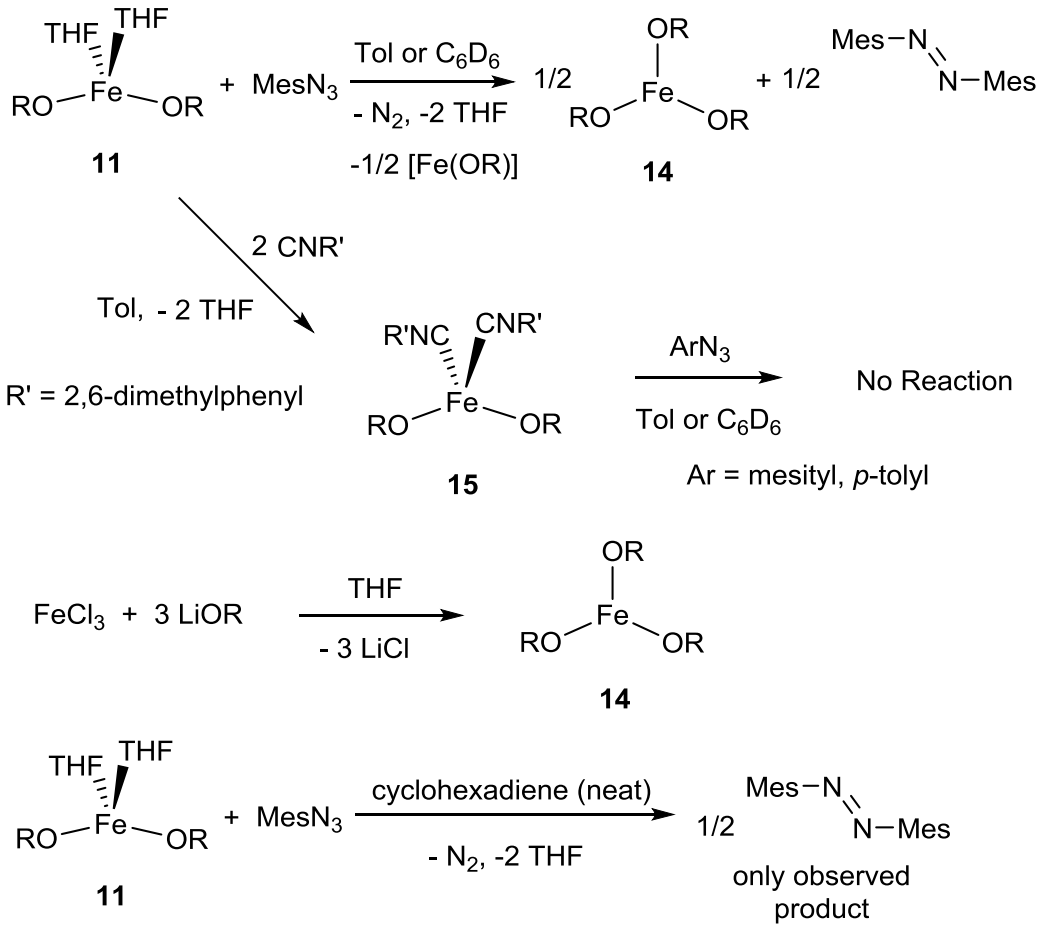

Figure 46. Reactivity of $Fe(OR)_2(THF)_2$ (**11**) with mesityl azide and related reactions.

The formation of an azoarene in the above reaction suggests the presence of a transient nitrene. It is possible that a reactive iron imido complex forms as an intermediate in this process. Thus, it may be possible to transfer the nitrene to other substrates. To investigate this, we first tried C−H activation of cyclohexadiene. When the same reaction is run using cyclohexadiene as a solvent, only the azoarene is observed by NMR, with no evidence of C−H activation. We next tested if the nitrene could be transferred to 2,6-dimethylphenyl isocyanide via C-N bond formation: addition of a 1:1 mixture of the isocyanide and mesityl azide to a solution of **11** in C_6D_6 leads to the formation of a green solution. No azoarene formation is detected, and no other new peaks are visible in the NMR. The isocyanide peaks also disappear completely, presumably due to isocyanide coordination to the metal. To test this hypothesis, we

also independently synthesized the isocyanide adduct $Fe(OR)_2(CNR')_2$ (**15**, R' = 2,6-dimethylphenyl). Green crystals of $Fe(OR)_2(CNR')_2$ were obtained by the addition of two equivalents of the isocyanide to a toluene solution of **11** (**Figure 46**). X-ray diffraction confirmed the structure, and the complex was also characterized by ^{1}H NMR and IR spectroscopies. Finally, we attempted to perform nitrene transfer with **15** by addition of mesityl azide. NMR demonstrates that no reaction of the azide takes place, suggesting that the more strongly bound isocyanide ligands prevent the azide from accessing the iron center. A summary of this reactivity can be found in **Figure 46**. Crystal structures of $Fe(OR)_3$, azomesitylene, and the isocyanide adduct **15** can be found in **Figures 47-49**. Experimental crystallographic parameters are given in **Table 9**.

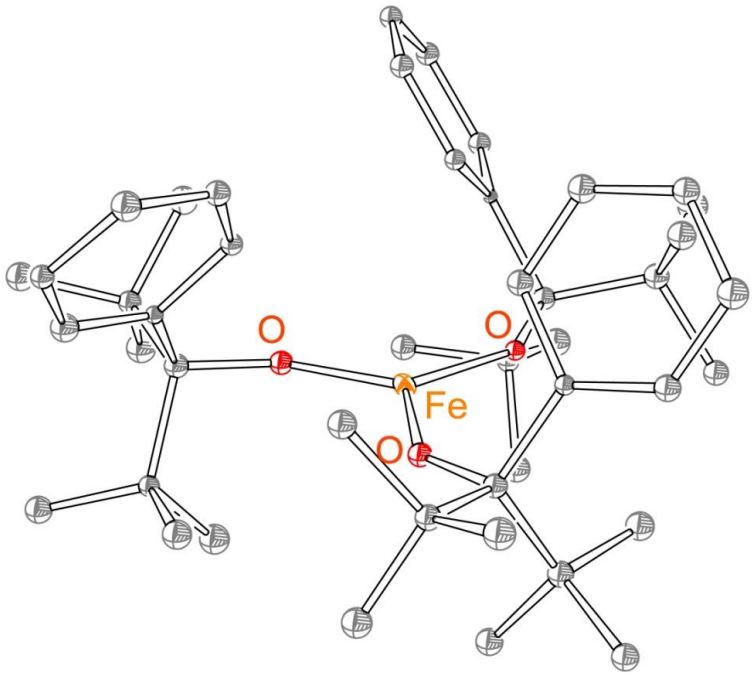

Figure 47. X-ray crystal structure of $Fe(OR)_3$ (**14**).

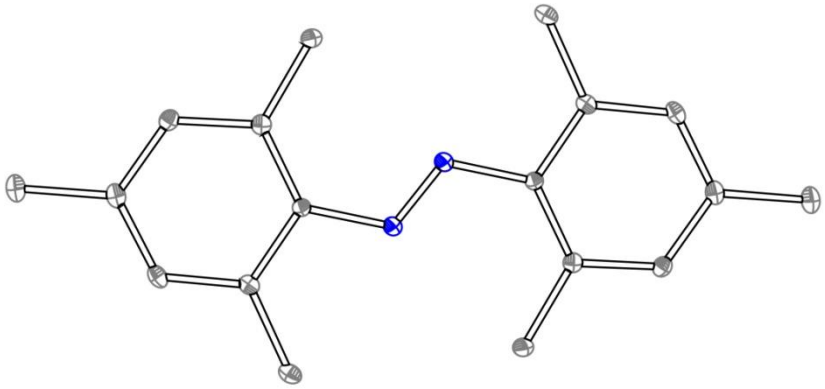

Figure 48. X-ray crystal structure of MesNNMes.

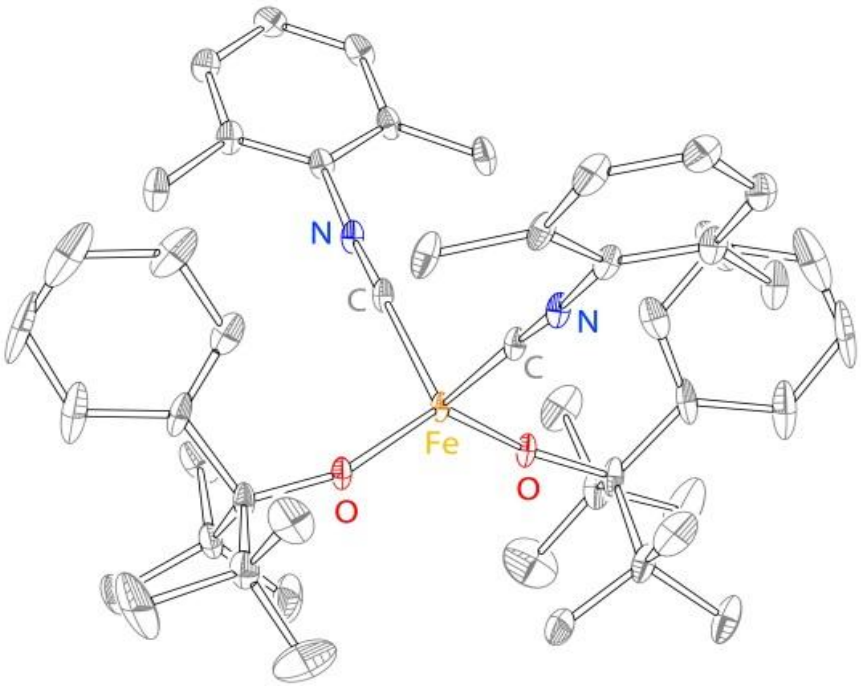

Figure 49. X-ray crystal structure of **15**.

Table 9. Experimental crystallographic parameters for **14**, MesNNMes, and **15**.

compound	**14**	**MesNNMes**	**15**
formula	$C_{45}H_{69}O_3Fe$	$C_{18}H_{22}N_2$	$C_{48}H_{58}FeN_2O_2$
fw	713.85	266.38	750.82
crystal system	hexagonal	monoclinic	monoclinic
space group	*P-3*	$P2_1/n$	*C2/c*
a (Å)	12.2741(19)	4.7927(6)	23.3174(18)
b (Å)	12.2741(19)	9.8612(12)	9.2385(7)
c (Å)	14.995(3)	15.4094(17)	21.1985(16)
α (deg)	90.00	90.00	90.00
β (deg)	90.00	92.167(5)	110.977(4)
γ (deg)	120.00	90.00	90.00
V (Å^3)	1956.4(6)	727.75(15)	4263.9(6)
D_c (g cm^{-3})	1.212	1.216	1.170
Z	6	4	4
μ (mm^{-1})	0.424	0.071	0.392
T (K)	100(2)	100(2)	100(2)
R_1 (%)	4.57	4.04	8.06
GOF	0.961	1.048	1.101

The nitrene coupling was also found to be catalytic (**Figure 50**, top). Using 1-10 mol% loading of the catalyst **11**, mesityl azide can be cleanly converted to azomesitylene in a matter of hours (see **Table 10** for reaction conditions and yields). NMR spectroscopy in the presence of an internal standard (1,3,5-trimethoxybenzene) demonstrates that the conversion is nearly quantitative; pure azomesitylene can be isolated in 95% yield at 1 mol % of catalyst. Similar catalytic conversion of 2,6-diethylphenyl azide to the corresponding azoarene is also possible. NMR monitoring of the reaction mixture demonstrates full

conversion within 48 hours. Pure azo(2,6-diethylbenzene) was isolated in 93% yield at 5 mol % catalyst. In addition to the symmetric coupling products, asymmetric nitrene coupling is also possible through the use of two different aryl azides. Using an equal number of equivalents of mesityl azide and 2,6-diethylphenyl azide with 10% catalyst loading led to catalytic formation of all three possible azoarene products in similar quantities, as confirmed by NMR yield (35% of azomesitylene, 30% of the mixed azoarene, and 25% of azo(2,6-diethylbenzene)). All symmetric and asymmetric azoarenes in the above experiments were identified by both NMR spectroscopy and mass spectrometry. Several control experiments were also performed to confirm the catalytic activity of **11** (**Figure 51**). Replacing the catalyst with either iron(II) chloride or iron(III) chloride leads to no observed nitrene coupling. Similarly, attempting the catalysis in the presence of only the internal standard, or of LiOR leads to no reaction. This confirms that **11** is indeed essential for stoichiometric and catalytic nitrene coupling.

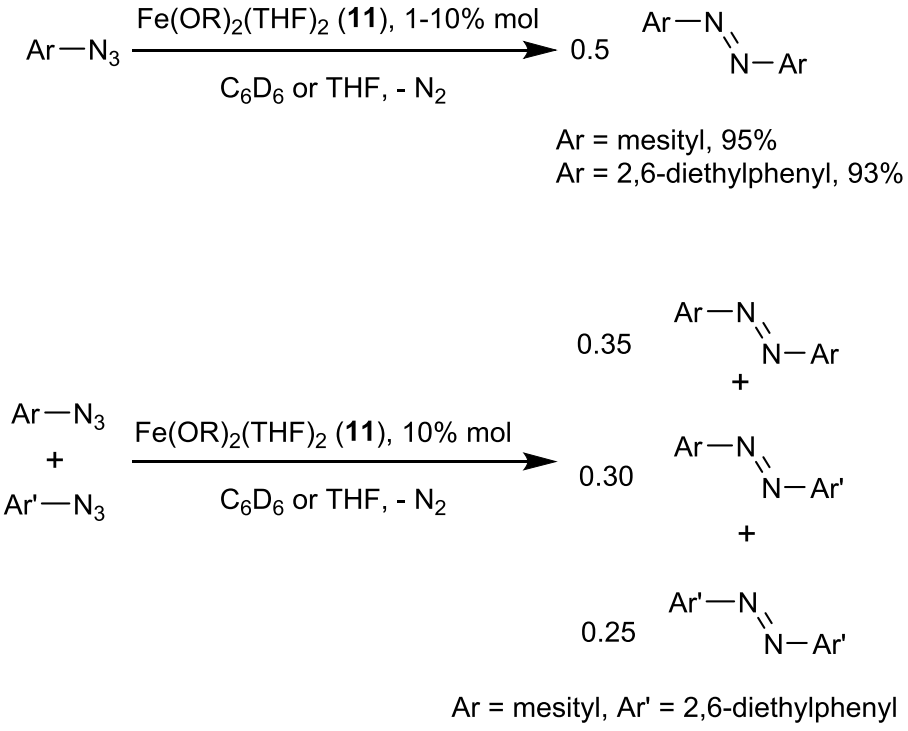

Figure 50. Symmetric (top) and asymmetric (bottom) catalytic formation of azoarenes from aryl azides using $Fe(OR)_2(THF)_2$ (**11**).

Table 10. Catalysis data for the reaction of **11** with various aryl azides.

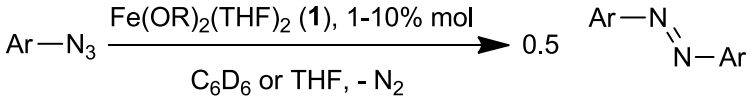

Ar	Catalyst Loading (%)	Reaction Time (h)	NMR Yield (%)	Isolated Yield (%)
2,4,6-Me_3Ph	5	4	>90	92
2,4,6-Me_3Ph	1	24	>90	95
2,6-Et_2Ph	5	48	>90	93
4-F_3CPh	10	24	0	-
Ph	10	24	0	-
3,5-Me_2Ph	10	24	0	-
4-MeOPh	10	24	0	-
4-MePh	10	24	0	-
2-MePh	10	24	0	-
2,4,6-Me_3Ph and 3,5-Me_2Ph	10	4	$50^a/0^b/0^c$	-
2,4,6-Me_3Ph and 2,6-Et_2Ph	10	4	$36^a/30^d/26^e$	-

[a] Azomesitylene. [b] Azo(3,5-dimethylphenyl-mesitylene). [c]Azo(3,5-dimethylbenzene). [d]Azo(2,6-diethylbenzene) [e]Azo(2,6-diethylbenzene).

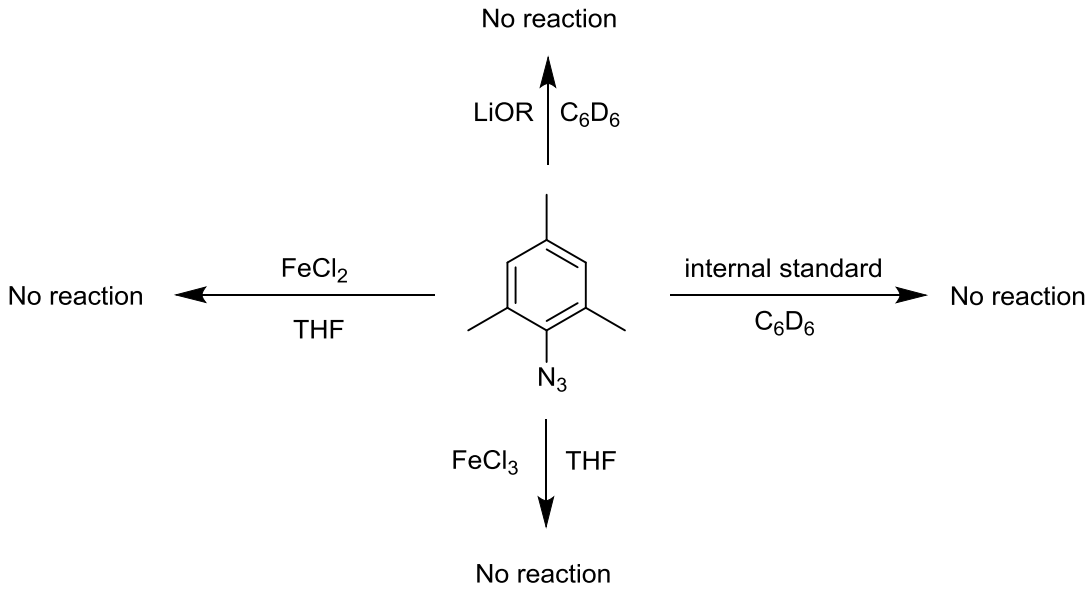

Figure 51. Control experiments performed to confirm the catalytic nature of **11**.

While there is precedence for stoichiometric and catalytic nitrene coupling, it is nonetheless a rare transformation, having only been reported in a handful of cases.[8] There are only three published cases of catalytic nitrene coupling. The first two, as reported by Peters and coworkers, are via iron(III) and ruthenium(III) imido complexes stabilized by a silyl ligand with chelating phosphine arms.[8e, 8g] The third case, as reported by Heyduk and coworkers, involves a tantalum(V) complex in a chelating aryloxide ligand framework.[8f] In all of these previously reported cases though, elevated temperatures (up to 70 °C) and extended reaction times (up to seven days) are required, whereas in our system, we can catalytically couple nitrenes at room temperature in a matter of hours. This further corroborates the high reactivity of our bis(alkoxide) system compared to other systems.

5.3. Formation of the Stable Bridging Imido Complexes (RO)(THF)Fe(μ-NAr)$_2$Fe(OR)(THF)

Surprisingly, reacting less sterically bulky aryl azides such as *para*-tolyl, *ortho*-tolyl, 3,5-dimethylphenyl, or phenyl azides with **11** leads to no azoarene formation, even at elevated temperatures, as evidenced by NMR (see **Table 10**). However, a color change to red-brown and gas evolution were observed in all four cases, suggesting formation of a metal-imido species. A similar lack of nitrene coupling was observed for the electron-rich 4-methoxyphenyl azide, as well as the electron-poor 4-

(trifluoromethyl)phenyl azide. These data suggest that the nature of azoarene formation in our system is governed by a steric effect. The only azides that appear to undergo nitrene coupling are those possessing R groups in the *ortho* positions on the aryl ring, like mesityl or 2,6-dimethylphenyl azides. In an additional experiment, asymmetric nitrene coupling using mesityl azide and 3,5-dimethylphenyl azide was attempted; however, the only organic product confirmed by NMR was azomesitylene. No inclusion of the 3,5-dimethylphenyl azide was observed.

The lack of detection of any organic products forming in the reaction of **11** with nonbulky aryl azides indicates that stable metal-imido complexes may be forming in these cases. To determine the product formed, a stoichiometric reaction of **11** with 4-(trifluoromethyl)phenyl azide was attempted (**Figure 52**). Subsequent crystallization led to the isolation of black crystals confirmed to be the iron mono(alkoxide) dimer (RO)(THF)Fe(μ-NAr)$_2$Fe(OR)(THF) (**16**, Ar = 4-(trifluoromethyl)phenyl), possessing two bridging imido moieties (**Figure 53**). The Fe$_2$(μ-NAr)$_2$ diamond core motif depicted in the crystal structure of **16** is rare in diiron species, but cluster compounds containing several iron centers with bridging aryl imidos are more numerous.[71] Analogous bis(imido) products were also isolated for 3,5-dimethylphenyl azide (**17**), and the smaller phenyl azide (**18**) (**Figure 52**). The crystal structure of **17** is shown in **Figure 54**. Crystals suitable for X-ray diffraction could not be isolated for **18**, but elemental analysis confirmed the identity of the bulk product. Experimental crystallographic parameters for **16** and **17** can be found in **Table 11**. The structures of **16** and **17** are consistent with the iron(III) oxidation state, as indicated by the Fe−OR bond distances and the presence of the Fe$_2$(μ-NAr)$_2$ core (observed only for iron(III) in previously synthesized complexes).[35c, 71d-g] The structures of both **16** and **17** are centrosymmetric, containing only half of the complex in the asymmetric unit. Two distinct, albeit very similar, Fe−N bond lengths are observed (see **Figures 53** and **54**). The observed Fe−Fe distances of 2.543(1) Å (**16**) and 2.5268(4) Å (**17**) are closely related to the Fe−Fe distances in the previously reported (NHC)(X)Fe(μ-NAr)$_2$Fe(NHC)(X) complexes synthesized by Deng and coworkers, which were in the 2.424(4)-2.527(1) range (NHC = N-heterocyclic carbene, X = Cl, F).[71g]

Additionally, we also postulate that the formation of **16**−**18**, containing mono(alkoxide) centers,

is accompanied by the formation of the iron tris(alkoxide) **14** (see **Figure 52**). Formation of **14** as a byproduct was observed in the stoichiometric and catalytic coupling of azoarenes (see above), so from a stoichiometric standpoint, it makes sense that it may be forming as a byproduct here as well. Unfortunately, the presence of **14** could not be detected due to its featureless UV-vis and NMR spectra, as well as its overall instability.

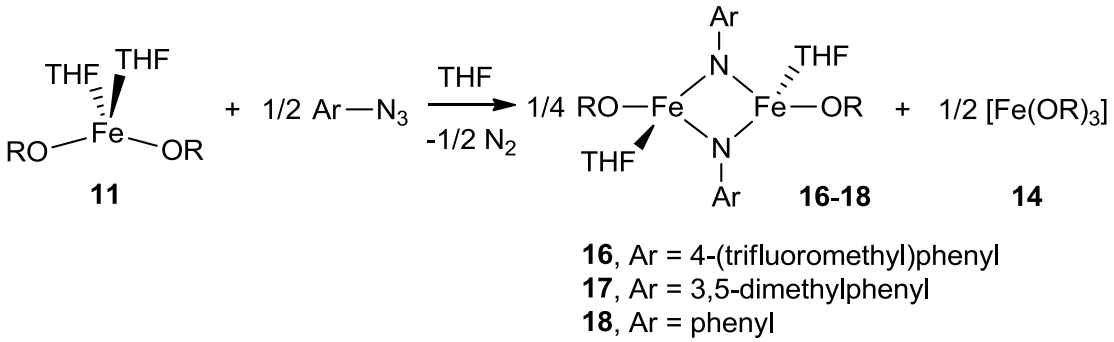

Figure 52. Reaction of $Fe(OR)_2(THF)_2$ (**11**) with aryl azides yielding $(RO)(THF)Fe(\mu\text{-}NAr)_2Fe(OR)(THF)$ (**16**-**18**).

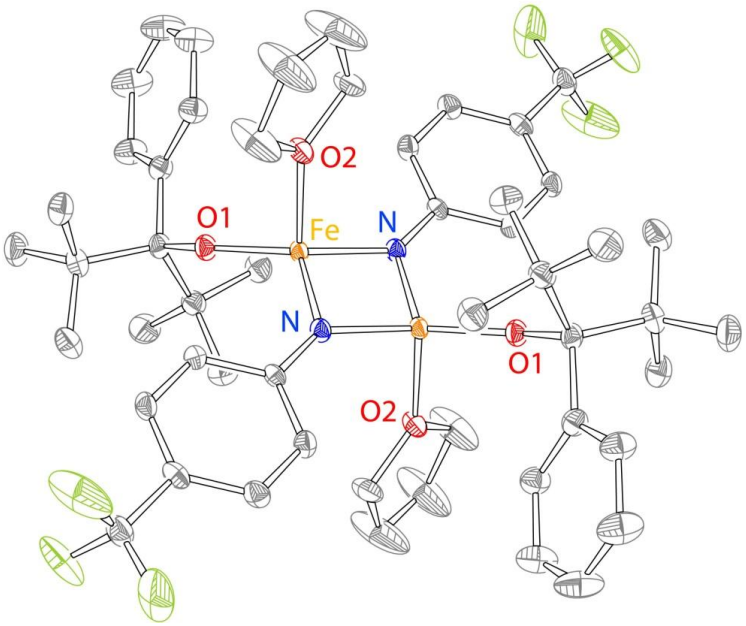

Figure 53. X-ray crystal structure of **16**, 40% probability ellipsoids. H-atoms are omitted for clarity. Selected bond distances (Å) and angles (°): Fe–N, 1.881(3)/1.897(3); Fe–O1, 1.803(2); Fe–O2, 2.075(2); N–Fe–N, 96.03(6); O1–Fe–O2, 102.58(2).

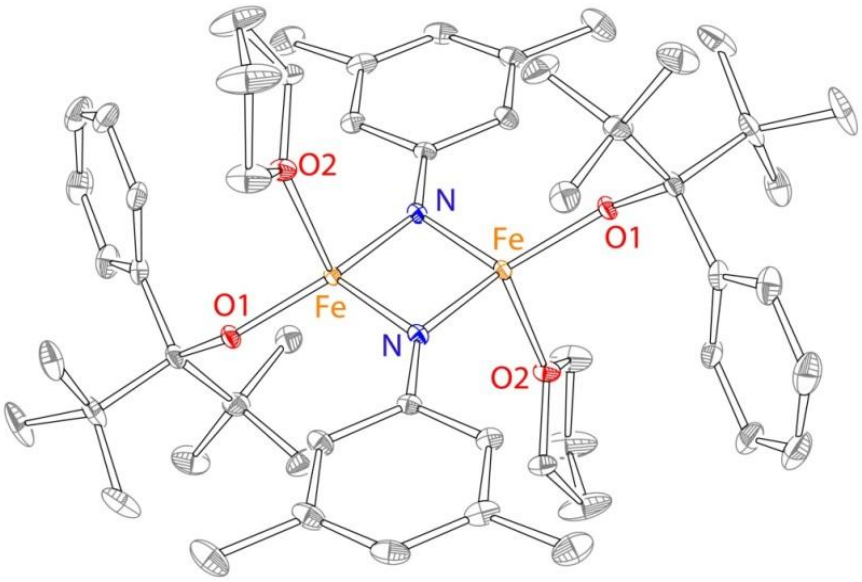

Figure 54. X-ray crystal structure of **17**, 40% probability ellipsoids. H-atoms are omitted for clarity. Selected bond distances (Å) and angles (°): Fe−N, 1.875(1)/1.902(1); Fe−O1, 1.833(1); Fe−O2, 2.085(1); N−Fe−N, 96.03(6); O1−Fe−O2, 102.58(2).

Table 11. Experimental crystallographic parameters for **16** and **17**.

complex	**16**	**17**
formula	$C_{50}H_{72}N_2O_4F_6Fe_2$	$C_{54}H_{80}N_2O_4Fe_2$
fw	1012.80	932.90
crystal system	monoclinic	monoclinic
space group	*C2/c*	$P2_1/c$
a (Å)	25.1613(8)	9.3779(6)
b (Å)	13.7596(4)	19.846(2)
c (Å)	17.3302(6)	14.4267(11)
α (deg)	90.00	90.00
β (deg)	113.417(2)	106.326(3)
γ (deg)	90.00	90.00
V (Å^3)	5505.7(3)	2576.8(4)
D_c (g cm^{-3})	1.299	1.202
Z	8	4
μ (mm^{-1})	0.594	0.607
T (K)	100(2)	100(2)
R_1 (%)	5.39	3.94
GOF	1.041	1.043

Complexes **16**-**18** all appear to be stable molecules that are unreactive toward additional equivalents of azide: after treating **17** with an excess of mesityl azide and stirring for 24 hours, no color change was observed, and no new peaks appeared in the ^{1}H NMR spectrum. The reaction of **16** with 2,6-dimethylphenyl isocyanide gave similar results. Additionally, heating a solution of **17** to 50 °C for four hours in an attempt to force formation of the azoarene from the bridging imido groups led to no reaction. This suggests that the bridging imido complexes are stable species that form when bulky groups are not

present on the aryl ring of the azide. When bulky groups are present, it is possible that the bridging imido complex cannot form due to steric constraints.

5.4. Mechanistic Discussion and Computational Studies

A proposed mechanism to rationalize the differing reactivity modes of **11** with aryl azides is presented in **Figure 55** below. A plausible first step consists of initial coordination of the azide to the metal followed by dinitrogen extrusion to give the reactive iron imido intermediate $Fe(OR)_2(NAr)$. We were not able to directly observe the formation of $Fe(OR)_2(NAr)$; however, its electronic structure was investigated computationally (see below). Complexes similar to $Fe(OR)_2(NAr)$ have been proposed as intermediates in other related systems.[2b, 3b, 72] Specifically, an iron(IV) imido complex was postulated as an intermediate on the route to intramolecular C−H activation using adamantyl azide in the similar bis(aryloxide) system $Fe(OC_6H_2\text{-}2,6\text{-}Ad\text{-}4\text{-}R)_2$ (R = Me, ^{i}Pr).[58b] The postulated intermediate $Fe(OR)_2(NAr)$ is strongly oxidizing, and it thus reacts with a second equivalent of the reducing iron(II) bis(alkoxide) complex **11** in a comproportionating fashion to yield two iron(III) complexes—the iron(III) tris(alkoxide) complex, **14**, and the iron(III) mono(alkoxide) dimer $(RO)(THF)Fe(\mu\text{-}NAr)_2Fe(OR)(THF)$, **16**-**18**. It is possible that the formation of these dimers is preceded by the formation of the monomer Fe(OR)(NAr)(THF); however, we were not able to obtain any evidence to this end. Both $Fe(OR)_2(NAr)$ and $(RO)(THF)Fe(\mu\text{-}NAr)_2Fe(OR)(THF)$ can be responsible for the observed catalytic nitrene coupling, either via a mononuclear metallatetrazene intermediate ([FeN(Ar)N(Ar)NN], as previously described by Hillhouse and proposed in the reaction mechanism by Peters)[4a, 8e] or a dinuclear mechanism (coupling of bridging imidos).

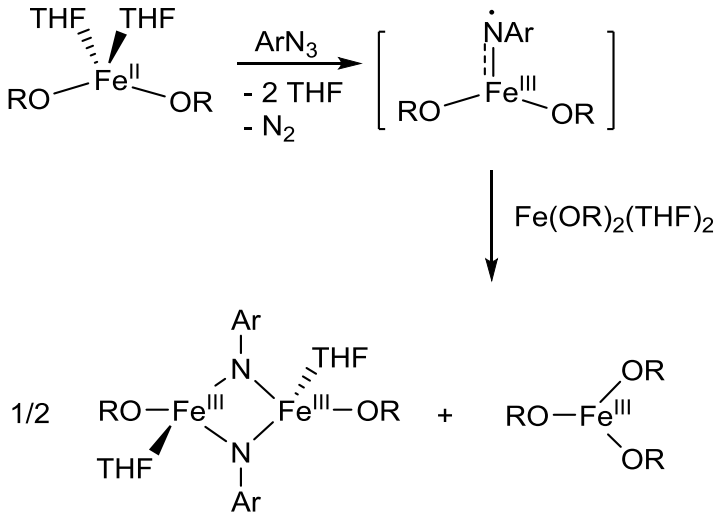

Figure 55. Proposed "comproportionation" reaction explaining the formation of the iron-imido dimers and $Fe(OR)_3$.

Kinetic experiments using 2,6-diethylphenyl azide demonstrate that the reaction appears to be of second order in the azide (**Figure 56**); this finding may be consistent with both mechanisms. To elucidate the reaction order in iron, we attempted the initial rate method, in which we changed the concentration of the iron precursor while following the decrease in the concentration of the azide. However, several different measurements did not lead to a definitive integer rate (see Appendix E). It is possible that several mechanisms are responsible for the nitrene coupling in our system, and the prevalence of the given mechanism is determined by the concentration of the iron species.

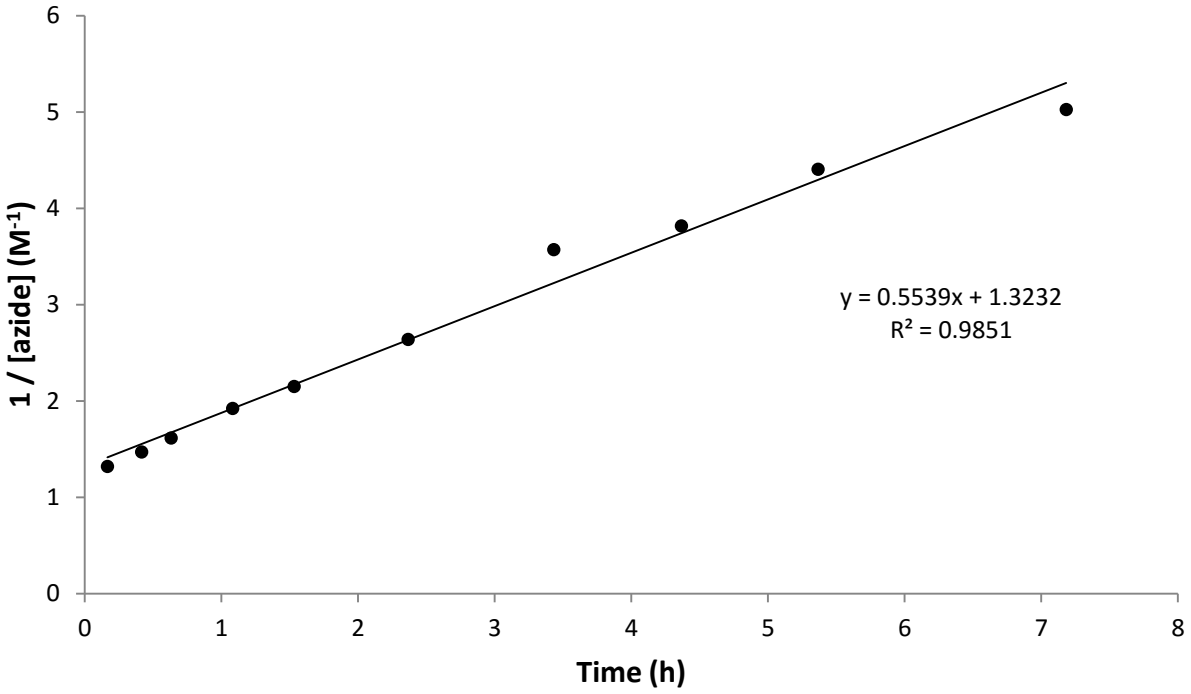

Figure 56. Kinetics plot of 1/[azide] vs. time, indicating a second order rate in azide (see kinetics experiment procedure below).

To better understand the electronic structure of the putative intermediate $Fe(OR)_2(NAr)$, it was explored using DFT at the B3LYP/6-311G(d) level of theory (in collaboration with Professor Richard Lord and his group, Grand Valley State University).[63, 73] Spin states ranging from singlet to septet were optimized, and the high-spin quintet state was found to be lowest in energy. B3LYP is documented to overstabilize high-spin states due to its paramagnetic dependence on the amount of Hartree-Fock exchange,[74] so single-point energies at the optimized B3LYP structures were performed with OPBE,[75] a functional known to produce accurate spin-state splittings.[69a, 76] The quintet was still the lowest energy spin state with OPBE (See Appendix E). In principle, this quintet species should be high-spin iron(IV) with two OR^- and one NAr^{2-} ligands and therefore should only exhibit α spin density at the metal. The computed spin density is shown in **Figure 57** below. In addition to α spin density at the iron center, there is significant β spin density on the NAr ligand. A corresponding orbital analysis (See Appendix E) showed five α electrons at iron overlapping between a d–π orbital ($S\alpha\beta$ ~0.53) and an NAr π orbital, which suggests that this species is best described as a high-spin iron(III) antiferromagnetically coupled to

NAr$^{-\bullet}$. This description is consistent for OPBE, which does not have explicit exchange and therefore should not overstabilize an electronic configuration with maximal exchange (d^5) at the metal center. Our formulation of the electronic structure of $Fe(OR)_2(NAr)$ is consistent with previous calculations by Betley and coworkers on a similar high-spin iron-imido species, in which they also found iron to be iron(III) antiferromagnetically coupled with an imido radical.[4b] However, we note that while DFT describes our $Fe(OR)_2(NAr)$ species as an imido radical, it did not activate C−H bonds, contrary to Betley's system.

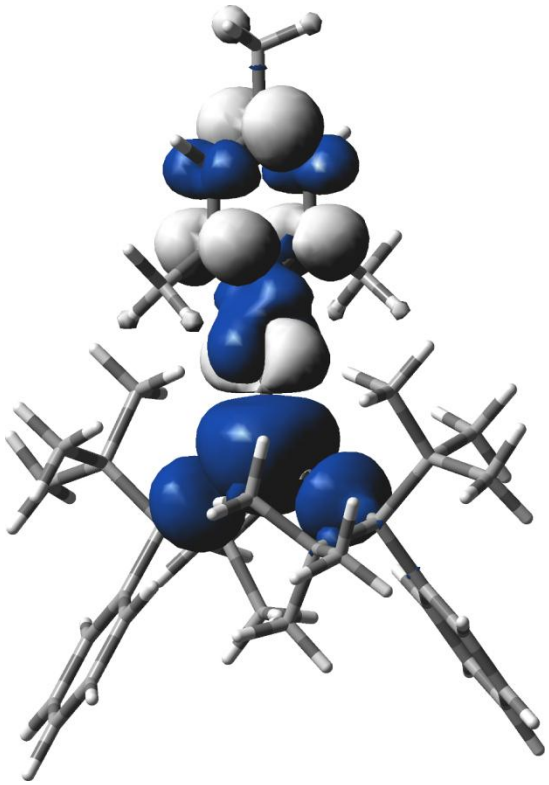

Figure 57. Spin density isosurface plot (iso = 0.002 a.u.) for quintet $Fe(OR)_2(NAr)$.

5.5. Summary and Conclusions

In summary, both stoichiometric and catalytic nitrene coupling can be performed using the iron bis(alkoxide) complex **11**. Nitrene coupling is a rare transformation that has only been reported in a handful of instances. While our complex can selectively couple nitrenes from aryl azides, its substrate scope is limited to aryl azides with sterically hindering groups in the 2- and 6-positions on the aryl ring.

For azides that do not possess these groups, bridging bis(imido) complexes can be isolated. These bis(imido) complexes do not react with additional equivalents of azide, nor do they decompose upon heating to give azoarenes, suggesting that they are stable species that do not undergo nitrene coupling. Observation of the iron tris(alkoxide) **14** as a byproduct of catalysis hints at a comproportionation process occurring, whereby an initially formed iron imido complex reacts with a second equivalent of **11** to give **14** and a bridging imido dimer. One of the major limitations of our system, as seen in this chapter, is the unexpected lability of the alkoxide ligand, which allows for unwanted side products such as the tris(alkoxide) complex **14** to be formed. One way to circumvent this issue is by synthesizing an even more bulky alkoxide ligand to prevent formation of the tris(alkoxide), or to design and use a chelating bis(alkoxide) ligand, thus eliminating the issue of alkoxide lability altogether. This may allow greater control over the iron-imido intermediates and could lead to more versatile nitrene transfer chemistry.

5.6. Experimental Details

General Methods and Procedures. All reactions involving air-sensitive materials were executed in a nitrogen-filled glovebox. Mesityl azide, 2,6-diethylphenyl azide, and 3,5-dimethylphenyl azide were synthesized according to literature procedures.[70] Other aryl azides were purchased as solutions from Aldrich and dried over molecular sieves overnight prior to use. All other materials were used as purchased from Aldrich. All solvents were purchased from Fisher Scientific and were of HPLC grade. The solvents were purified using an MBRAUN solvent purification system and stored over 3-Å molecular sieves. The complexes were characterized using NMR and IR spectroscopies, mass spectrometry, X-ray crystallography, elemental analysis, and the Evans method. NMR spectra were recorded at the Lumigen Instrument Center (Wayne State University) on a Varian Mercury 400 MHz NMR Spectrometer in C_6D_6 at room temperature. IR spectra of powdered samples were recorded on a Shimadzu IR Affinity-1 FT-IR Spectrometer outfitted with a MIRacle10 attenuated total reflectance accessory with a monolithic diamond crystal stage and pressure clamp. UV-visible spectra were obtained on a Shimadzu UV-1800 spectrometer. Low resolution mass spectra were obtained on a Shimadzu LCMS 2020 using a 1:1 mixture of acetonitrile and water as the eluent, with 0.1% formic acid added. Elemental analyses were performed

by Midwest Microlab LLC and Galbraith Laboratories Inc. NMR spectra from the above described experiments, additional spectra, computational details, and additional computational data can be found in Appendix E.

X-ray Crystallographic Details. The structures of **14**-**18** were confirmed by X-ray analysis. The crystals were mounted on a Bruker APEXII/Kappa three circle goniometer platform diffractometer equipped with an APEX-2 detector. A graphic monochromator was employed for wavelength selection of the Mo Kα radiation (λ = 0.71073 Å). The data were processed and the structure was solved using the APEX-2 software supplied by Bruker-AXS. The structure was refined by standard difference Fourier techniques with SHELXL (6.10 v., Sheldrick G. M., and Siemens Industrial Automation, 2000). Hydrogen atoms were placed in calculated positions using a standard riding model and refined isotropically; all other atoms were refined anisotropically.

Stoichiometric Reaction of $Fe(OR)_2(THF)_2$ (11) with Mesityl Azide. A 5.0 mL toluene solution of mesityl azide (7.9 mg, 0.0488 mmol) was added dropwise to a 5.0 mL toluene solution of 1 (31.2 mg, 0.0488 mmol), leading to a gradual color change from yellow to a dark red-orange. Gas evolution was also observed. The reaction was stirred for one hour, upon which the volatiles were removed in vacuo to give a red-orange residue. This residue was dissolved in a minimum amount of hexane and placed in the freezer. After 24 hours, two different types of orange crystals had formed. The products (characterized by X-ray crystallography) were determined to be the iron tris(alkoxide), **14**, and the azoarene MesNNMes. An analogous experiment was run in C_6D_6 in the presence of 1,3,5-trimethoxybenzene as an internal standard. After stirring the reaction for four hours, NMR revealed total consumption of the starting azide, with 3 as the only NMR-active product, formed in near-quantitative (96%) yield.

Preparation of $Fe(OR)_3$ (14) Using an Fe(III) Precursor. A 5.0 mL THF solution of the lithium salt of the ligand LiOR (62.1 mg, 0.275 mmol) was prepared, along with a 5.0 mL THF solution of $FeCl_3$ (14.9 mg, 0.0915 mmol). The ligand salt was added to the metal chloride with stirring, upon which the solution color changed from yellow to orange. After stirring for 15 minutes, a THF solution of $TlPF_6$ (63.9 mg, 0.275 mmol) was added dropwise, leading to immediate formation of a white precipitate. The

reaction was stirred for an hour, upon which the precipitate was filtered off, and the volatiles from the remaining filtrate were removed in vacuo to give an orange residue. This residue was redissolved in a minimum amount of hexane and placed in the freezer to afford orange crystals. (52.9 mg, 63%). IR (cm^{-1}): 2974 (m), 2873 (m), 1558 (m), 1485 (w), 1386 (m), 1155 (w), 1053 (s), 1018 (m), 901 (w), 769 (m), 745 (w). μ_{eff} = 6.3 ± 0.2 μ_B (calc. 5.9). λ_{max} (ε_M) 317 (10823), 519 (656). The compound was also characterized by X-ray crystallography. Anal. Calcd. for $C_{45}H_{69}O_3Fe$: C, 75.7; H, 9.7. Found: C, 73.8; H, 9.6. The compound is unstable at room temperature, even under inert atmosphere. After 24 h at room temperature in the solid state, orange crystals of **14** deform into an oily, dark green-brown residue. ^1H NMR of this green-brown residue reveals the presence of decomposed ligand. Even submitting a single crystal of this complex for elemental analysis under dry ice did not yield satisfactory elemental analysis results.

$Fe(OR)_2(CNAr)_2$ (15). To a stirred toluene solution of the iron bis(alkoxide) **11** (60.3 mg, 0.09 mmol) was added a toluene solution of 2,6-dimethylphenyl isocyanide (24.8 mg, 0.19 mmol) in one portion. Immediately the solution color changed to green. The reaction was stirred for one hour, upon which the volatiles were removed in vacuo. The resulting green residue was dissolved in a minimum amount of hexane, filtered, and placed in the freezer to afford green X-ray quality crystals (42.0 mg, 59%). IR (cm^{-1}): 2978 (m), 2955 (m), 2878 (m), 2129 (s), 1489 (w), 1381 (m), 1358 (w), 1096 (s), 1072 (s), 1022 (m), 887 (m), 772 (s), 745 (s), 702 (s), 648 (m). μ_{eff} = 4.9 ± 0.1 μ_B (calc. 4.9). Anal. Calcd. for $C_{48}H_{64}N_2O_2Fe$: C, 76.2; H, 8.5; N, 3.7. Found: C, 76.1; H, 8.3; N, 3.8.

(RO)Fe(THF)(μ-$NAr)_2$Fe(THF)(OR) (Ar = 4-(trifluoromethyl)phenyl) (16). A 5.0 mL THF solution of 4-(trifluoromethyl)phenyl azide (14.1 mg, 0.075 mmol) was added dropwise to a 5.0 mL THF solution of **11** (48.1 mg, 0.075 mmol). Immediately gas evolution was observed, along with a solution color change to dark green. Over the course of a half hour the solution color gradually changed to black. The reaction was stirred for four hours, upon which the volatiles were removed in vacuo to yield a black residue. Recrystallization from hexane at -35 ^oC afforded the product as black crystals (9.2 mg, 48%). IR (cm^{-1}): 2963 (w), 2941 (w), 2880 (w), 1607 (w), 1489 (w), 1389 (w), 1319 (s), 1161 (m), 1107 (m), 1065

(s), 1015 (m), 839 (m), 745 (m), 706 (m). μ_{eff} = 3.8 ± 0.1 μ_B. The compound was also characterized by X-ray crystallography. Anal. Calcd. for $C_{50}H_{72}O_4N_2F_6Fe_2$: C, 61.7; H, 7.0; N, 2.8. Found: C, 61.3; H, 6.9; N, 3.0.

(RO)Fe(THF)(μ-NAr)$_2$Fe(THF)(OR) (Ar = 3,5-dimethylphenyl) (17). A 5.0 mL THF solution of 3,5-dimethylphenyl azide (10.4 mg, 0.0707 mmol) was added dropwise to a 5.0 mL THF solution of **11** (45.3 mg, 0.0709 mmol). Immediately gas evolution was observed, along with a solution color change to dark green. Over the course of a half hour the solution color gradually changed to a dark maroon. The reaction was stirred for four hours, upon which the volatiles were removed in vacuo to yield a brown residue. Recrystallization from pentane at -35 ^oC afforded the product as sticky brown crystals (7.3 mg, 44%). IR (cm^{-1}): 3003 (w), 2974 (w), 2938 (m), 2880 (m), 2833 (w), 1647 (w), 1593 (m), 1541 (w), 1506 (w), 1476 (s), 1435 (m), 1206 (m), 1140 (w), 1096 (m), 1049 (w), 1018 (s), 746 (s), 708 (w). μ_{eff} = 4.8 ± 0.2 μ_B. The compound was also characterized by X-ray crystallography. Anal. Calcd. for $C_{54}H_{80}O_4N_2Fe_2$: C, 69.5; H, 8.6; N, 3.0. Found: C, 68.0; H, 8.6; N, 1.9. Product was sticky and difficult to transfer in appreciable amounts. As such, satisfactory elemental analysis could not be obtained, even after repeated attempts.

(RO)Fe(THF)(μ-NAr)$_2$Fe(THF)(OR) (Ar = phenyl) (18). A 5.0 mL THF solution of phenyl azide (7.7 mg, 0.065 mmol) was added dropwise to a 5.0 mL THF solution of **11** (41.3 mg, 0.065 mmol). Immediately gas evolution was observed, along with a solution color change to dark green. Over the course of a half hour the solution color gradually changed to a dark maroon. The reaction was stirred for four hours, upon which the volatiles were removed in vacuo to yield a brown residue. Precipitation from hexane at -35 ^oC afforded the product as a red-brown solid (7.4 mg, 52%). IR (cm^{-1}): 2920 (w), 2851 (w), 1520 (m), 1489 (w), 1462 (m), 1387 (m), 1119 (m), 1049 (s), 1016 (s), 968 (m), 845 (w), 721 (m), 710 (m). μ_{eff} = 4.5 ± 0.1 μ_B. Anal. Calcd. for $C_{52}H_{70}O_4N_2Fe_2$: C, 68.5; H, 8.3; N, 3.2. Found: C, 68.4; H, 8.1; N, 3.5.

General Procedure for the Synthesis of Azoarenes. $Fe(OR)_2(THF)_2$ (25.0 mg, 0.039 mmol) (**11**) was dissolved in either THF or C_6D_6 in a scintillation vial. The aryl azide (~120-140 mg for 5 mol % of **11**) and the internal integration standard 1,3,5-trimethoxybenzene (65.0 mg, 0.39 mmol) were dissolved in the same solvent in a separate vial. The azide solution was then added dropwise to the solution of **11**, upon which gas evolution was observed, along with a gradual solution color change to red-orange. The reaction was stirred for the appropriate time, upon which NMR spectra were obtained for an aliquot of the solution, confirming complete consumption of the starting azide. The solution was then passed through a plug of silica to obtain the purified azoarene product, which was massed to obtain a yield. The nature of the product was verified using mass spectrometry and ^{1}H NMR spectroscopy.

Procedure for the Synthesis of Asymmetric Azoarenes. Same procedure as above (general procedure for the synthesis of azoarenes) was used, but an equal number of equivalents of both azides were first combined prior to dropwise addition to the catalyst. The reaction was stirred for the appropriate time, upon which NMR of an aliquot was taken. Mass spectrometry confirmed the presence of the asymmetric product for the reaction of mesityl azide and 2,6-diethylphenyl azide.

Control Experiments. Four separate control experiments were conducted. First, mesityl azide was stirred in the presence of iron(II) chloride and the internal standard for 24 hours. NMR revealed that no reaction had taken place. Next, mesityl azide was stirred in the presence iron(III) chloride and the internal standard for 24 hours. NMR revealed that no reaction had taken place. Next, mesityl azide was stirred in the presence of the lithium salt of the ligand, LiOR, and the internal standard for 24 hours. NMR revealed that no reaction had taken place. Finally, mesityl azide alone was stirred in the presence of the internal standard for 24 hours. NMR revealed that no reaction had taken place.

Kinetics Experiments. 2,6-diethylphenyl azide (628.2 mg, 3.59 mmol) and the internal standard 1,3,5-trimethoxybenzene (142.4 mg, 0.85 mmol) were dissolved in C_6D_6. This solution was then added in one portion to a stirred solution of 1 mol % of **11** (22.9 mg, 0.036 mmol). NMR spectra of an aliquot of the solution were taken at regular intervals over a period of 7.5 hours. The integration ratio with the standard was used to calculate the concentration of the azide, and its decrease was monitored. A plot of

1/[azide] vs time revealed a linear progression, suggesting that the catalysis is second order in azide. Plots of the additional kinetics experiments using different concentrations of 1 and 2,6-diethylphenyl azide are given in Appendix E.

CHAPTER 6: REACTIVITY OF IRON AND COBALT BIS(ALKOXIDE) COMPLEXES WITH DIAZOALKANES: FORMATION OF A STABLE HIGH-VALENT COBALT CARBENE

Portions of the text in this chapter were reprinted or adapted with permission from: Bellow, J. A.; Stoian, S. A.; van Tol, J.; Ozarowski, A.; Lord, R. L.; Groysman, S. *J. Am. Chem. Soc.* **2016**, *138*, 5531-5534.

6.1. Introduction

As previously mentioned, transition metal carbene complexes are commonly encountered intermediates in a variety of C−C bond formation reactions, including cyclopropanation, olefin metathesis, and C−H activation. Carbene complexes are generally classified into one of two groups—Fischer carbenes or Schrock carbenes.[3c] The type of carbene formed depends heavily on the type of metal used, the substituents on the carbene, as well as the ligand environment on the metal. Fischer carbenes are generally found with low-valent middle to late transition metals with π-accepting ligands, while Schrock carbenes are found with high-valent early transition metals with π-donating ligands. Carbene complexes that fall outside of these two classifications do exist, but are far less numerous. In a similar fashion to the synthesis of metal-imido complexes, metal-carbene complexes can be synthesized via dinitrogen extrusion from diazoalkanes (R_2CN_2), which are reactive, highly colored, and occasionally explosive compounds that are often used as carbene transfer agents themselves.

We have shown that our bis(alkoxide) system is a capable nitrene-transfer agent that is highly selective toward nitrene coupling to form azoarenes. While this reactivity was unexpected, it still suggested that our bis(alkoxide) ligand platform can generate reactive metal-ligand multiple bonds. As such, we next decided to see if that reactivity could carry over to metal-carbon multiple bonds. Because investigation of the iron bis(alkoxide) complex **11** proved to be fruitful with azides, we chose **11** as a starting point for our entry into carbene chemistry. The objective of this chapter was to explore the reactivity of our bis(alkoxide) system with diazoalkanes.

6.2. Reaction of Iron and Cobalt Bis(alkoxide) Complexes with Diazoalkanes

The diazoalkane we chose for our preliminary investigation was diphenyldiazomethane (Ph_2CN_2). The diphenylcarbene moiety has been previously found to form stable carbene complexes with other first-

row transition metals.[26a, 26d, 26e] The presence of two phenyl groups provides electronic stabilization via charge delocalization on the carbene carbon, as well as through steric protection. Additionally, diphenyldiazomethane is not shock-sensitive and far less dangerous to handle than the lower molecular weight diazoalkanes. Finally, diphenyldiazomethane can be prepared readily by the oxidation of the corresponding hydrazone with activated manganese(IV) oxide.[77] As an initial reaction, one equivalent of diphenyldiazomethane was added to one equivalent of the iron bis(alkoxide) complex **11** in hexanes, leading to an instantaneous color change to red. Reaction workup afforded colorless crystals as the major product in 60% yield, confirmed to be benzophenone azine, $(Ph_2CN)_2$ (**Figure 58**). Attempts to isolate or characterize the inorganic byproducts from this reaction were unsuccessful. Presumably the iron carbene complex $Fe(OR)_2(CPh_2)$ is generated, but it rapidly reacts with additional diazoalkane present in solution to yield the azine. The formation of benzophenone azine from the decomposition of diphenyldiazomethane has been previously reported in the literature for both the reaction of diphenyldiazomethane with transition metal compounds,[78] as well as in the thermal decomposition of diphenyldiazomethane.[79] An analogous reaction setup was attempted for the reaction with the manganese bis(alkoxide) complex **10**, but no reaction occurred.

The reaction of the cobalt bis(alkoxide) complex **12** with diphenyldiazomethane was next attempted, with markedly different results (**Figure 58**). Upon diphenyldiazomethane addition, the solution color gradually changed to red-brown over the course of a few minutes. Workup and crystallization led to the isolation of brown crystals in high yield (85%), confirmed by X-ray crystallography to be the novel cobalt carbene complex $Co(OR)_2(CPh_2)$ (**19**). This molecule is noteworthy in that, to the best of our knowledge, it is the first example of an isolable, structurally characterized cobalt carbene complex in a weak-field ligand environment. Carbene complexes of the later first-row transition metals that possess high-valent metal centers or that are stabilized by weak-field ligands are largely nonexistent, although a few cases for iron have been reported.[80] The first spectroscopically and structurally characterized dirhodium carbenes were also recently reported.[81] Intriguingly, **19** is stable at room temperature in the

solid state under inert atmosphere, and crystals of it can be stored for weeks at −35 °C without any evidence of degradation.

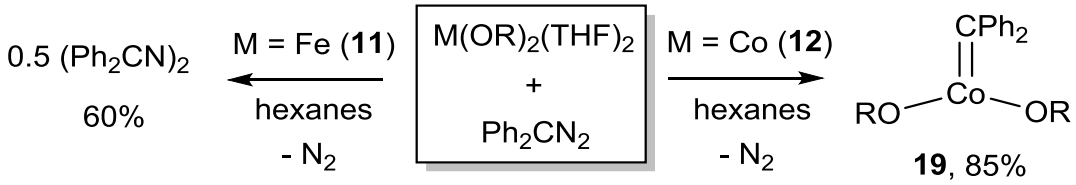

Figure 58. Reaction of iron (**11**) and cobalt (**12**) bis(alkoxide) complexes with diphenyldiazomethane.

The crystal structure of **19** is shown in **Figure 59** below. Experimental crystallographic parameters can be found in **Table 12**. The structure depicts a Co=C bond length of 1.773(3) Å, which, of the eleven reported terminal cobalt-carbene structures, is among the shortest, with the shortest Co=C bond length being 1.74 Å for the cobalt fluorocarbene complex Co(Cp)(PCy_3)(CF(CF_3)).[82] This short carbene bond suggests increased metal-carbon π-bonding and directly contrasts with the longer (1.9-2.0 Å) bond lengths reported for cobalt(I) terminal carbenes. Additionally, the cobalt-alkoxide bond lengths are 1.765(2) Å, significantly shorter than those of the bis(alkoxide) precursor **12**, at 1.849(1) Å. This suggests that the oxidation state of the cobalt in **19** is likely higher than 2+ and that the carbene here is not behaving as a Fischer carbene. Solution magnetic measurements and cyclic voltammetry further corroborate this possibility. Compound **19** demonstrates a magnetic moment of 2.0 ± 0.1 μ_B, consistent with a low-spin complex (S = 1/2). In contrast, the cobalt bis(alkoxide) **12** is high spin (S = 3/2), which is typical of low-coordinate metal(II) species in weak-field ligand environments.[4c, 78e, 83] The full cyclic voltammogram of **19** (**Figure 60**) demonstrates several quasi-reversible reductions at −1.37 V, −2.62 V, and −3.16 V. No complex oxidation was observed in the accessible solvent window. This finding supports the presence of a highly oxidized cobalt center in **19**. Also, no change was observed in the CV when cycled after the second redox event (**Figure 61**), suggesting that independent redox events are taking place.

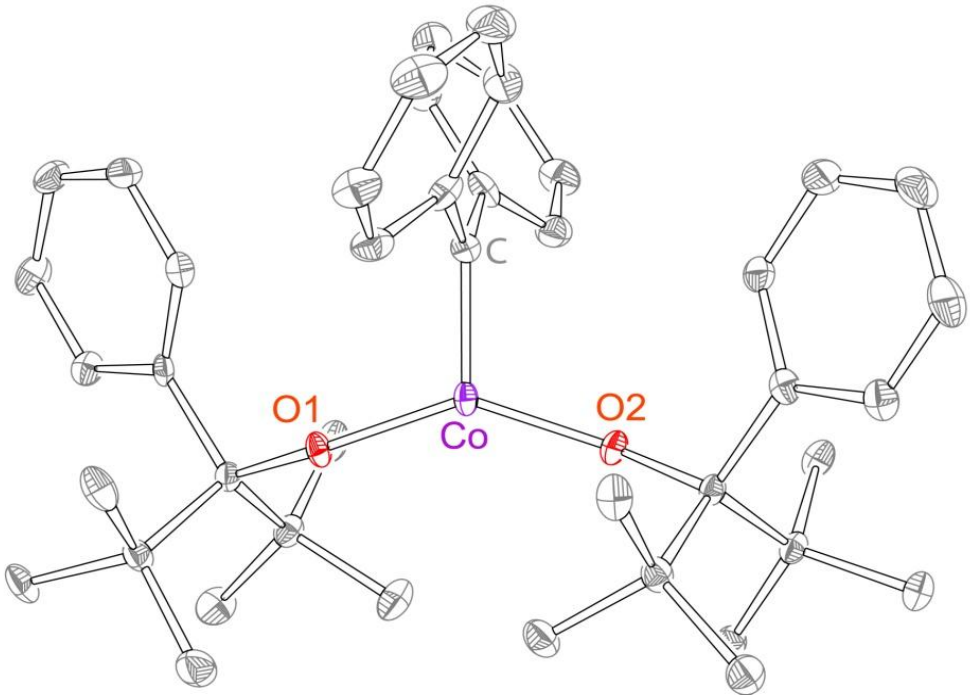

Figure 59. X-ray crystal structure of Co(OR)(CPh_2) (**19**), 40% probability ellipsoids. H-atoms are omitted for clarity. Selected bond distances (Å) and angles (°): Co-C, 1.773(3) Å, Co-O1, 1.765(2) Å, O1-Co-O2, 140.8(1).

Table 12. Experimental crystallographic parameters for **19**.

complex	**19**
formula	$C_{43}H_{56}O_2Co$
fw	663.81
crystal system	triclinic
space group	*P-1*
a (Å)	8.5434(4)
b (Å)	11.3181(5)
c (Å)	19.6570(10)
α (deg)	106.087(2)
β (deg)	96.817(2)
γ (deg)	97.583(2)
V (Å^3)	1786.12(15)
D_c (g cm^{-3})	1.234
Z	2
μ (mm^{-1})	0.516
T (K)	100(2)
R_1 (%)	6.38
GOF	1.120

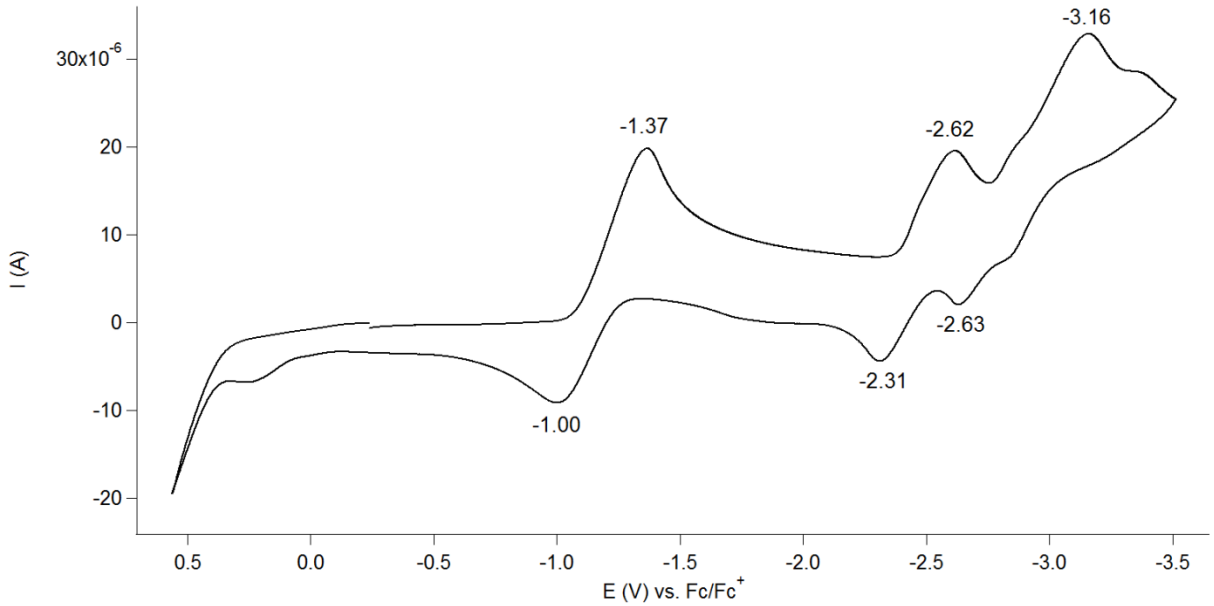

Figure 60. CV of **19** in THF across full working potential range (0.1 M $[NBu_4](PF_6)$, 25 °C, platinum working electrode, 100 mV/s scan rate).

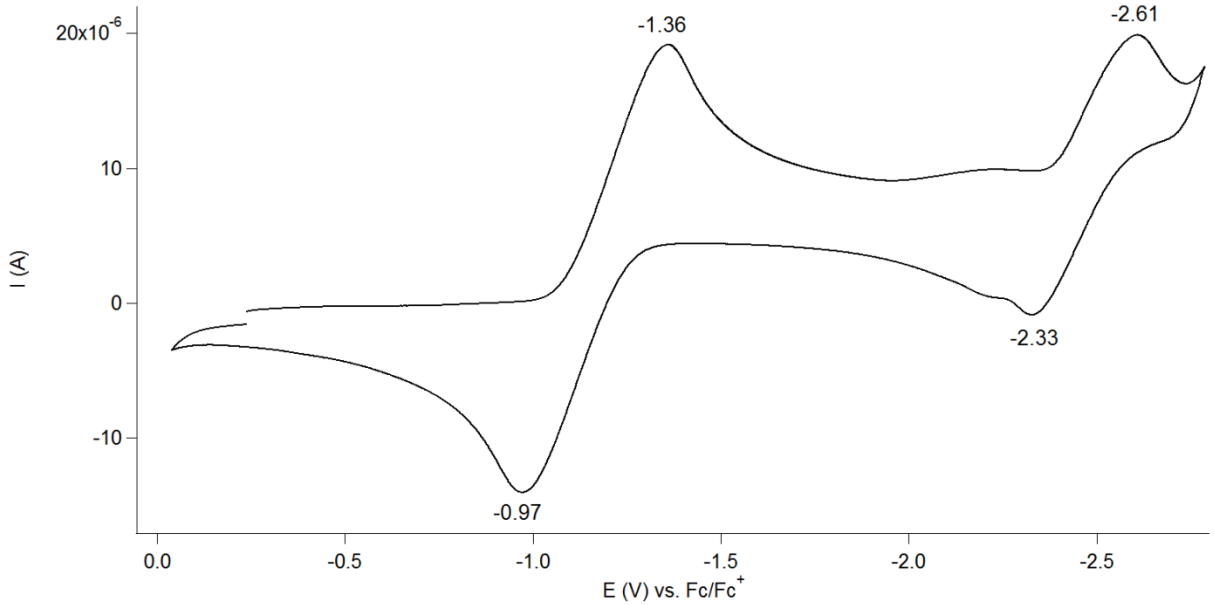

Figure 61. CV of **19** in THF, cycled after the second redox event (0.1 M $[NBu_4](PF_6)$, 25 °C, platinum working electrode, 100 mV/s scan rate).

High-valent cobalt carbene species are often postulated intermediates in the catalytic cyclopropanation of olefins.[84] These intermediates are generally elusive to isolatation are often only

studied using spectroscopic and computational methods.[85] Terminal carbene complexes of cobalt that have been structurally characterized are all formulated as low-valent cobalt(I) species containing Fischer carbenes.[26d, 82, 86] Our complex is the first structurally characterized non-NHC cobalt carbene complex with an oxidation state greater than 1+. Based on the evidence given above, it is also the first structurally characterized high-valent cobalt carbene complex as well.

6.3. EPR and Computational Investigations of $Co(OR)_2(CPh_2)$

The EPR spectra recorded for **19** (**Figure 62**, additional EPR data in Appendix F), support an S = 1/2 ground spin state (EPR studies performed in collaboration with Dr. Sebastian Stoian, National High Magnetic Field Laboratory). Resonance fields in the 50 - 400 GHz spectra exhibit a linear dependence on the microwave frequency, demonstrating that the spin ground state of **19** is an isolated Kramers doublet (S = 1/2 spin state). Simulations of the individual spectra, as well as the linear fit of the field vs. frequency dependence of the resonant field values, yield a rhombic g tensor such that g_x = 3.04(1), g_y = 2.17(1) and g_z = 1.91(1). The X-band spectra exhibit well-defined, eight-line hyperfine splitting patterns for which the individual features become progressively broader as their effective g-value increases. These eight-line patterns establish that the observed hyperfine structure is dominated by coupling to the I = 7/2 spin of the ^{59}Co ion. Analysis of the spin functions in our coupled system shows that the $|S=1/2, M_S=\pm1/2>$ states should exhibit effective g values according to $g_{eff} = (4g_{Co} - g_{radical})/3$. Reasonable cobalt g components $g_{x,Co}$, $g_{y,Co}$, and $g_{z,Co}$ of 2.78, 2.12, and 1.93, respectively, can thus be extracted from the experimental values (see Appendix F for more details). Interestingly, the spectra observed for **19** are dramatically different from those associated with the Co(TPP)-supported (TPP = tetraphenylporphyrin) bridging and terminal carbene species described by Dzik and co-workers.[85a] In particular the terminal carbene, the only Co(TPP)-based species that exhibits unpaired spin density delocalized over the carbene moiety, is characterized by $g \sim 2$ and small ^{59}Co hyperfine coupling constants. This behavior demonstrates the presence of a S = 0 cobalt(III) ion and that the unpaired spin density is found nearly exclusively on the carbene. In contrast, the parameters observed for **19** prove that this species contains a paramagnetic Co ion. To better understand the electronic structure of **19**, we turned to DFT calculations.

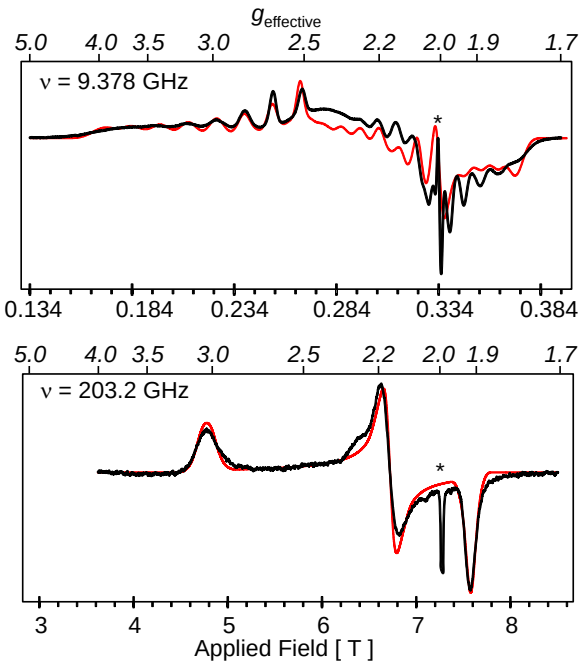

Figure 62. Continuous-wave, variable-frequency EPR spectra recorded at 9.38 GHz, 20 K (top) and 203.20 GHz, 10 K (bottom) for frozen toluene solutions of **19**. Solid red lines are simulations obtained using a $S = 1/2$ spin-Hamiltonian that includes hyperfine coupling to a $I = 7/2$, ^{59}Co nucleus. The feature marked by (*) appears at g = 2.0023 and originates from a minor, radical-based impurity. Shown in red are simulations obtained using a $S = 1/2$ spin-Hamiltonian, $g_x = 3.04(4)$, $g_y = 2.17(5)$, $g_z = 1.91(3)$, $\sigma(g_x) = 0.03(2)$, $\sigma(g_y) = 0.01(1)$, $\sigma(g_z) = 0.01(1)$, $A_x = 585$ MHz, $A_y = 280$ MHz, $A_z = 230$ MHz, $\sigma(A_x) = 25$ MHz, $\sigma(A_y) = 10$ MHz, $\sigma(A_z) = 5$ MHz.

Calculations were performed at the B3LYP/6-31G(d) level of theory (collaboration with Professor Richard Lord and his group at Grand Valley State University). Despite the tendency of B3LYP to favor high-spin configurations,[74a] the doublet species was calculated to be lower in energy than the quartet and sextet states (See Appendix F), consistent with the EPR and magnetic data. This doublet, with a Co–C bond length of 1.818 Å, was obtained from two distinct starting geometric and electronic structures: (i) a Co–C distance of 1.6 Å and $S = 1/2$ localized at Co to test for Co^{IV}=C and (ii) a Co–C distance of 2.0 Å and a $S = 1$ Co^{III} center antiferromagnetically coupled to a carbene radical.[87] The quartet state, which features Co^{III} ferromagnetically coupled to a carbene radical, shows significant elongation of Co–C to 1.930 Å.

The spin density for **19** is shown in **Figure 63**, with α spin at cobalt and β spin on the carbene. Significant spin on cobalt is consistent with the g tensor deviating from 2, and contrasts to the cobalt-

porphyrin system, whose spin density was entirely localized on the carbene.[85] Mulliken spin densities of 1.77 on Co and –0.68 on the carbene carbon suggest two α electrons on Co and one β electron on the carbene. A corresponding orbital analysis[88] (**Figure 64**) partially supports this assignment, but the overlap of 0.64 between the cobalt d orbital and the carbene p orbital indicates significant π-bonding. Calculation of the quartet at the doublet geometry produces an electronic structure that is qualitatively different than the doublet (Mulliken spins of 2.51 and 0.09 on Co and C) and is best described as a genuine high-spin cobalt(IV) complex. Thus, while we were unable to calculate the energy of the ferromagnetically coupled Co^{III}–$C^{\bullet}$ state, the $^{HS}Co^{IV}$ state obtained places a lower bound on J of 4135 cm^{-1}. This large coupling constant, combined with elongation of Co–C by 0.11 Å from the doublet to quartet state, suggests that **19** is an intermediate-spin Co^{III} (S = 1) *strongly* coupled to a CR_2^{-} radical. Moreover, re-evaluation of this wavefunction with OPBE[69] (which has been shown to excel at spin state energetic, which influences the metal oxidation state, see Appendix F) predicts less spin density on the carbon (suggesting more Co^{IV}=C character), with values approaching those predicted for an analogous, hypothetical Rh complex that should be Rh^{IV}=C. Thus, DFT predicts that **19** falls on the spectrum between cobalt(III) and cobalt(IV), but with significant Co^{IV}–alkylidene character. A HYSCORE experiment (see Appendix F) confirms the presence of unpaired spin density on the diphenylcarbene moiety.

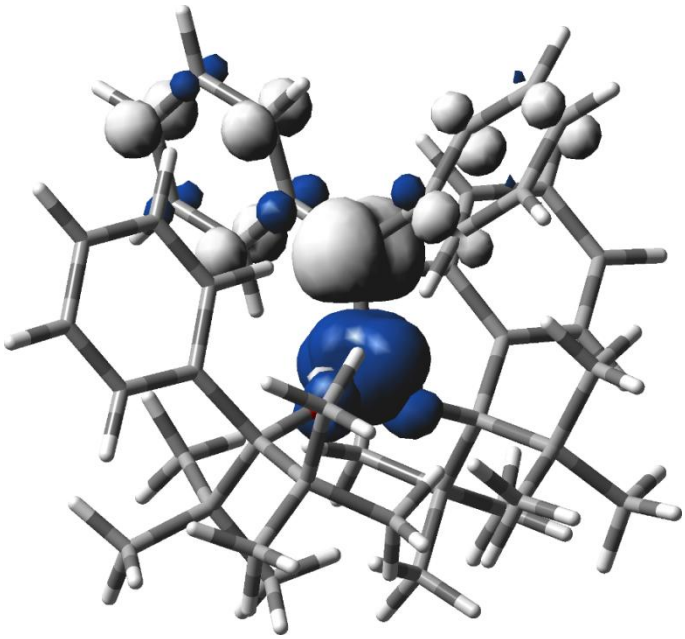

Figure 63. Spin density isosurface plot (iso = 0.005 a.u.) for **19**, with α spin represented by blue and β spin represented by white.

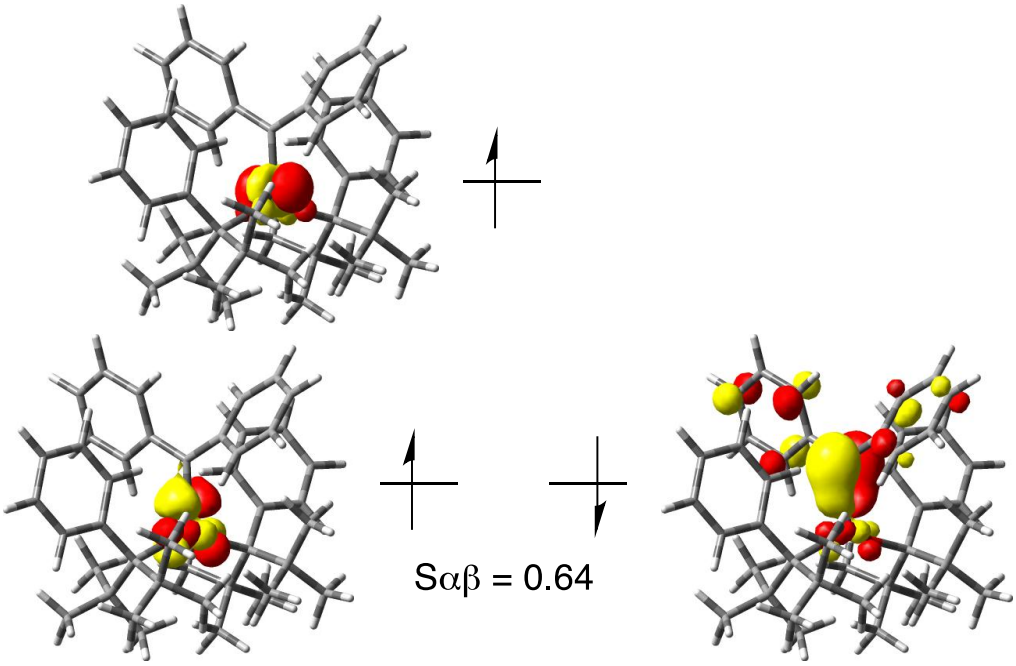

Figure 64. Corresponding orbital diagram (iso = 0.05 a.u.) for **19**.

6.4. Cyclopropanation Reactivity Studies of $Co(OR)_2(CPh_2)$

There is little doubt that **19** is an unusual molecule: a late transition metal like cobalt possessing a

carbene with significant alkylidene character is unprecedented. A high-valent cobalt carbene like this could be highly reactive. Indeed, the porphyrin-ligated low-spin cobalt(III)-carbene radical is a proposed intermediate in olefin cyclopropanation.[85] Consequently, we tested **19** for carbene-transfer reactivity. Two olefins were chosen for this investigation: styrene and methyl acrylate. The previously reported cobalt porphyrin complexes proved to be excellent catalysts for the efficient and selective cyclopropanation with both of these substrates, albeit with different carbenes (primarily derived from diazoesters).[84f, 84i] We also note that while transfer of the [CPh_2] carbene moiety to olefins has been reported, it is not common with cobalt.[26d, 89] Reaction of a stoichiometric amount of **19** with styrene at either 60 or 90 °C led to about 15% conversion to 1,1,2-triphenylcyclopropane after one hour;[89e] no further conversion occurred with additional heating. Similarly, under catalytic conditions (10 mol % of **19** at 60 °C) the formation of about one equivalent of the cyclopropane was observed after one hour, as demonstrated by ^{1}H NMR (see Appendix F). Conversely, no cyclopropane formation was observed for a stoichiometric reaction of **19** with methyl acrylate at 60 °C. Ultimately, our preliminary studies seem to reinforce the high stability of the complex, as evidenced by its isolation. The diminished reactivity of **19** may be partly due to the unprecedented electronics at the metal center. More likely though, the use of a bulky carbene, coupled with the bulky alkoxide ligands, may simply be sterically hindering the carbene itself, limiting further reactivity. Perhaps this may be why we were able to isolate this stable complex in the first place.

6.5. Summary and Conclusions

Similarly to the previously detailed metal-imido reactivity, metal-carbene reactivity with our bis(alkoxide) system also seems to offer up rich, exciting new chemistries. While an iron-carbene complex could not be isolated, we were able to synthesize and structurally characterize the first example of a high-valent cobalt carbene complex. An exceptionally short Co=C bond, along with shorter Co−OR bonds compared to the starting bis(alkoxide) confirm **19**'s high-valent nature. EPR and DFT studies conclude that while the oxidation state of the metal lies on a continuum between cobalt(III) and cobalt(IV), there is significant alkylidene character present. Initial reactivity studies with **19** show that it is a stable, largely unreactive molecule, likely due to the steric constraints of the carbene and the alkoxide

ligands. It is possible that the larger size of iron as opposed to cobalt prevented the isolation of a stable iron-carbene complex using diphenyldiazomethane. However, utilizing an even more bulky carbene may allow for isolation of such a species by providing additional steric protection. In a similar argument, reacting smaller carbenes with the cobalt bis(alkoxide) **12** may lead to greater reactivity, and perhaps even catalytic reactivity, due to increased accessibility to the metal.

6.6. Experimental Details

General Methods and Procedures. All reactions involving air-sensitive materials were executed in a nitrogen-filled glovebox. Diphenyldiazomethane was synthesized according to a reported literature procedure.[77] All solvents were purchased from Fisher Scientific and were of HPLC grade. The solvents were purified using an MBRAUN solvent purification system and stored over 3-Å molecular sieves. The complexes were characterized using NMR, IR, UV/Vis and EPR spectroscopies, X-ray crystallography, elemental analysis, and the Evans method. NMR spectra were recorded at the Lumigen Instrument Center (Wayne State University) on a Varian Mercury 400 MHz NMR Spectrometer in C_6D_6 at room temperature. IR spectra of powdered samples were recorded on a Shimadzu IR Affinity-1 FT-IR Spectrometer outfitted with a MIRacle10 attenuated total reflectance accessory with a monolithic diamond crystal stage and pressure clamp. UV-visible spectra were obtained on a Shimadzu UV-1800 spectrometer. Elemental analyses were performed by Midwest Microlab LLC. Electrochemical properties were determined using cyclic voltammetry on a BAS Epsilon system in a nitrogen-filled glovebox. Samples were prepared in anhydrous THF with 0.1 M tetrabutylammonium hexafluorophosphate $[NBu_4](PF_6)$ as the supporting electrolyte. Redox potentials were determined with a scan rate of 100 mV/s at 25 °C by using a platinum disc working electrode (2 mm diameter), a platinum wire counter electrode, and a nonaqueous Ag^+/Ag reference electrode, and referenced to $FeCp_2/FeCp_2^+$ couple. Large peak separations on the order of 300 mV or greater were observed for each redox event, suggesting quasi-reversible processes. Cyclic voltammetry measurements were also taken at various scan rates from 25-100 mV/s. Small decreases in the peak separations were observed at lower scan rates, further supporting quasi-reversible processes. Additional spectra, as well as EPR and DFT details, can be found in Appendix

F.

X-ray Crystallographic Details. The structure of **19** was confirmed by X-ray analysis. The crystals were mounted on a Bruker APEXII/Kappa three circle goniometer platform diffractometer equipped with an APEX-2 detector. A graphic monochromator was employed for wavelength selection of the Mo Kα radiation (λ = 0.71073 Å). The data were processed and the structure was solved using the APEX-2 software supplied by Bruker-AXS. The structure was refined by standard difference Fourier techniques with SHELXL (6.10 v., Sheldrick G. M., and Siemens Industrial Automation, 2000). Hydrogen atoms were placed in calculated positions using a standard riding model and refined isotropically; all other atoms were refined anisotropically.

Reaction of 11 with Ph_2CN_2. To a stirring hexane solution of **11** (27.1 mg, 0.042 mmol) was added dropwise a hexane solution of diphenyldiazomethane (8.2 mg, 0.042 mmol), leading to an instantaneous color change to red. The reaction was stirred for an hour, upon which the volatiles were removed in vacuo to give a red residue. This residue was dissolved in pentane, filtered, and concentrated. Crystallization at -35°C afforded colorless crystals confirmed by NMR to be benzophenone azine, $Ph_2CNNCPh_2$ (4.6 mg, 60%).

$Co(OR)_2(CPh_2)$ (19). To a stirring hexane solution of $Co(OR)_2(THF)_2$ (30.1 mg, 0.05 mmol) was added dropwise a hexane solution of diphenyldiazomethane (9.1 mg, 0.05 mmol). Gradually the solution color changed from violet to red. The reaction was stirred for an hour, upon which the volatiles were removed in vacuo. The resulting red-brown residue was redissolved in pentane, filtered, and concentrated. Crystallization at -35 ^oC afforded the product as red-brown crystals (26.6 mg, 85%). IR (cm^{-1}): 3051 (w), 3001 (w), 2963 (w), 2878 (w), 2832 (w), 1474 (w), 1439 (m), 1400 (w), 1385 (w), 1188 (w), 1153 (w), 1084 (w), 1042 (s), 991 (s), 899 (m), 756 (s), 702 (s), 687 (s), 648 (m). $\mu_{eff} = 2.0 \pm 0.1\ \mu_B$ (calc. 1.7). λ_{max} (ε_M) 483 (2041). The compound was also characterized by X-ray crystallography. Anal. Calcd. for $C_{43}H_{56}O_2Co$: C, 77.8; H, 8.5. Found: C, 77.9; H, 8.6.

Stoichiometric reaction of 19 with styrene. Complex **19** (15.5 mg, 0.023 mmol) and styrene (2.4 mg, 0.023 mmol) were combined in deuterated toluene in an NMR tube under an atmosphere of

dinitrogen. The tube was sealed with parafilm and heated in an oil bath at either 60 or 90 ^{o}C for four hours. Gradually the solution color changed to green-brown. NMR indicated about 15% conversion of the styrene to the respective cyclopropane, whose peaks were similar to those reported in the literature.[8] After one hour, no further increase in cyclopropane formation was observed.

Stoichiometric reaction of 19 with methyl acrylate. Complex **19** (17.9 mg, 0.027 mmol) and methyl acrylate (2.3 mg, 0.027 mmol) were combined in deuterated toluene in an NMR tube under an atmosphere of dinitrogen. The tube was sealed with parafilm and heated in an oil bath at 90 ^{o}C for four hours. Gradually the solution color changed to blue-violet. NMR indicated no formation of cyclopropane, accompanied by some decomposition of the carbene complex.

Catalytic reaction of 19 with styrene. Diphenyldiazomethane (31.2 mg, 0.16 mmol) and styrene (16.7 mg, 0.16 mmol) were combined in an NMR tube, along with 10 mol % of **19** and 1,3,5-trimethoxybenzene as an internal standard. Gas evolution was immediately observed. The NMR tube was sealed with parafilm and heated in an oil bath at 90 ^{o}C for four hours. About one equivalent of the respective cyclopropane was formed, but no additional cyclopropane formation was observed after one hour of continued heating.

CHAPTER 7: CONCLUSIONS AND FUTURE DIRECTIONS

As worldwide supplies of the less accessible second- and third-row transition metals continue to deplete, the use of base metals in catalysis is becoming more and more relevant as scientists look toward a sustainable future. Base metal catalysis continues to be under intense investigation, with the majority of base metal catalysts utilizing soft, σ-donor-type ligand platforms, often in low-coordination environments. Later first-row transition metals in these low-coordination environments have been shown to support reactive metal-ligand multiple bonds toward various group-transfer reactions in catalysis. One alternative that has yet to be fully explored is the use of hard, π-donating alkoxide ligands to yield more reactive metal-ligand multiple bonds. In this thesis we have investigated this hypothesis by designing a new bulky alkoxide ligand for the stabilization of later first-row transition metals. We have also explored the synthesis and reactivity of metal-nitrogen (imido) and metal-carbon (carbene) multiple bonds in our system. Ultimately, we have demonstrated the feasibility of base metal complexes stabilized by alkoxide ligands for use in new stoichiometric and catalytic reactions.

Along the route to our proposed bis(alkoxide) system, we were able to synthesize several novel cluster complexes of the middle to late first-row transition metals. For chromium-cobalt, these complexes were able to dimerize, displaying the rare seesaw geometry. Spectroscopic and computational investigations confirm that the steric bulk imparted by the ligand enforces this unusual geometry. For nickel, which has a smaller atomic radius compared to the earlier metals, only a three-coordinate monomer was observed. In the case of copper, reduction of the copper(II) complex by one equivalent of the ligand afforded a copper(I) tetramer in a reduction unusual in alkoxide chemistry. Through the observed formation of several byproducts, a tentative mechanism for this reduction was proposed. While not directly contributing toward the goals of this research, several novel molecules have been synthesized that seem to bend the basic rules of chemistry, making them intriguing nonetheless. Future studies could aim toward further investigation of the synthesis of chromium and nickel bis(alkoxide) complexes, which were not explored in this research. These species may yield intriguing and unprecedented reactivity that could be applied toward small molecule catalysis. Specifically, chromium-ligand multiple bonds in an

alkoxide ligand environment could also prove to be reactive. Low-coordinate nickel alkoxide complexes may yield intriguing reactivity as well.

Use of thallium(I) hexafluorophosphate as a chloride abstractor afforded our desired bis(alkoxide) system for manganese, iron, and cobalt. Cyclic voltammetry suggested that the iron bis(alkoxide) complex would prove to be the most easily oxidized, so our studies with azides focused on this complex. No reactivity was observed between azides and the manganese or cobalt bis(alkoxides). Reaction of the iron bis(alkoxide) with adamantyl azide led to one-electron reduction of the azide followed by coupling to give a rare hexazene complex, as opposed to the expected two-electron reduction of the azide to give nitrene. As dictated by DFT studies, this complex likely forms via a dimeric intermediate in which the iron centers are oxidized to iron(III), and the azides are both reduced. N−N bond formation can then occur. While not entirely novel, hexazene formation is indeed rare, and our hexazene complex is the first example of one not synthesized by a highly reducing metalloradical such as iron(I) or magnesium(I). While our bis(alkoxide) system can be synthesized in two steps from LiOR, future studies could focus on eliminating the chloride abstraction step, thus circumventing the need to use poisonous thallium(I) hexafluorophosphate. Alternative routes include the synthesis of either NaOR or KOR and then reacting with metal halides, or using crown ethers to trap the lithium ions instead of the chloride ions. In terms of hexazene chemistry, future studies involve the synthesis of additional hexazene complexes using other alkyl azides, as well as exploring the possibility for either stoichiometric or catalytic removal of hexazene from the complex. Reducing agents and/or hexazene transfer agents could lead to isolation of either inorganic hexazene salts or organic hexaazadienes, both of which could be investigated for their potential as energetic materials. Additionally, reactivity with diazides could be investigated, leading to the formation of hexazene polymers, novel materials that may also display energetic properties.

Looking to expand our investigation of the reactivity of azides with the iron bis(alkoxide) we next explored aryl azides. Interestingly, differing reactivity results, whereby two-electron reduction of the azide occurs, followed by nitrene coupling to give azoarenes. This process is catalytic and highly selective, only working for aryl azides with bulky groups on the *ortho* positions of the aryl ring. Smaller

aryl azides allow for the isolation of stable bis(imido) complexes that appear to be an endpoint of the reaction. Observation of the iron tris(alkoxide), along with spectroscopic and kinetics experiments, suggest that a comproportionation process may be occurring between a reactive iron-imido intermediate and another equivalent of the iron bis(alkoxide). DFT studies calculate this intermediate to be an iron(III) center antiferromagnetically coupled to an imido radical. The unforeseen lability of the alkoxide ligand in our system undoubtedly plays a role in the unusual reactivity observed here. While the nitrene coupling reactivity of our system is limited, future studies could investigate the application of our selective nitrene coupling catalyst toward the synthesis of azo polymers via diazides. Azo polymers are materials of interest as diffraction gratings and as molecular switches, but they are challenging to synthesize. Our catalyst could provide ease of access to these materials, allowing for exploration of their properties. Additional studies involve attempting to react the bis(imido) complexes in the presence of other substrates while heating in a further attempt to afford nitrene transfer or nitrene coupling.

We also observe novel reactivity with diazoalkanes, toward the formation of metal-carbene complexes. Specifically for cobalt, we were able to isolate the first example of a high-valent cobalt carbene complex, which is also the first example of a cobalt-carbene in a weak-field ligand environment. High-valent cobalt carbenes are proposed intermediates in olefin cyclopropanation, and our stable, structurally characterized system may help to shed light on the specific nature of that mechanism. EPR and DFT studies conclude that the oxidation state of the cobalt in this complex lies on a continuum between cobalt(III) and cobalt(IV) but that it possesses significant alkylidene character. A lack of observed reactivity of this carbene may be due to unforeseen electronic stabiliziation or enhanced steric protection offered by both the ligand and the bulky carbene. Olefin reactivity with carbene complexes can be very selective. Because we did not test the reaction of an electron-donating olefin with our complex, future studies could begin by exploring this reaction. Future studies could also be aimed at studying the reactivity of the cobalt bis(alkoxide) complex with smaller diazoalkanes. These reactions may produce more reactive cobalt carbene complexes that can undergo exciting new types of reactivity, including cyclopropanation, C−H activation, and even olefin metathesis. Finally, because we were unable to isolate

an iron carbene complex, we could also investigate using excessively bulky diazoalkanes to attempt to isolate an iron(IV) carbene complex. While this complex would likely be unreactive toward carbene transfer, it could still be an interesting molecule with electronic properties worth investigating.

Further modifications could also be made to our ligand system. Even more sterically hindered alkoxide ligands may lead to differing or even new types of reactivity beyond that which we have already investigated. Future studies could focus on the synthesis of excessively bulky alkoxide ligands via the addition of bulky groups to the phenyl ring on our alkoxide ligand. To counteract the alkoxide dissociation issues we observed in the reactivity of the iron bis(alkoxide) complex with aryl azides, a chelating bis(alkoxide) ligand could be employed. The synthesis of a chelating bis(alkoxide) system could allow for greater catalytic control in the activation of azides, diazoalkanes, and other small molecules. These systems would be more rigid, and their steric properties could further be tuned, allowing for a wide variety of ligand types to be synthesized. In terms of new reactivity, other types of metal-ligand multiple bonds could be investigated, including oxo, sulfido, and even silylene ligands. The activation of other small molecules, including olefins, carbonyls, and carbon dioxide, by our bis(alkoxide) system could also be explored. In addition, other metals may be suitable for investigation in our system, including earlier first-row transition metals such as vanadium and titanium, as well as divalent lanthanides. These complexes are expected to be highly reducing, and their reductive properties could be investigated.

In conclusion, we have demonstrated that bulky alkoxides show promise as ligand scaffolds for the support of reactive metal-ligand multiple bonds. Our exploration of their reactivity with both azides and diazoalkanes shows that metal-nitrene and metal-carbene formation, along with their subsequent transfer, is indeed possible. In the future, using alternative ligand structures that eliminate the lability issue observed with [OR] in our system would be a step forward toward the design of novel first-row transition metal alkoxide catalysts. Ultimately the discoveries we have made in this research have revived bulky alkoxide chemistry and present access toward new types of complexes that are certainly worth pursuing. Further modifications to our system will likely lead to the discovery of more surprising

reactivity that will continue to push the known boundaries of transition metal chemistry and may lead to viable new base metal catalysts for a variety of transformations.

APPENDIX A: PERSONAL/LICENSE AGREEMENTS FOR COPYRIGHTED MATERIAL

Portions of **Chapter 2** have been reproduced from **Bellow, J. A.**; Fang, D.; Kovacevic, N.; Martin, P. D.; Shearer, J.; Cisneros, G. A.; Groysman, S. "Novel Cluster Topologies Featuring Rare Seesaw Geometry at Transition Metal Centers" *Chem. Eur. J.* **2013**, *19*, 12225-12228. Below is the license agreement.

JOHN WILEY AND SONS LICENSE
TERMS AND CONDITIONS

Apr 27, 2016

This Agreement between James Bellow ("You") and John Wiley and Sons ("John Wiley and Sons") consists of your license details and the terms and conditions provided by John Wiley and Sons and Copyright Clearance Center.

License Number	3856620131714
License date	Apr 26, 2016
Licensed Content Publisher	John Wiley and Sons
Licensed Content Publication	Chemistry - A European Journal
Licensed Content Title	Novel Alkoxide Cluster Topologies Featuring Rare Seesaw Geometry at Transition Metal Centers
Licensed Content Author	James A. Bellow,Dong Fang,Natalija Kovacevic,Philip D. Martin,Jason Shearer,G. Andrés Cisneros,Stanislav Groysman
Licensed Content Date	Aug 9, 2013
Pages	4
Type of use	Dissertation/Thesis
Requestor type	Author of this Wiley article
Format	Electronic
Portion	Full article
Will you be translating?	No
Title of your thesis / dissertation	Design of First-Row Transition Metal Bis(alkoxide) Complexes and Their Reactivity Toward Nitrene and Carbene Transfer
Expected completion date	Jun 2016
Expected size (number of pages)	235
Requestor Location	James Bellow 5101 Cass Ave.

	DETROIT, MI 48202 United States Attn: James Bellow
Billing Type	Invoice
Billing Address	James Bellow 5101 Cass Ave. DETROIT, MI 48202 United States Attn: James Bellow
Total	0.00 USD

Terms and Conditions

TERMS AND CONDITIONS

This copyrighted material is owned by or exclusively licensed to John Wiley & Sons, Inc. or one of its group companies (each a"Wiley Company") or handled on behalf of a society with which a Wiley Company has exclusive publishing rights in relation to a particular work (collectively "WILEY"). By clicking "accept" in connection with completing this licensing transaction, you agree that the following terms and conditions apply to this transaction (along with the billing and payment terms and conditions established by the Copyright Clearance Center Inc., ("CCC's Billing and Payment terms and conditions"), at the time that you opened your RightsLink account (these are available at any time athttp://myaccount.copyright.com).

Terms and Conditions

- The materials you have requested permission to reproduce or reuse (the "Wiley Materials") are protected by copyright.

- You are hereby granted a personal, non-exclusive, non-sub licensable (on a stand-alone basis), non-transferable, worldwide, limited license to reproduce the Wiley Materials for the purpose specified in the licensing process. This license, **and any CONTENT (PDF or image file) purchased as part of your order,** is for a one-time use only and limited to any maximum distribution number specified in the license. The first instance of republication or reuse granted by this license must be completed within two years of the date of the grant of this license (although copies prepared before the end date may be distributed thereafter). The Wiley Materials shall not be used in any other manner or for any other purpose, beyond what is granted in the license. Permission is granted subject to an appropriate acknowledgement given to the author, title of the material/book/journal and the publisher. You shall also duplicate the copyright notice that appears in the Wiley publication in your use of the Wiley Material. Permission is also granted on the understanding that nowhere in the text is a previously published source acknowledged for all or part of this Wiley Material. Any third party content is expressly excluded from this permission.

- With respect to the Wiley Materials, all rights are reserved. Except as expressly granted by the terms of the license, no part of the Wiley Materials may be copied, modified, adapted (except for

minor reformatting required by the new Publication), translated, reproduced, transferred or distributed, in any form or by any means, and no derivative works may be made based on the Wiley Materials without the prior permission of the respective copyright owner.**For STM Signatory Publishers clearing permission under the terms of the STM Permissions Guidelines only, the terms of the license are extended to include subsequent editions and for editions in other languages, provided such editions are for the work as a whole in situ and does not involve the separate exploitation of the permitted figures or extracts,**You may not alter, remove or suppress in any manner any copyright, trademark or other notices displayed by the Wiley Materials. You may not license, rent, sell, loan, lease, pledge, offer as security, transfer or assign the Wiley Materials on a stand-alone basis, or any of the rights granted to you hereunder to any other person.

- The Wiley Materials and all of the intellectual property rights therein shall at all times remain the exclusive property of John Wiley & Sons Inc, the Wiley Companies, or their respective licensors, and your interest therein is only that of having possession of and the right to reproduce the Wiley Materials pursuant to Section 2 herein during the continuance of this Agreement. You agree that you own no right, title or interest in or to the Wiley Materials or any of the intellectual property rights therein. You shall have no rights hereunder other than the license as provided for above in Section 2. No right, license or interest to any trademark, trade name, service mark or other branding ("Marks") of WILEY or its licensors is granted hereunder, and you agree that you shall not assert any such right, license or interest with respect thereto

- NEITHER WILEY NOR ITS LICENSORS MAKES ANY WARRANTY OR REPRESENTATION OF ANY KIND TO YOU OR ANY THIRD PARTY, EXPRESS, IMPLIED OR STATUTORY, WITH RESPECT TO THE MATERIALS OR THE ACCURACY OF ANY INFORMATION CONTAINED IN THE MATERIALS, INCLUDING, WITHOUT LIMITATION, ANY IMPLIED WARRANTY OF MERCHANTABILITY, ACCURACY, SATISFACTORY QUALITY, FITNESS FOR A PARTICULAR PURPOSE, USABILITY, INTEGRATION OR NON-INFRINGEMENT AND ALL SUCH WARRANTIES ARE HEREBY EXCLUDED BY WILEY AND ITS LICENSORS AND WAIVED BY YOU.

- WILEY shall have the right to terminate this Agreement immediately upon breach of this Agreement by you.

- You shall indemnify, defend and hold harmless WILEY, its Licensors and their respective directors, officers, agents and employees, from and against any actual or threatened claims, demands, causes of action or proceedings arising from any breach of this Agreement by you.

- IN NO EVENT SHALL WILEY OR ITS LICENSORS BE LIABLE TO YOU OR ANY OTHER PARTY OR ANY OTHER PERSON OR ENTITY FOR ANY SPECIAL, CONSEQUENTIAL, INCIDENTAL, INDIRECT, EXEMPLARY OR PUNITIVE DAMAGES, HOWEVER CAUSED, ARISING OUT OF OR IN CONNECTION WITH THE DOWNLOADING, PROVISIONING, VIEWING OR USE OF THE MATERIALS REGARDLESS OF THE FORM OF ACTION, WHETHER FOR BREACH OF CONTRACT, BREACH OF WARRANTY, TORT, NEGLIGENCE, INFRINGEMENT OR OTHERWISE (INCLUDING, WITHOUT LIMITATION, DAMAGES BASED ON LOSS OF PROFITS, DATA, FILES, USE, BUSINESS OPPORTUNITY OR CLAIMS OF THIRD PARTIES), AND WHETHER OR NOT THE PARTY HAS BEEN ADVISED OF THE POSSIBILITY OF SUCH DAMAGES. THIS LIMITATION SHALL APPLY NOTWITHSTANDING ANY FAILURE OF ESSENTIAL PURPOSE OF ANY LIMITED REMEDY PROVIDED HEREIN.

- Should any provision of this Agreement be held by a court of competent jurisdiction to be illegal, invalid, or unenforceable, that provision shall be deemed amended to achieve as nearly as possible the same economic effect as the original provision, and the legality, validity and enforceability of the remaining provisions of this Agreement shall not be affected or impaired thereby.

- The failure of either party to enforce any term or condition of this Agreement shall not constitute a waiver of either party's right to enforce each and every term and condition of this Agreement. No breach under this agreement shall be deemed waived or excused by either party unless such waiver or consent is in writing signed by the party granting such waiver or consent. The waiver by or consent of a party to a breach of any provision of this Agreement shall not operate or be construed as a waiver of or consent to any other or subsequent breach by such other party.

- This Agreement may not be assigned (including by operation of law or otherwise) by you without WILEY's prior written consent.

- Any fee required for this permission shall be non-refundable after thirty (30) days from receipt by the CCC.

- These terms and conditions together with CCC's Billing and Payment terms and conditions (which are incorporated herein) form the entire agreement between you and WILEY concerning this licensing transaction and (in the absence of fraud) supersedes all prior agreements and representations of the parties, oral or written. This Agreement may not be amended except in writing signed by both parties. This Agreement shall be binding upon and inure to the benefit of the parties' successors, legal representatives, and authorized assigns.

- In the event of any conflict between your obligations established by these terms and conditions and those established by CCC's Billing and Payment terms and conditions, these terms and conditions shall prevail.

- WILEY expressly reserves all rights not specifically granted in the combination of (i) the license details provided by you and accepted in the course of this licensing transaction, (ii) these terms and conditions and (iii) CCC's Billing and Payment terms and conditions.

- This Agreement will be void if the Type of Use, Format, Circulation, or Requestor Type was misrepresented during the licensing process.

- This Agreement shall be governed by and construed in accordance with the laws of the State of New York, USA, without regards to such state's conflict of law rules. Any legal action, suit or proceeding arising out of or relating to these Terms and Conditions or the breach thereof shall be instituted in a court of competent jurisdiction in New York County in the State of New York in the United States of America and each party hereby consents and submits to the personal jurisdiction of such court, waives any objection to venue in such court and consents to service of process by registered or certified mail, return receipt requested, at the last known address of such party.

WILEY OPEN ACCESS TERMS AND CONDITIONS

Wiley Publishes Open Access Articles in fully Open Access Journals and in Subscription journals offering Online Open. Although most of the fully Open Access journals publish open access articles under the terms of the Creative Commons Attribution (CC BY) License only, the subscription journals and a few of the Open Access Journals offer a choice of Creative Commons Licenses. The license type is

clearly identified on the article.

The Creative Commons Attribution License

The Creative Commons Attribution License (CC-BY) allows users to copy, distribute and transmit an article, adapt the article and make commercial use of the article. The CC-BY license permits commercial and non-

Creative Commons Attribution Non-Commercial License

The Creative Commons Attribution Non-Commercial (CC-BY-NC)License permits use, distribution and reproduction in any medium, provided the original work is properly cited and is not used for commercial purposes.(see below)

Creative Commons Attribution-Non-Commercial-NoDerivs License

The Creative Commons Attribution Non-Commercial-NoDerivs License (CC-BY-NC-ND) permits use, distribution and reproduction in any medium, provided the original work is properly cited, is not used for commercial purposes and no modifications or adaptations are made. (see below)

Use by commercial "for-profit" organizations

Use of Wiley Open Access articles for commercial, promotional, or marketing purposes requires further explicit permission from Wiley and will be subject to a fee.

Further details can be found on Wiley Online Libraryhttp://olabout.wiley.com/WileyCDA/Section/id-410895.html

Other Terms and Conditions:

v1.10 Last updated September 2015

Portions of **Chapters 3** and **4** were reproduced from the following reference: **Bellow, J. A.**; Martin, P. D.; Lord, R. L.; Groysman, S. "Reductive Coupling of Azides Mediated by an Iron(II) Bis(alkoxide) Complex" *Inorg. Chem.* **2013**, *52*, 12335-12337. with permission of the American Chemical Society.

Title: Reductive Coupling of Azides Mediated by an Iron(II) Bis(alkoxide) Complex

Author: James A. Bellow, Philip D. Martin, Richard L. Lord, et al

Publication: Inorganic Chemistry

Publisher: American Chemical Society

Date: Nov 1, 2013

Copyright © 2013, American Chemical Society

PERMISSION/LICENSE IS GRANTED FOR YOUR ORDER AT NO CHARGE

This type of permission/license, instead of the standard Terms & Conditions, is sent to you because no fee is being charged for your order. Please note the following:

- Permission is granted for your request in both print and electronic formats, and translations.
- If figures and/or tables were requested, they may be adapted or used in part.
- Please print this page for your records and send a copy of it to your publisher/graduate school.
- Appropriate credit for the requested material should be given as follows: "Reprinted (adapted) with permission from (COMPLETE REFERENCE CITATION). Copyright (YEAR) American Chemical Society." Insert appropriate information in place of the capitalized words.
- One-time permission is granted only for the use specified in your request. No additional uses are granted (such as derivative works or other editions). For any other uses, please submit a new request.

Portions of **Chapter 5** were reproduced from the following reference: **Bellow, J. A.**; Yousif, M.; Cabelof, A. C.; Lord, R. L.; Groysman, S. "Reactivity Modes of an Iron Bis(alkoxide) Complex with Aryl Azides: Catalytic Nitrene Coupling vs. Formation of Iron(III) Imido Dimers" *Organometallics* **2015**, *34*, 2917-2923. with permission of the American Chemical Society.

Title:	Reactivity Modes of an Iron Bis(alkoxide) Complex with Aryl Azides: Catalytic Nitrene Coupling vs Formation of Iron(III) Imido Dimers
Author:	James A. Bellow, Maryam Yousif, Alyssa C. Cabelof, et al
Publication:	Organometallics
Publisher:	American Chemical Society
Date:	Jun 1, 2015

Copyright © 2015, American Chemical Society

PERMISSION/LICENSE IS GRANTED FOR YOUR ORDER AT NO CHARGE

This type of permission/license, instead of the standard Terms & Conditions, is sent to you because no fee is being charged for your order. Please note the following:

- Permission is granted for your request in both print and electronic formats, and translations.
- If figures and/or tables were requested, they may be adapted or used in part.
- Please print this page for your records and send a copy of it to your publisher/graduate school.
- Appropriate credit for the requested material should be given as follows: "Reprinted (adapted) with permission from (COMPLETE REFERENCE CITATION). Copyright (YEAR) American Chemical Society." Insert appropriate information in place of the capitalized words.
- One-time permission is granted only for the use specified in your request. No additional uses are granted (such as derivative works or other editions). For any other uses, please submit a new request.

Portions of **Chapters 2** and **3** were reproduced from the following reference: **Bellow, J. A.**; Yousif, M.; Fang, D.; Kratz, E. G.; Cisneros, G. A.; Groysman, S. “Synthesis and Reactivity of 3d Metal Complexes with the Bulky Alkoxide Ligand [OC^{t}Bu$_2$Ph]” *Inorg. Chem.* **2015**, *54*, 5624-5633. with permission of the American Chemical Society.

Title:	Synthesis and Reactions of 3d Metal Complexes with the Bulky Alkoxide Ligand [OCtBu2Ph]
Author:	James A. Bellow, Maryam Yousif, Dong Fang, et al
Publication:	Inorganic Chemistry
Publisher:	American Chemical Society
Date:	Jun 1, 2015

Copyright © 2015, American Chemical Society

PERMISSION/LICENSE IS GRANTED FOR YOUR ORDER AT NO CHARGE

This type of permission/license, instead of the standard Terms & Conditions, is sent to you because no fee is being charged for your order. Please note the following:

- Permission is granted for your request in both print and electronic formats, and translations.
- If figures and/or tables were requested, they may be adapted or used in part.
- Please print this page for your records and send a copy of it to your publisher/graduate school.
- Appropriate credit for the requested material should be given as follows: "Reprinted (adapted) with permission from (COMPLETE REFERENCE CITATION). Copyright (YEAR) American Chemical Society." Insert appropriate information in place of the capitalized words.
- One-time permission is granted only for the use specified in your request. No additional uses are granted (such as derivative works or other editions). For any other uses, please submit a new request.

Portions of **Chapter 1** were reproduced from the following reference: **Bellow, J. A.**; Yousif, M.; Groysman, S. "Discrete Complexes of 3d Metals with Monodentate Bulky Alkoxide Ligands and Their Reactivity in Bond Activation and Bond Formation Reactions" *Comments Inorg. Chem.* **2016**, *36*, 92-122. with permission of the Taylor and Francis Group.

Title: Discrete Complexes of 3d Metals with Monodentate Bulky Alkoxide Ligands and Their Reactivity in Bond Activation and Bond Formation Reactions

Author: James A. Bellow, Maryam Yousif, Stanislav Groysman

Publication: Comments on Inorganic Chemistry

Publisher: Taylor & Francis

Date: Mar 3, 2016

Copyright © 2016 Taylor & Francis

Thesis/Dissertation Reuse Request

Taylor & Francis is pleased to offer reuses of its content for a thesis or dissertation free of charge contingent on resubmission of permission request if work is published.

Portions of **Chapter 6** were reproduced from the following reference: **Bellow, J. A.**; Stoian, S. A.; van Toll, H.; Ozarowsky, A.; Lord, R. L.; Groysman, S. “Synthesis and Characterization of A Stable High-Valent Cobalt Carbene Complex” *J. Am. Chem. Soc.* **2016**, *138*, 5531-5534. with permission of the American Chemical Society.

Title: Synthesis and Characterization of a Stable High-Valent Cobalt Carbene Complex
Author: James A. Bellow, Sebastian A. Stoian, Johan van Tol, et al
Publication: Journal of the American Chemical Society
Publisher: American Chemical Society
Date: Apr 1, 2016
Copyright © 2016, American Chemical Society

PERMISSION/LICENSE IS GRANTED FOR YOUR ORDER AT NO CHARGE

This type of permission/license, instead of the standard Terms & Conditions, is sent to you because no fee is being charged for your order. Please note the following:

- Permission is granted for your request in both print and electronic formats, and translations.
- If figures and/or tables were requested, they may be adapted or used in part.
- Please print this page for your records and send a copy of it to your publisher/graduate school.
- Appropriate credit for the requested material should be given as follows: "Reprinted (adapted) with permission from (COMPLETE REFERENCE CITATION). Copyright (YEAR) American Chemical Society." Insert appropriate information in place of the capitalized words.
- One-time permission is granted only for the use specified in your request. No additional uses are granted (such as derivative works or other editions). For any other uses, please submit a new request.

APPENDIX B: SUPPLEMENTARY MATERIAL FOR CHAPTER 2

1. Crystal Structures Not Shown in Chapter 2

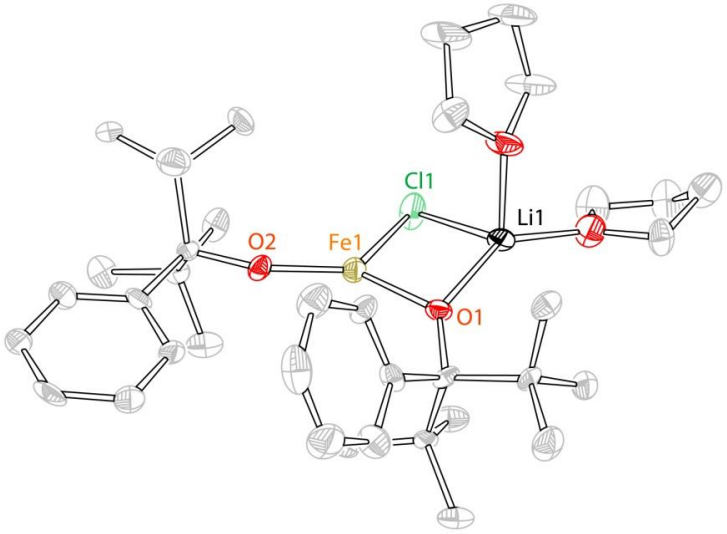

Figure B.1. Crystal structure of **2**, 50% probability ellipsoids. Hydrogen atoms omitted for clarity. Selected bond distances and angles. Bond lengths and angles not reported due to poor crystal quality.

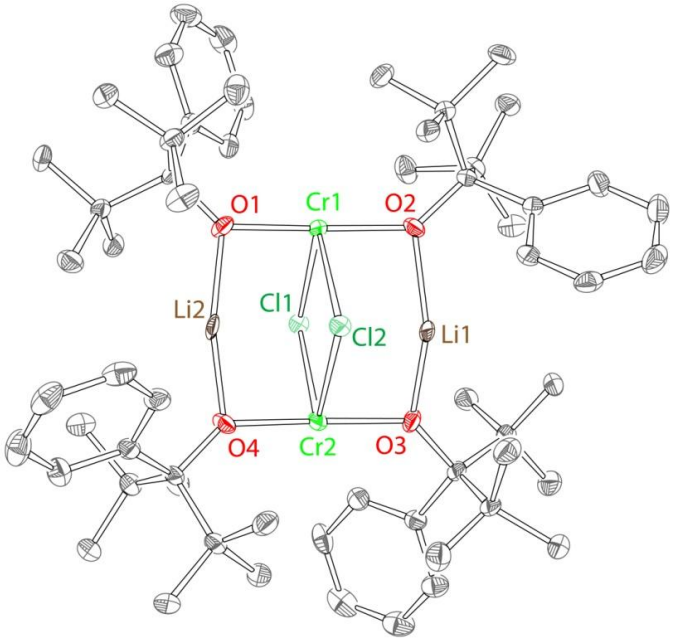

Figure B.2. Crystal structure of **4**, 50% probability ellipsoids. Selected bond distances and bond angles: Cr1-O1 1.906(2) Å, Cr1-O2 1.908(2) Å, Cr1-Cl1 2.493(2) Å, Cr1-Cl2 2.603(2) Å, O1-Cr1-O2 175.2(1)°, Cl1-Cr1-Cl2 84.43(6)°.

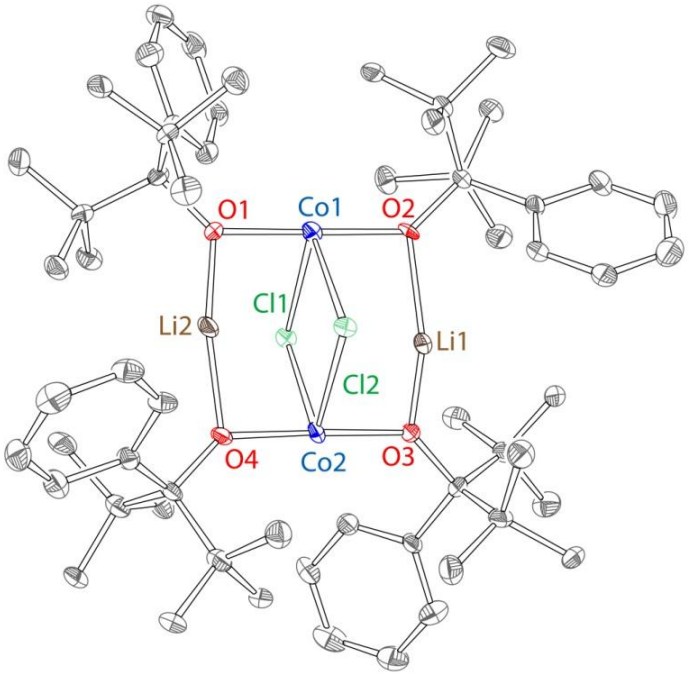

Figure B.3. Crystal structure of **6**, 50% probability ellipsoids. Selected bond distances and bond angles: Co1-O1 1.893(2) Å, Co1-O2 1.877(2) Å, Co1-Cl1 2.540(3) Å, Co1-Cl2 2.457(3) Å, O1-Co1-O2 175.5(2)°, Cl1-Co1-Cl2 84.47(7)°.

2. Evans Method Formula and Procedure

The Evans method[49] was performed on **3**-**8** using a Wilmad coaxial insert (purchased from Aldrich) and a standard NMR tube. The sample was carefully weighed, and a precise amount of the appropriate NMR solvent was added to afford solutions with known concentrations for the calculations. The solutions were added to the insert, and the insert was placed inside the outer NMR tube, which contained blank NMR solvent. NMR spectra were taken as indicated previously. The molar susceptibility χ_m of the compound was first calculated using Equation 1

$$\chi_m = \left[\frac{3\Delta\nu}{4\pi m\nu_0} + \chi_0\right] M \qquad (1)$$

where $\Delta\nu$ is the peak separation in Hertz, m is the concentration of the solution in grams per milliliter, ν_0 is the spectrometer operating frequency in Hertz, χ_0 is the molar susceptibility of the solvent (in cm^3/g), and M is the molar mass of the compound (g/mol).

The solution state effective magnetic moment (μ_{eff}) was calculated using Equation 2:

$$\mu_{eff} = \sqrt{(2.383 \times 10^3)(\chi_m)} \quad (2)$$

Diamagnetic corrections were calculated using Pascal's constants.[55] Two or three measurements were taken, and the average of the three was taken. The data is reported below in **Tables B.1** and **B.2** below. We also calculate standard deviation and report it alongside the average values. We note however that we estimate the uncertainty in the calculated values to be at least 5%, even if the standard deviation values are lower.

Table B.1. Spin-only magnetic moments calculated for **3**-**6** using the Evans method.

Complex	μ_{calc} (μ_B)	μ_{obs} (μ_B)
3	8.9	8.8
4	8.9	8.4
5	11.0	11.6
6	6.9	7.8

Table B.2. Spin-only magnetic moments calculated for **7** and **8** using the Evans method.

Complex	μ_{calc} (μ_B)	μ_{obs} (1) (μ_B)	μ_{obs} (2) (μ_B)	μ_{obs} (3) (μ_B)	μ_{obs} (average) (μ_B)
7	2.8	3.1	3.1	2.9	3.0 ± 0.1
8	2.8	3.2	3.0	3.1	3.1 ± 0.1

3. NMR Spectra

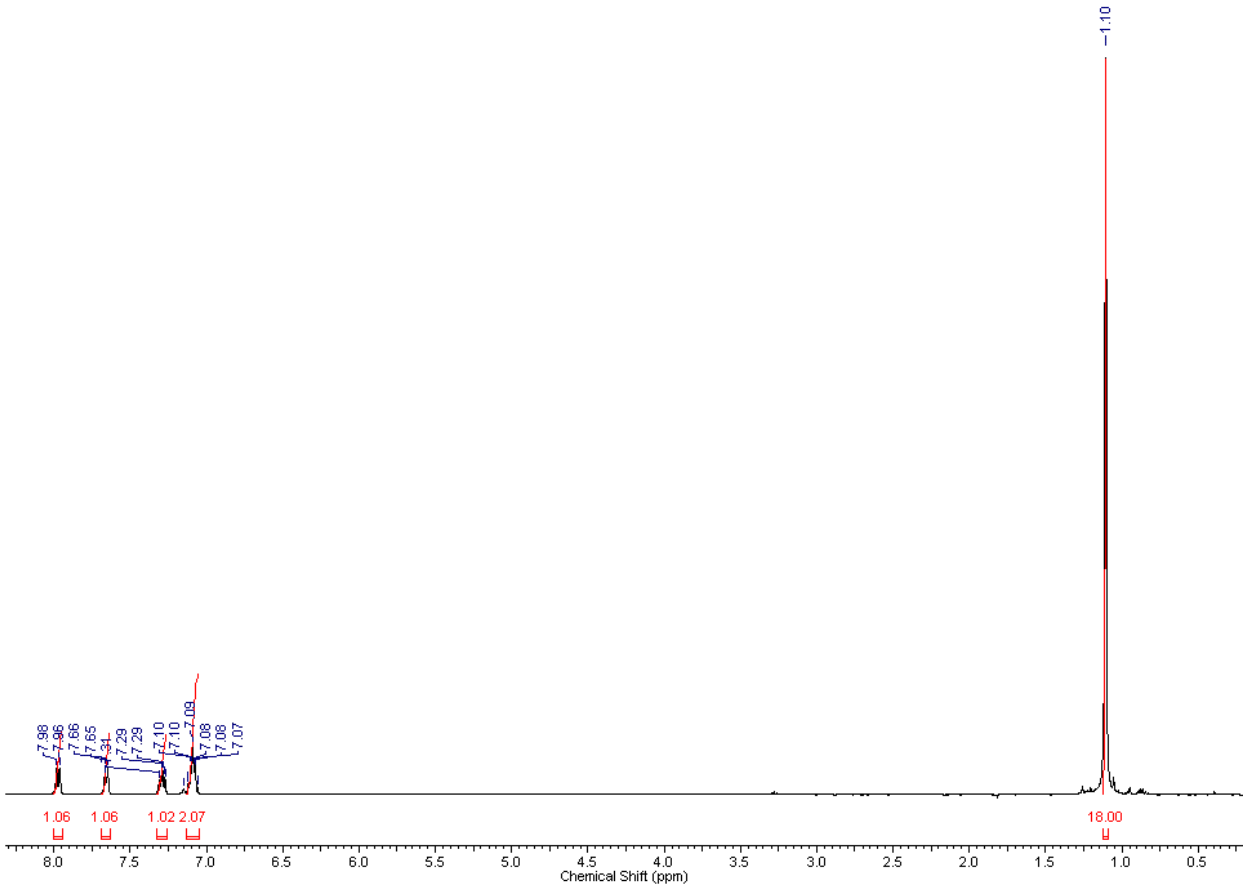

Figure B.4. ^{1}H NMR spectrum of LiOR, **1**.

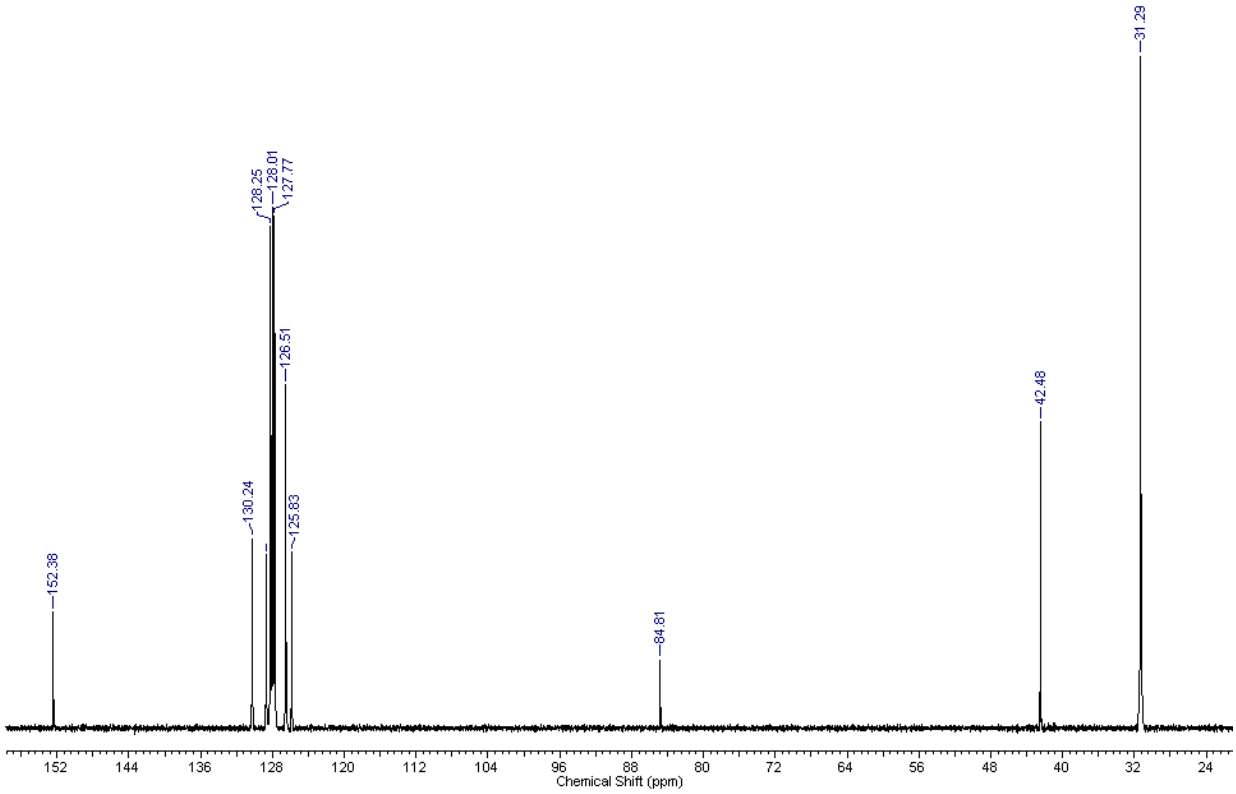

Figure B.5. ^{13}C NMR spectrum of LiOR, **1**.

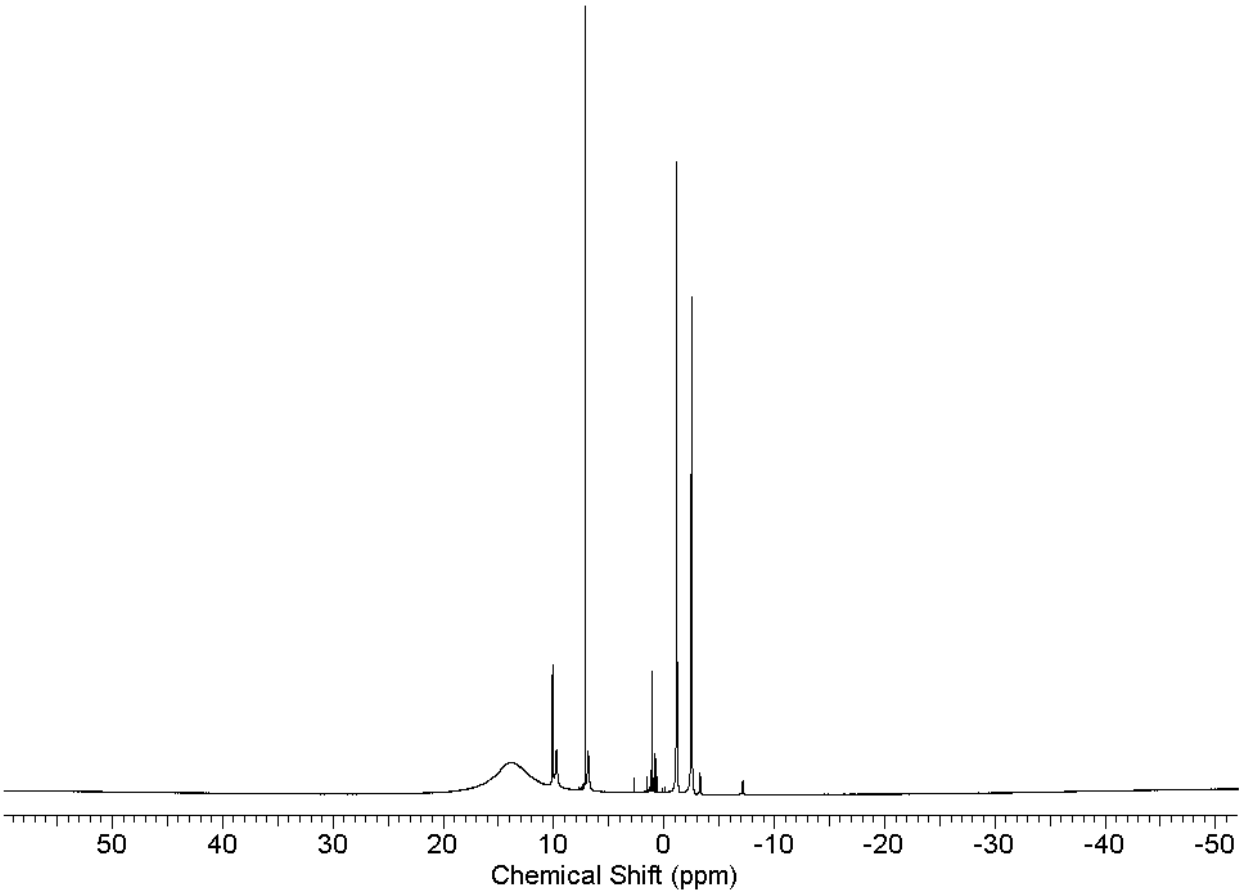

Figure B.6. ^{1}H NMR spectrum of **8**.

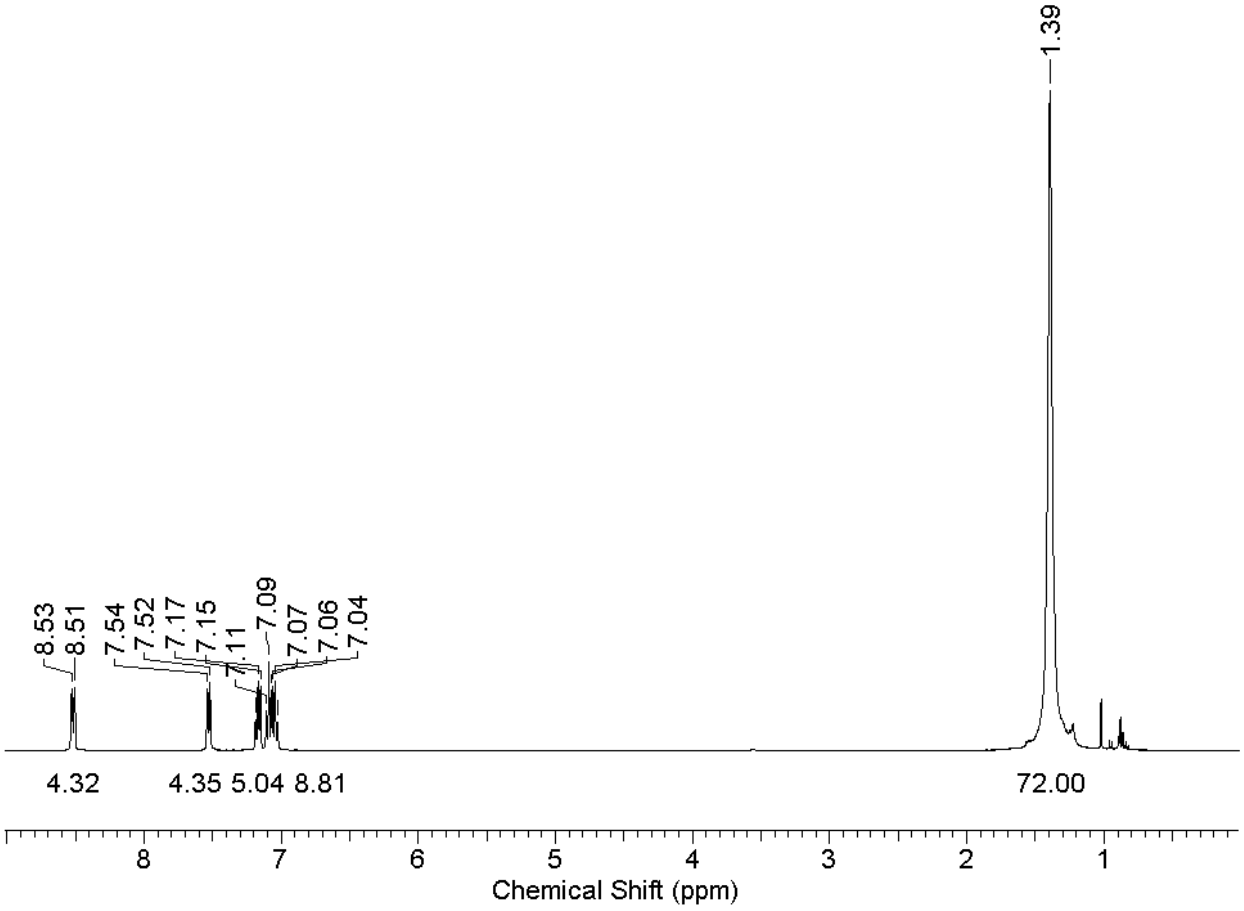

Figure B.7. ^{1}H NMR spectrum for **9**.

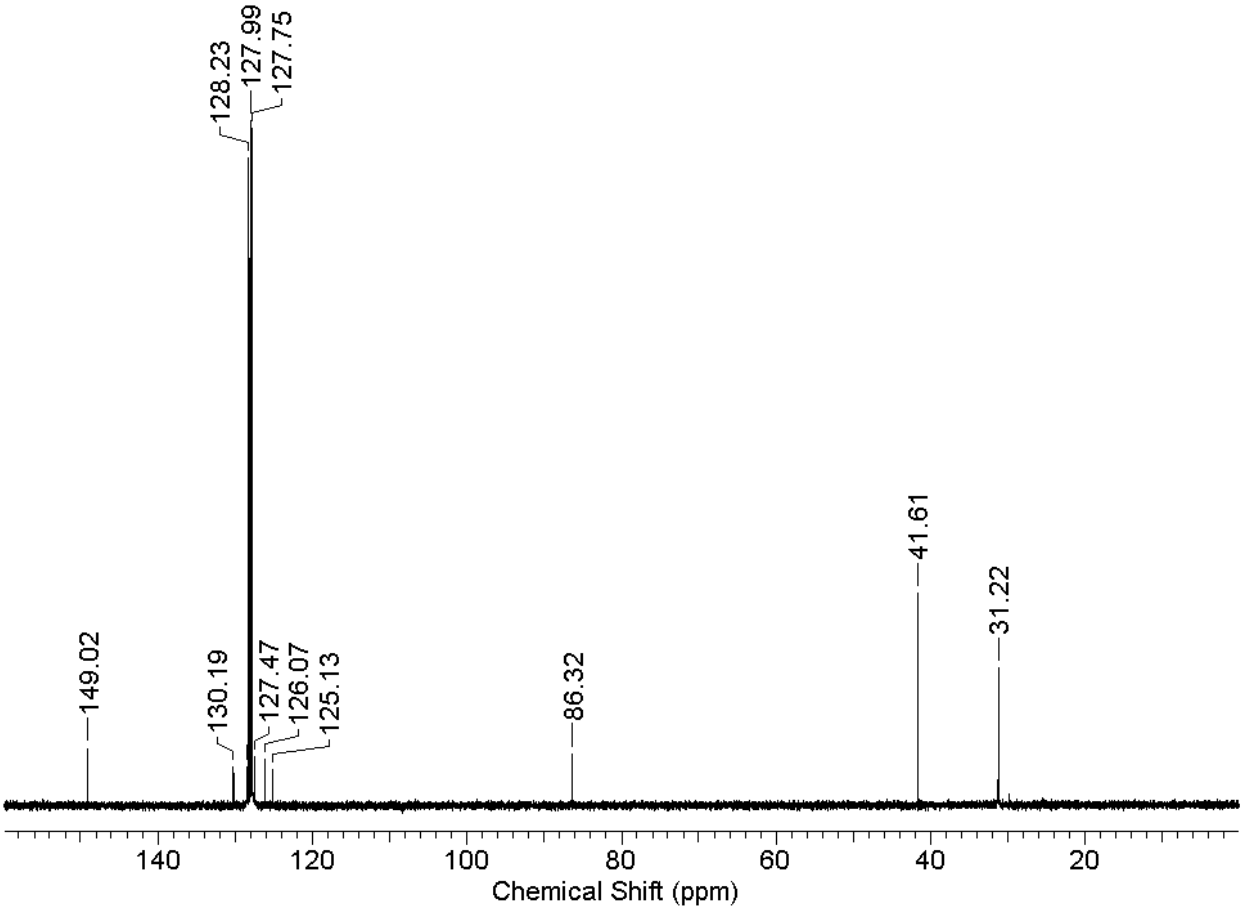

Figure B.8. ^{13}C NMR spectrum for **9**.

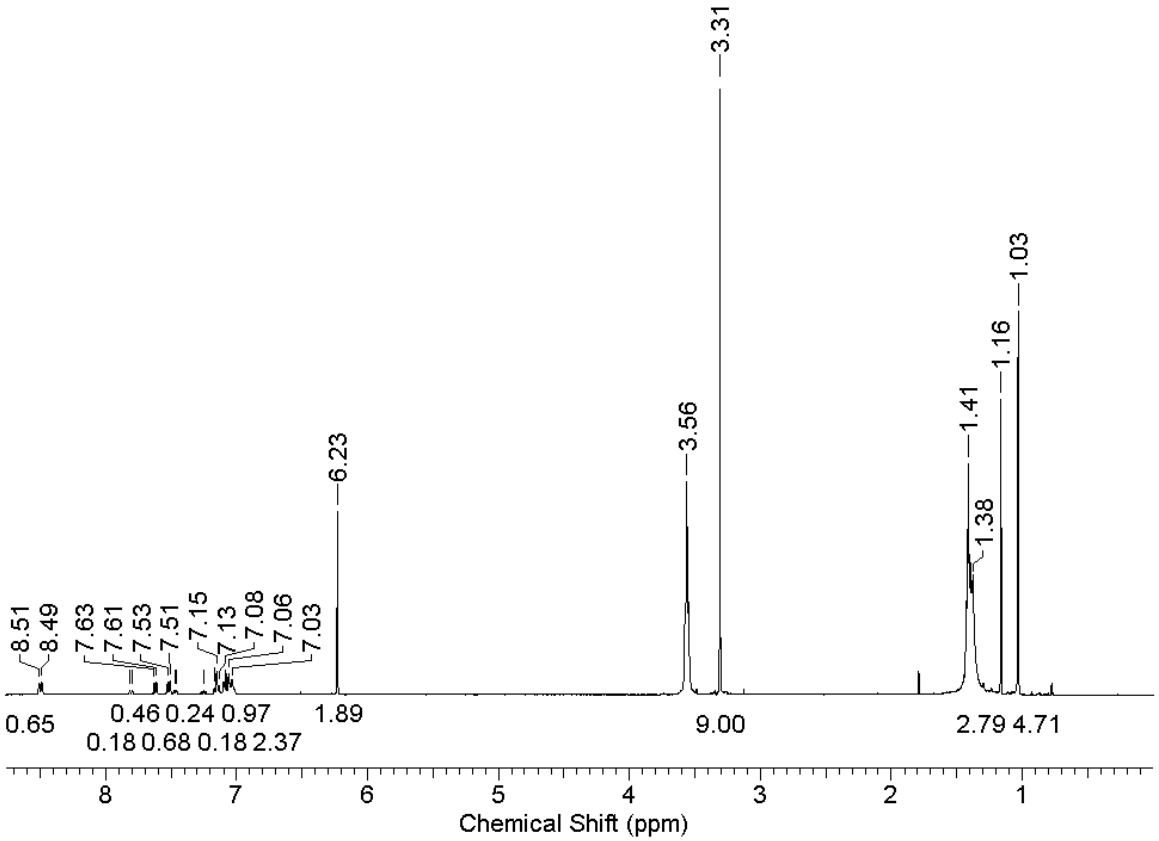

Figure B.9. Full ^{1}H NMR spectrum of the crude reaction mixture of $CuBr_2$ with 2 LiOR. The reaction mixture contains an internal standard trimethoxybenzene (peak at 6.23 and 3.31 ppm).

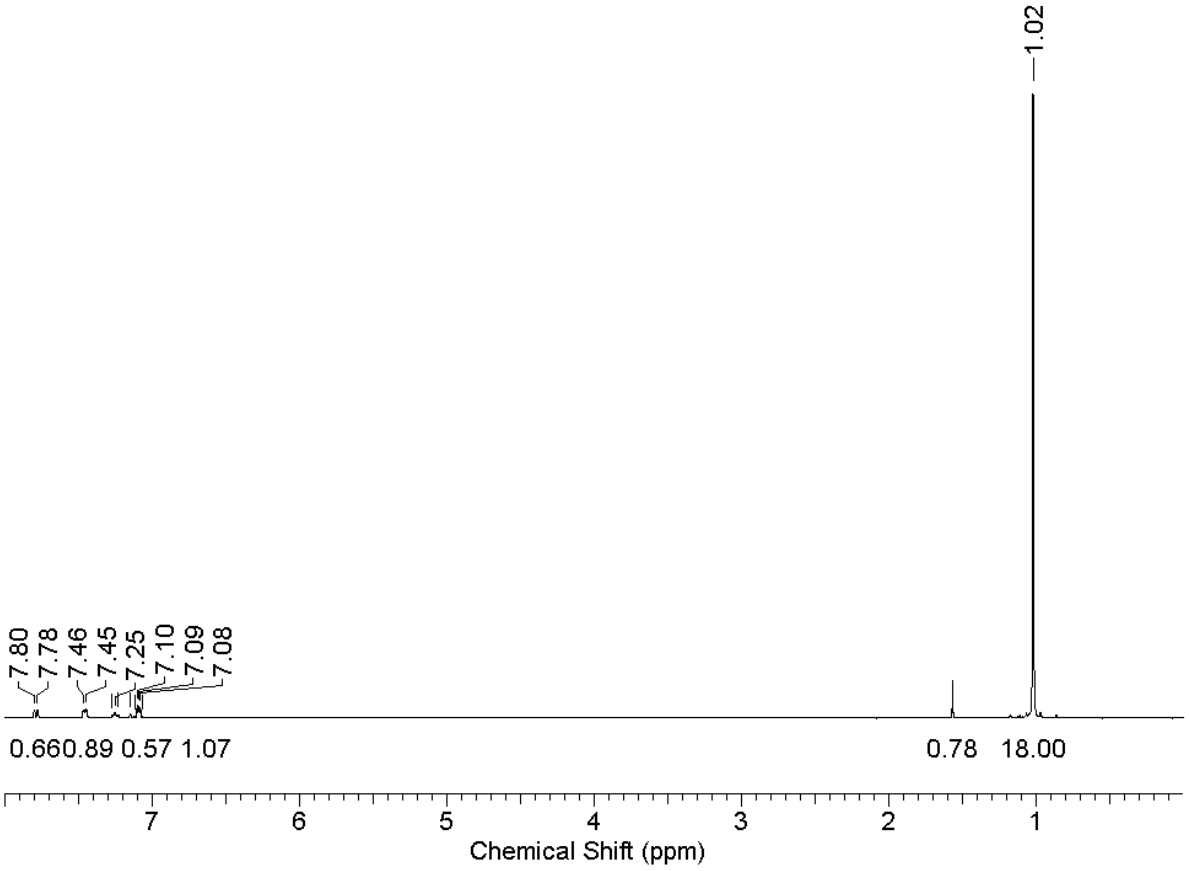

Figure B.10. Full ^{1}H NMR spectrum of HOR in C_6D_6.

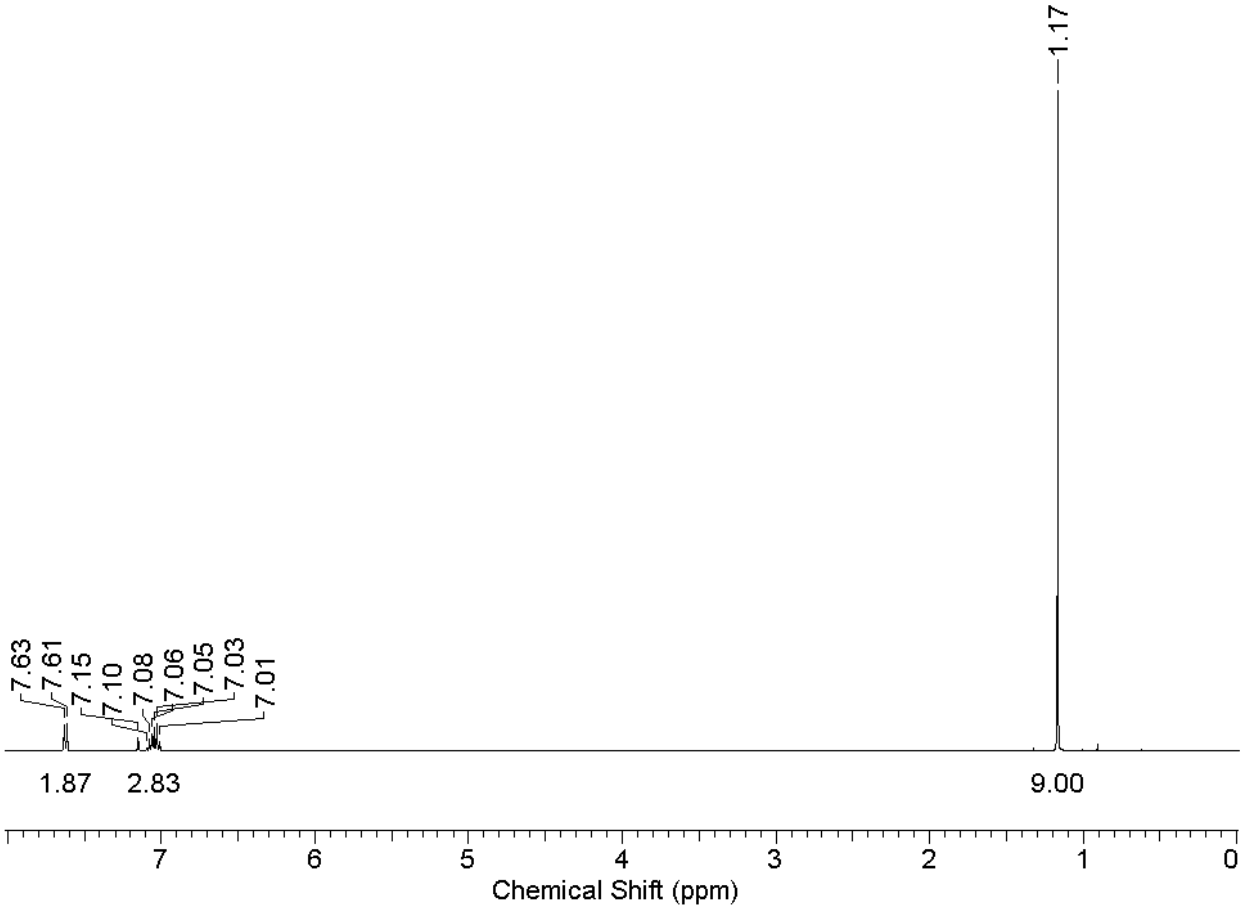

Figure B.11. Full ^{1}H NMR spectrum of tert-butyl phenyl ketone in C_6D_6.

4. IR Spectra

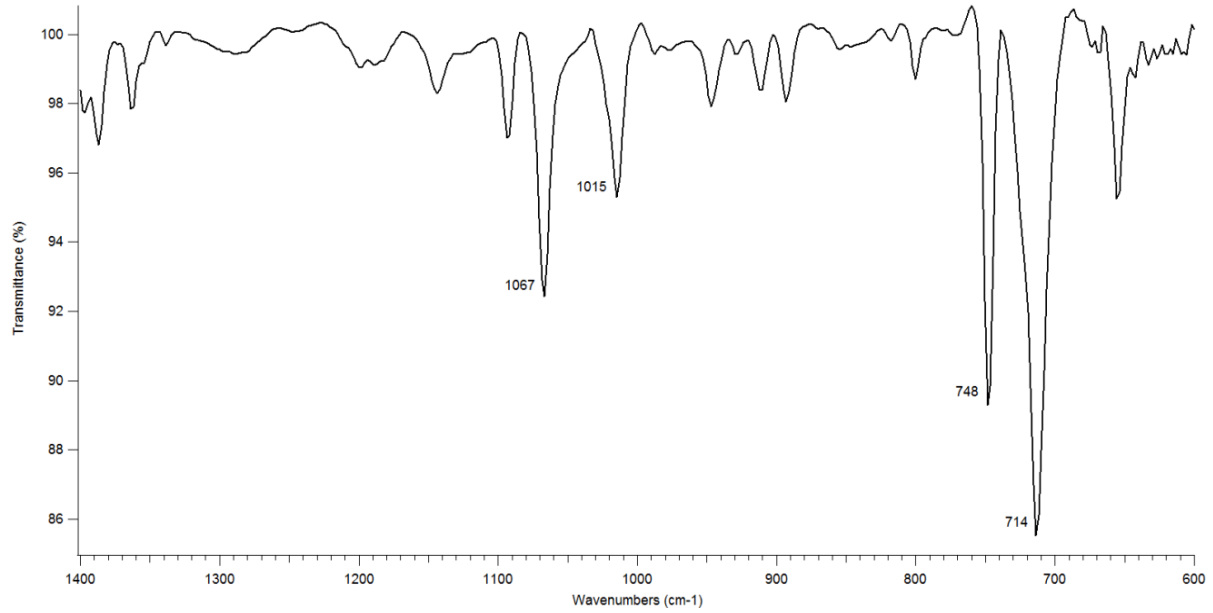

Figure B.12. IR spectrum of LiOR, **1**.

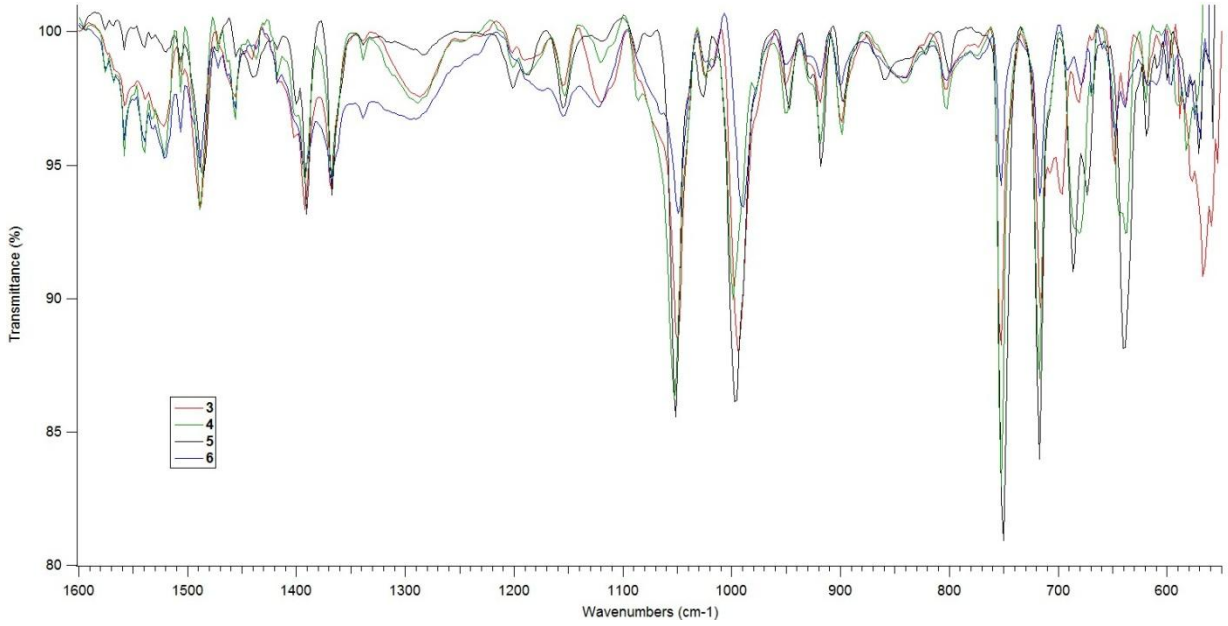

Figure B.13. IR spectra of the seesaw dimers, **3**-**6**, showing their similar stretches.

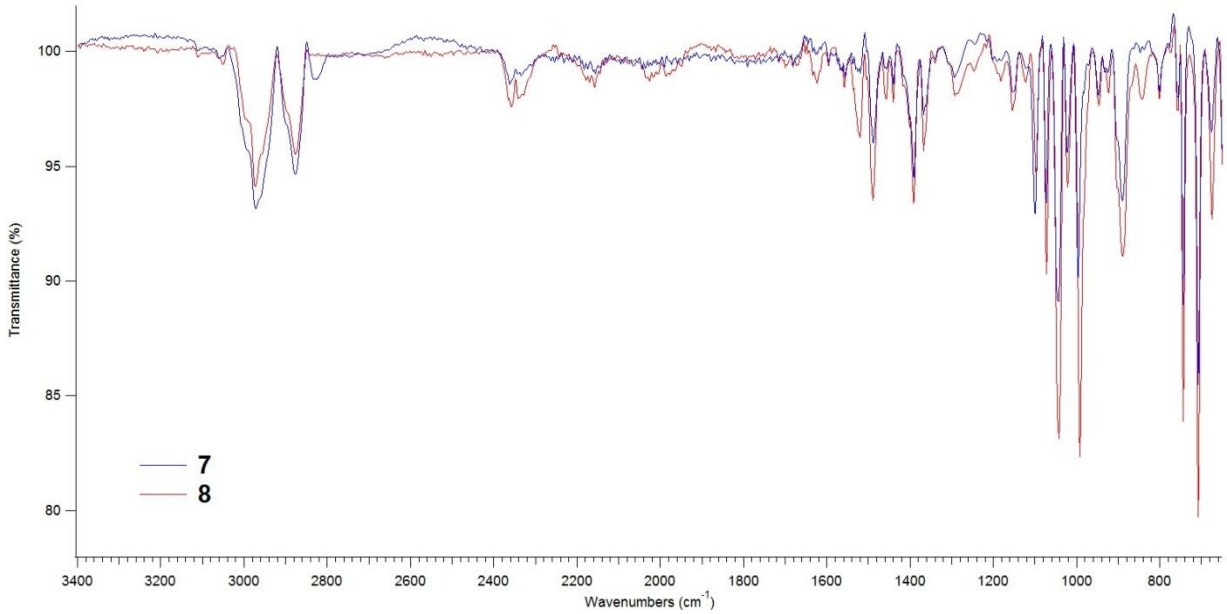

Figure B.14. IR spectra of **7** and **8**.

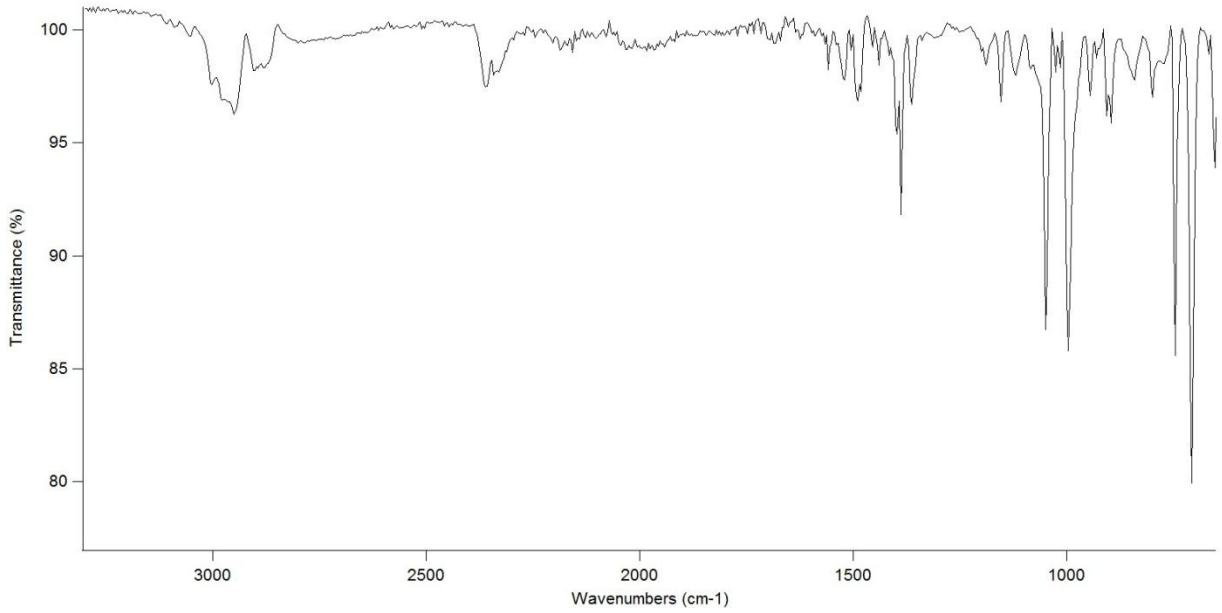

Figure B.15. IR spectrum for **9**.

5. UV-vis Spectra

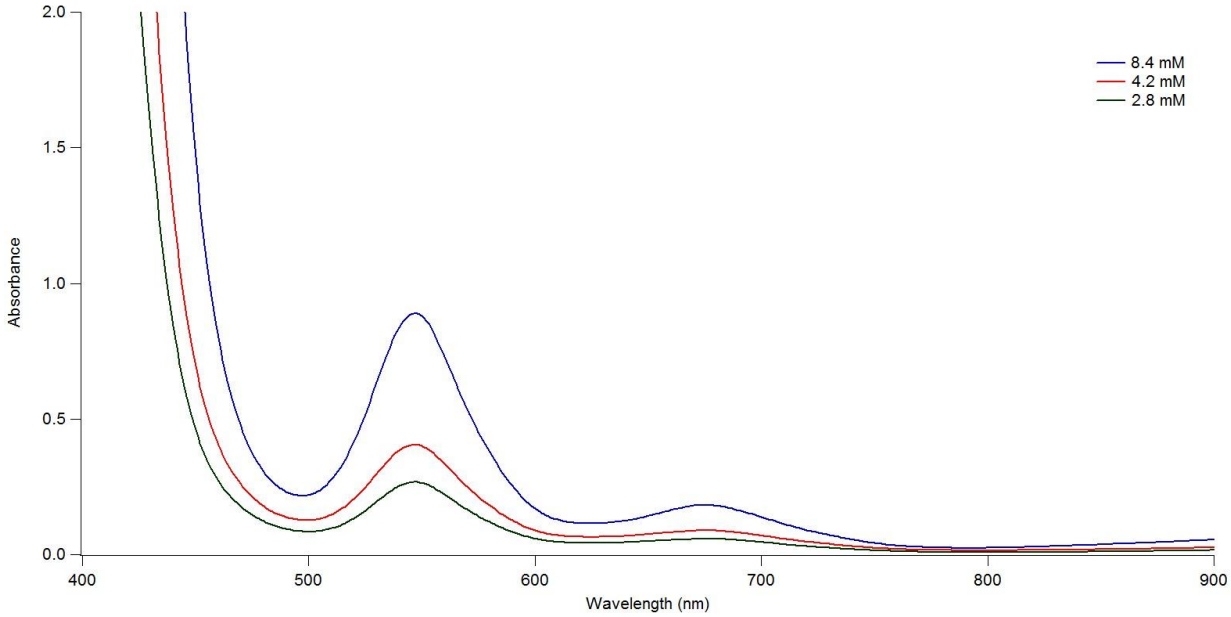

Figure B.16. UV-vis spectrum for **7** at three different concentrations. λ_{max} (ε_M): 676 (22), 547 (99).

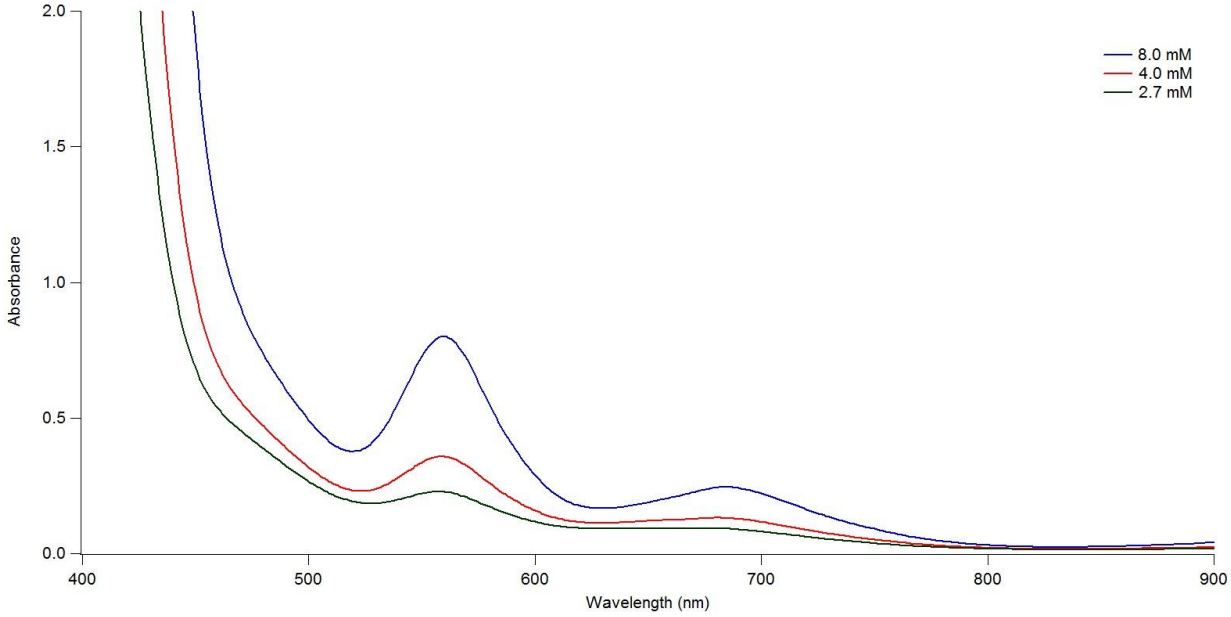

Figure B.17. UV-vis spectrum for **8** at three different concentrations. λ_{max} (ε_M): 682 (33), 559 (91).

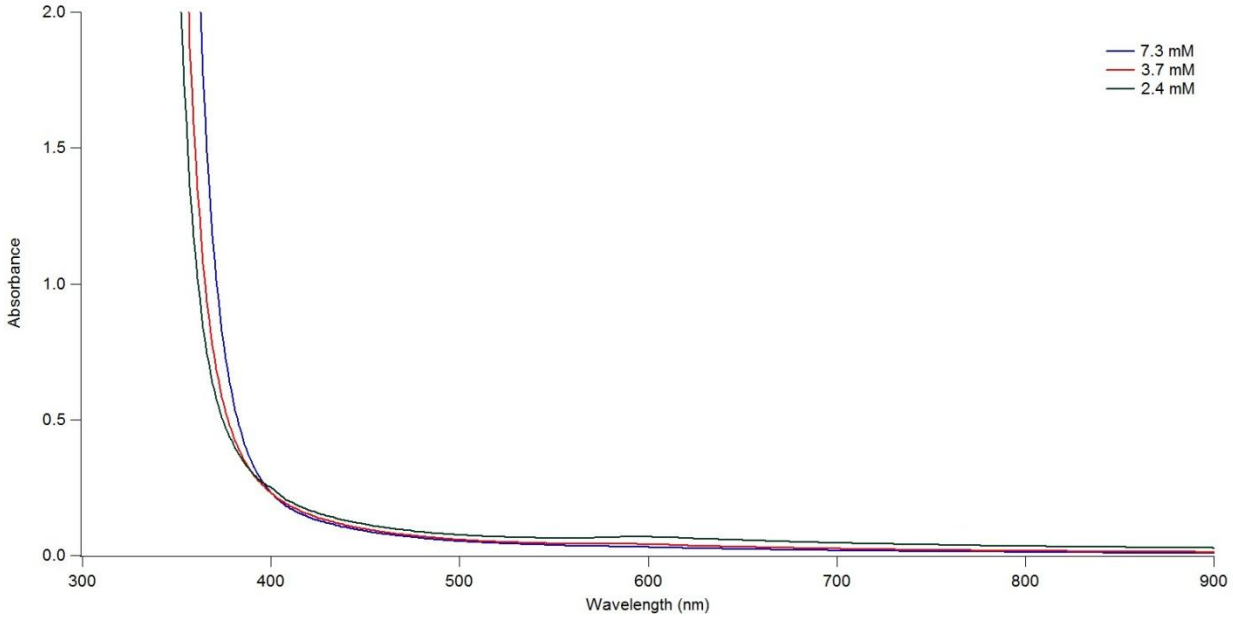

Figure B.18. UV-vis spectrum for **9** ($Cu_4(OR)_4$) at three different concentrations.

6. **Metal k-edge X-ray Abosorption Spectroscopy Details**

Data Collection

Samples of **3**, **5**, and **6** were prepared as finely ground samples dispersed in nujol and placed in aluminum sample holders between two windows made from Kapton tape (cat. no. 1205; 3M, Minneapolis, MN). Data were collected at the NSLS (Brookhaven National Laboratories; Upton, NY) on beamline X3b (ring operating conditions: 2.8 GeV; 305 – 200 mA). All data were obtained at 20 K (temperature maintained using a He displex cryostat) and obtained in transmission mode. A focused Si(111) double monochromater was used for energy selection along with a low angle Ni mirror for harmonic rejection. The energy were calibrated by simultaneously recording the spectrum of elemental metal foil. Data were collected in 5 eV steps in the pre-edge region (200 to 20 eV below the edge jump), 0.3 eV steps in the edge region (–20 to +20 eV relative to the edge jump), 2 eV steps in the near edge region (+20 to +200 eV relative to the edge jump) and 5 eV steps in the far edge region (+200 to 19 *k* relative to the edge jump). All spectra represent the averaged sum of 7 scans.

Data Analysis

Data analysis was performed using the XAS data analysis package EXAFS123 (version 0.3b).[90] The EXAFS region of the K-edge spectra were analyzed as unfiltered $k^3(\chi)$ from k = 2.0 – 17.5 Å^{-1} for **3** and **5**. Analysis for Co-containing **6** was only performed over the range of k = 2.0 – 14.3 Å^{-1} because of irresolvable artifacts resulting from the Ni mirror. Phase and amplitude functions were generated using the software package FEFF 8.2.[91] Single scattering pathways for M–O, M–Cl and M–M scatterers were generated as previously described.[92] Multiple scattering pathways for the remainder of the complexes were generated as follows. A series of DFT generated structures for **3** were prepared. The Fe-Fe, Cl-Fe-Cl and O-Fe-O bond lengths and angles were constrained from: Fe-Fe (r): 3.4 – 3.8 Å, Cl-Fe-Cl(θ): 75 – 105° and O-Fe-O(φ): 170 – 190°. Restrained geometry optimizations using TeraChem v. 1.5K[7,8] on a GPU-based workstation were then performed using the BLYP functional and VDZ-P basis set on Fe and all ligating atoms and a SVZ-P basis set on all other atoms. The low level of theory and small basis sets were justified by the fact that a large number of structures needed to be generated for FEFF input files, the pertinent bond length and angles were restrained and a high degree fidelity outside of the metal core was deemed unnecessary; as latter confirmed by the data analysis. A total of 40 DFT structures were thus generated. These were systematically "tweaked" resulting in 512 structures for FEFF input files. For **5** and **6** the Fe atoms were replaced by Mn and Co, respectively. All pathways that had an amplitude of 5% or more relative to the M-Cl pathways were retained in the simulated spectra. Once the individual spectra were generated the pathways contributing to the M-M, M-Cl and M-O vectors were subtracted from the total chi.dat output files, resulting in all of the significant single and multiple scatterering pathways. Phase (α_{MS}) and amplitude (f_{MS}) functions were generated according to the formula:

$$F_{MS} = F_0 + rF_1 + \theta F_2 + \theta^2 F_3 + \varphi^2 F_4$$

where $F = \alpha_{MS}$ or f_{MS}. Best fits to the data were compared using by comparison of the error parameter ε^2.

Table B.3. Best fits to the XAS data of **3**, **5** and **6** and fit without the MS-pathways.

	3	**5**	**6**
Pre-edge peak position (eV)	7112.3(2)	6539.3(1)	7709.6(10
Area (%eV relative to edge)	8.2(1)	12.5(2)	7.9(2)
Edge energy (eV)	7117.9(3)	6545.8(3)	7716.4(3)
E_O (eV)	7124.20	6548.11	7720.93
Best Fit			
M-O shell			
n[a]	2	2	2
r (Å)	1.887(2)	1.901(2)	1.872(6)
σ^2 (Å^{-2})	0.0016(2)	0.0014(2)	0.0021(3)
M-Cl shell			
n[a]	2	2	2
r (Å)	2.482(7)	3.001(8)	2.410(9)
σ^2 (Å^{-2})	0.0011(5)	0.0031(5)	0.0016(2)
M-M shell			
n[a]	1	1	1
r (Å)	3.60(2)	4.48(11)	3.64(2)
σ^2 (Å^{-2})	0.0020(8)	0.0027(5)	0.0013(2)
MS shell			
n[a]	1	1	1
r (Å)[b]	3.60	4.48	3.64
σ^2 (Å^{-2})	0.0017(4)	0.0014(8)	0.001(1)
θ (°)	86(2)	89(3)	81(3)
φ (°)	174(2)	172(1)	175(2)

ε^2	0.88	0.92	0.83
Fit Without the MS Shell			
M-O shell			
n[a]	2	2	2
r (Å)	1.911(5)	1.826(28)	1.944(13)
σ^2 (Å^{-2})	0.0028(1)	0.0003(1)	0.0008(1)
M-Cl shell			
n[a]	2	2	3
r (Å)	2.476(3)	2.89(3)	2.51(1)
σ^2 (Å^{-2})	0.0025(4)	0.0006(12)	0.006(1)
M-M shell			
n[a]	1	1	1
r (Å)	3.62(4)	4.5(3)	3.6(1)
σ^2 (Å^{-2})	0.0001(14)	0.0004(29)	0.0007(3)
ε^2	1.52	1.74	1.40

a) restrained to nearest whole number following the initial refinement cycle. b) length restrained to the M-M shell distance.

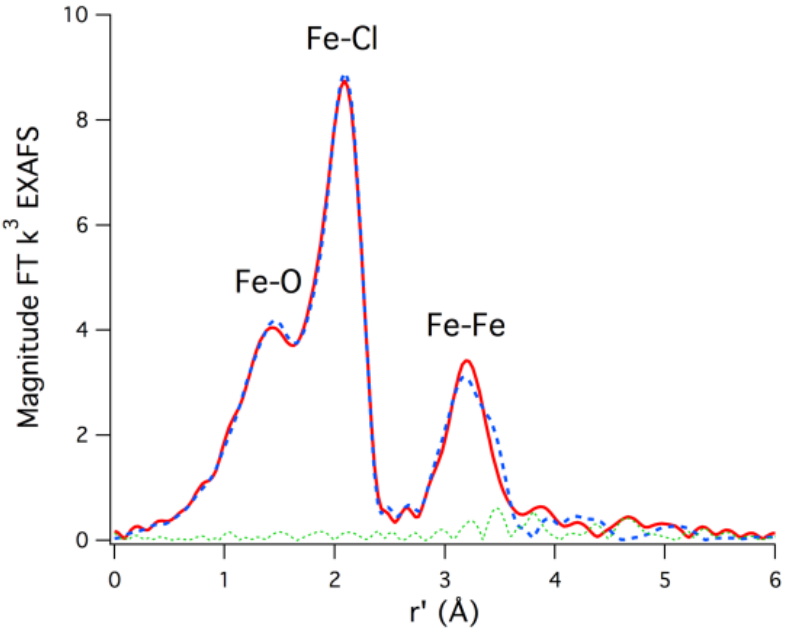

Figure B.19. Magnitude FT $k^3(\chi)$ for **3** (FT from k = 2.0 to 17.5 $Å^{-1}$). The red spectrum is the real data, the simulated data is the blue spectrum and the difference spectrum is in green.

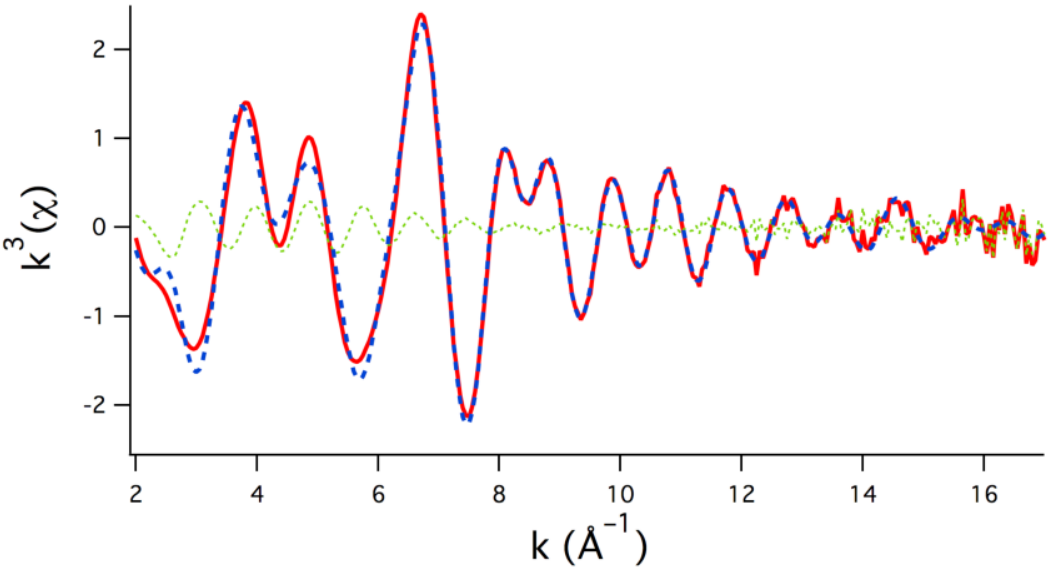

Figure B.20. $k^3(\chi)$ for **5**. The red spectrum is the real data, the simulated data is the blue spectrum and the difference spectrum is in green.

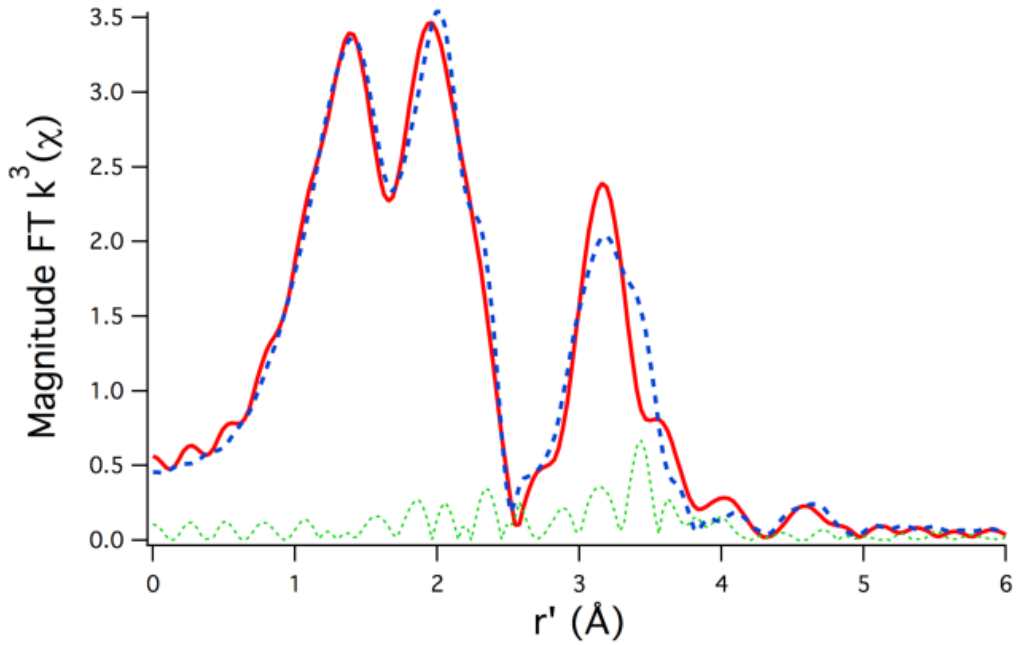

Figure B.21. Magnitude FT $k^3(\chi)$ for **5** (FT from k = 2.0 to 17.5 Å^{-1}). The red spectrum is the real data, the simulated data is the blue spectrum and the difference spectrum is in green.

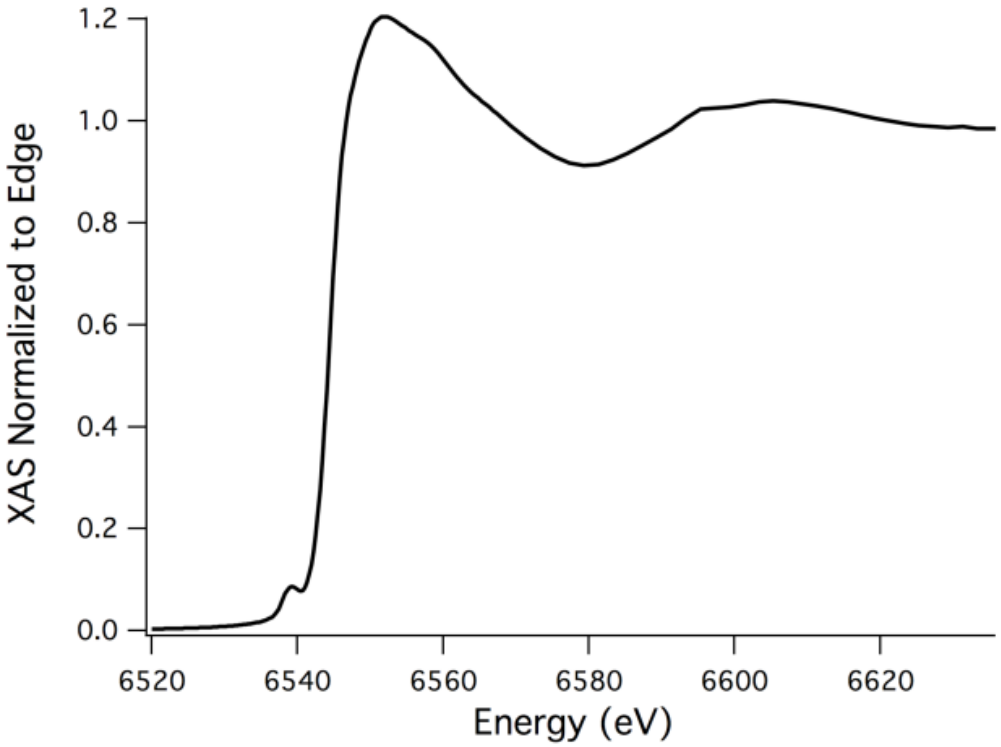

Figure B.22. XANES region of the XAS for **5**.

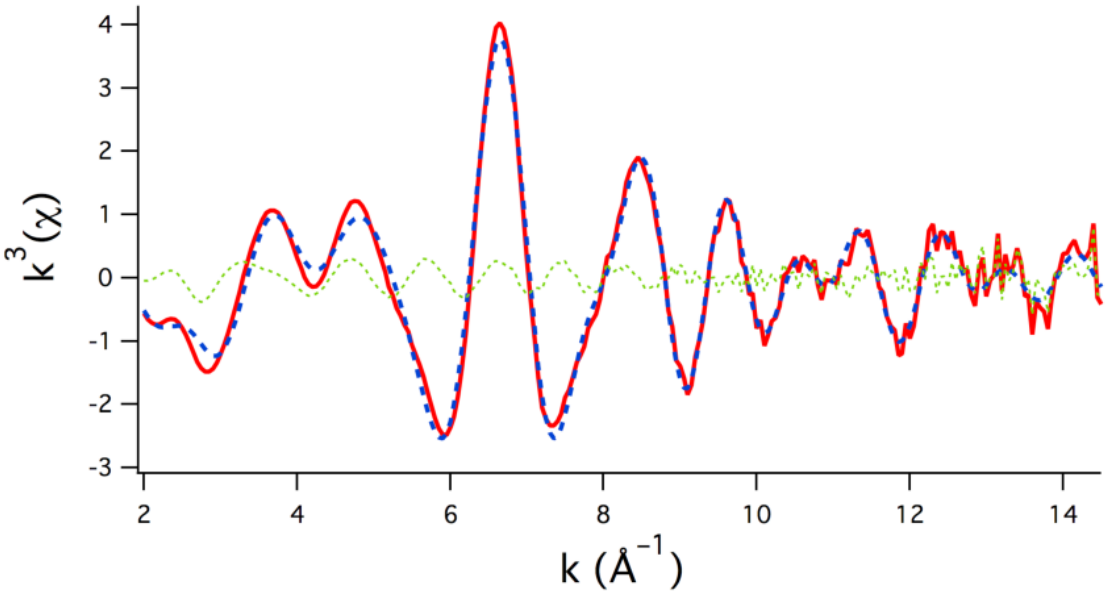

Figure B.23. $k^3(\chi)$ for **6**. The red spectrum is the real data, the simulated data is the blue spectrum and the difference spectrum is in green.

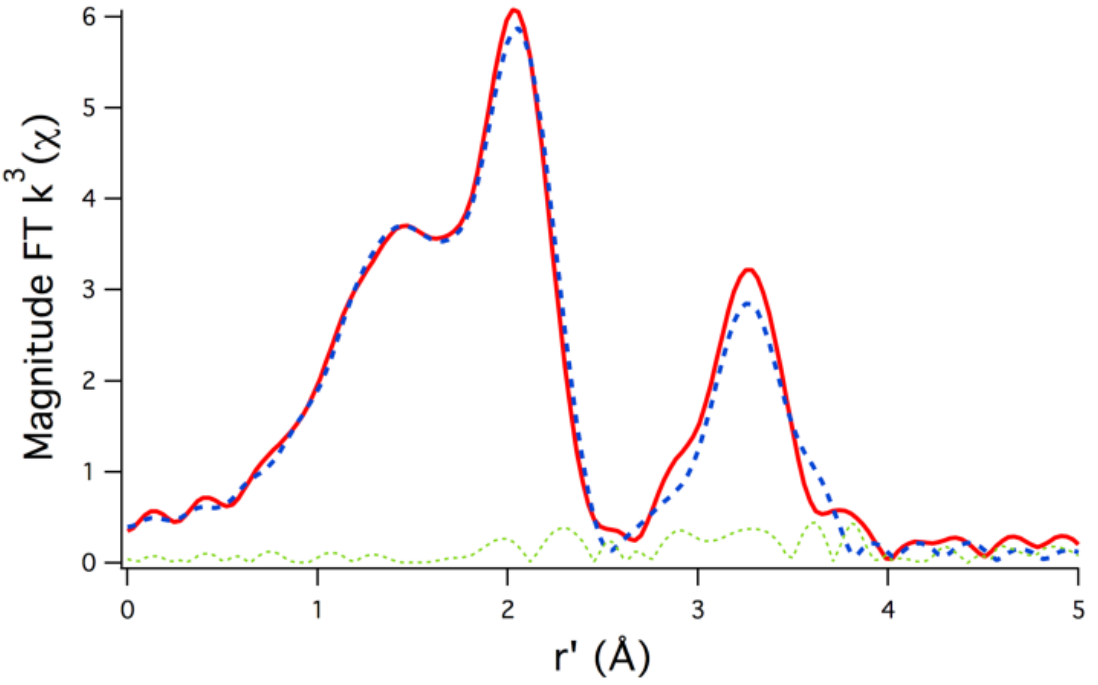

Figure B.24. Magnitude FT $k^3(\chi)$ for **6** (FT from k = 2.0 to 14.3 Å^{-1}). The red spectrum is the real data, the simulated data is the blue spectrum and the difference spectrum is in green.

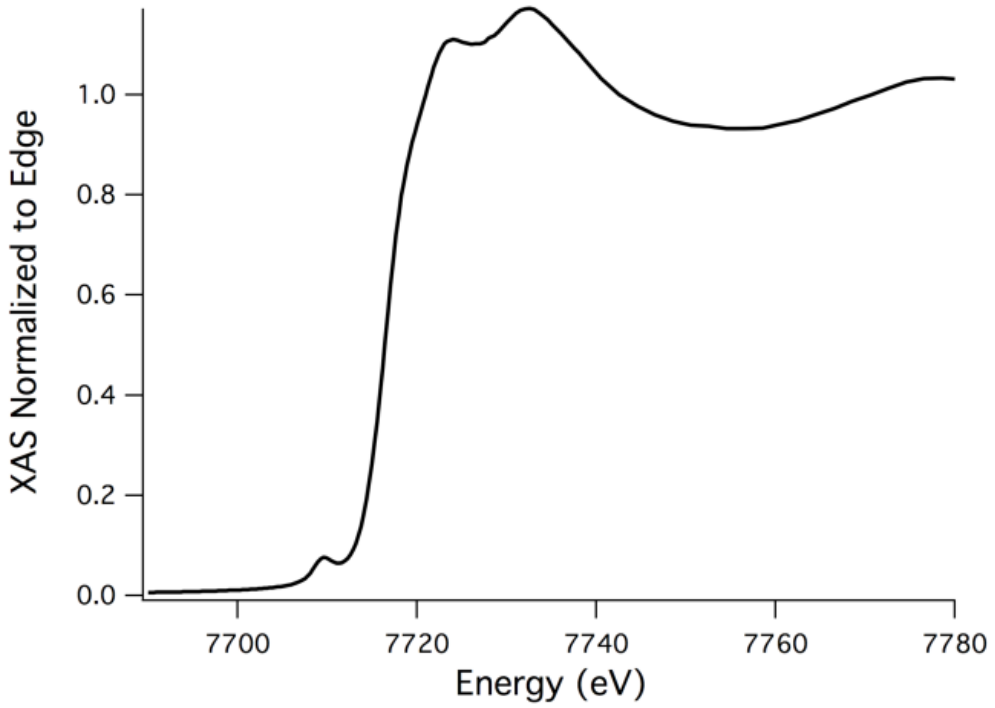

Figure B.25. XANES region of the XAS for **6**.

7. Computational Details

All geometry optimizations on **3**-**8** and their respective models were performed at the B3LYP/SDD level using the Gaussian09 program.[93] For calculation efficiency, the *tert*-butyl substituents were replaced by methyl groups in all complexes under consideration. The wavefunctions for ELF and NCI calculations were obtained from single point calculations using B3LYP/6-31(d). ELF results were calculated with a modified TopMod package.[94] A size of 200^3 au with a step size of 0.1 au grid was used for the ELF calculations. The NCI calculations were performed with the NCIPLOT program.[51] The correction to the Gibbs free energy (G) was calculated using the harmonic approximation using a scaling factor of 0.9806.[55] Since both Ni-Cl (**7**) and Ni-Br (**8**) show identical chemistry, both structures were considered for the calculations as a consistency check. No difference was observed between the complexes with the two different halides. In the case of the Mn and Ni complexes, solvation was modeled with the self-consistent reaction field (SCRF) method using

the SMD solvation approach.[93] Two solvents were modeled: THF (ε=7.4257) and hexane (ε=1.8819). All optimized structures were confirmed by frequency calculations to have no imaginary frequencies. The relative stability between dimer and monomer structures was calculated by determining the Gibbs free energy change as described in **Figure 36**. The NCI surfaces were calculated by the NCIPLOT[51] program. NCI plots the reduced density gradient versus the product of the sign of the second eigenvalue (λ_2) of the electron-density Hessian matrix and the electron density. The peaks at low electron density characterize the non-covalent interactions.

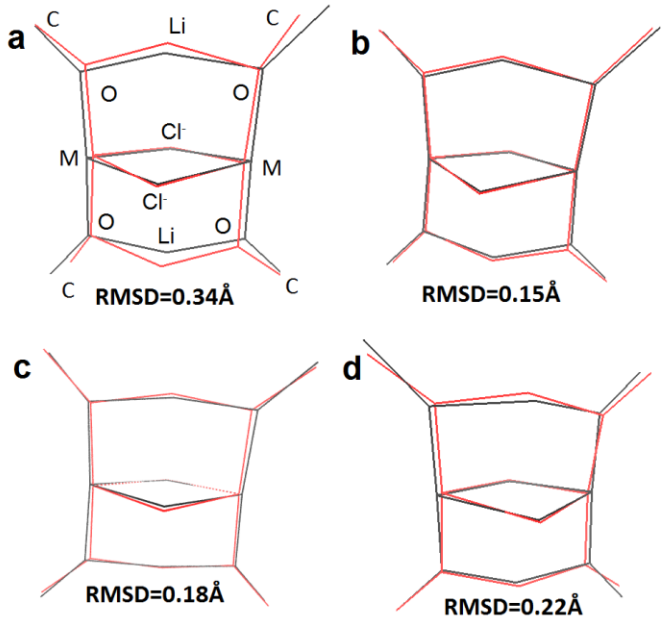

Figure B.26. Superposition of the crystal structures of **3-6** (black) and the calculated structures (red). Only the core part is shown. The letters in panel a are the atomic names; M stands for metals. For (a) Cr; (b) Mn; (c) Fe; (d) Co.

Electron Localization Function

The electron localization function (ELF), which was originally proposed based on the HF approach,[95] and extended for DFT[50] can be used as a measure of the electron localization in molecular systems. The topological analysis of ELF, a continuous and differentiable scalar field in three-dimensional space, is

performed by calculating its gradient vector field and associated Hessian matrix. The points where the gradient is zero and the three eigenvalue of the Hessian are all negative are attractors. The points whose gradient paths end at the same attractor belong to the same basin. The ELF basins resemble the domains of the models from the valence shell electron pair repulsion (VSEPR) theory.[96] For the ELF calculation, the wavefunction are truncated and only includes the O and the connected C (same as the structure in **Figure B.25**). As shown in **Figure B.26**, the ELF basins for the outer shell electrons of the transition metals are split into several small basins (in circle). This is due to the metal interactions with its surrounding ligands.[97] Different metals have different orientations for the splitting basins.

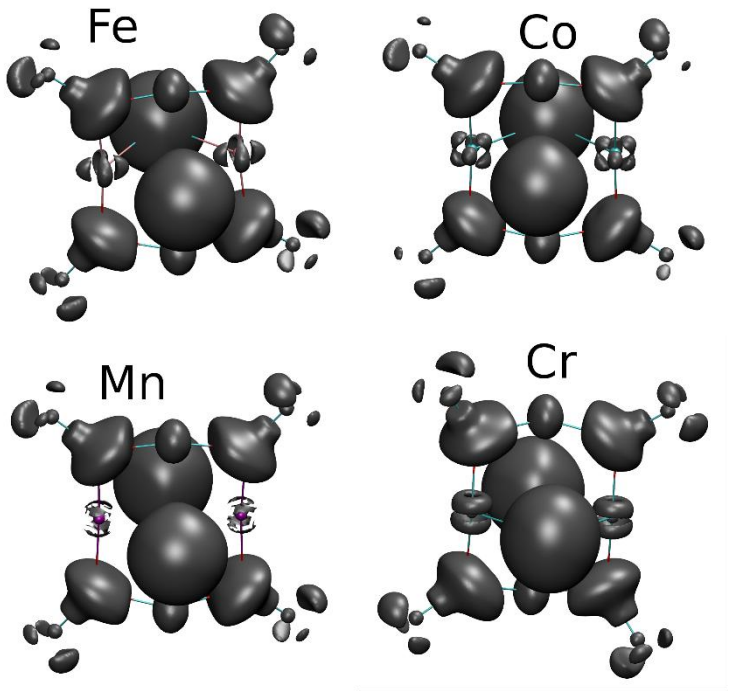

Figure B.27. The ELF (a) and NCI (b) surfaces for the Cr complex. For ELF, the isovalue is 0.735.

Non-Covalent Interaction

Non-Covalent Interaction (NCI) plots the reduced density gradient versus the product of the sign of the second eigenvalue (λ2) of the electron-density Hessian matrix and the electron density in order to visualize the non-covalent interaction. The desired non-covalent interaction can be characterized by the peaks at low electron density.

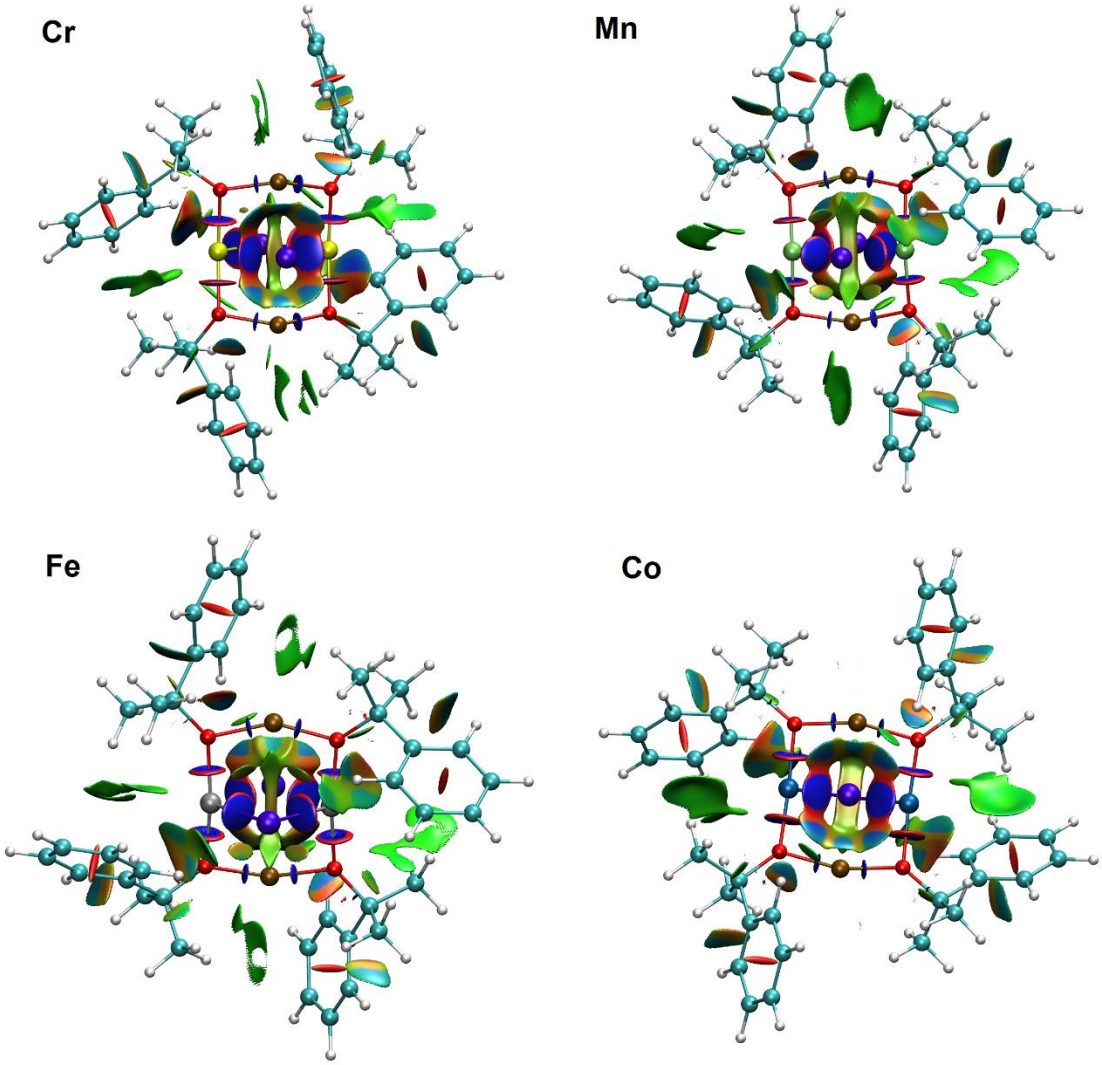

Figure B.28. The NCI for **3-6** with *tert*-butyl being replaced with methyl**.** The isovalue is 0.5 and -0.02<sign(λ_2)ρ<0.02 au.

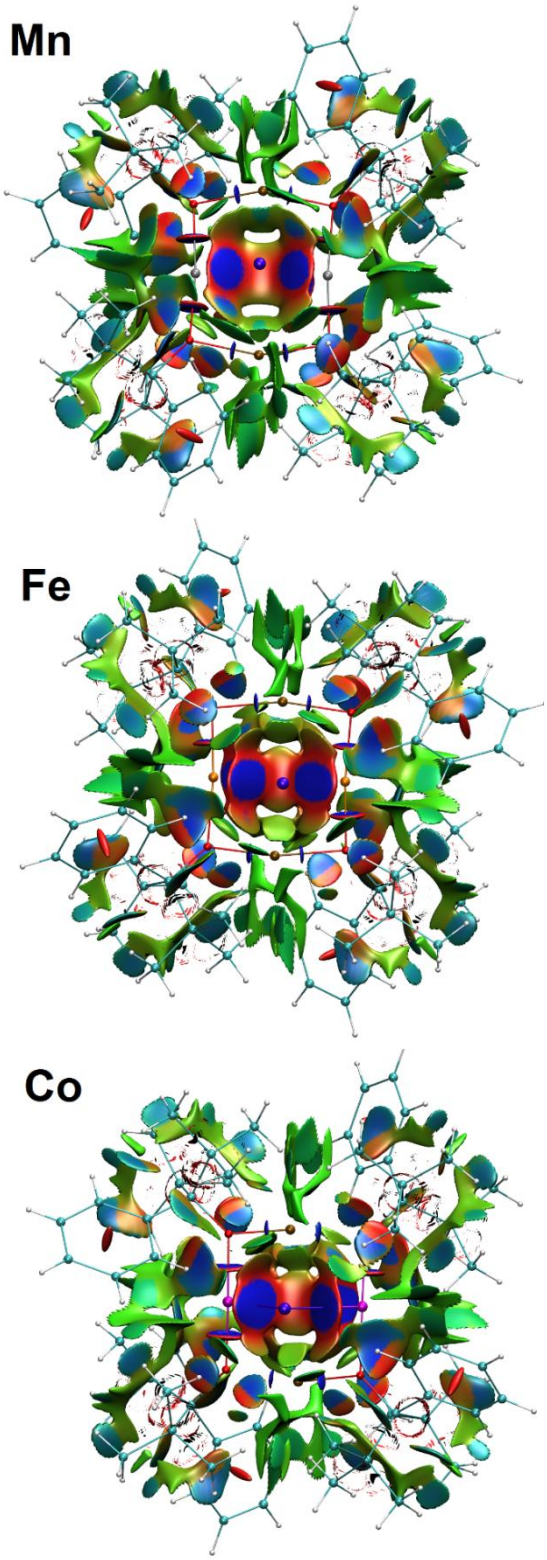

Figure B.29. The NCI for the crystal structures of **4**-**6**. The isovalue is 0.5, and -0.02<sign(λ_2)ρ<0.02 au.

Optimized structures with R from [OR] replaced with H

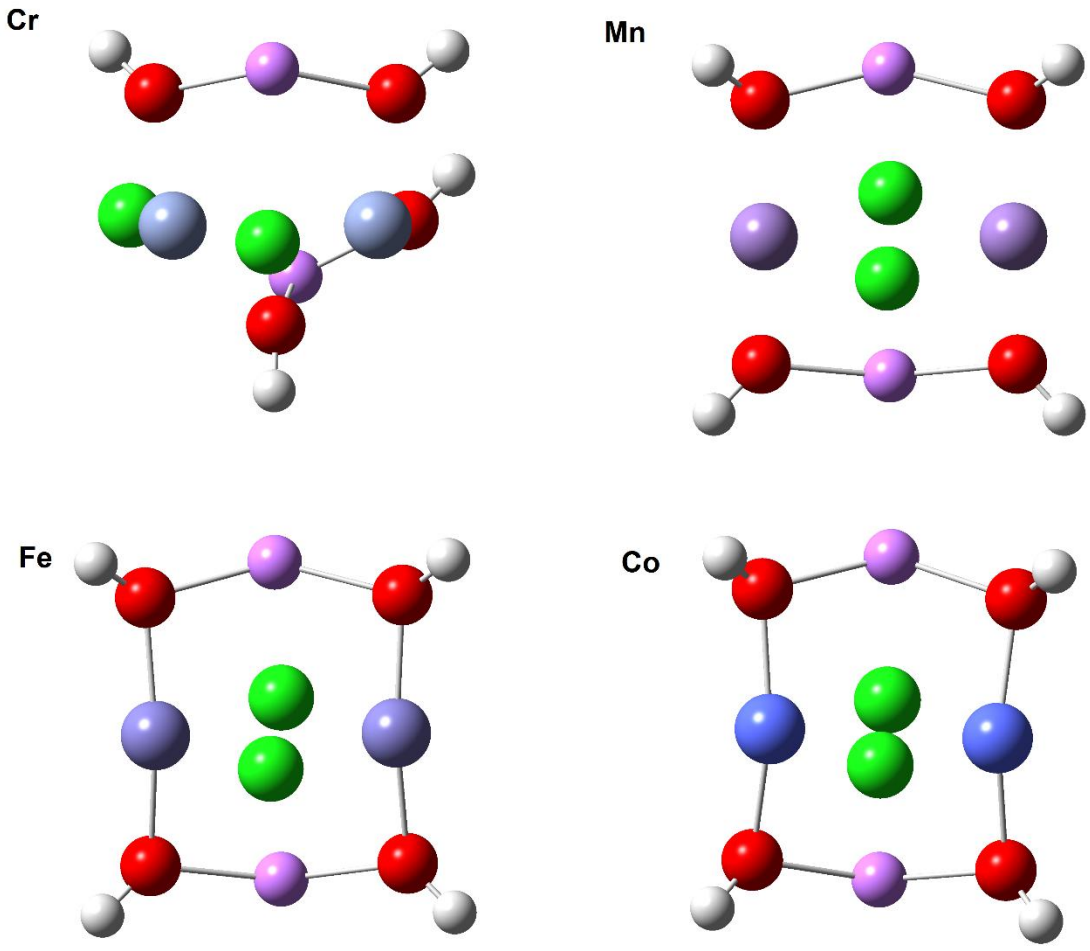

Figure B.30. Optimized structures with the R (C^tBu_2Ph) group being replaced with H.

Orbital analyses

Isovalue for the surfaces is 0.04 au. All *tert*-butyl groups are replaced by methyl groups.

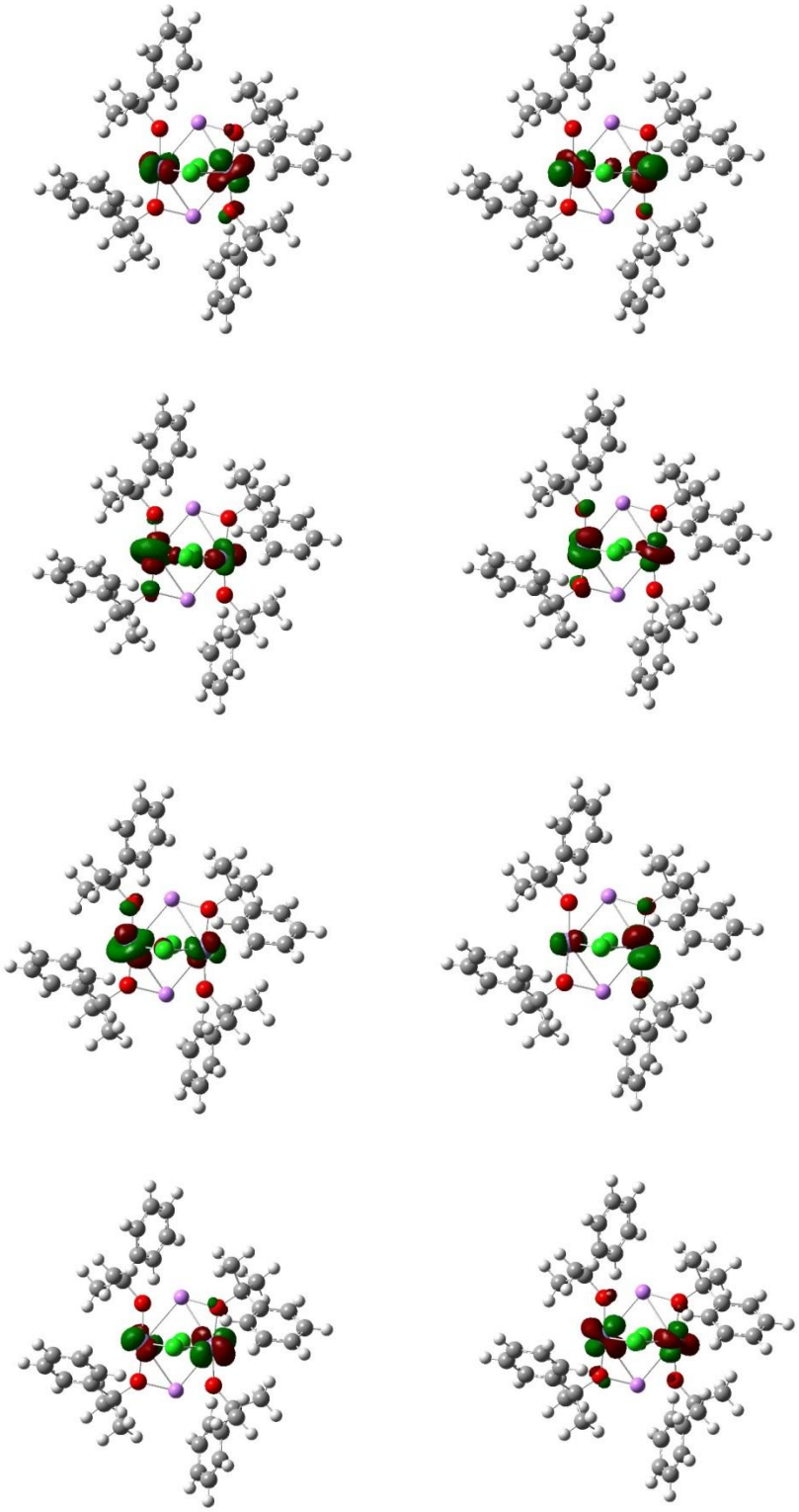

Figure B.31. Corresponding orbital analysis for **3**.

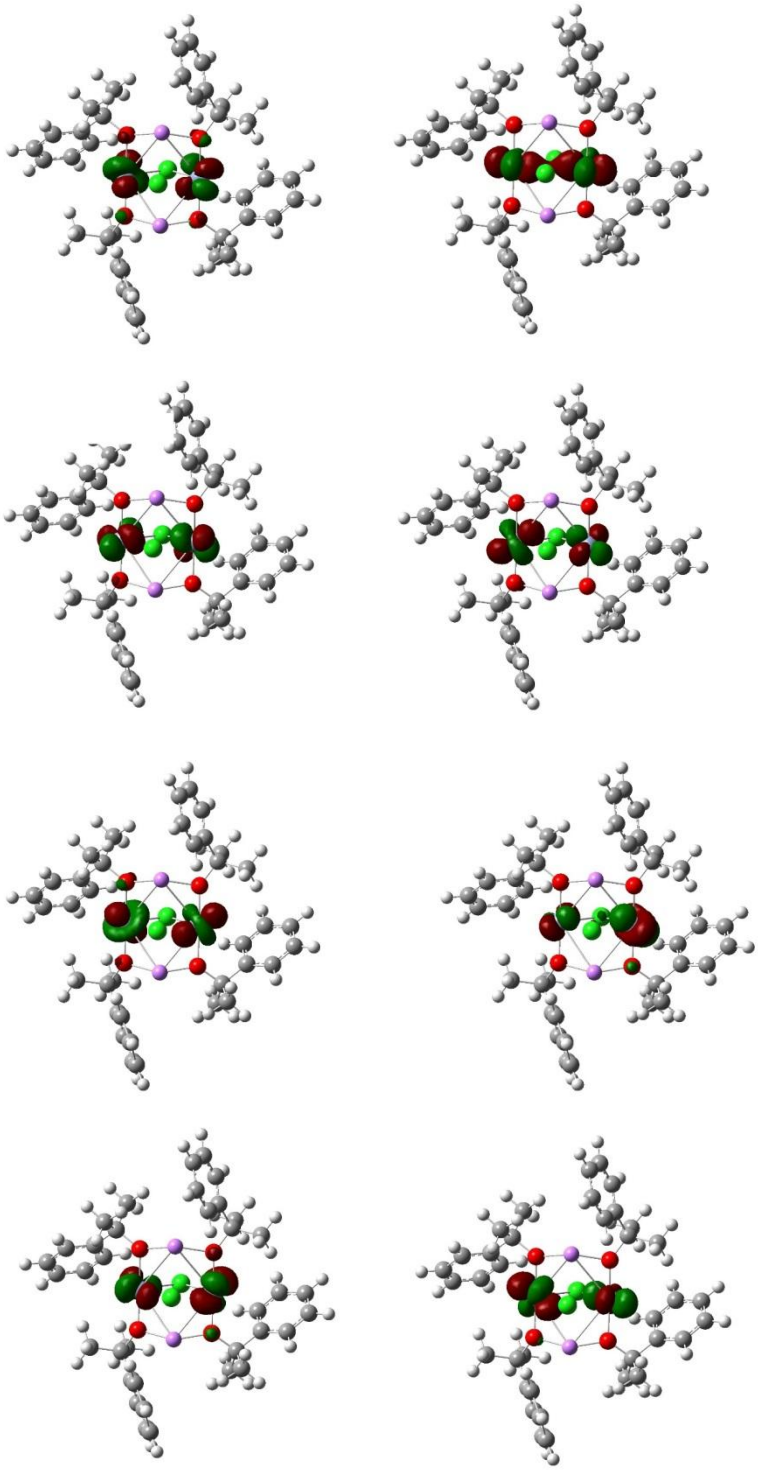

Figure B.32. Corresponding orbital analysis for **4**.

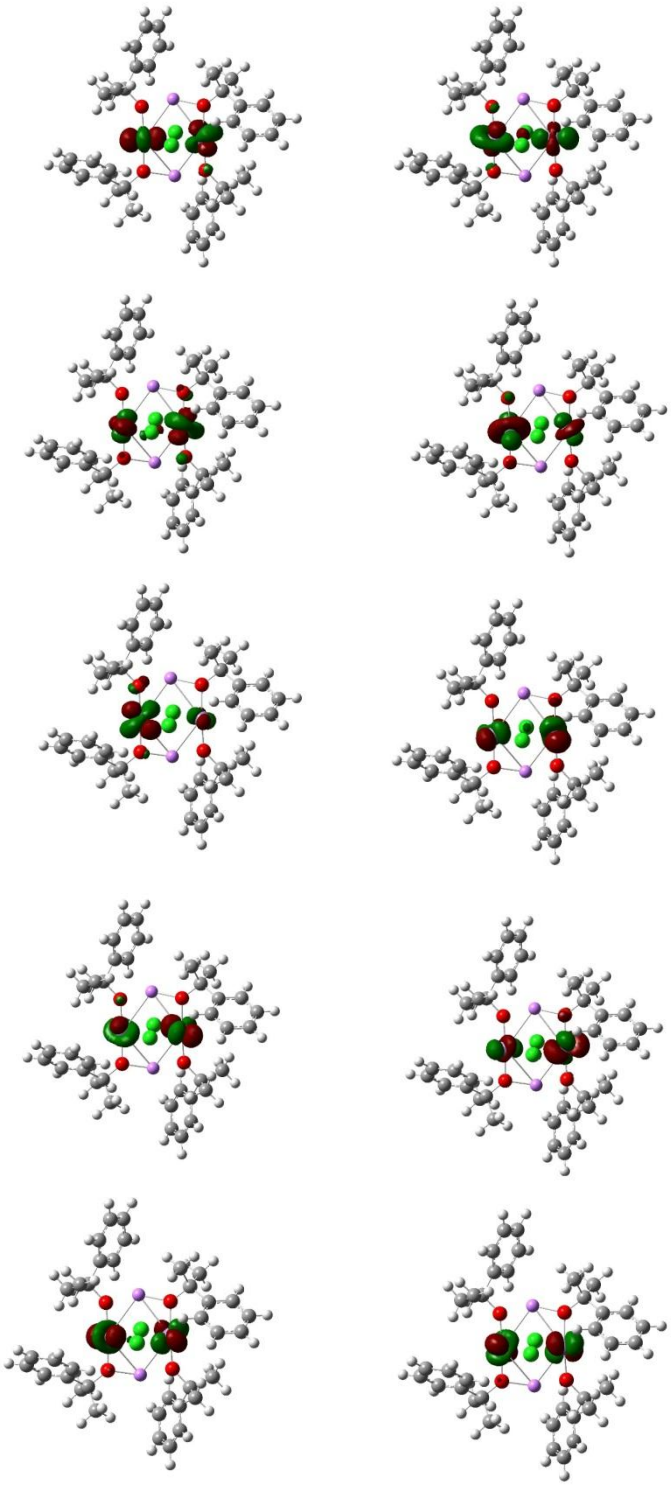

Figure B.33. Corresponding orbital analysis for **5**.

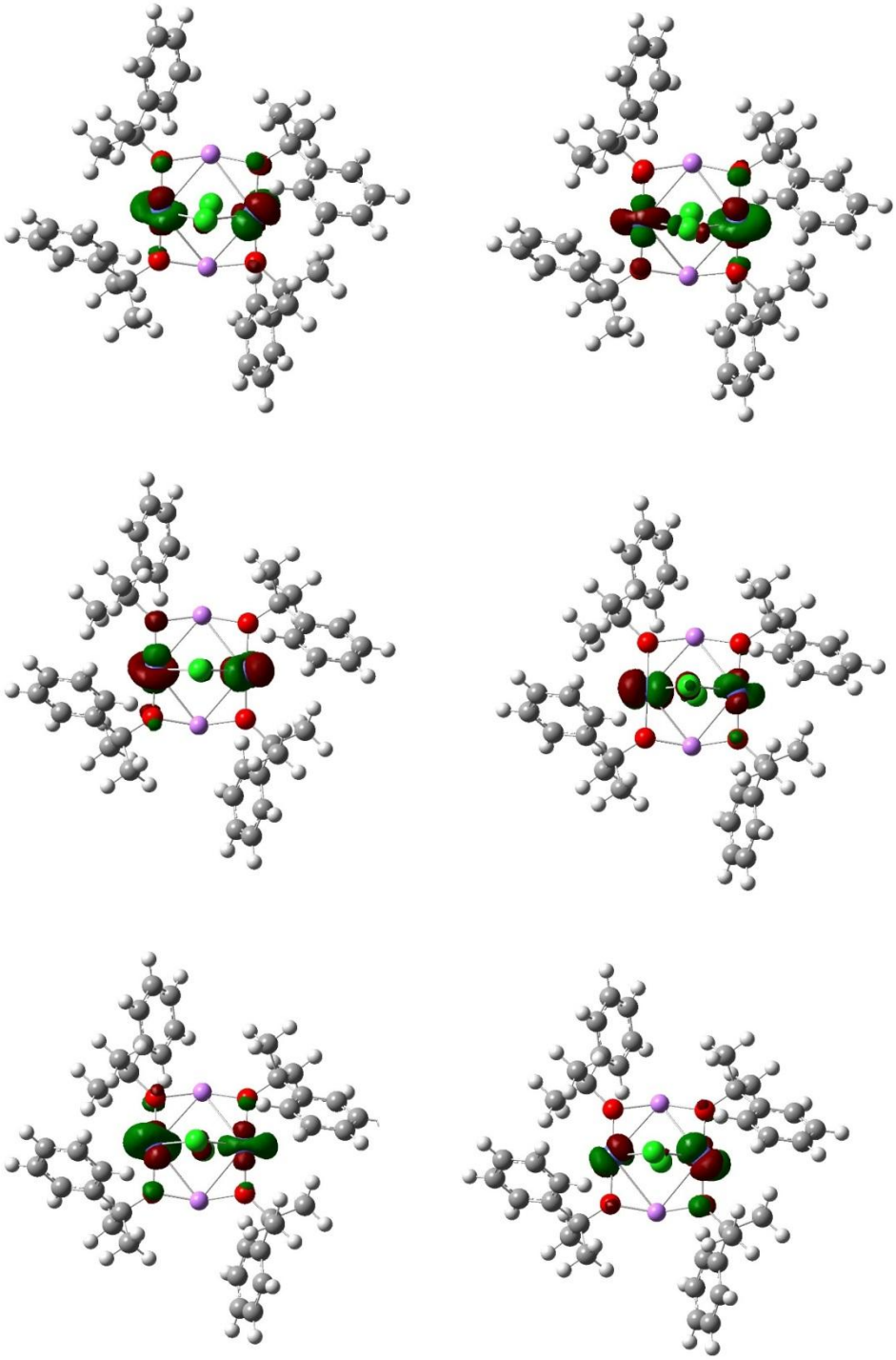

Figure B.34. Corresponding orbital analysis for **6**.

Canonical MOs

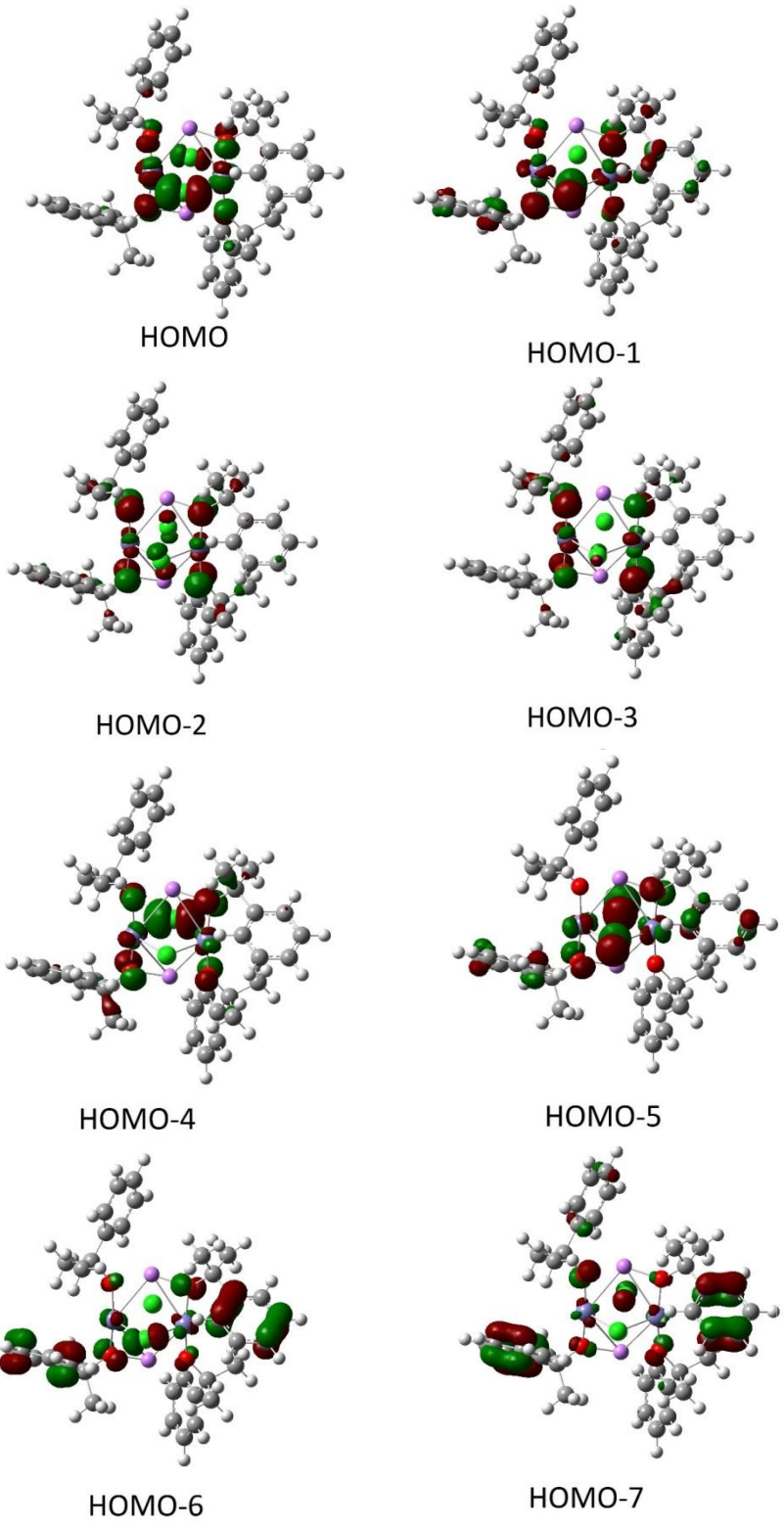

Figure B.35. Canonical molecular orbitals for **3**, HOMO-n (n from 0 to 7).

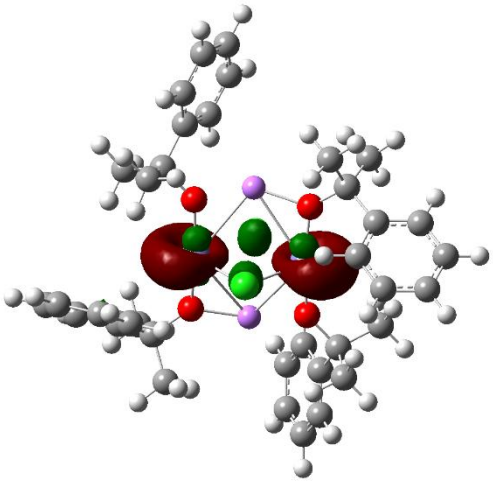

Figure B.36. LUMO for **3**, E(LUMO-HOMO) = 5.0 ev.

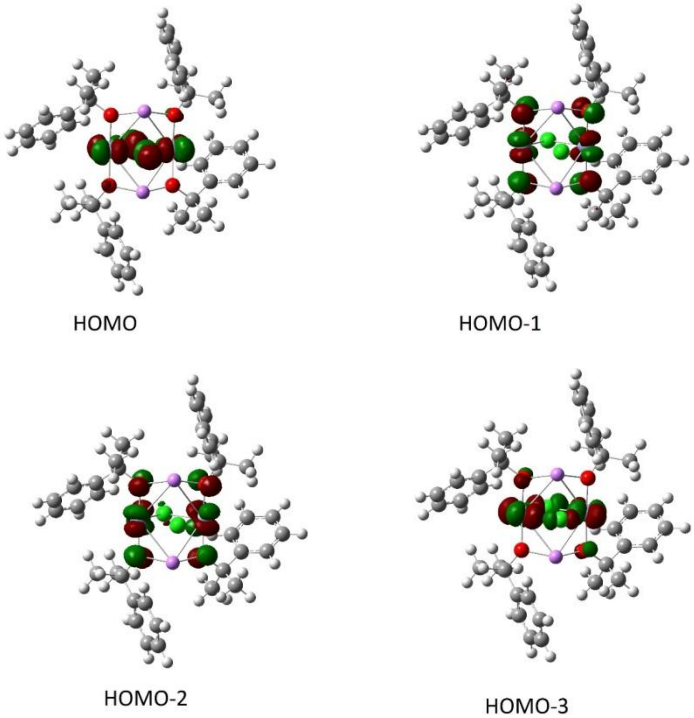

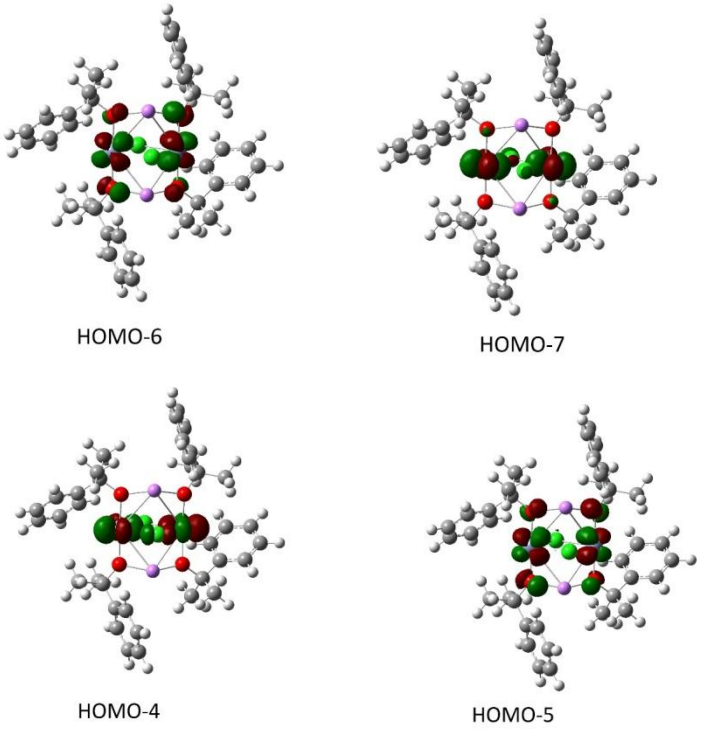

Figure B.37. Canonical molecular orbitals for **4**, HOMO-n (n from 0 to 7).

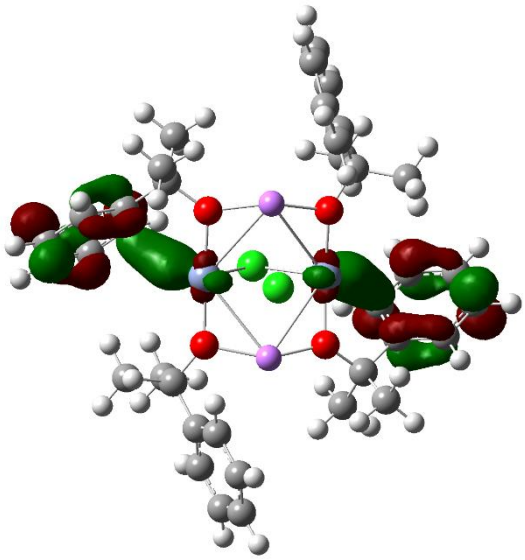

Figure B.38. LUMO for **4**, E(LUMO-HOMO) = 4.4 ev.

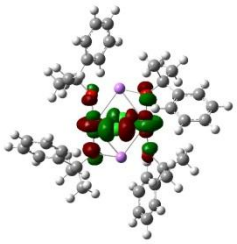

HOMO

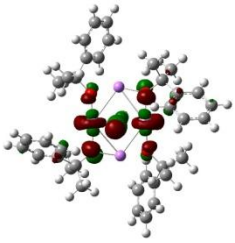

HOMO-1

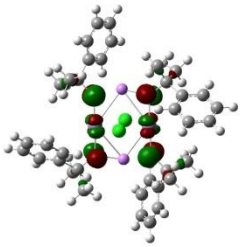

HOMO-2

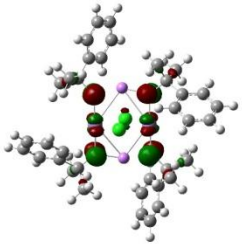

HOMO-3

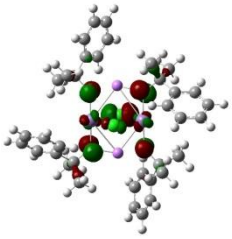

HOMO-4

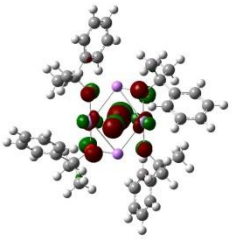

HOMO-5

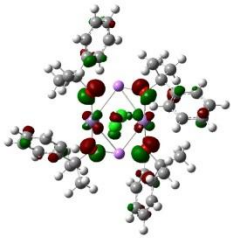

HOMO-6

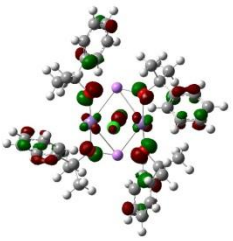

HOMO-7

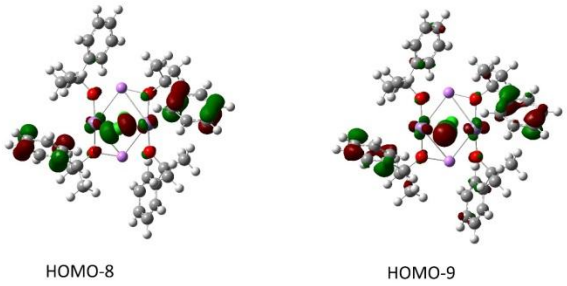

Figure B.39. Canonical molecular orbitals for **5**, HOMO-n (n from 0 to 9).

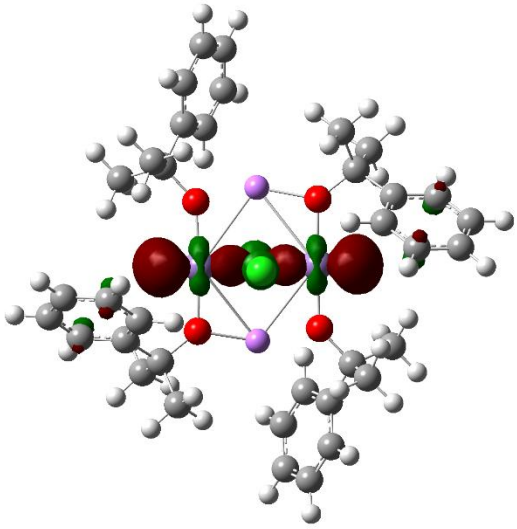

Figure B.40. LUMO for **5**, E(LUMO-HOMO) = 5.0 ev.

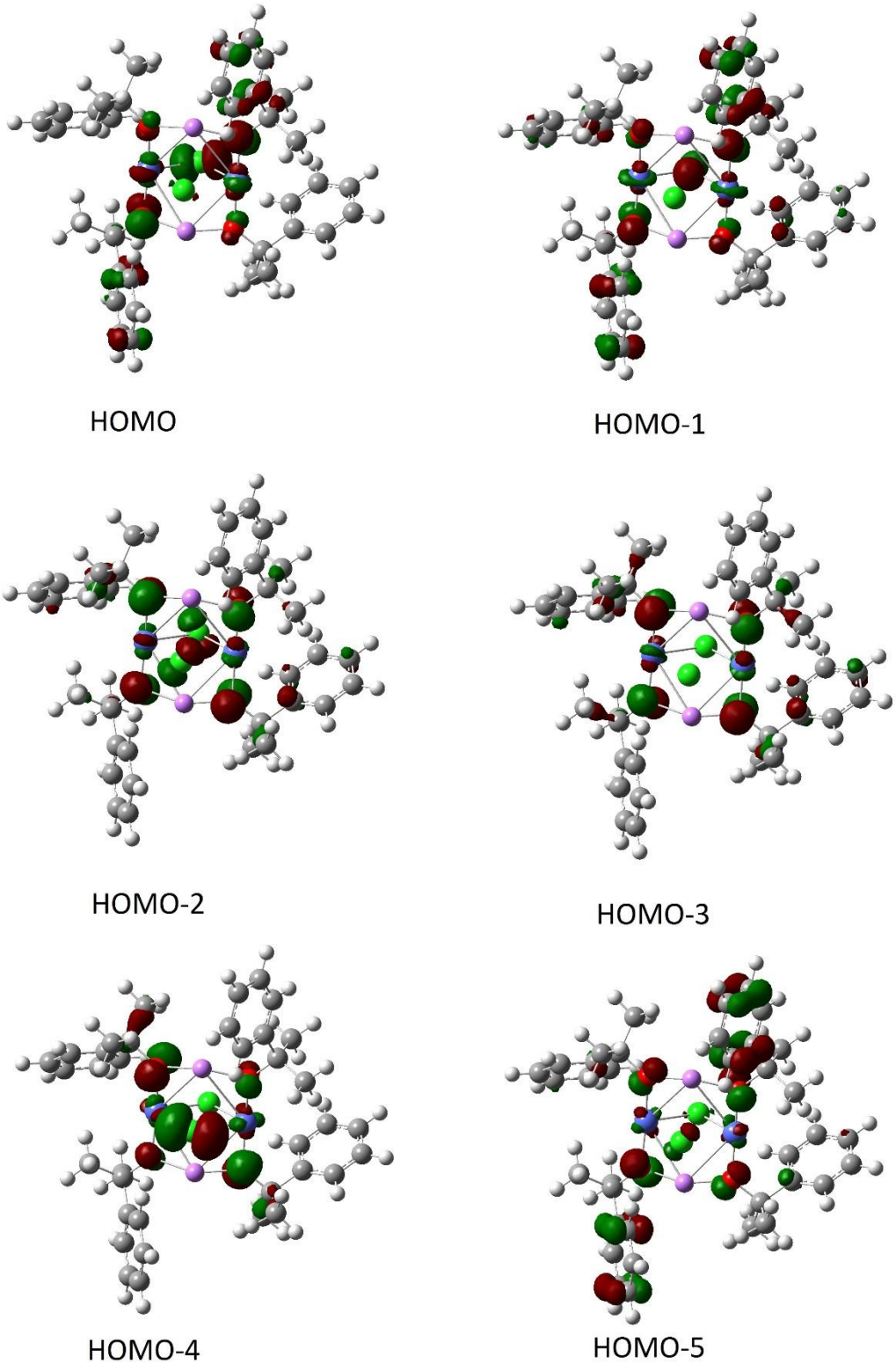

Figure B.41. Canonical molecular orbitals for **6** (HOMO-n (from 0 to 5)).

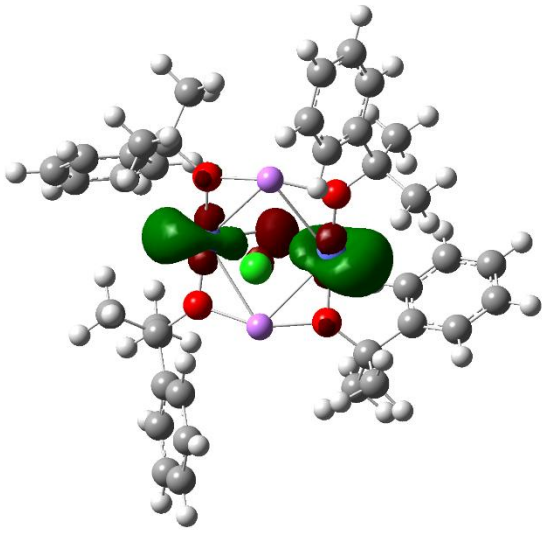

Figure B.42. LUMO for **6**, E(LUMO-HOMO) = 4.8 ev.

APPENDIX C: SUPPLEMENTARY MATERIAL FOR CHAPTER 3

1. Evans Method Formula and Procedure

The procedure for the Evans method is the same as that reported in Appendix B.

Table C.1. Spin-only magnetic moments calculated for **10**-**12** using the Evans method.

Complex	μ_{calc} (μ_B)	μ_{obs} (1) (μ_B)	μ_{obs} (2) (μ_B)	μ_{obs} (3) (μ_B)	μ_{obs} (average) (μ_B)
10	5.9	5.2	5.6	5.8	5.5 ± 0.3
11	4.9	4.8	4.4	4.9	4.7 ± 0.3
12	3.9	3.8	3.7	3.3	3.6 ± 0.3

2. NMR Spectra

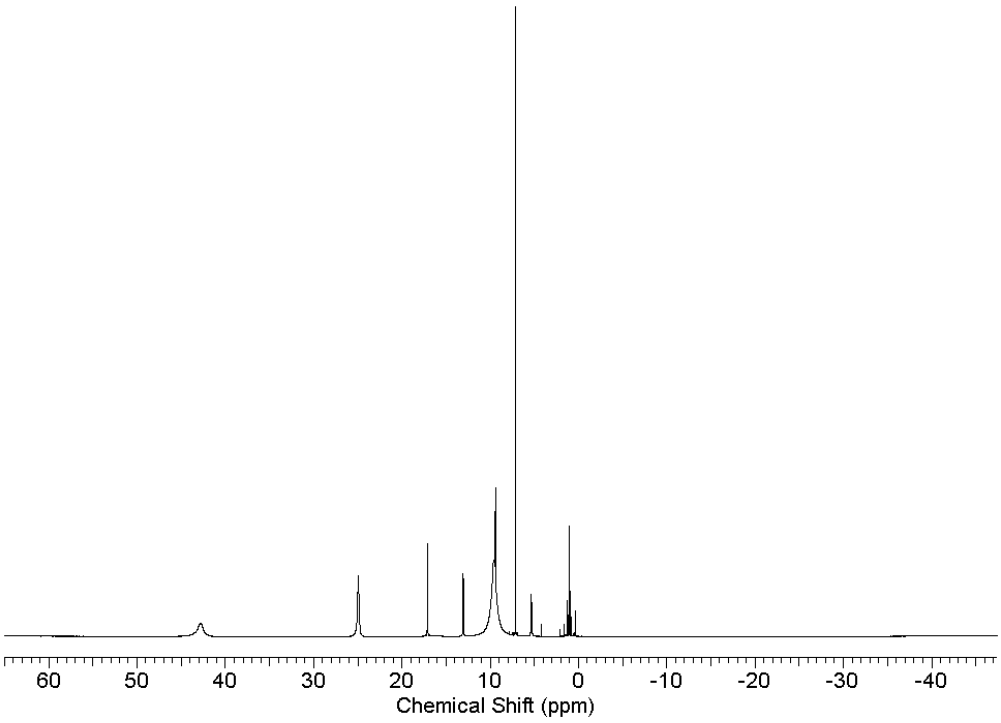

Figure C.1. ^{1}H NMR spectrum of **12**.

3. IR Spectra

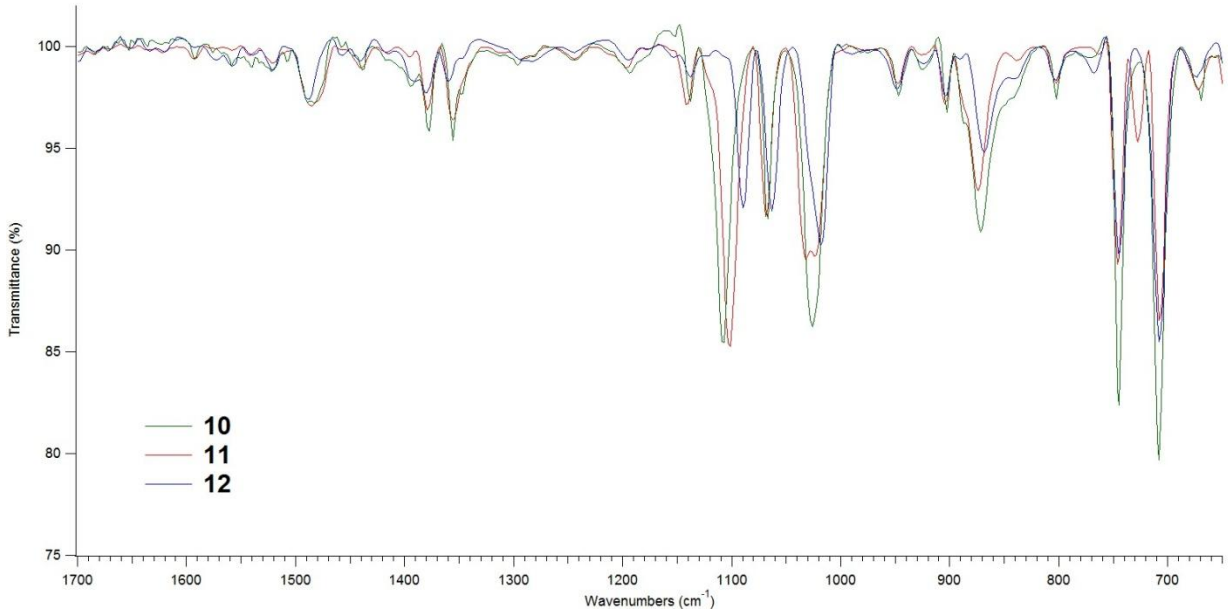

Figure C.2. IR spectra of $M(OR)_2(THF)_2$ (**10**-**12**) in the 1700-650 range.

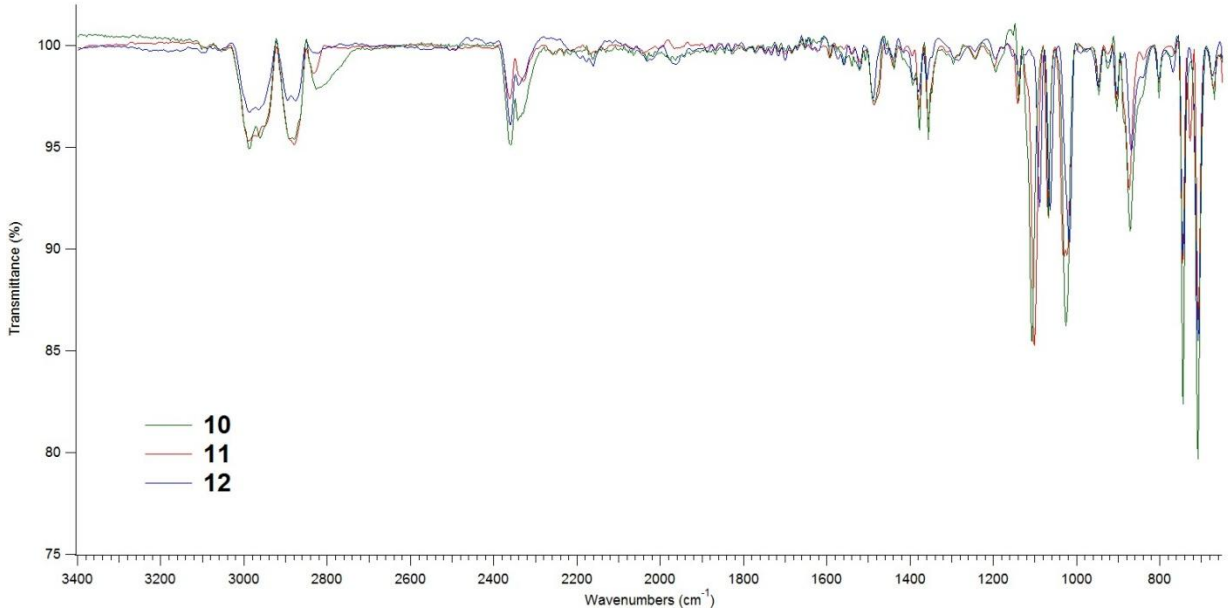

Figure C.3. IR spectra of $M(OR)_2(THF)_2$ (**10**-**12**) in 3400-650 cm^{-1} range.

4. UV-vis Spectra

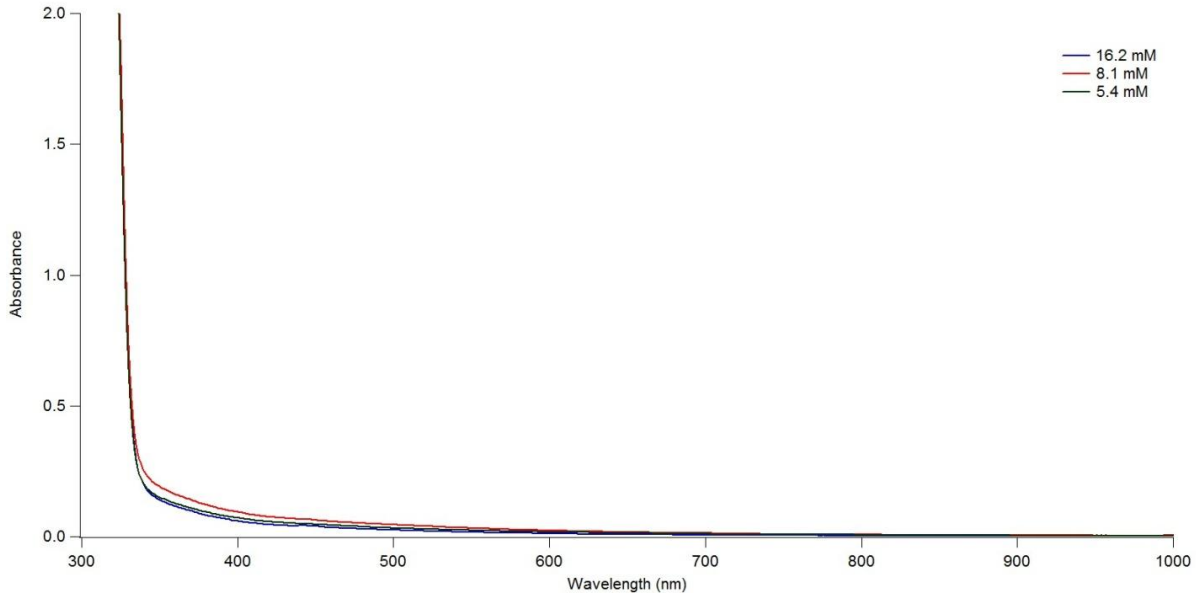

Figure C.4. UV-vis spectrum for **10** ($Mn(OR)_2(THF)_2$) at three different concentrations.

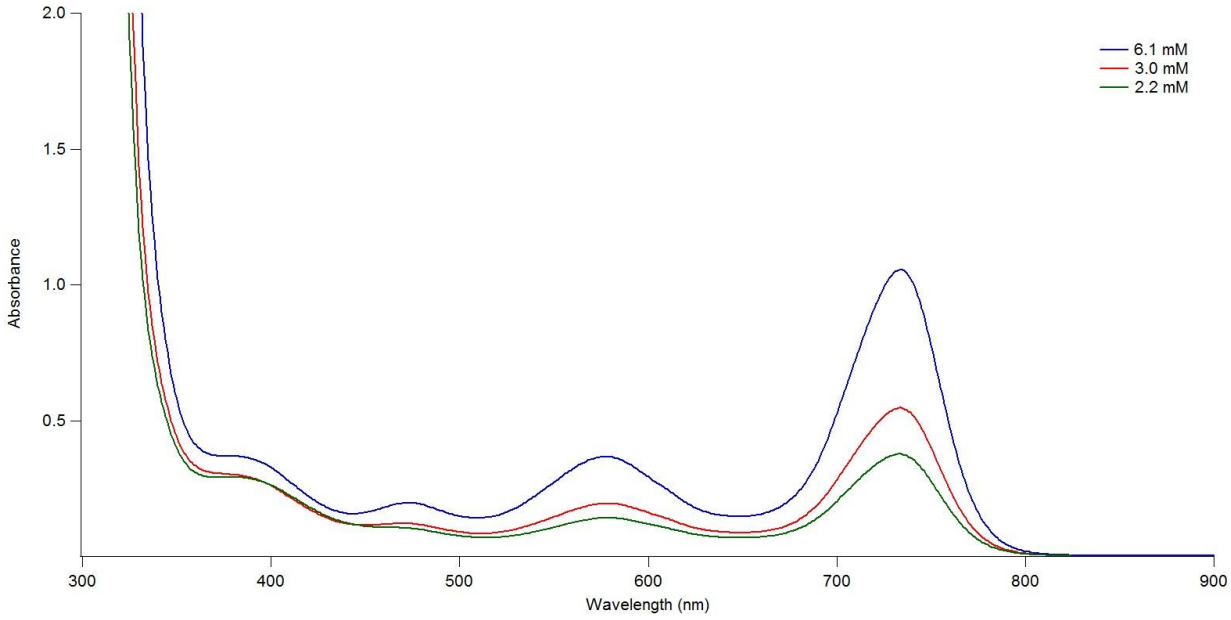

Figure C.5. UV-vis spectrum for **12** ($Co(OR)_2(THF)_2$) at three different concentrations. λ_{max} (ε_M): 734 (176), 578 (64), 472 (40), 386 (98).

APPENDIX D: SUPPLEMENTARY MATERIAL FOR CHAPTER 4

1. Evans Method Formula and Procedure

The procedure for the Evans method is the same as that reported in Appendix B.

Table D.1. Spin-only magnetic moments calculated for **13** using the Evans method.

Complex	μ_{calc} (μ_B)	μ_{obs} (1) (μ_B)	μ_{obs} (2) (μ_B)	μ_{obs} (average) (μ_B)
13	11.0	11.1	11.3	11.2 ± 0.2

2. IR Spectra

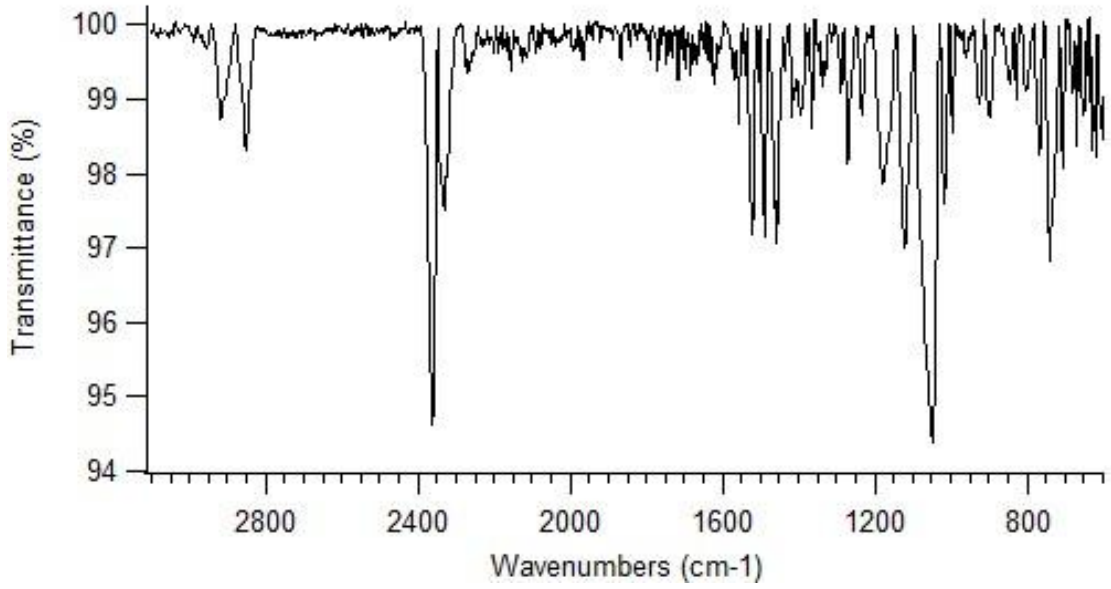

Figure D.1. IR spectrum of **13**.

3. Computational Details

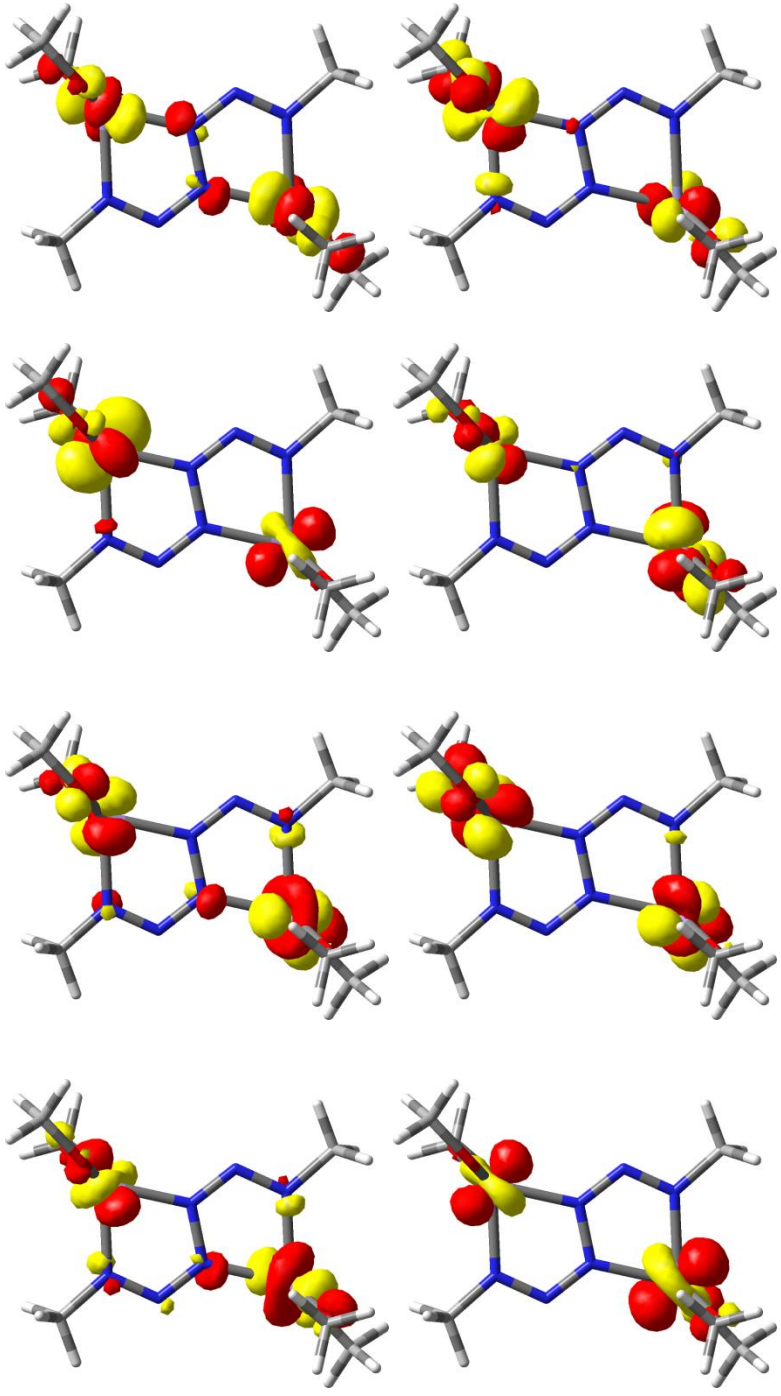

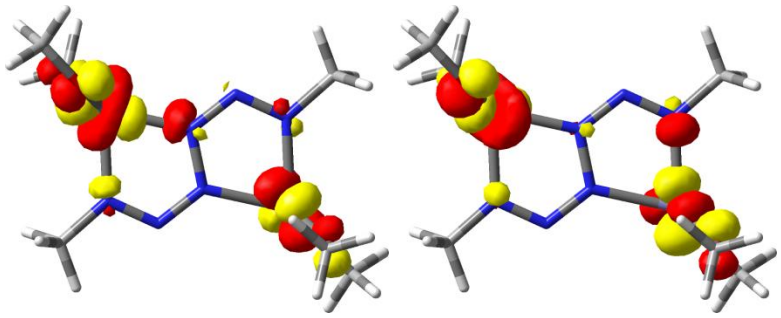

Figure D.2. Corresponding orbital analysis for the *S* = 10/2 hexazene complex. All orbitals are singly occupied.

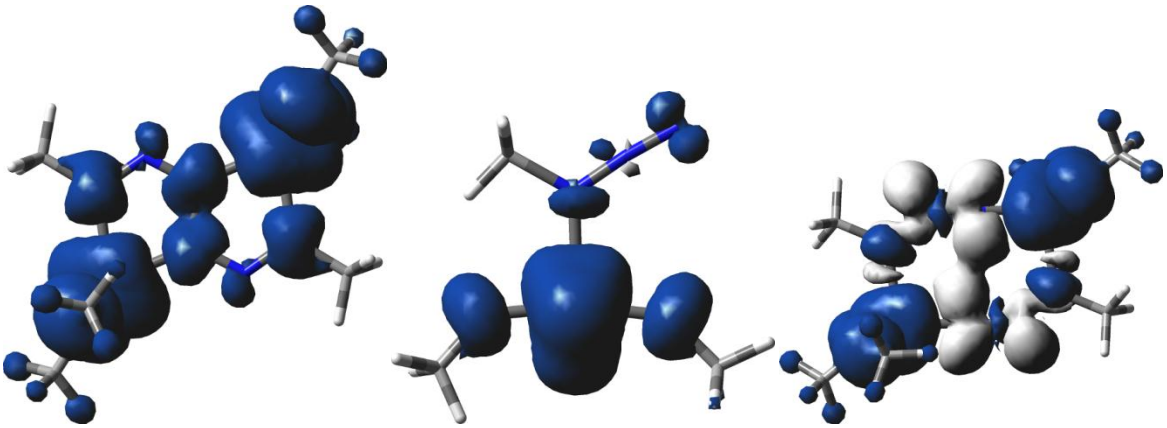

Figure D.3. Spin density isosurface plots for the hexazene (left), monomeric azide compound (middle), and dimer (right). The lack of spin density at the azide for the monomer, but not the dimer, demonstrates that the azide is only reduced in the latter.

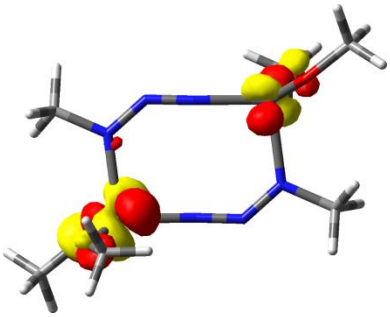

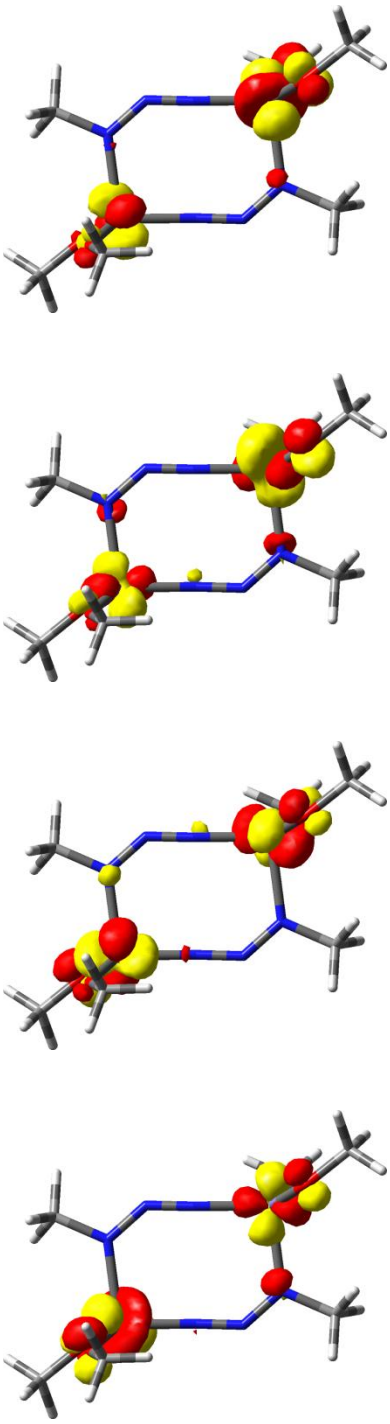

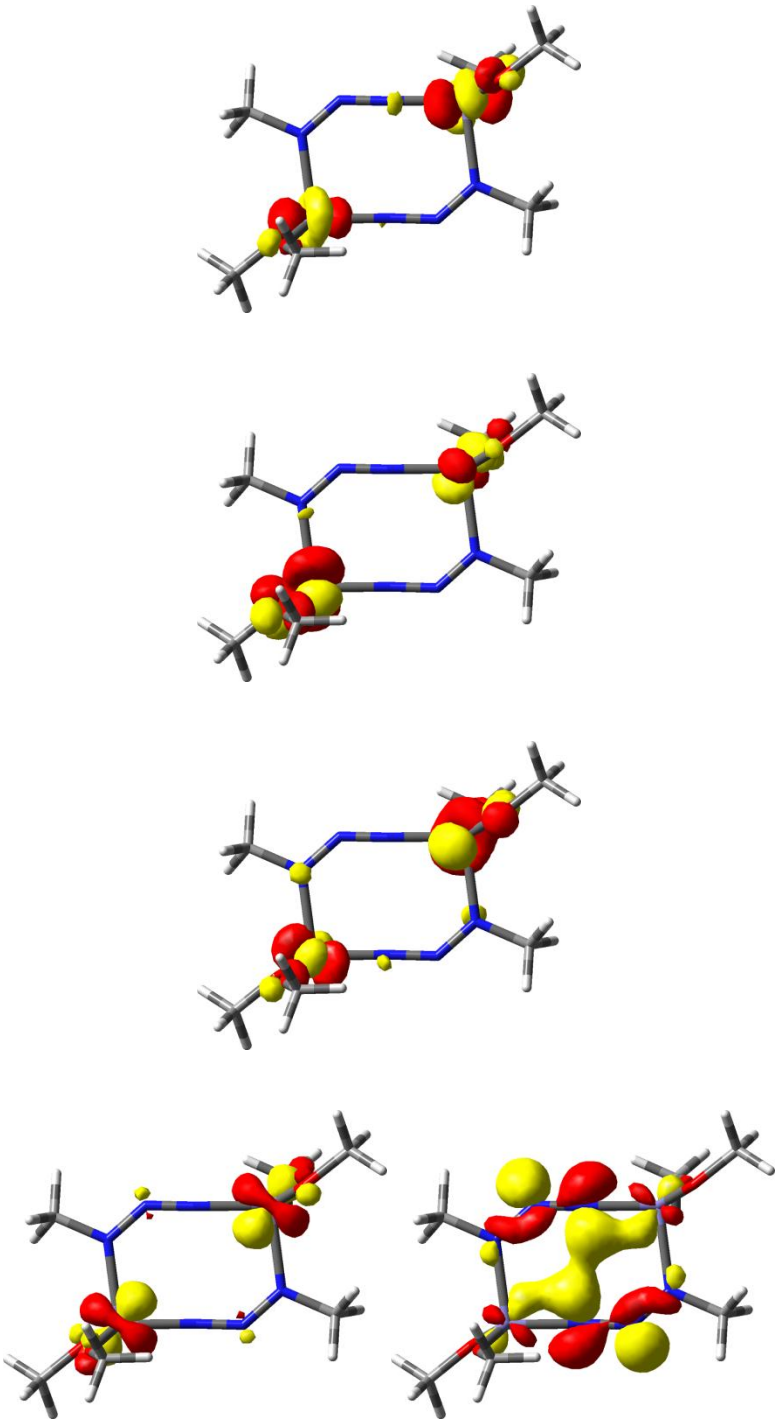

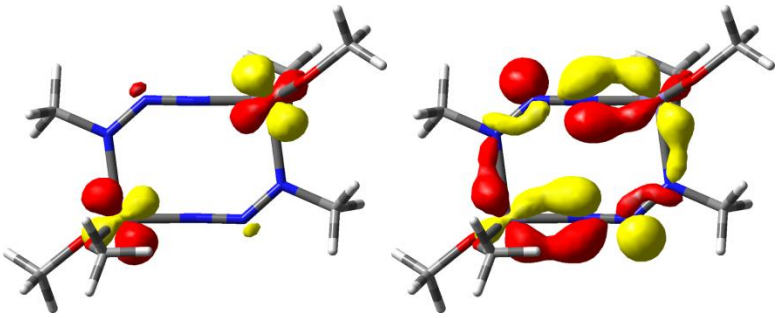

Figure D.4. Corresponding orbital analysis for the *S* = 8/2 diazide complex. Singly occupied orbitals are shown with one orbital per line, while the two antiferromagnetically coupled orbitals are shown with the α orbital on the left and the β orbital on the right.

Table D.2. Comparison of reaction thermodynamics (in kcal/mol) with the B3LYP, BLYP, OLYP, and OPBE functionals. Energies include def2TZVP single point energy refinements and are done at the B3LYP optimized geometries. The latter functionals based on OPTX, favored for energetics involving spin state changes, suggest that the dimer formation is favored by enthalpy and free energy.

	B3LYP	**BLYP**	**OLYP**	**OPBE**
Monomer->Dimer (ΔH)	–7.86	–26.78	–20.95	–23.02
Dimer -> Hexazene (ΔH)	–19.68	–2.63	–11.86	–18.83
Monomer -> Dimer (ΔG)	+8.61	–10.30	–4.48	–6.54
Dimer -> Hexazene (ΔG)	–14.99	+2.07	–7.16	–14.13

Table D.3. Energetics (E_h) for optimized species based on **13**.

Species	Spin (*S*)	H(gas)	G(gas)
hexazene	0/2	-1115.386207	-1115.468844
hexazene	2/2	-1115.380204	-1115.465660
hexazene	4/2	-1115.405140	-1115.491427
hexazene	6/2	-1115.422988	-1115.509344
hexazene	8/2	-1115.431387	-1115.521798
hexazene	10/2	-1115.434023	-1115.526747
monomer (N-terminal)	2/2	-557.650304	-557.711549
monomer (N-terminal)	4/2	-557.687716	-557.751688
monomer (N-Me)	2/2	-557.657683	-557.747304
monomer (N-Me)	4/2	-557.696027	-557.759257
dimer	0/2	-1115.313177	-1115.402460
dimer	2/2	Re-optimized to hexazene structure	
dimer	4/2	-1115.349138	-1115.439409
dimer	6/2	-1115.367323	-1115.461497
dimer	8/2	-1115.398485	-1115.498692
dimer	10/2	Re-optimized to hexazene structure	

APPENDIX E: SUPPLEMENTARY MATERIAL FOR CHAPTER 5

1. Evans Method Formula and Procedure

The procedure for the Evans method is the same as that reported in Appendix B.

Table E.1. Spin-only magnetic moments calculated for **14-18** using the Evans method.

Complex	μ_{calc} (μ_B)	μ_{obs} (1) (μ_B)	μ_{obs} (2) (μ_B)	μ_{obs} (3) (μ_B)	μ_{obs} (average) (μ_B)
14	5.9	6.5	6.1	6.3	6.3 ± 0.2
15	4.9	4.8	4.9	5.0	4.9 ± 0.1
16	4.0	3.8	3.9	3.7	3.8 ± 0.1
17	4.0	5.0	4.6	4.9	4.8 ± 0.2
18	4.0	4.6	4.5	4.4	4.5 ± 0.1

2. IR Spectra

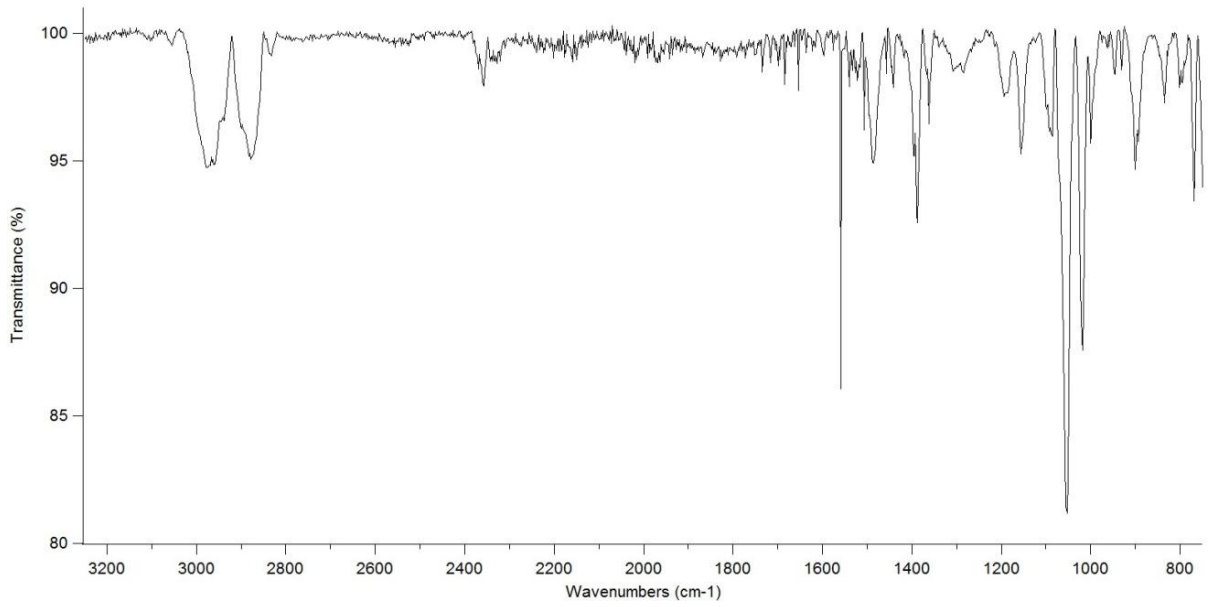

Figure E.1. IR spectrum of $Fe(OR)_3$, **14**.

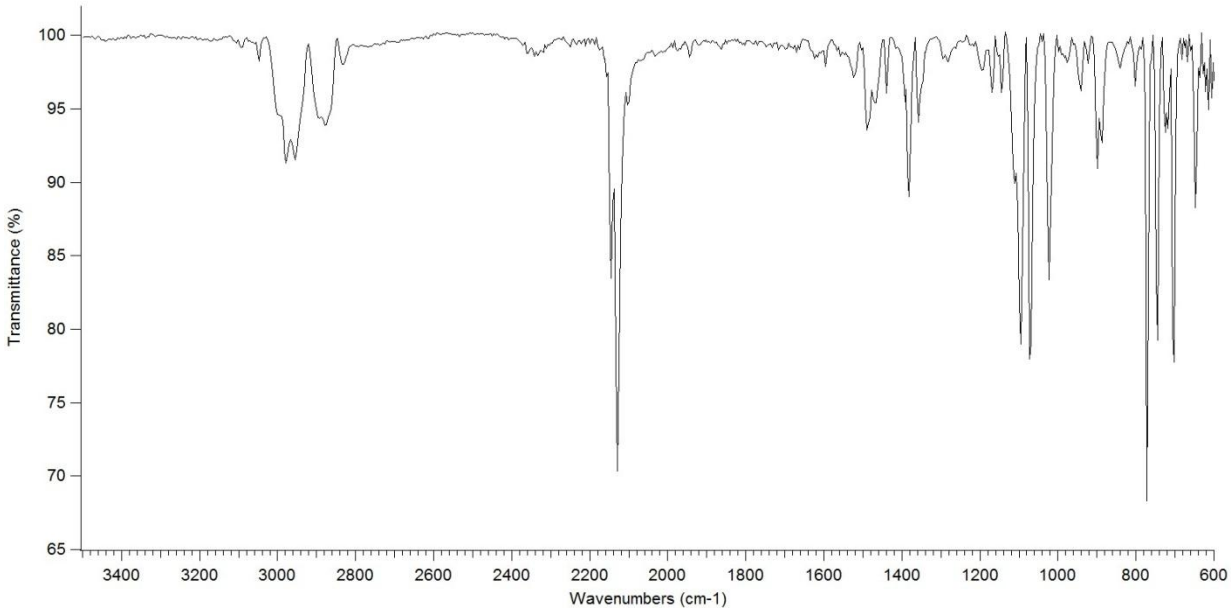

Figure E.2. IR spectrum of $Fe(OR)_2(CNAr)_2$, **15.**

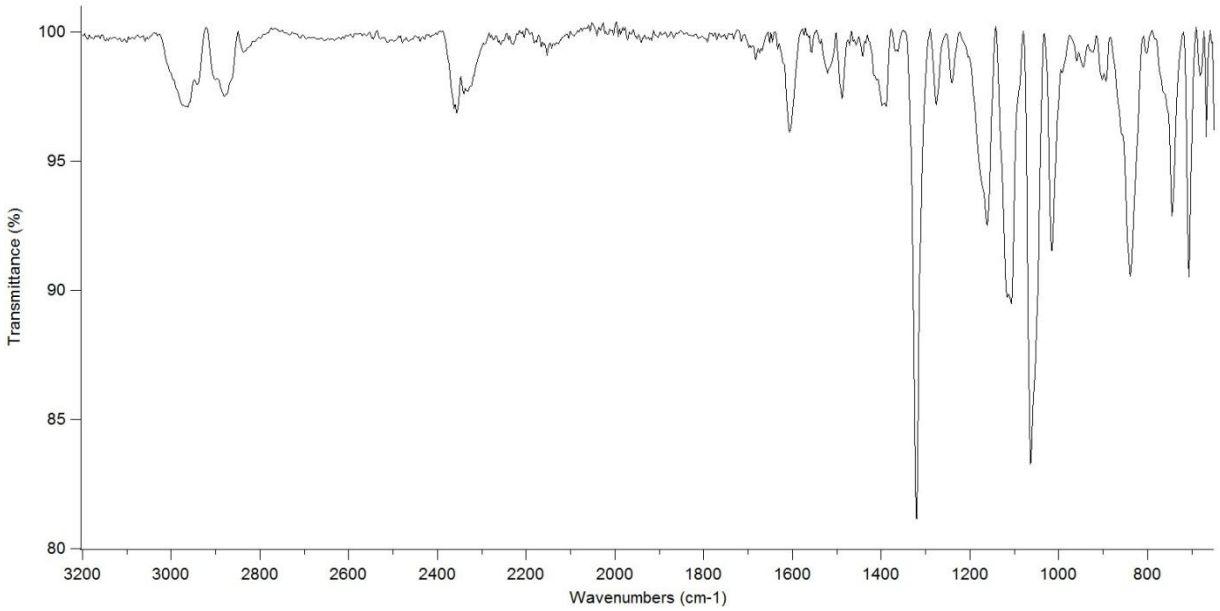

Figure E.3. IR spectrum of **16**.

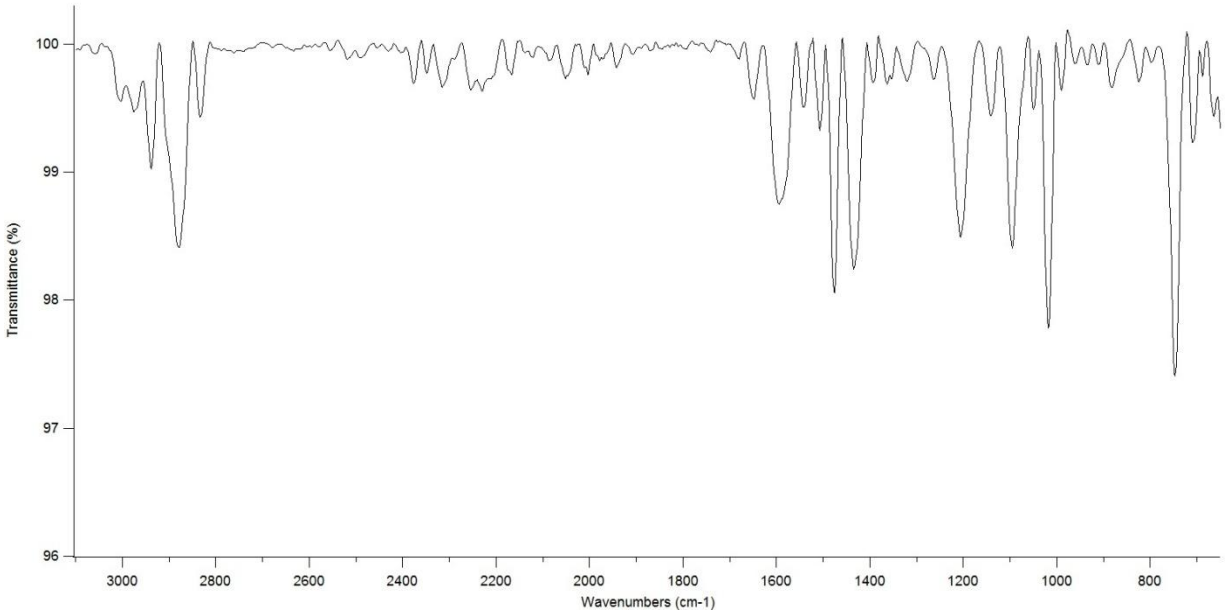

Figure E.4. IR spectrum of **17**.

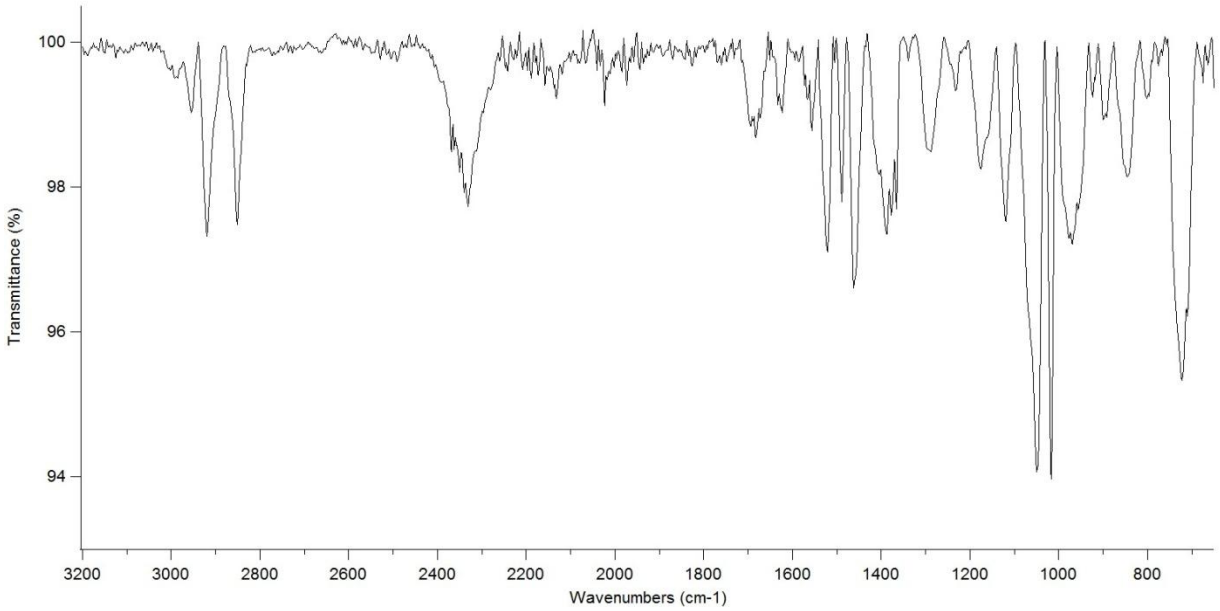

Figure E.5. IR spectrum of **18**.

3. NMR Spectra

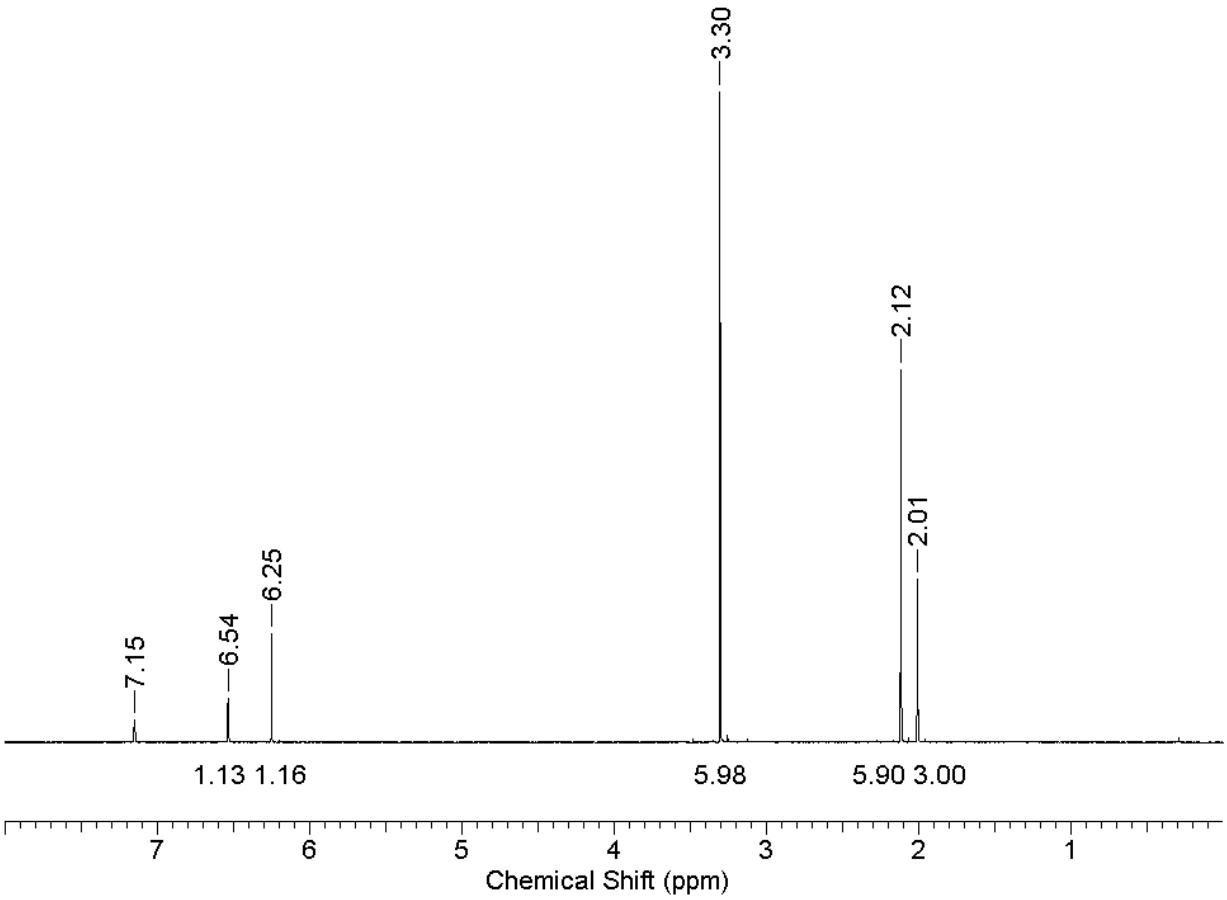

Figure E.6. ^{1}H NMR spectrum of 20 equivalents of mesityl azide with 1,3,5-trimethoxybenzene as an internal standard.

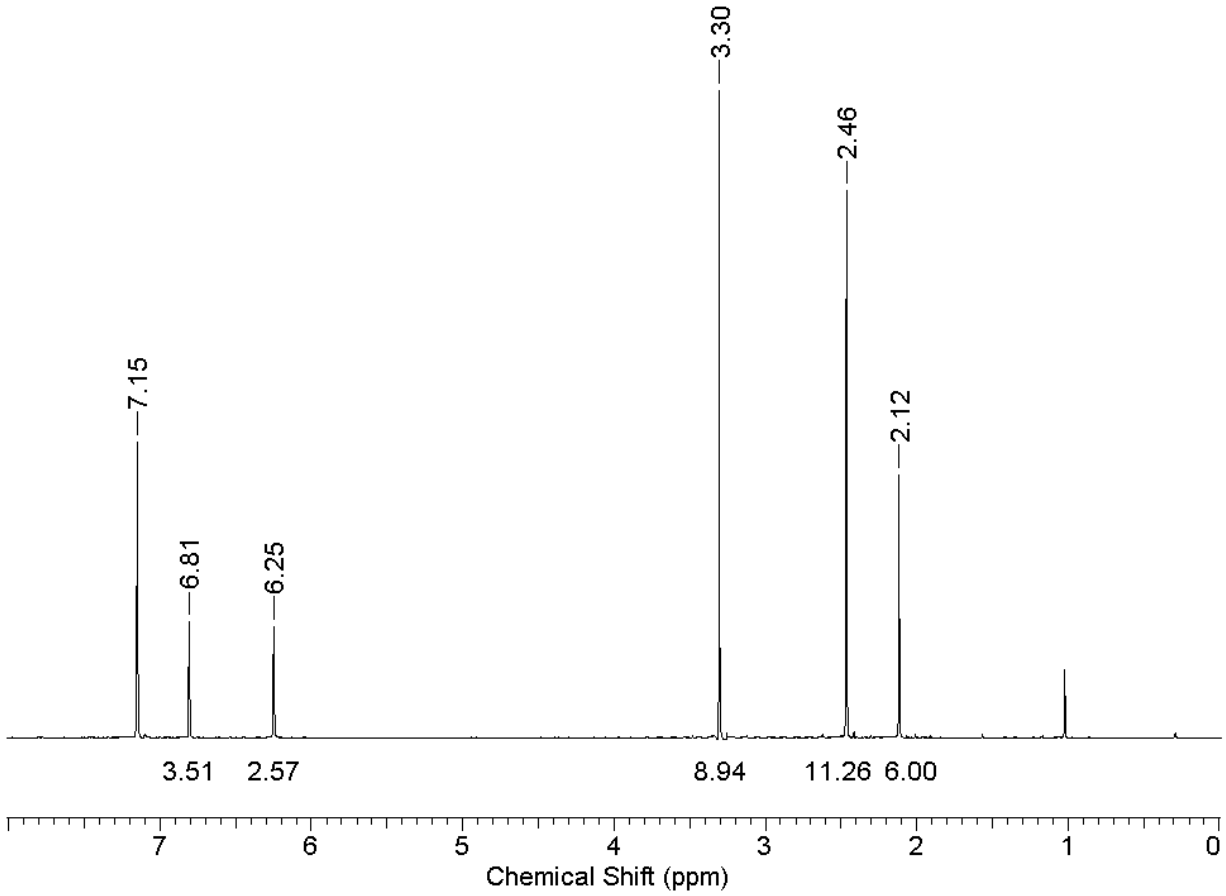

Figure E.7. ^{1}H NMR spectrum showing catalytic nitrene coupling from mesityl azide (5 mol % catalyst, internal standard and azoarene present).

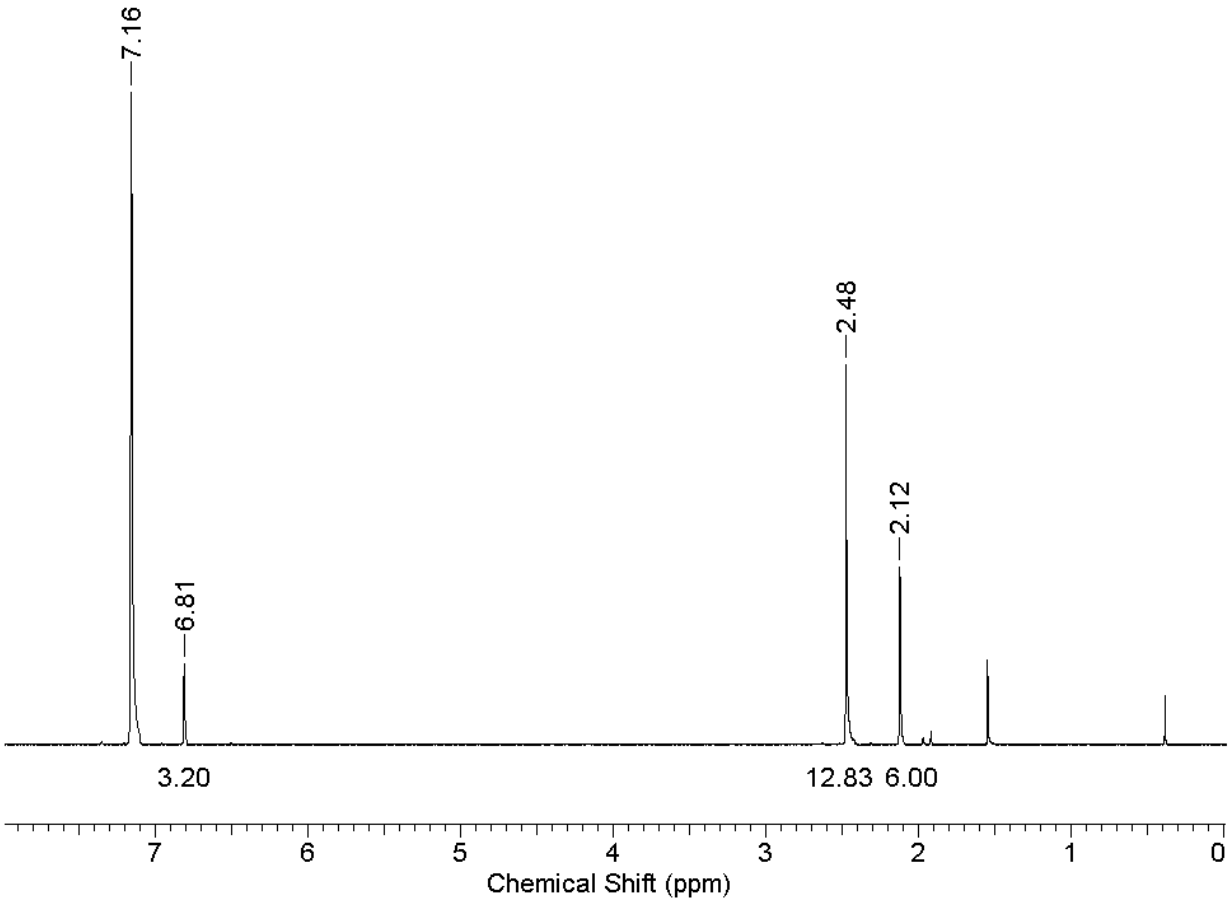

Figure E.8. ^{1}H NMR spectrum of isolated azomesitylene product (92% yield).

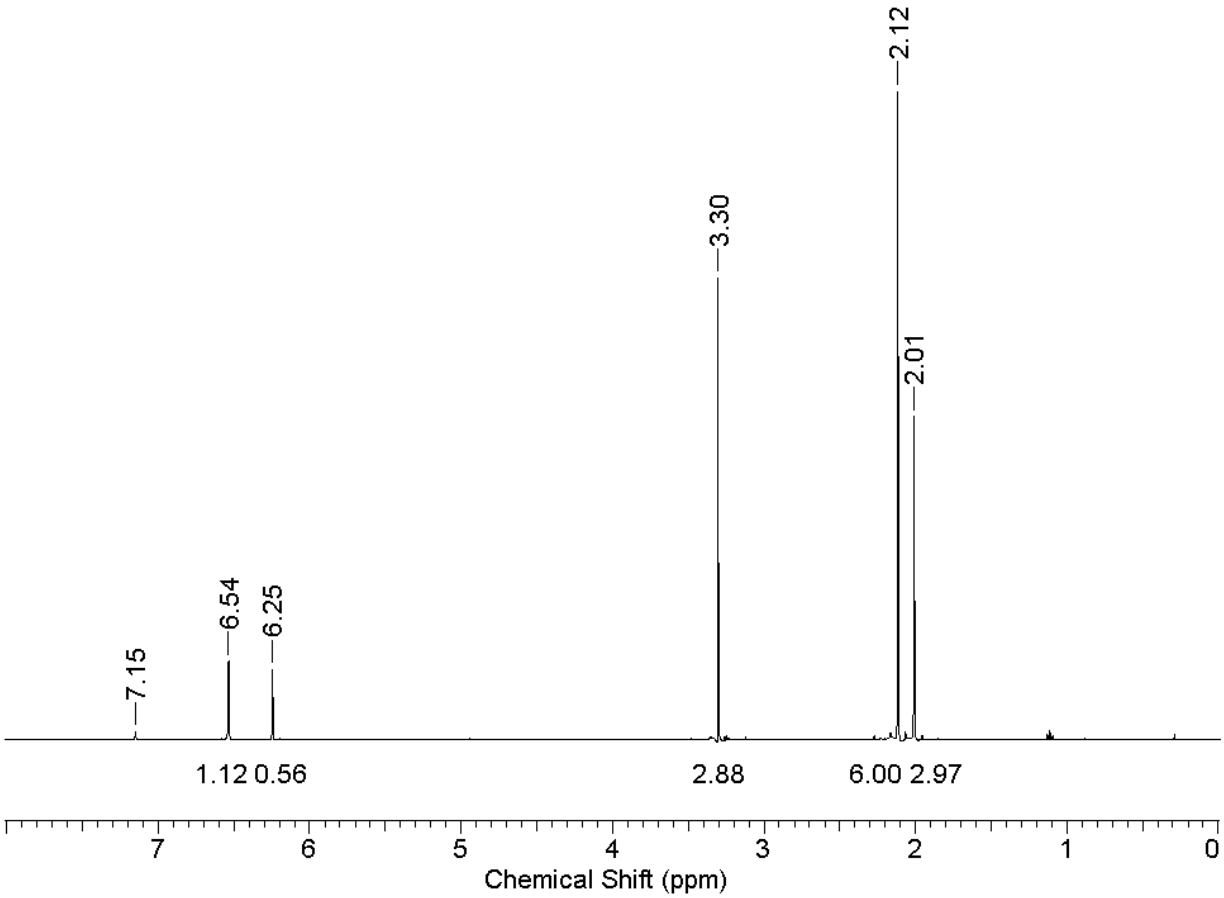

Figure E.9. ^{1}H NMR spectrum of 100 equivalents of mesityl azide with 1,3,5-trimethoxybenzene as an internal standard.

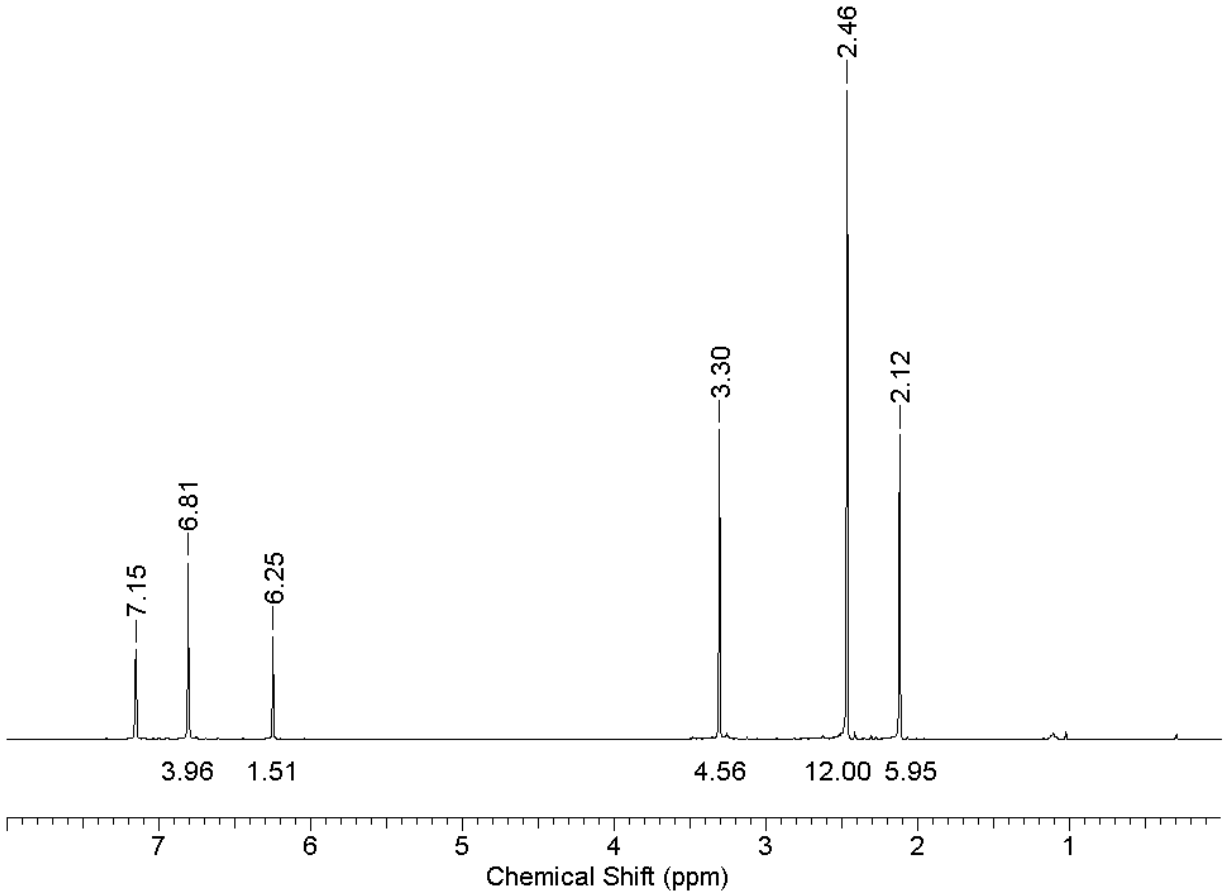

Figure E.10. ^{1}H NMR spectrum showing catalytic nitrene coupling from mesityl azide (1 mol % catalyst, internal standard and azoarene present).

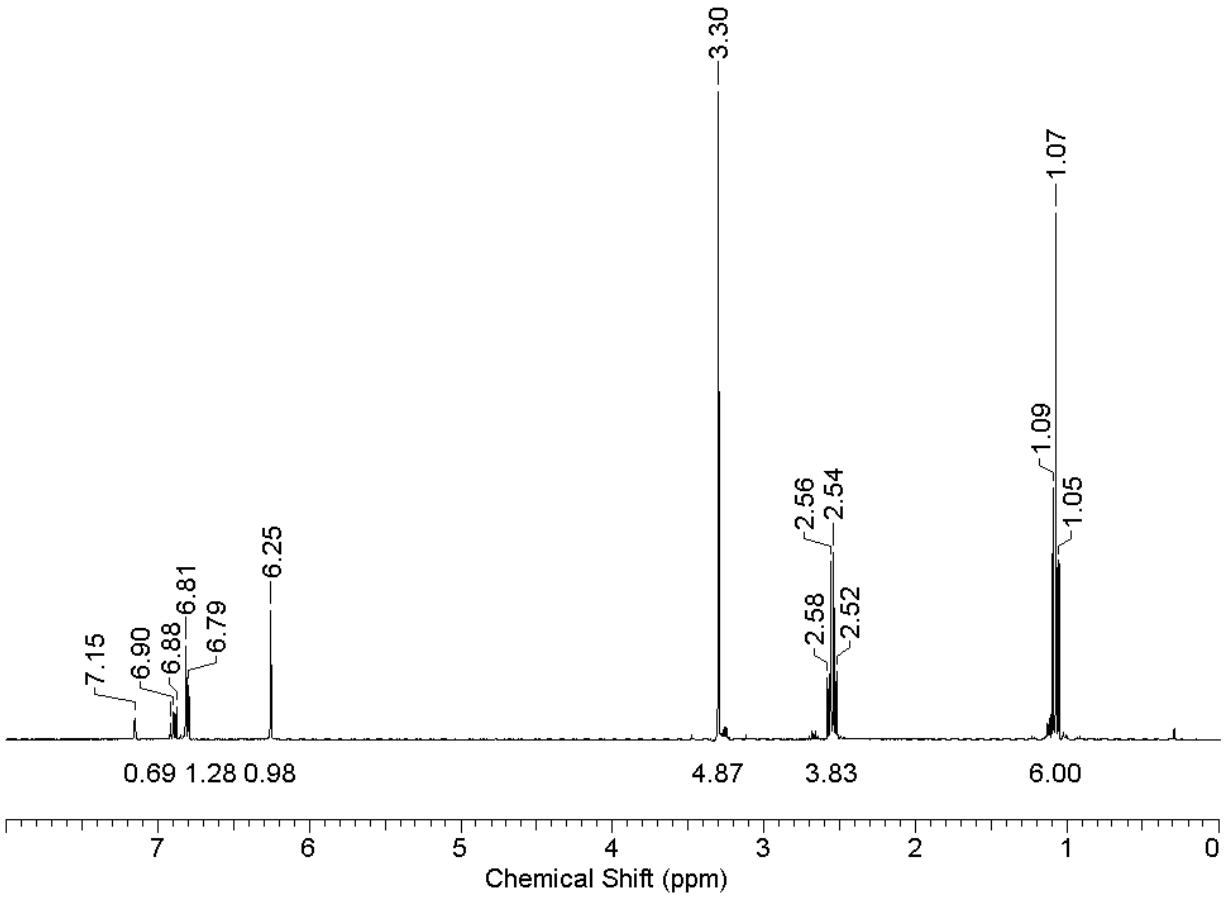

Figure E.11. ^{1}H NMR spectrum of 20 equivalents of 2,6-diethylphenyl azide with 1,3,5-trimethoxybenzene as an internal standard.

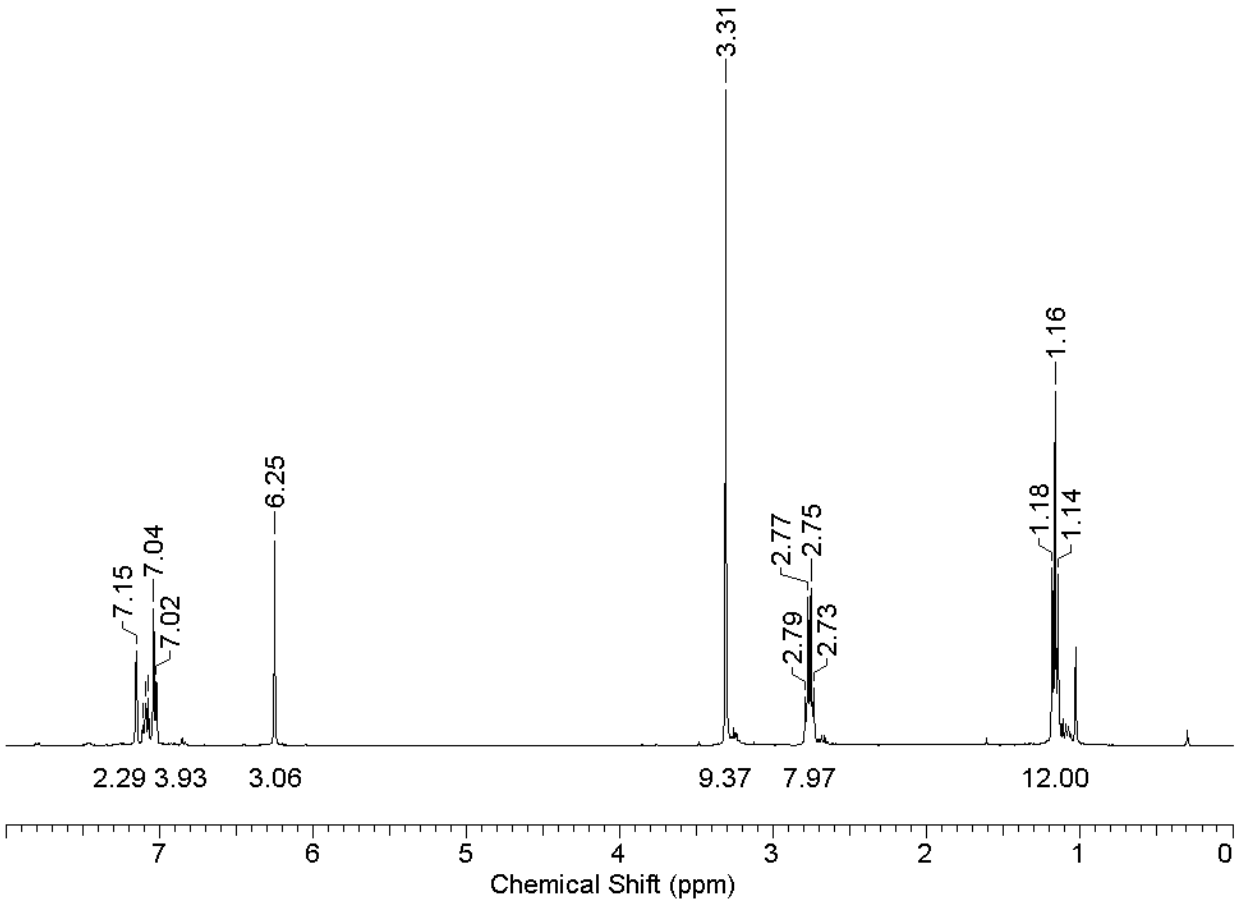

Figure E.12. ^{1}H NMR spectrum showing catalytic nitrene coupling from 2,6-diethylphenyl azide (5 mol % catalyst, internal standard and azoarene present).

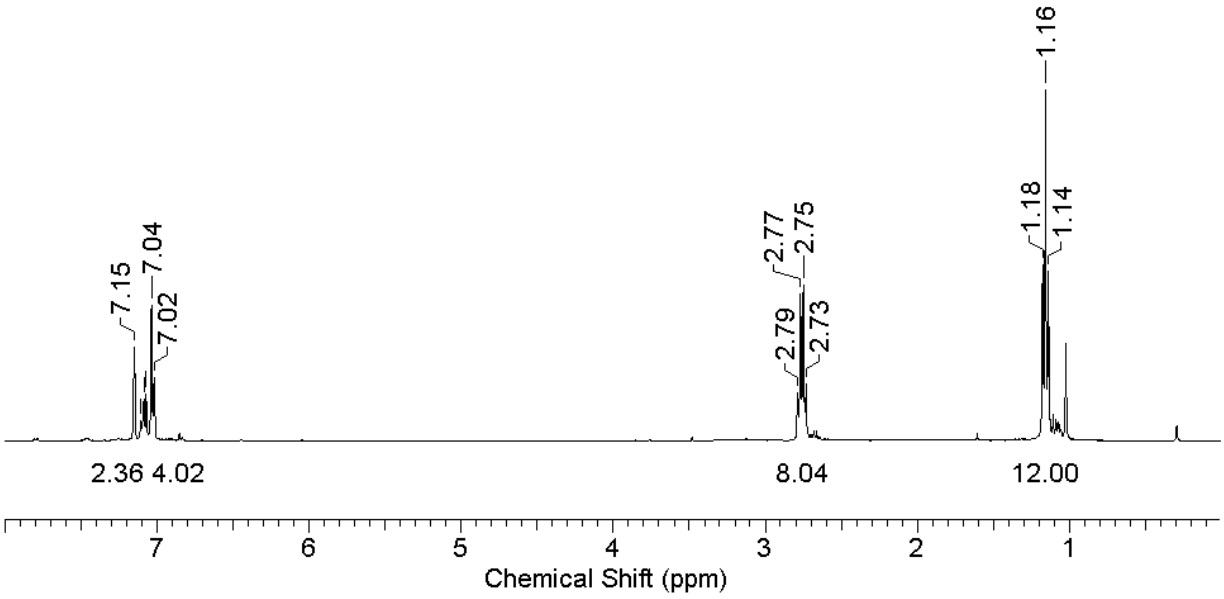

Figure E.13. ^{1}H NMR spectrum of isolated azo(2,6-diethylbenzene) product (93% yield).

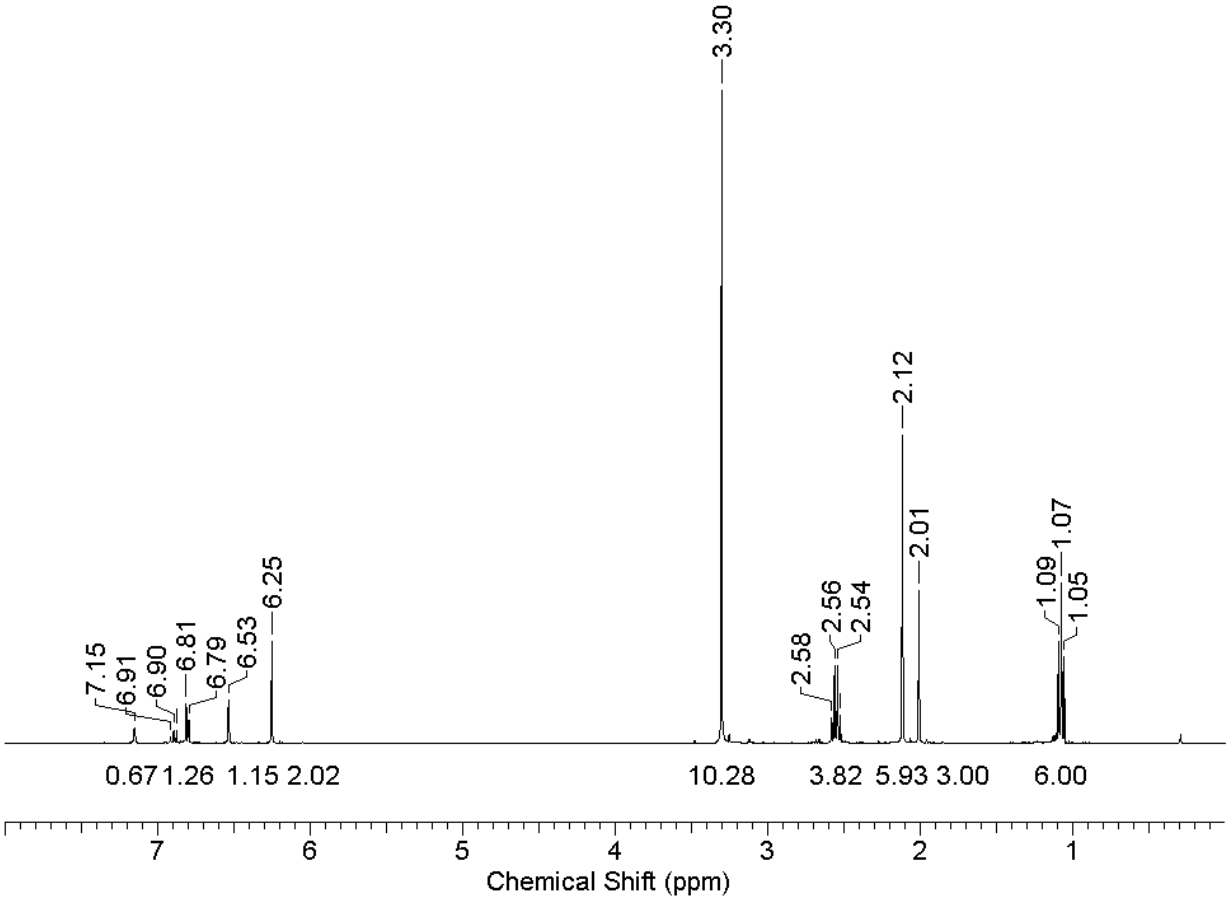

Figure E.14. [1]H NMR spectrum of 5 equivalents of mesityl azide and 5 equivalents of 2,6-diethylphenyl azide, with 1,3,5-trimethoxybenzene added as an internal standard.

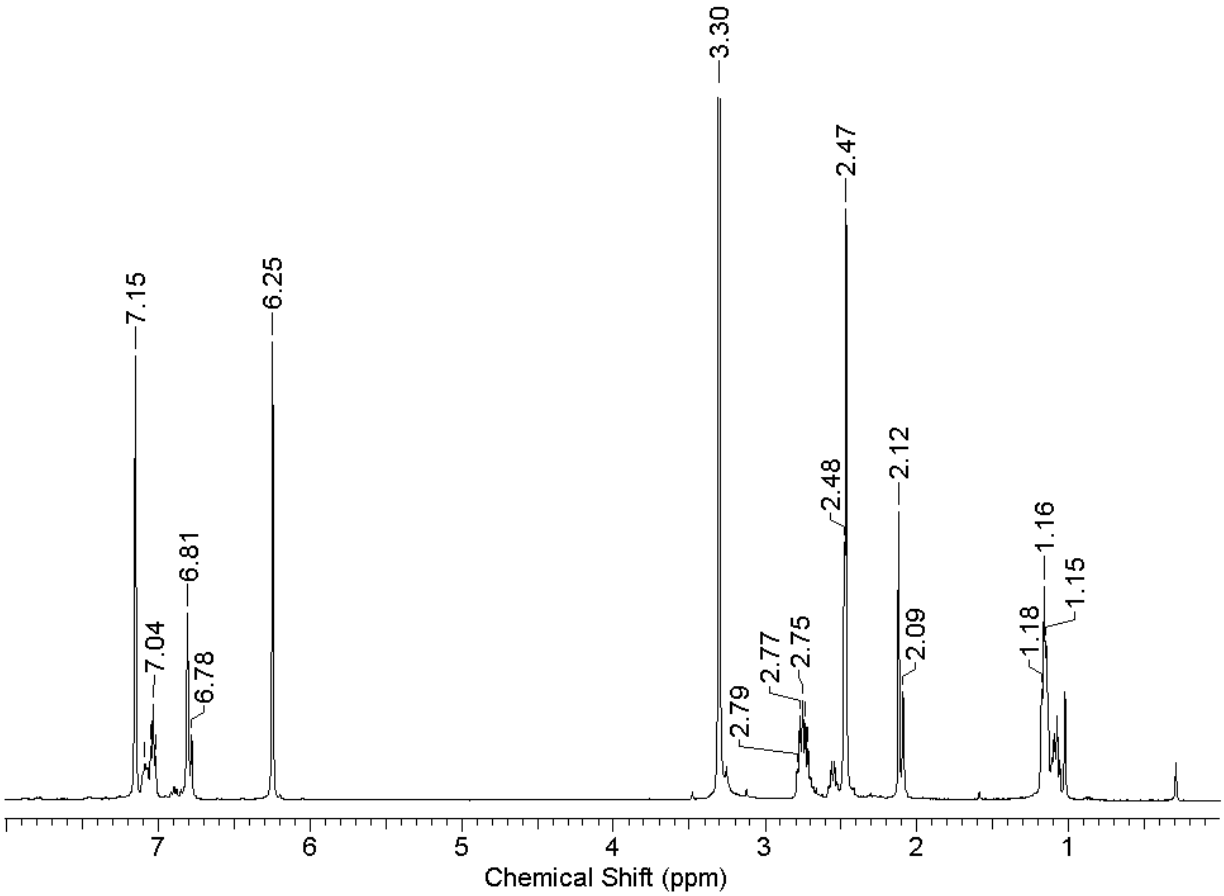

Figure E.15. [1]H NMR spectrum showing mixed catalytic nitrene coupling from mesityl azide and 2,6-diethylphenyl azide (5 mol % catalyst, 5 equivalents each) to form MesNNMes, DepNNMes, and DepNNDep.

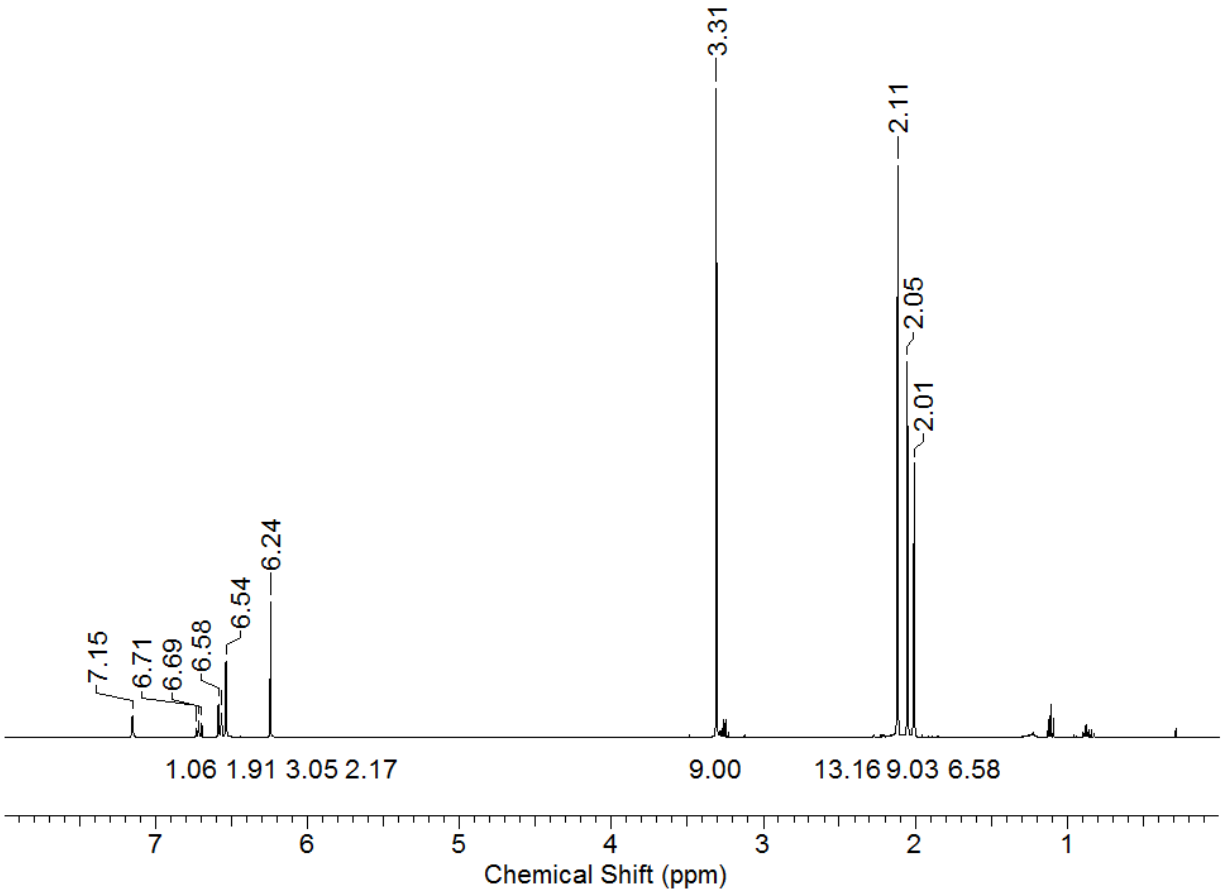

Figure E.16. ^{1}H NMR spectrum of 10 equivalents of mesityl azide and 10 equivalents of 2,6-dimethylphenyl isocyanide, with 1,3,5-trimethoxybenzene added as an internal standard.

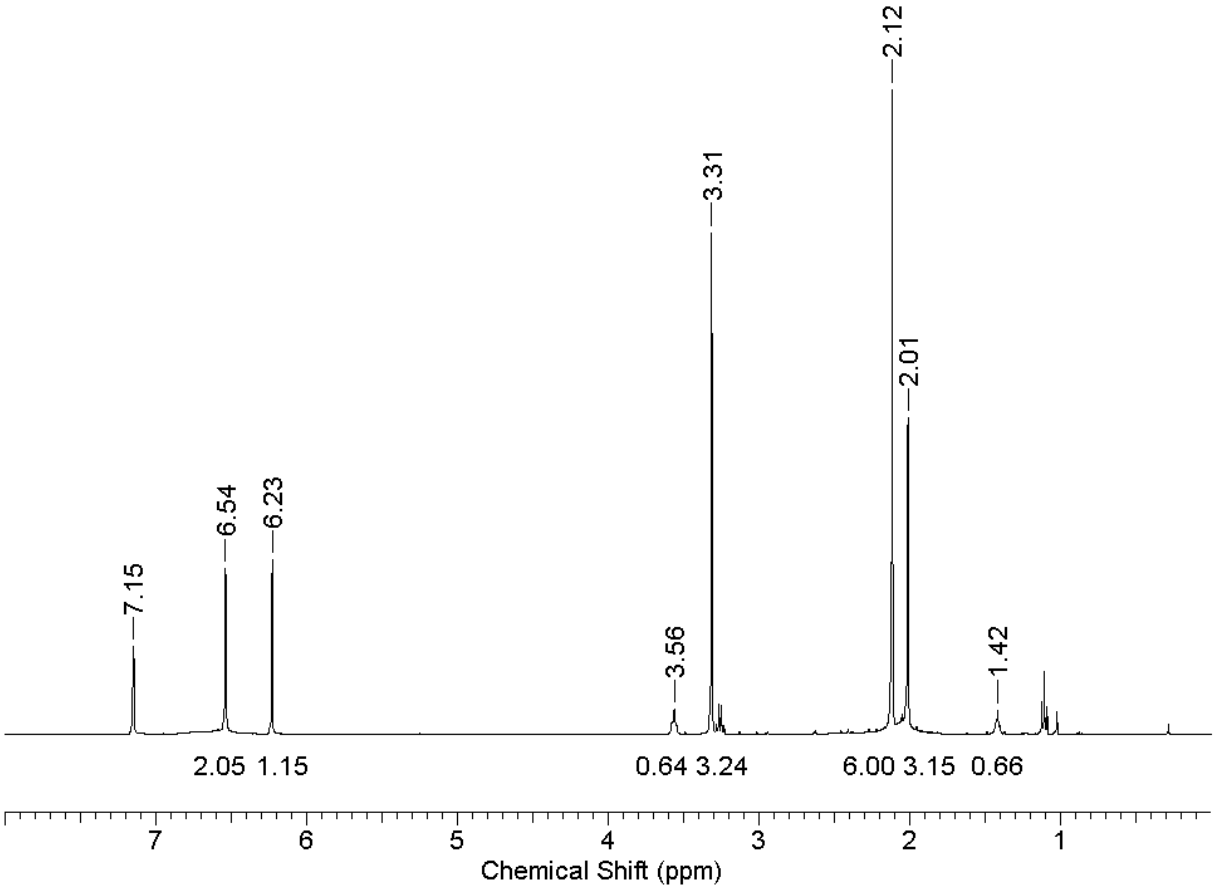

Figure E.17. ^{1}H NMR spectrum of the solution of 10 equivalents of mesityl azide and 10 equivalents of 2,6-dimethylphenyl isocyanide after stirring for four hours. No new products observed. The isocyanide peaks have disappeared.

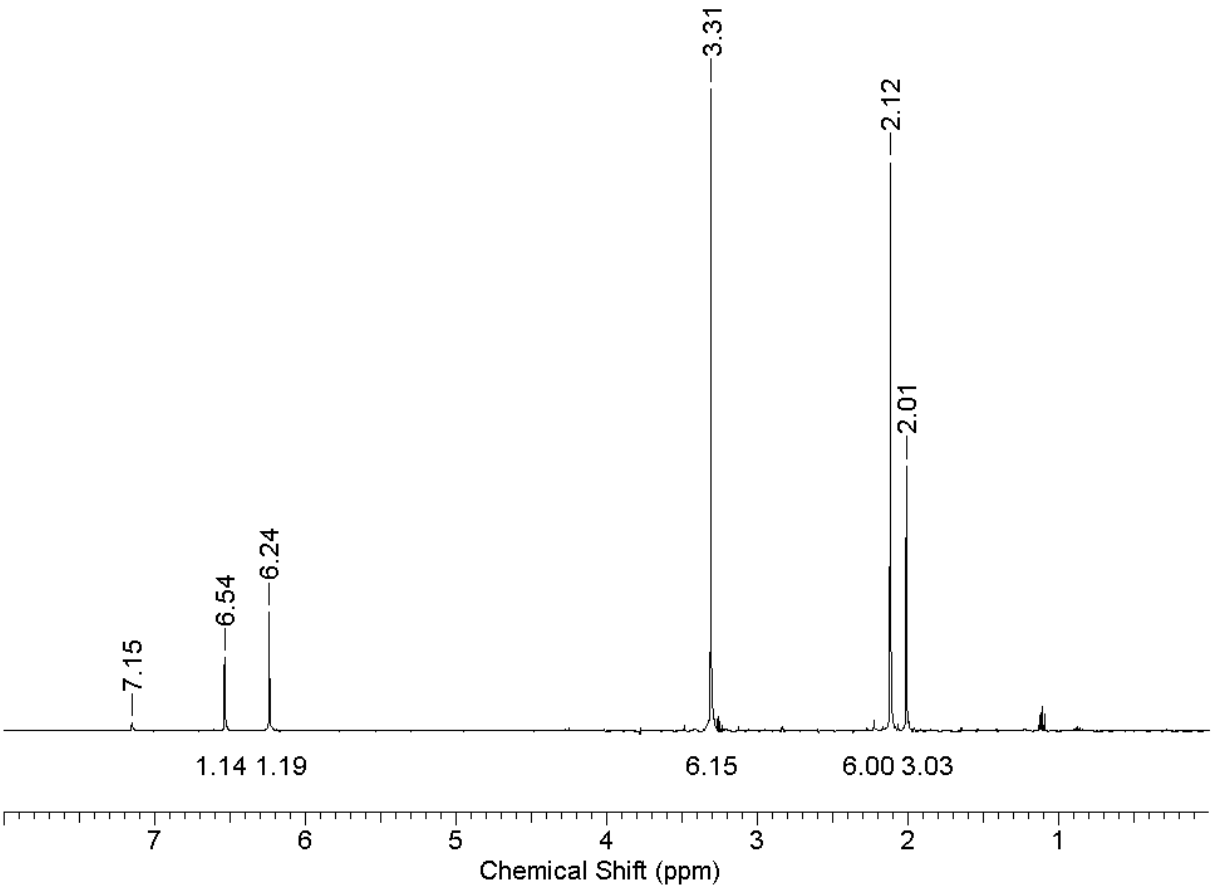

Figure E.18. ^{1}H NMR spectrum of the solution of 10 equivalents of mesityl azide after stirring in cyclohexadiene as a solvent for 24 hours. 1,3,5-trimethoxybenzene is used as an internal standard. No new products observed. Only mesityl azide is present.

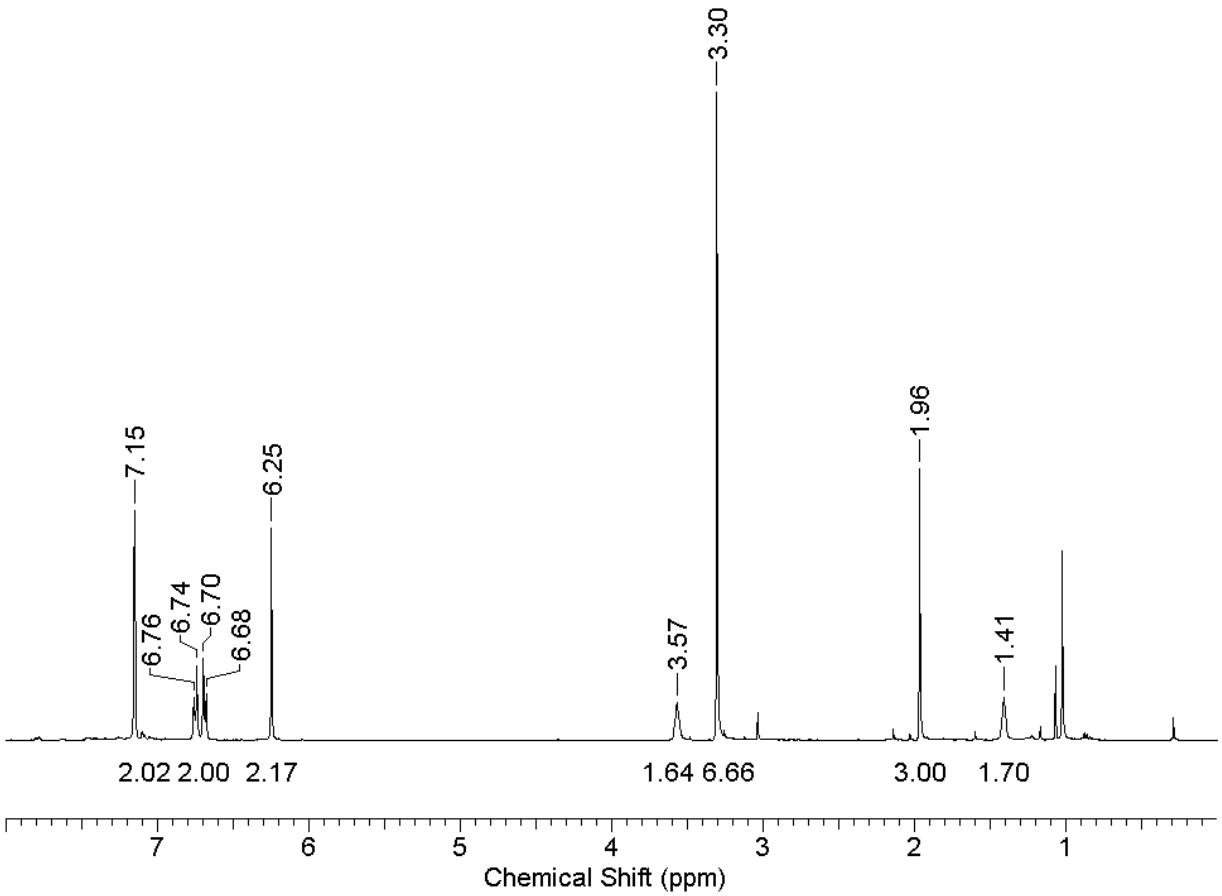

Figure E.19. ^{1}H NMR spectrum of the solution of 10 equivalents of tolyl azide and 1 equivalent of $Fe(OR)_2(THF)_2$, following heating to 50 °C for 5 hours. No new product formation is observed.

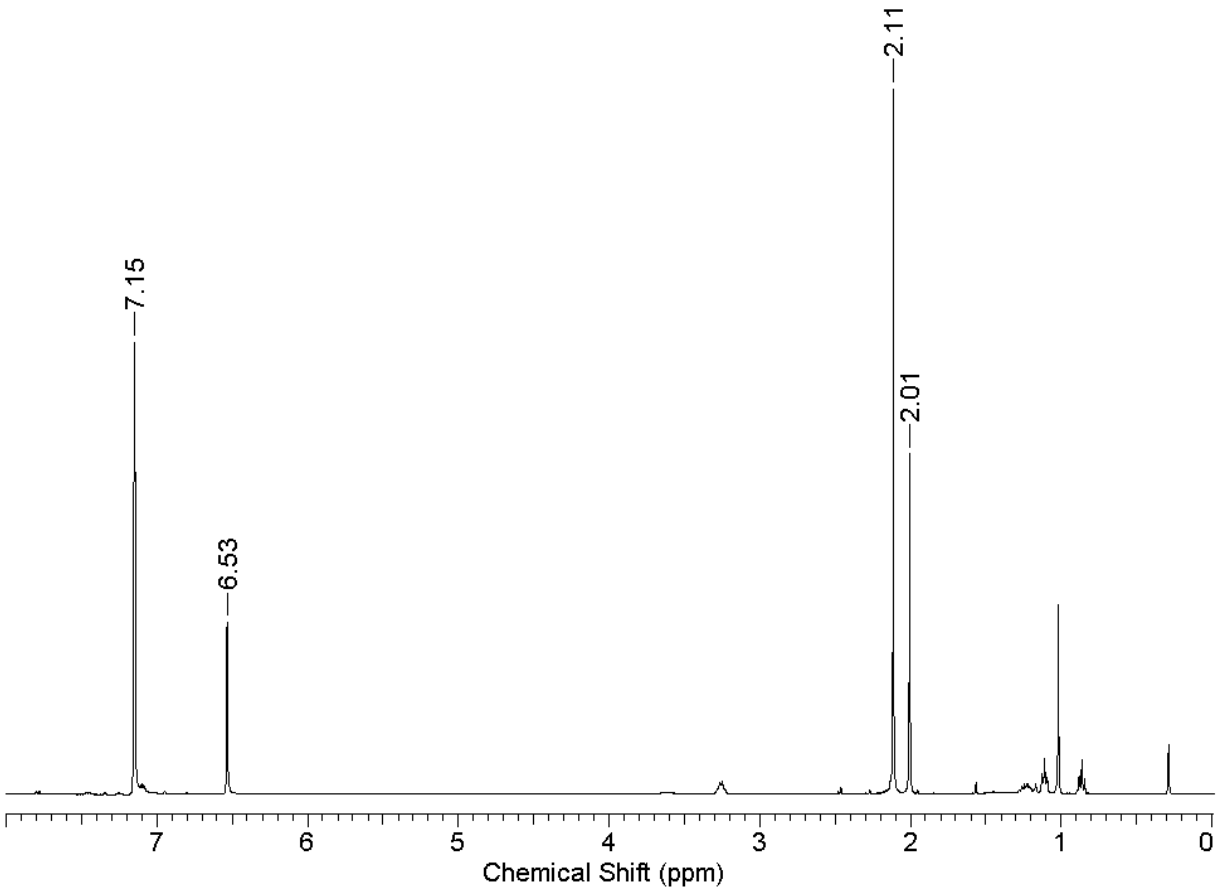

Figure E.20. ^{1}H NMR spectrum after four hours of stirring five equivalents of mesityl azide to a solution of **17**. No color change was observed. Stirred for four hours. NMR reveals no azoarene formation, with only the mesityl azide peaks present.

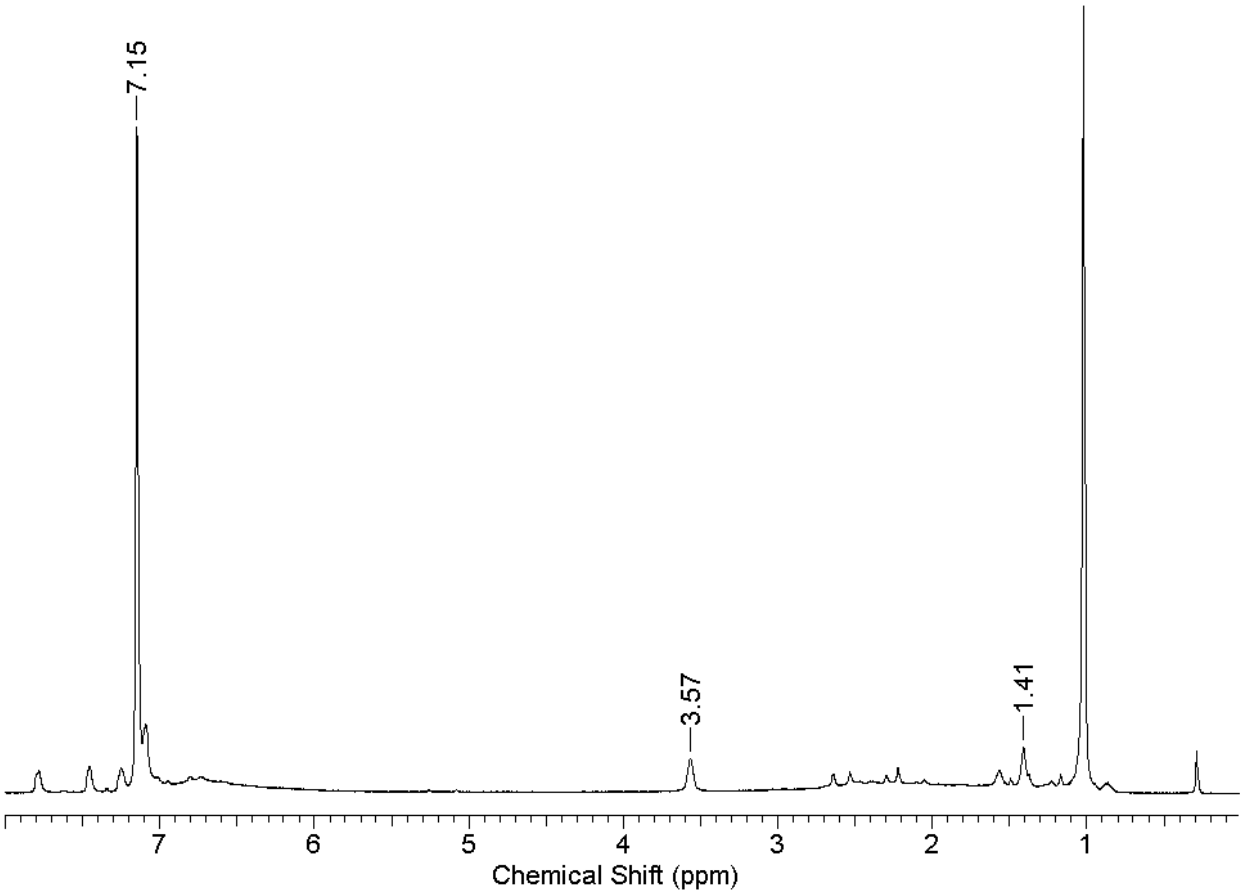

Figure E.21. ^{1}H NMR spectrum of the reaction of **18** with 2 equivalents of 2,6-dimethylisocyanide. No new products observed. The isocyanide peaks have disappeared.

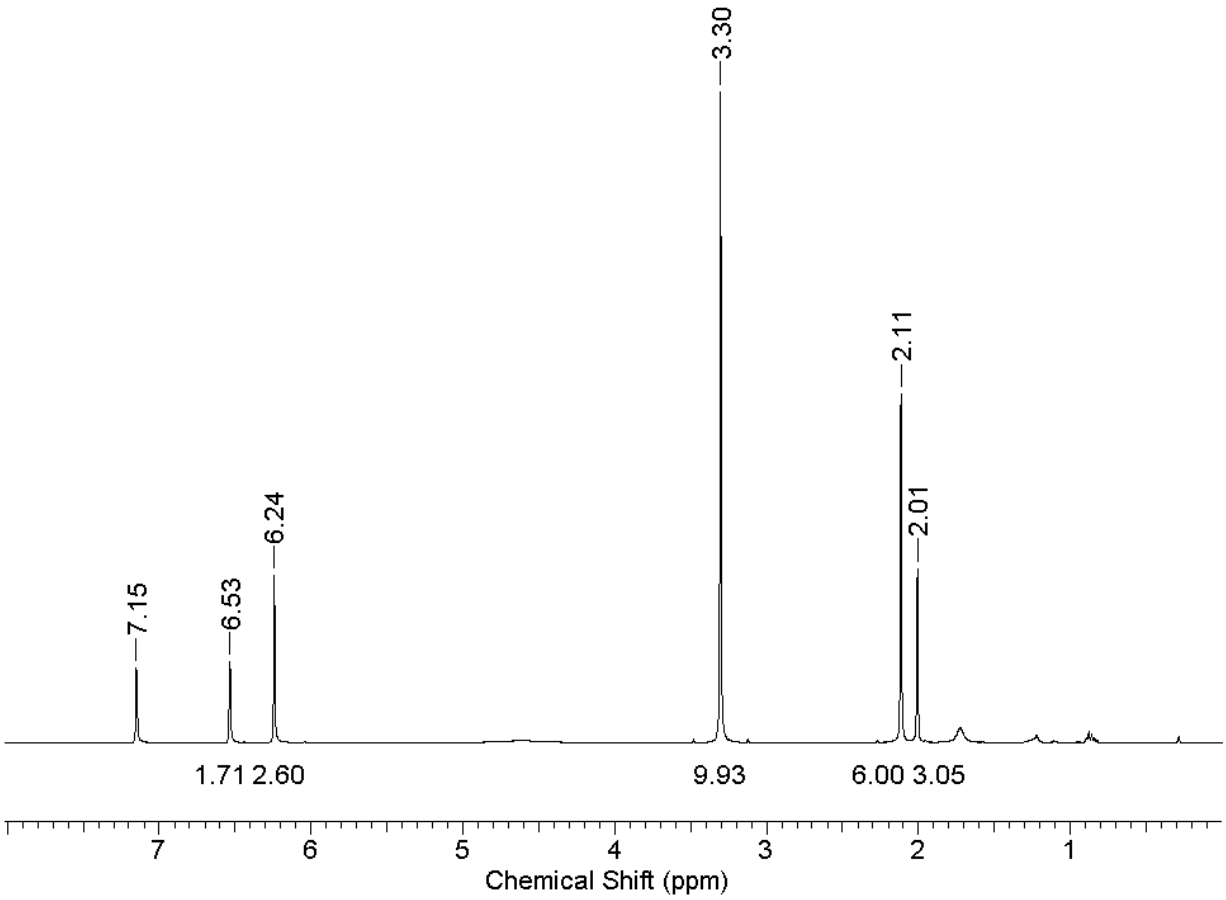

Figure E.22. ^{1}H NMR spectrum of control experiment using iron(II) chloride and mesityl azide. No reaction observed.

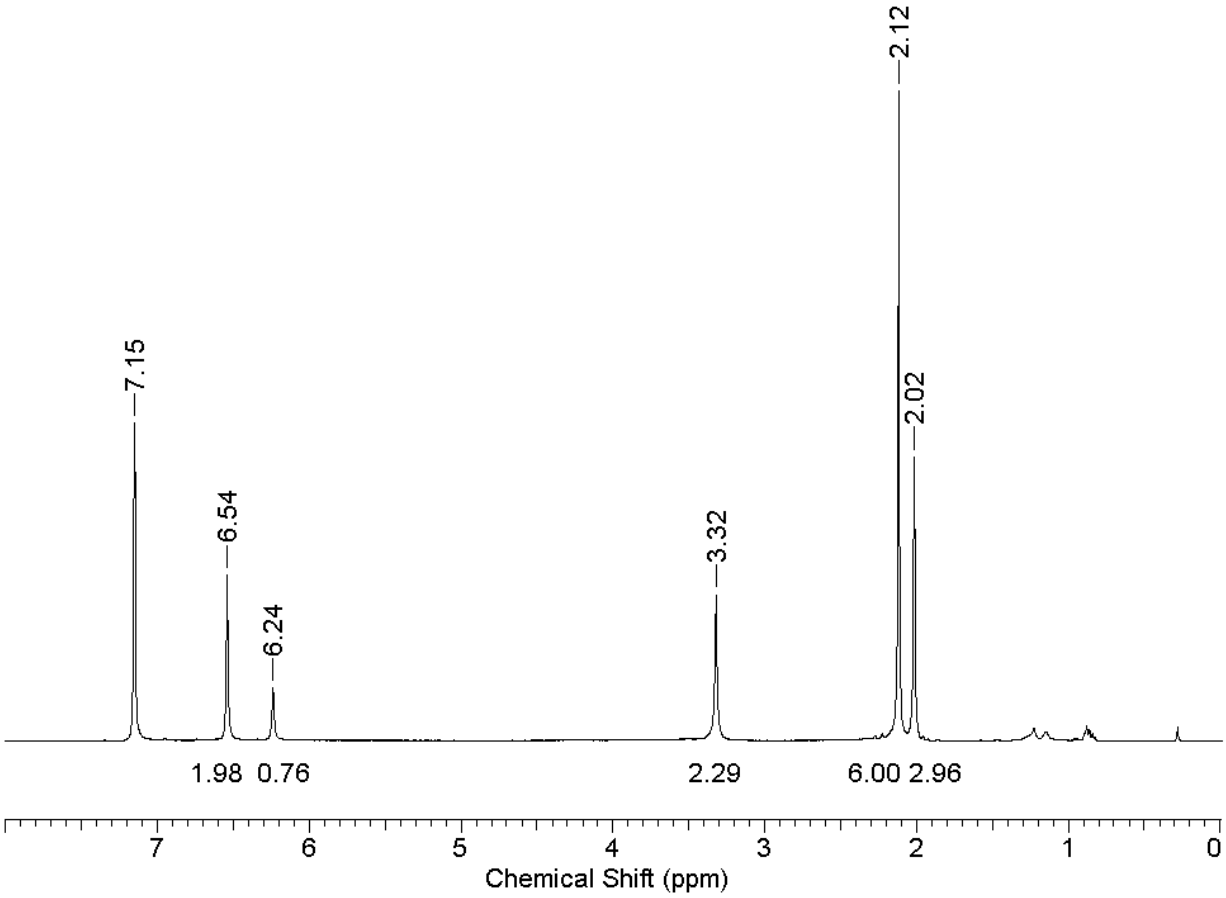

Figure E.23. ^{1}H NMR spectrum of control experiment using iron(III) chloride and mesityl azide. No reaction observed.

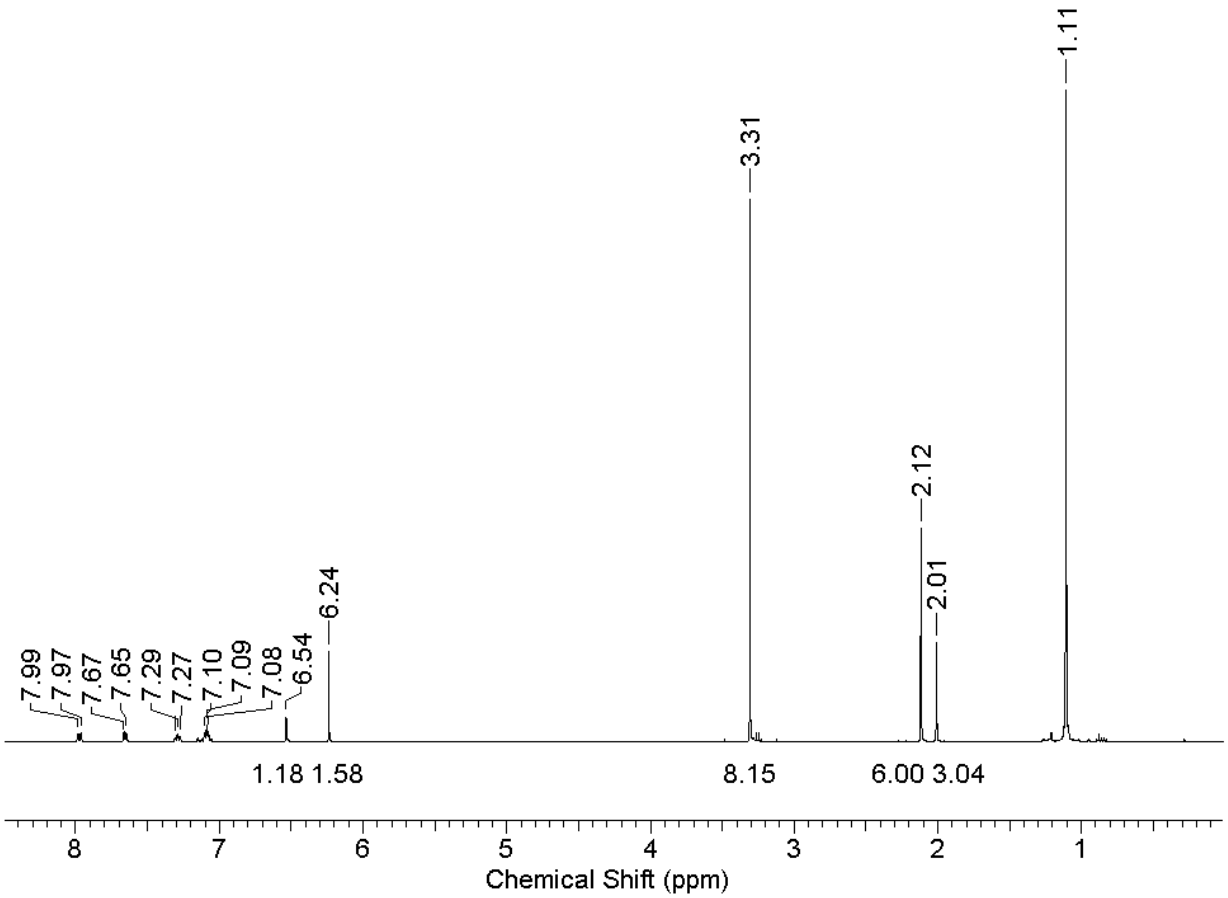

Figure E.24. ^{1}H NMR spectrum of control experiment using the lithium salt of the ligand, **1**, and mesityl azide. No reaction observed.

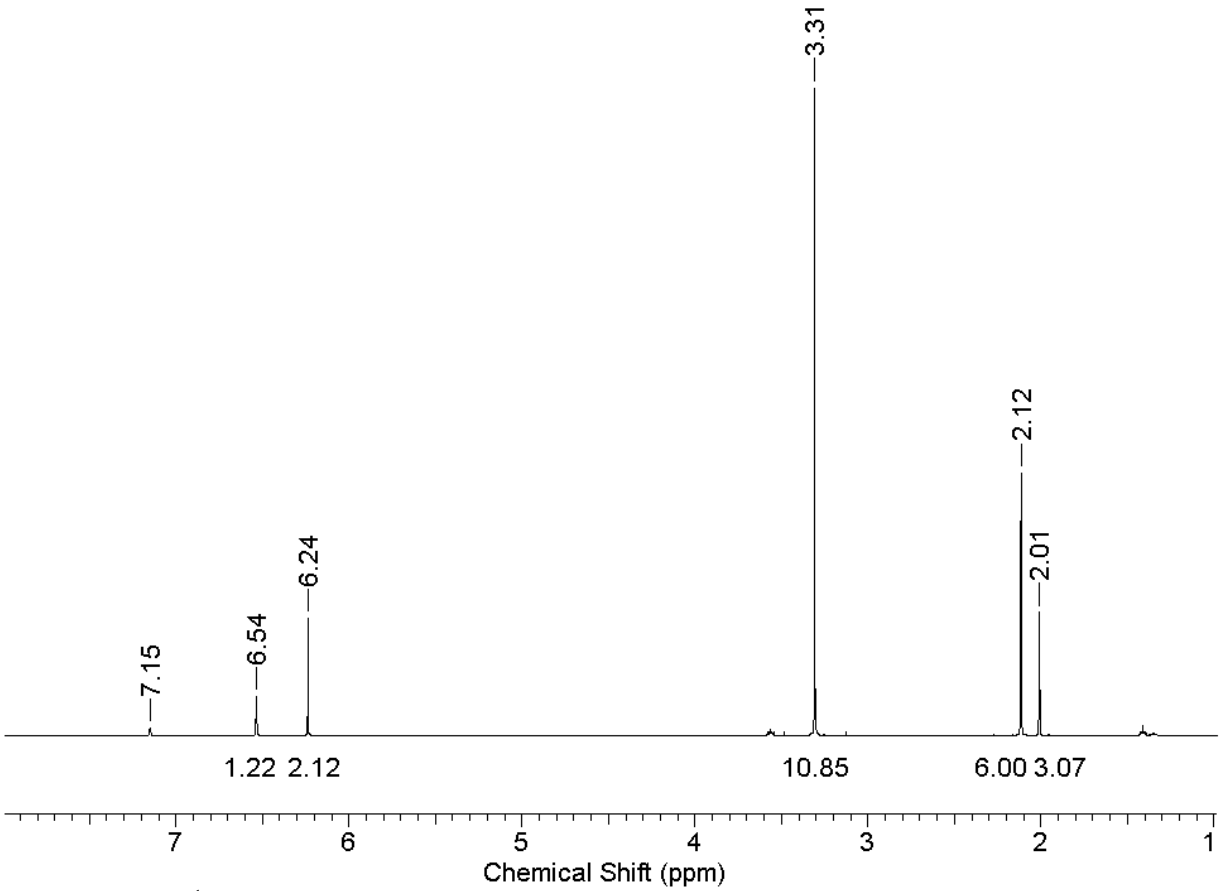

Figure E.25. ^{1}H NMR spectrum of the control experiment using mesityl azide and no catalyst. No reaction observed.

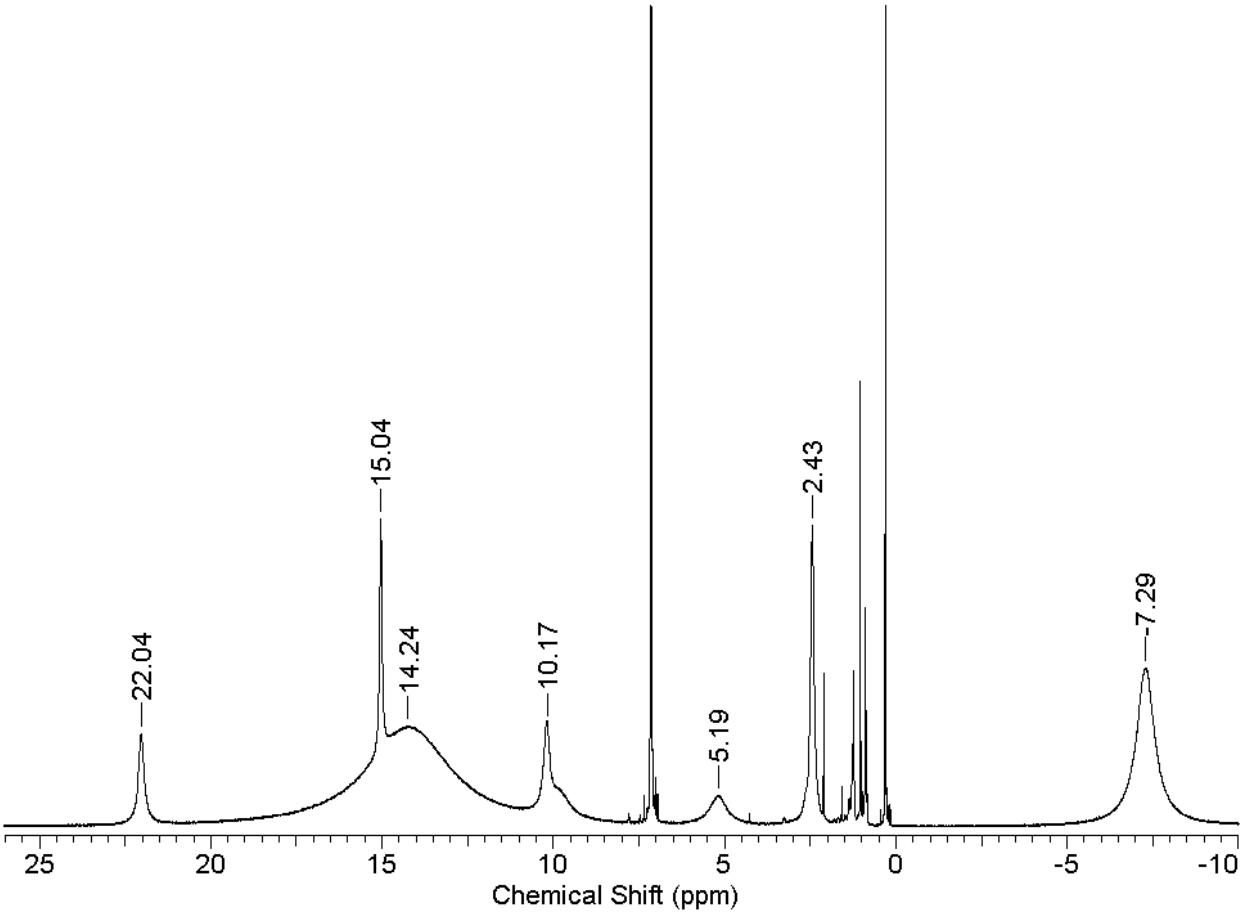

Figure E.26. ^{1}H NMR spectrum of **15**.

4. UV-vis Spectra

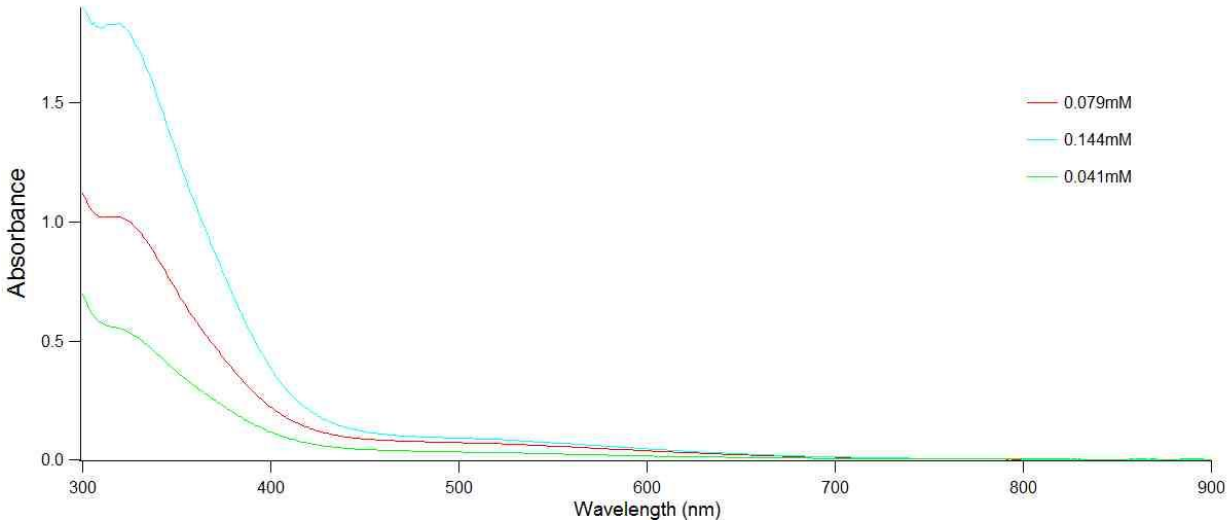

Figure E.27. UV-vis spectrum for **14** at three different concentrations.

5. Mass Spectra

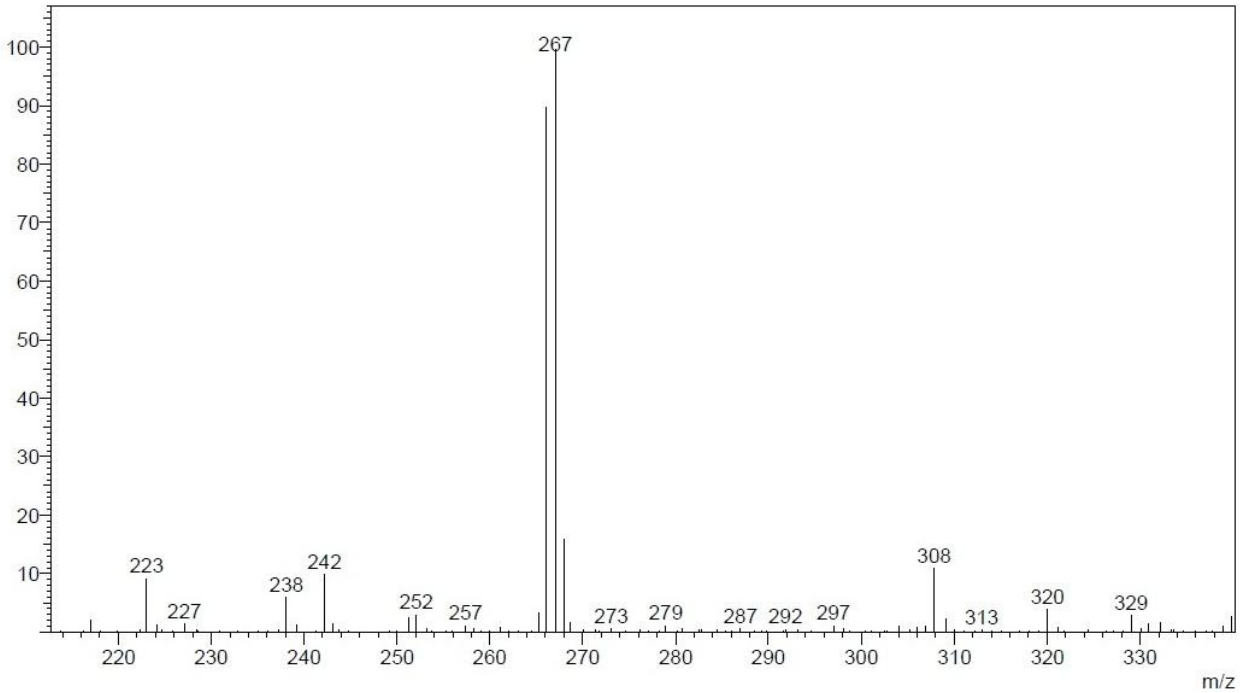

Figure E.28. Mass spectrum of azomesitylene. [M+H] = 267.

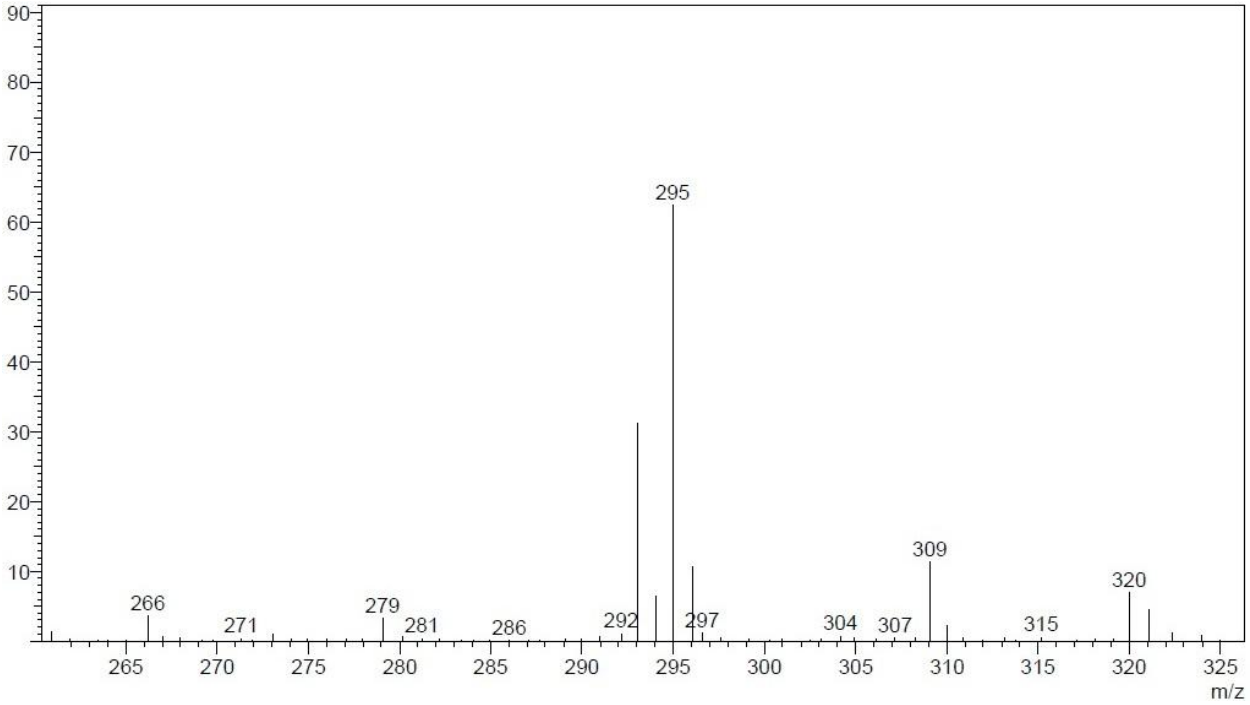

Figure E.29. Mass spectrum of azo(2,6-diethylbenzene). [M+H] = 295.

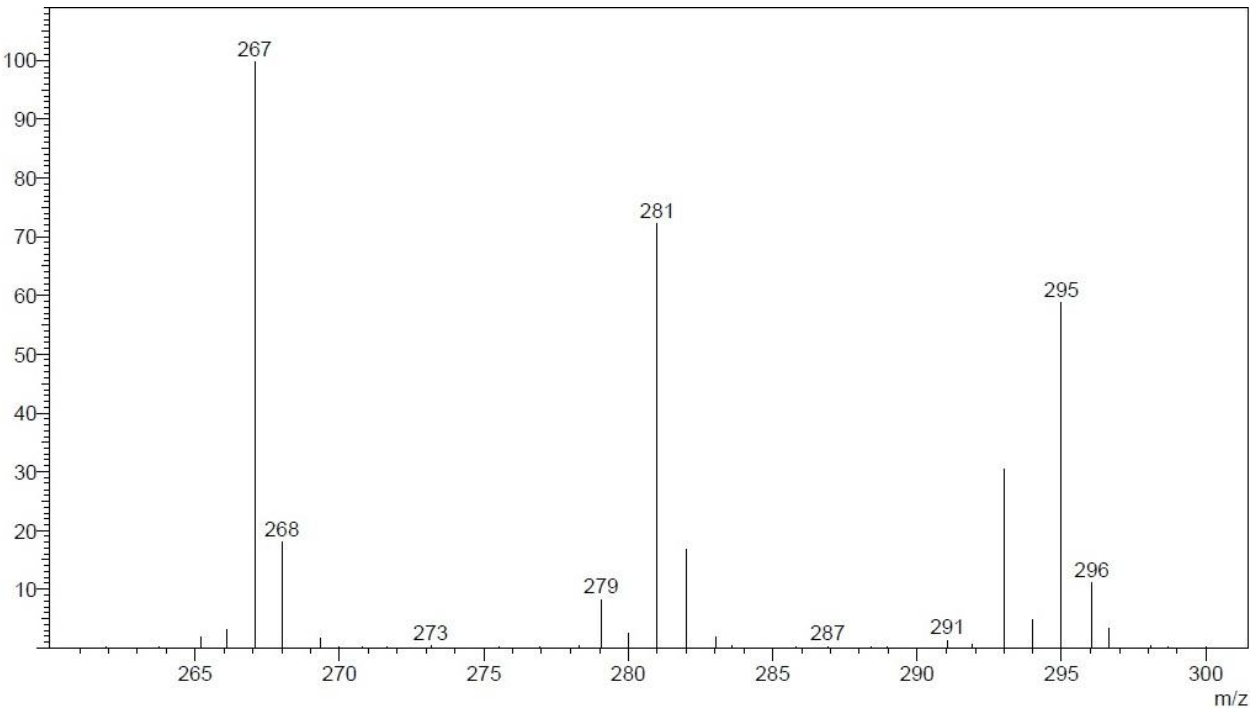

Figure E.30. Mass spectrum of the mixed azide reaction. Azomesitylene, [M+H] = 267. Azo(2,6-diethylbenzene), [M+H] = 295. Asymmetric azoarene, [M+H] = 281.

6. Kinetics Plots

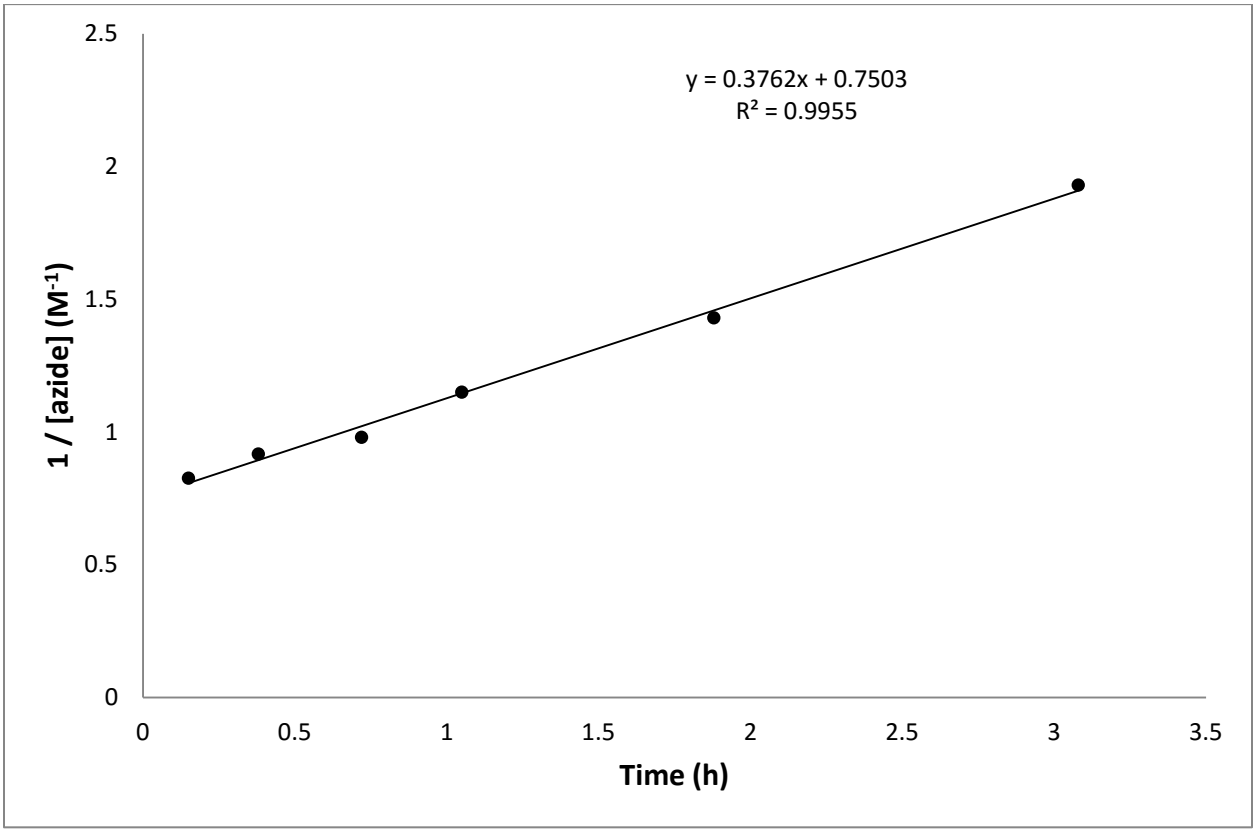

Figure E.31. Kinetics plot of 1/[azide] vs. time (1:100 [Fe]/azide, [Fe] = 14.4 mM).

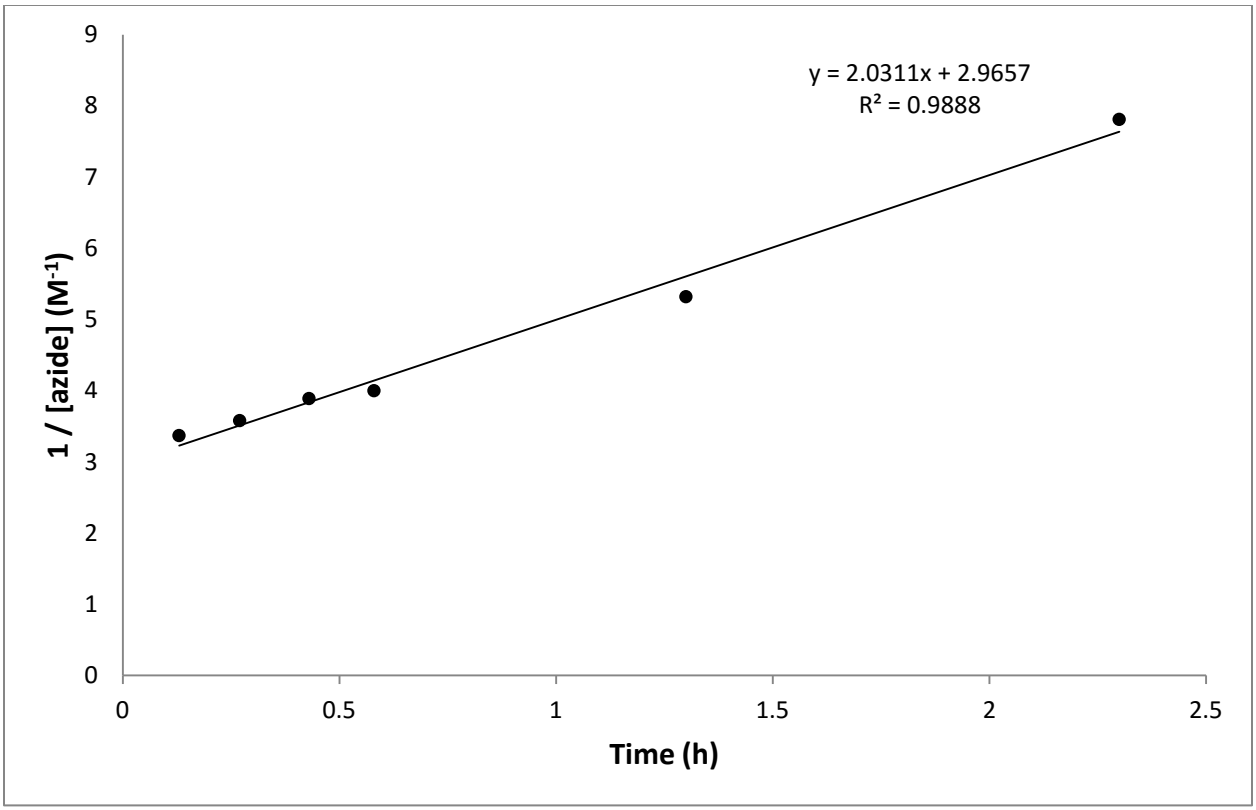

Figure E.32. Kinetics plot of 1/[azide] vs. time (1:10 [Fe]/azide, [Fe] = 31.6 mM).

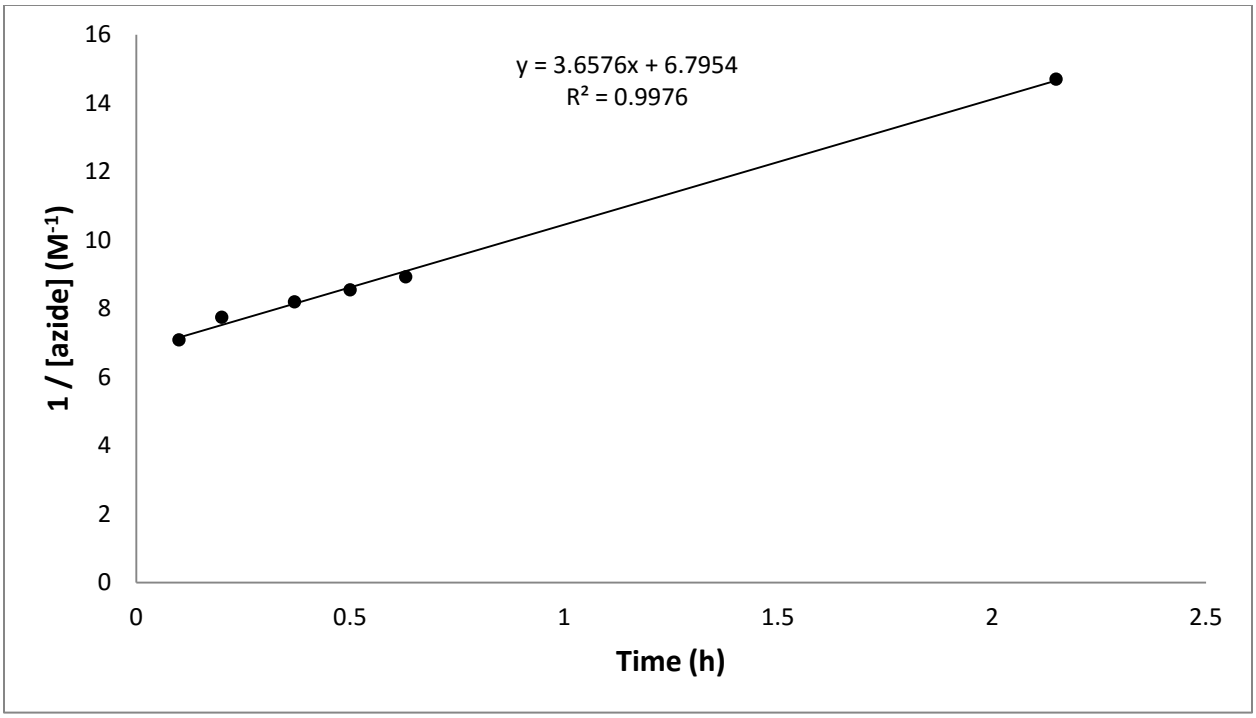

Figure E.33. Kinetics plot of 1/[azide] vs. time (1:10 [Fe] / azide, [Fe] = 15.8 mM).

7. Computational Details

Electronic structure calculations were carried out using DFT[98] as implemented in Gaussian09.[93] Geometry optimizations were performed at the B3LYP[63] level of theory using the 6-311G(d) basis set based on inadequacies we observed with doublt-ζ basis sets in a previous study.[99] No symmetry constraints were imposed during geometry optimizations. All optimized structures were confirmed to have stable wave functions[100] and to be local minima by analyzing the harmonic frequencies.[101] Frequencies and thermodynamics for all species in Chapter 5 can be found below.

Table E.2. Thermodynamics (in E_h) of all optimized $Fe(OR)_2(NAr)$ structures.

Species	E(SCF)B3LYP	H(gas)	G(gas)	E(SCF)OPBE
quintet	-2989.735100	-2988.814228	-2988.945615	-2989.190013
singlet	-2989.692567	-2988.770925	-2988.899766	-2989.140895
triplet	-2989.720699	-2988.798660	-2988.933338	-2989.173597
septet	-2989.727541	-2988.806085	-2988.941666	-2989.177988

Table E.3. Corresponding orbital isosurface (iso = 0.05 au) plots for quintet $Fe(OR)_2(NMes)$. α orbitals are in the left column, β orbitals are in the right column. The overlap between 168a and 168b is ~53%.

172a	
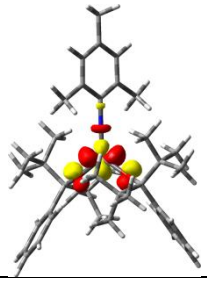	
171a	
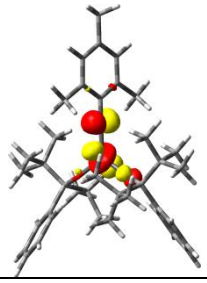	
170a	
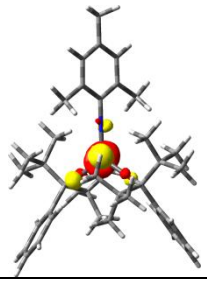	
169a	
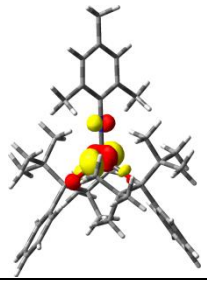	
168a	168b
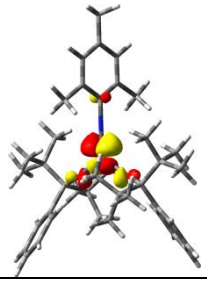	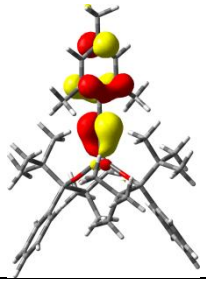

APPENDIX F: SUPPLEMENTARY MATERIAL FOR CHAPTER 6

1. Evans Method Formula and Procedure

The procedure for the Evans method is the same as that reported in Appendix B.

Table F.1. Spin-only magnetic moments calculated for **19** using the Evans method.

Complex	μ_{calc} (μ_B)	μ_{obs} (1) (μ_B)	μ_{obs} (2) (μ_B)	μ_{obs} (3) (μ_B)	μ_{obs} (average) (μ_B)
19	1.8	2.0	2.1	2.1	2.0 ± 0.1

2. IR Spectra

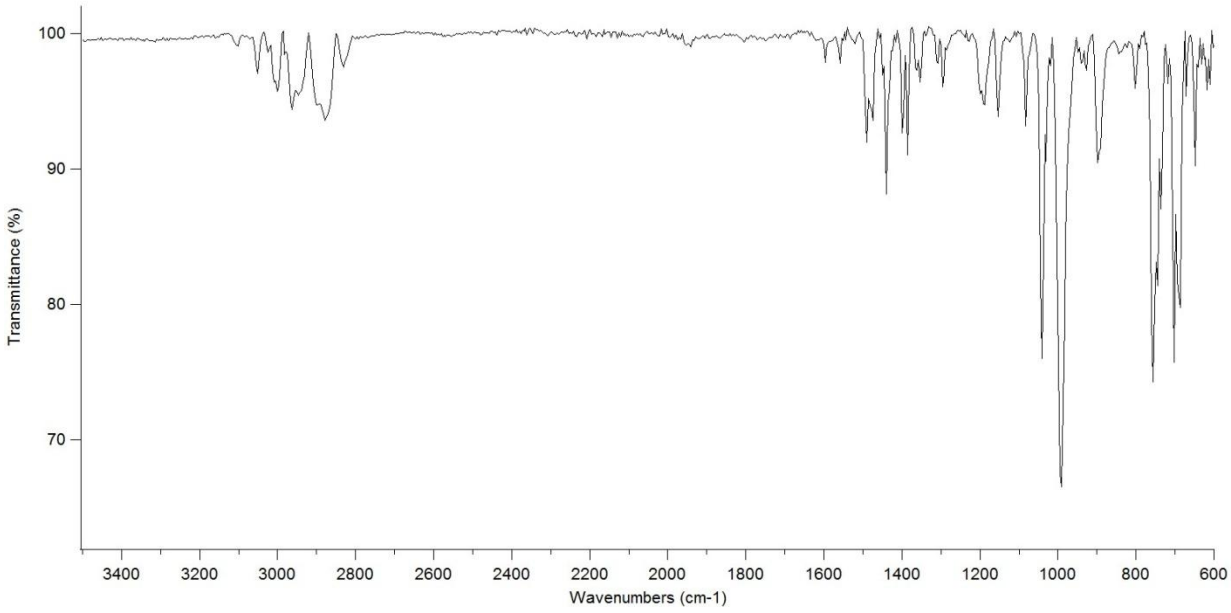

Figure F.1. IR spectrum of **19**.

3. NMR Spectra

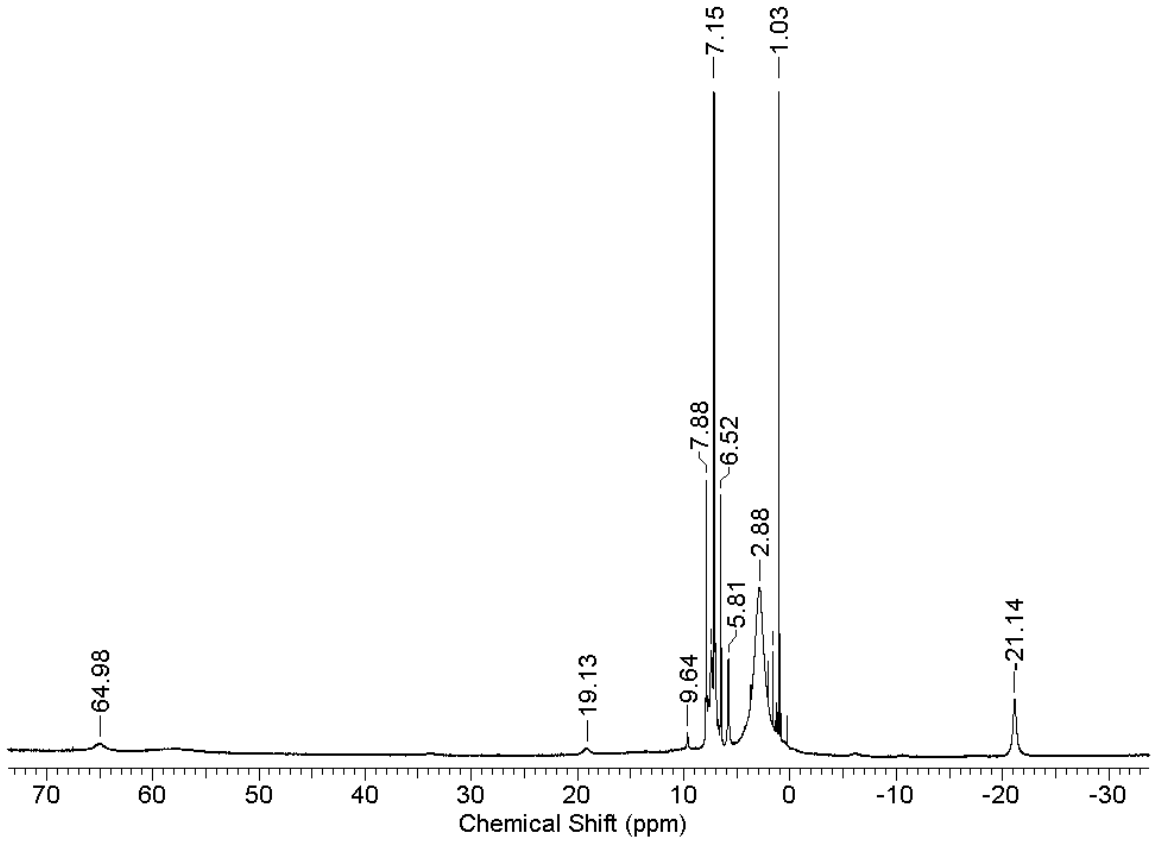

Figure F.2. ^{1}H NMR spectrum of **19**.

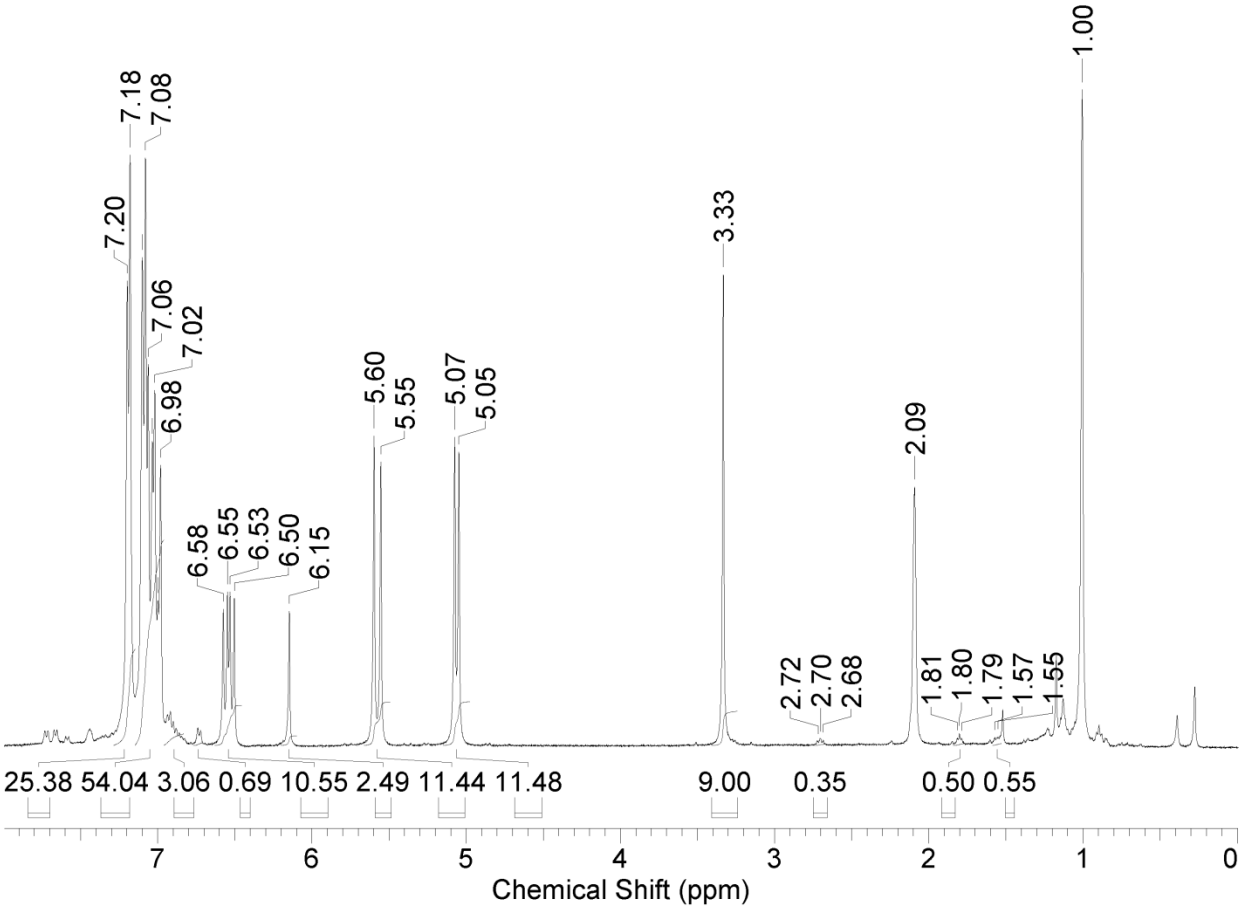

Figure F.3. ^{1}H NMR spectrum of a stoichiometric reaction of **19** with styrene. Approximately 15% conversion of the olefin to the cyclopropane after four hours of heating at 90 °C.

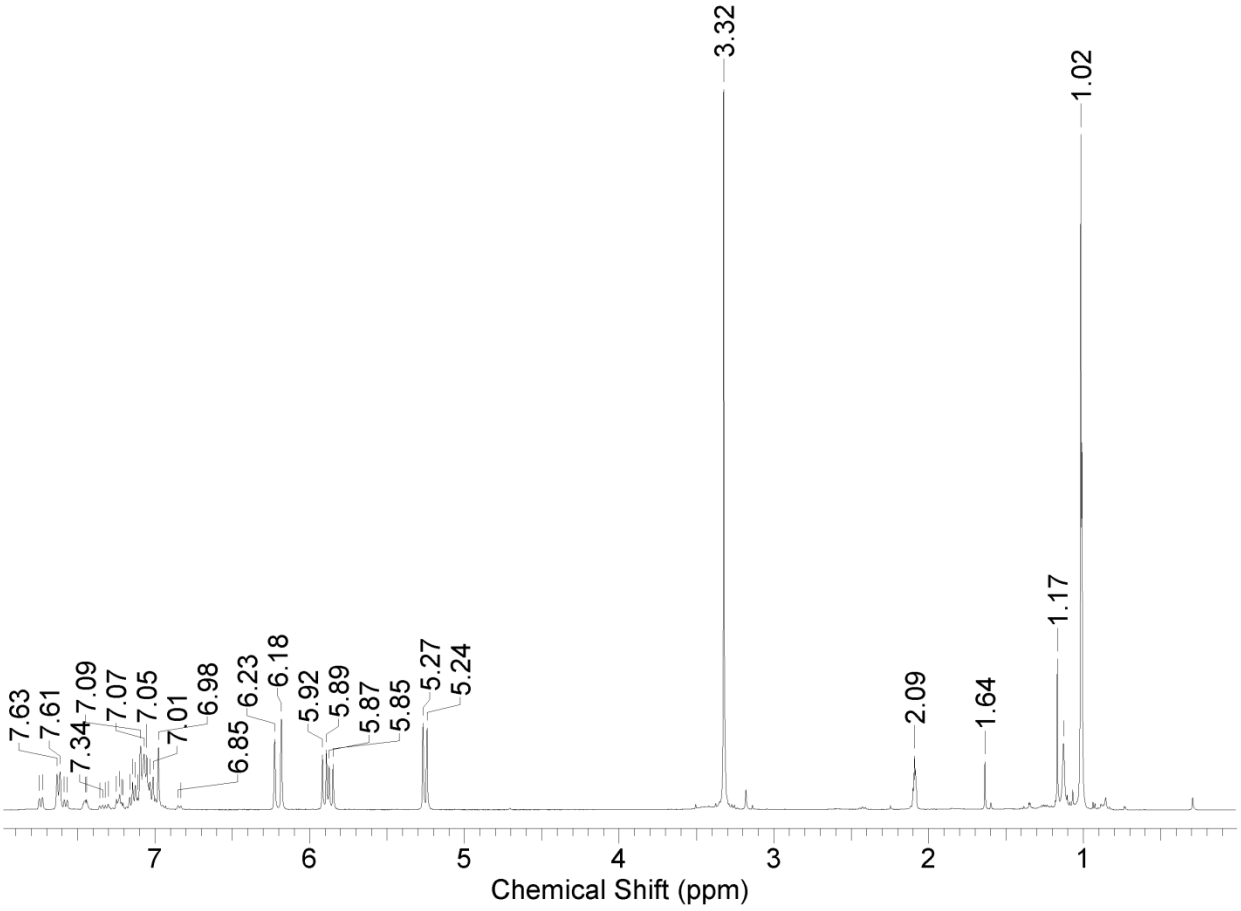

Figure F.4. [1]H NMR spectrum of the stoichiometric reaction of **19** with methyl acrylate. The reaction was heated for four hours at 90 °C. Decomposition of **19** is observed, with negligible cyclopropane formation.

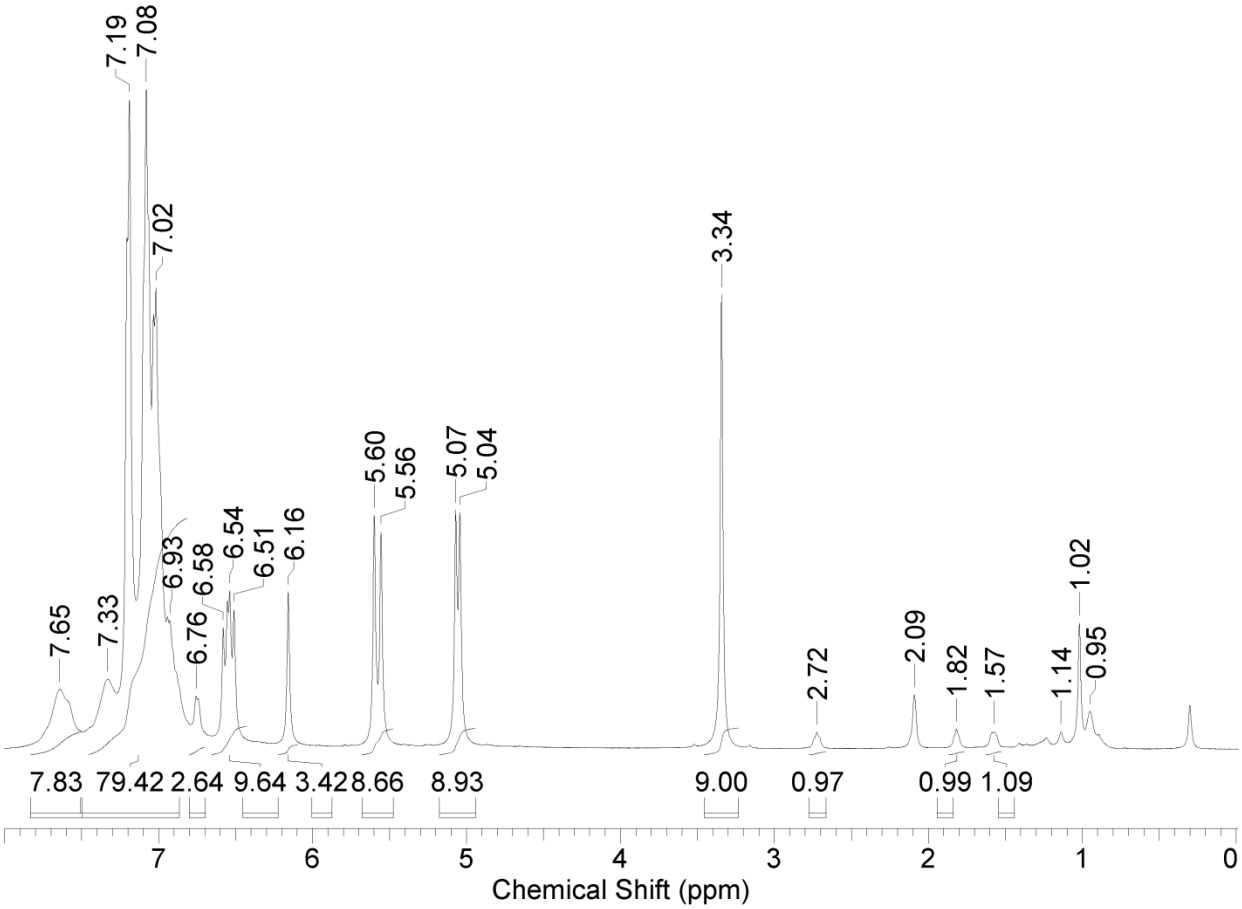

Figure F.5. ^{1}H NMR spectrum of the catalytic reaction of styrene with diphenyldiazomethane using 10 mol % of **19**. Trimethoxybenzene was used as an internal standard. About one equivalent of the corresponding cyclopropane was formed after four hours of heating at 90 °C.

4. UV-vis Spectra

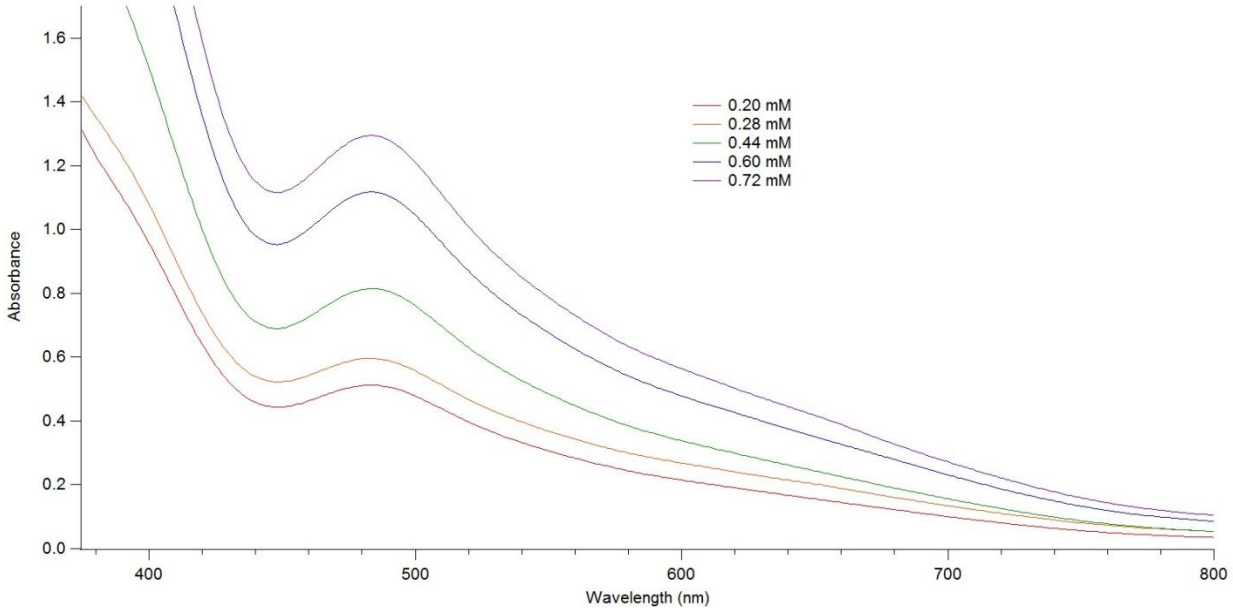

Figure F.6. UV-vis spectrum for **19** at five different concentrations.

5. EPR Experimental Details and Spectra

The continuous-wave and pulsed X-Band (9.4 GHz) EPR spectra were recorded using a Bruker ElexSys 680 spectrometer that is part of the instrumentation available to NHMFL users. All spectra were recorded at cryogenic temperatures using a helium-flow cryostat (Oxford). While all pulsed spectra were obtained using a cylindrical TE_{011} dielectric ring resonator (ER 4118X-MD-5, Bruker) some of those in continuous wave mode were recorded using a high-sensitivity cavity (ER 4119HS, Bruker). The HYSCORE spectra were recorded using a standard four-pulse sequence $\pi/2 - \tau - \pi/2 - t_1 - \pi - t_2 - \pi/2 - echo$.[102] Unwanted pulses were removed using an eight-step phase cycle.[103] The length of the π and $\pi/2$ pulses was 16 ns and a delay, τ, of 200 ns was employed. The echo was recorded as function of two dimensions, t_1 and t_2, with a step size $dt_{1,2}$ of 8 ns for 512 points per dimension. The experimentally determined time-domain data was processed to yield the frequency-domain plot presented in the main text. Thus, the background echo decay for both t_1 and t_2 was removed by subtracting a third order polynomial fitted to the individual data traces. Subsequently, both dimensions were expanded to 1024

points by zero-filling the empty data points followed by a convolution with a Hamming widow function. The resulting data set was submitted to a two-dimensional Fourier transform yielding the frequency-domain HYSCORE spectrum. For the current manuscript only the positive, (+,+), quadrant is presented. The high-frequency EPR spectra were obtained using a custom-built spectrometer available at the EMR facility of NHMFL. This spectrometer allows for recording spectra transmission mode. The microwaves are propagated through cylindrical lightpipes and were generated by a phase-locked oscillator (Virginia Diodes) operating at a frequency of 13 ± 1 GHz and generating its harmonics, of which the 4th, 8th, 16th, 24th and 32nd were available. A superconducting magnet (Oxford Instruments) capable of reaching a field of 17 T was employed. All spectral simulations were performed in the framework described by the spin-Hamiltonian of equation 1.

$$\hat{\mathrm{H}} = \beta_e \vec{\mathbf{B}} \cdot \tilde{\mathbf{g}} \cdot \tilde{\mathbf{S}} - \sum_{\xi} \left(\beta_n g_n \vec{\mathbf{B}} \cdot \tilde{\mathbf{I}}_{\xi} + \tilde{\mathbf{I}}_{\xi} \cdot \tilde{\mathbf{A}}_{\xi} \cdot \tilde{\mathbf{S}} \right) \quad (1)$$

The simulations of **Figure 62** were obtained using the SpinCount program written by Prof. Mike Hendrich at Carnegie Mellon University,[104] and relied on a first-order perturbative treatment of the hyperfine interaction. In contrast, the simulations of Figure S9 were obtained using a program written by Dr. Andrew Ozarowski and involved the diagonalization of the complex, 16×16 spin-Hamiltonian matrix. All spectra could be successfully simulated using $S = 1/2$, $g_x = 3.06(2)$, $g_y = 2.24(2)$, $g_z = 1.93(2)$, $\sigma(g_x) = 0.03(2)$, $\sigma(g_y) = 0.01(1)$, $\sigma(g_z) = 0.01(1)$, $A_x = 585$ MHz, $A_y = 280$ MHz, $A_z = 230$ MHz, $\sigma(A_x) = 25$ MHz, $\sigma(A_y) = 10$ MHz, $\sigma(A_z) = 5$ MHz, an intrinsic Lorentzian linewidth $\Gamma = 15$ G. While the X-band spectra were recorded for deuterated-toluene solutions those recorded at high-frequency were obtained using non-deuterated toluene solutions. The simulations of the HYSCORE spectra presented in Figure S17 were obtained using the EasySpin software package maintained and developed by Prof. Stefan Stoll.[105]

The magnitude of the coupling constants associated with the hyperfine splitting patterns of the g ⍰ 3 and 1.9 absorptions can be easily estimated from the peak-to-peak separation of the individual lines

i.e., 590(10) MHz and 230(10) MHz. In contrast, the hyperfine splitting of the g ⍰ 2.2 absorption, as well as the distribution in the A and g values, could be obtained only from spectral simulations. The progressive broadening of the absorptions belonging to a particular hyperfine splitting pattern originates from combined effects of a distribution the hyperfine coupling constants, $\sigma(A_\xi)$, and g values, $\sigma(g_\xi)$. Simulations of the X-band spectrum shown in **Figure 62** used a spin-Hamiltonian model with hyperfine coupling accounted for with first order perturbation of the electronic Zeeman effect and provided: g_x = 3.068, g_y =2.214, g_z = 1.955; $\sigma(g_x)$ = 0.03, $\sigma(g_y) = \sigma(g_z)$ = 0.00, A_x = 587 MHz, A_y = 280 MHz, A_z = 230 MHz, $\sigma(A_x)$ = 25 MHz, $\sigma(A_y)$ = 10 MHz, $\sigma(A_z)$ = 5 MHz, with an intrinsic Lorentzian linewidth Γ = 15 G. The difference in the X-band g values when compared with those of the high frequency spectra is an artifact that originates from the use when evaluating the hyperfine coupling of perturbation theory (see **Figure F.12**).

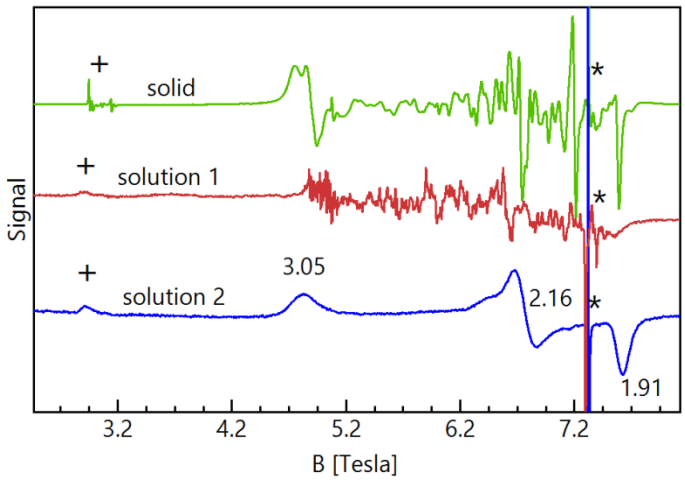

Figure F.7. High-frequency EPR spectra recorded at 203.2 GHz, 10 K for two frozen toluene solution and a ground solid samples of **19**. While the (+) sign labels resonances that originate from surface adsorbed molecular oxygen, (*) labels g = 2.00. The intense and narrow resonance associated with g = 2 originates from a radical impurity.

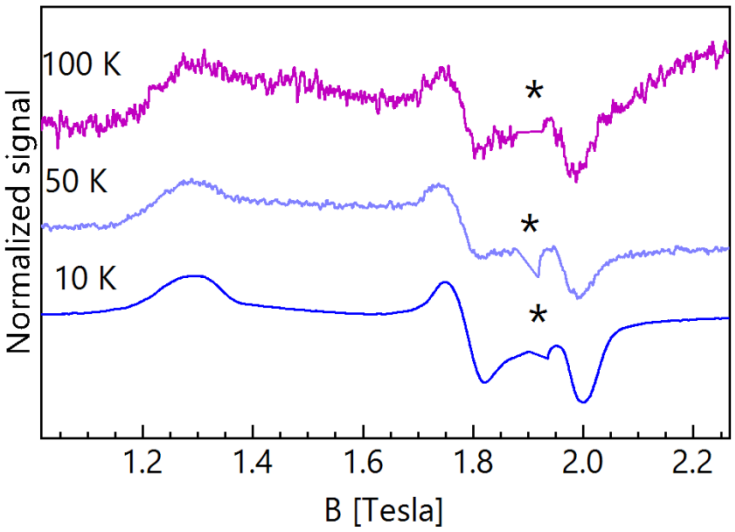

Figure F.8. Temperature dependent spectra recorded at 52 GHz for a frozen toluene solution of **19**. The spectra are normalized. The (*) denotes the position of g = 2.00. For sake of clarity the intense, radical impurity - based signal was removed from the spectra.

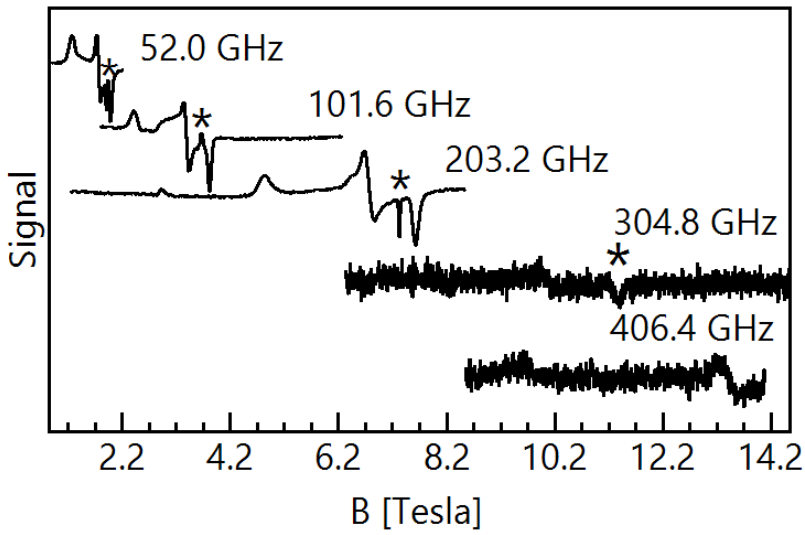

Figure F.9. Variable-frequency EPR spectra recorded at 10 K for a frozen toluene solution of **19**. The (*) denotes the position of g = 2.00. For sake of clarity the intense, radical impurity-based signal was removed from the spectra.

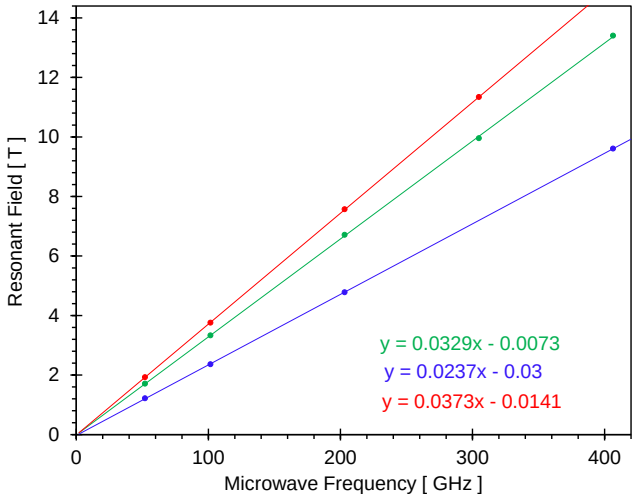

Figure F.10. Frequency-dependence of the resonant field values of the observed resonances. The linear fits obtained for these resonances are listed as an inset and yield the following effective g values: 2.171 (*green*), 3.014 (*blue*), and 1.915(*red*).

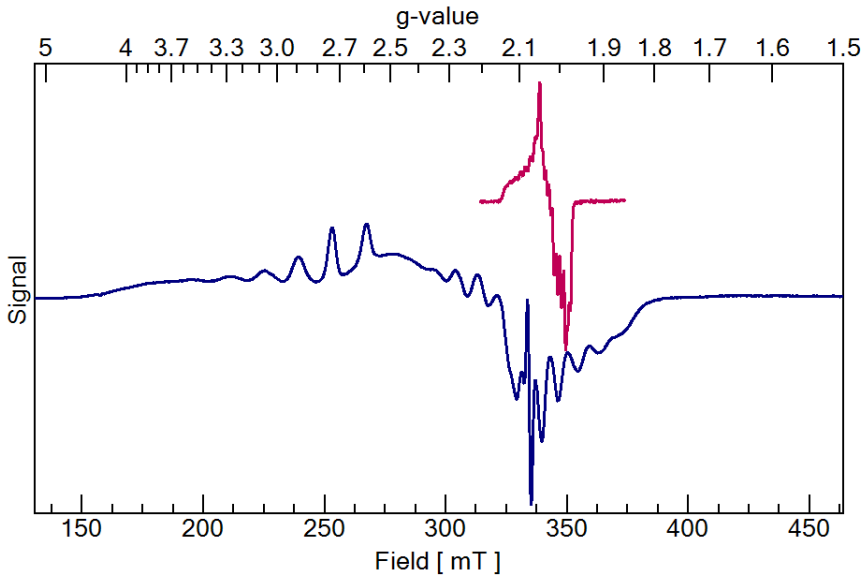

Figure F.11. X-band spectra recorded at 20 K for a frozen THF solution of [(corrole)Co]Cl (*top*) and frozen toluene solution of **19** (*bottom*). These spectra illustrate the difference between a ligand-based spin density i.e., cobalt coordinated corrole - radical, and a metal based spin density, **19**. Interestingly, both compounds enclose a formal cobalt(IV) site. However the corrole complex is not believed to contain a genuine Co^{4+} site but rather a $S = 0$, low-spin Co(III) center.[106]

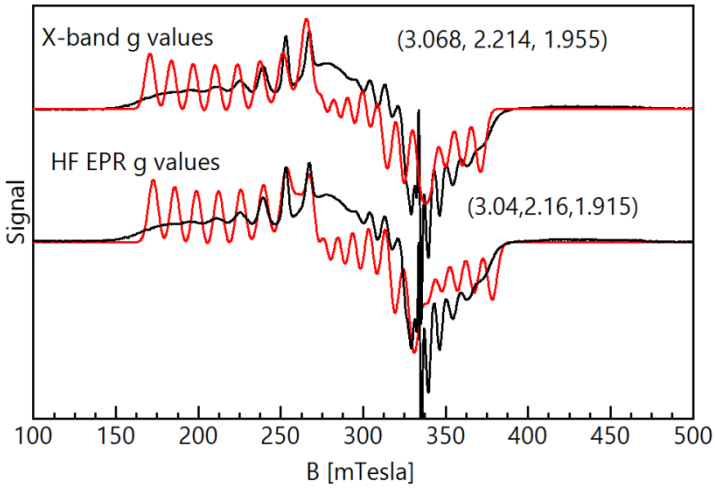

Figure F.12. Simulations of the 20 K, X-band spectrum recorded for a frozen toluene solution of **19** obtained from the full diagonalization of the $16 \times 16, \{(S = 1/2) \otimes (I = 7/2)\}$ complex spin-Hamiltonian[107] and the g-values determined from the analysis of the high-frequency EPR spectra (bottom) and those obtained from the simulations of the X-band spectrum obtained using a first order perturbation treatment of the hyperfine coupling. Comparison of the simulated spectra shown in red reveals that indeed, the higher g-values obtained from the simulations of the X-band spectra using a perturbative approach when compared with the values determined from the high-frequency EPR spectra is an artifact of the perturbative treatment of the hyperfine interaction.

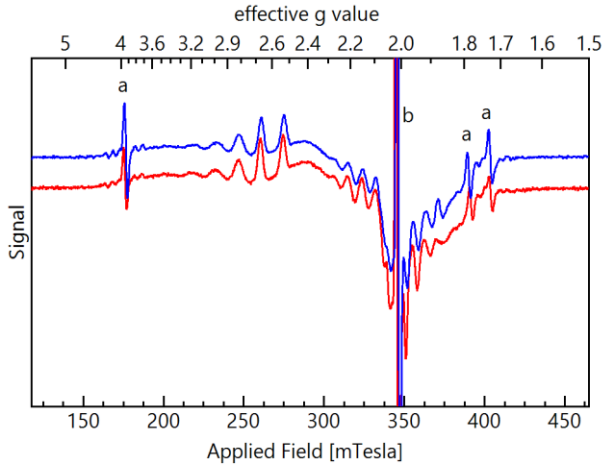

Figure F.13. X-band EPR spectra recorded at 10 K for a ^{13}C labeled (blue) and unlabeled (red) 5 mM solution of **19**. While the spectral features indicated by (a) originate from contaminants of the dielectric resonator, that observed at g = 2 labeled using (b) arises from a radical-based impurity.

Our attempts to estimate the magnitude of the ^{1}H superhyperfine couplings from the simulations of the continuous-wave X-band EPR spectra were unsuccessful. Consequently, we have performed a series of pulsed EPR measurements on deuterated toluene solutions of **19**. Inspection of **Figure F.14** that

shows a typical Hyperfine Sublevel Correlation spectrum (HYSCORE) recorded at X-band reveals two distinct sets of resonances one that is very intense and relatively narrow centered at ~ 2 MHz and another set that is considerably broader found in the 15 – 20 MHz region of the spectrum. Based on their values we assign the first set of resonance to the hyperfine coupling with the I = 1 nuclear spins of ^{2}D nuclei incorporated in the deuterated toluene solvent and the other to the interaction with the I = 1/2 of the ^{1}H nuclei of the cobalt-coordinated ligands.

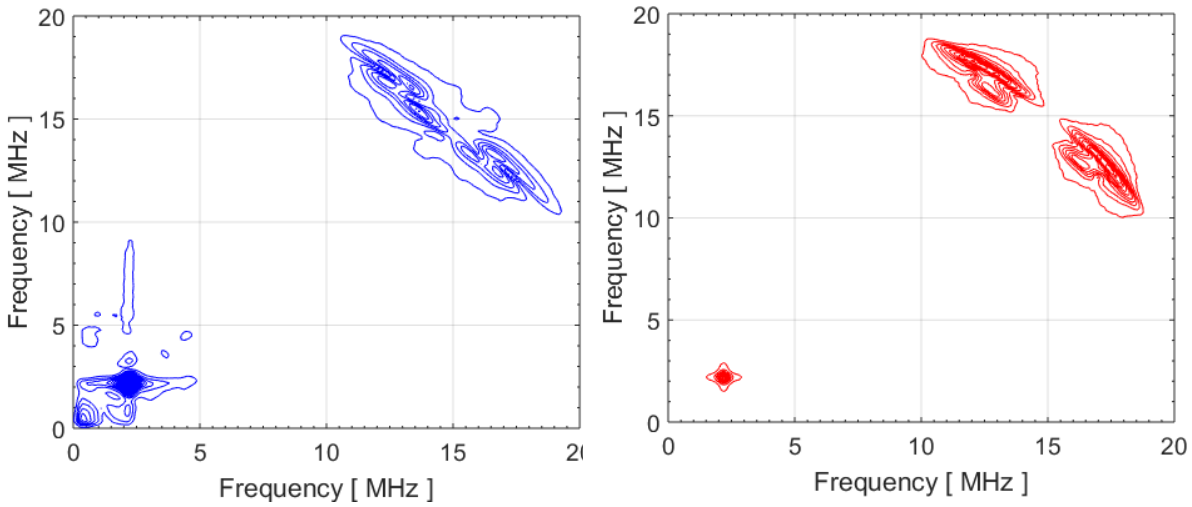

Figure F.14. *Left*: Typical X-band HYSCORE spectrum recorded at 10 K for a 5 mM deuterated toluene solution of **19**. The experimental conditions for the current spectrum are: microwave frequency, ν =9.70 GHz; temperature, shot repetition time, 499.8 ⍰s; $t_{⍰/2}$ = 16 ns; delay between the first and second microwave pulse, τ = 200 ns; magnetic field 340 mT (g = 2.004). *Right*: Simulated HYSCORE spectrum obtained considering the coupling of the S = 1/2 electronic spin to three distinct ^{1}H, I = 1/2 nuclei characterized by anisotropic tensors such that $A_{x,y,z}(1)$ = {-3, -1, -3} MHz, $A_{x,y,z}(2)$ = {1, 1, 9} MHz, $A_{x,y,z}(3)$ = {3, 0, 2} MHz and a ^{2}H, I = 1 with an isotropic HFC tensor A_{iso}= 0.05 MHz.

7. Computational Details

DFT[98] calculations were carried out using Revision D01 of Gaussian 09.[99] Geometry optimizations were performed at the B3LYP/6-31G(d) level of theory.[63] Reoptimization of the lowest energy spin state, **19** doublet, with the 6-311G(d) basis set did not improve the bond lengths and characterization of the wavefunction was the same based on Mulliken spin densites (**Table F.2**). Therefore, our analysis in the manuscript focuses on the double-zeta results. All optimized structures were

confirmed to have stable wavefunctions[100] and to be minima on the potential energy surface.[101] Thermodynamics for each species may be found in **Table F.6**.

Table F.2. Comparison of Co–L bond lengths (Å) and Mulliken spin densities.

	Exp.	**B3LYP 6-31G(d)**	**B3LYP 6-311G(d)**
Co–C	1.773	1.823	1.827
Co–O	1.765	1.759	1.768
Co spin	-	1.77	1.73
C spin	-	–0.68	–0.67
O spin	-	0.05	0.07

The electronic structure of **19** was re-evaluated at the B3LYP/6-31G(d) optimized geometry using (i) OPBE,[17] a functional that excels at predicting spin state energies,[18] and (ii) ωB97-XD,[19] a long-range corrected functional. As **Table F.3** demonstrates, the Co^{III}–$C^{\bullet}$ vs. Co^{IV}=C character, which is ideally 2.0 and –1.0 for the former and 1.0 and 0.0 for the latter, is sensitive to the functional choice. OPBE predicts the most Co^{IV}=C character and shows the least spin contamination, as tracked by the S^2 value after projection of the first spin contaminant, and ωB97-XD predicts the most Co^{III}–$C^{\bullet}$ character. Both the amount of spin contamination and the Co^{IV}=C character is correlated with the amount of explicit Hartree-Fock exchange in each functional, reminiscent of spin state energies (see Ref 12 in manuscript). To benchmark our expectations for a true M^{IV}=C system, we optimized the hypothetical species replacing Co with Rh at the B3LYP/SDD/6-31G(d) level of theory.[20] This complex has an optimized Rh–C bond length of 1.858 Å that is shorter than the dirhodium carbenes that are known experimentally. As shown in **Table F.3**, none of these wavefunctions suffer from spin contamination, yet the amount of spin density on the carbene C varies from –0.07 for OPBE to –0.25 for ωB97-XD. Thus, even in this ideal alkylidene system, spin polarization can place up to ~0.3 electrons worth of spin on the neighboring carbene C. While a

definitive answer would require multireference techniques (*e.g.* CASSCF) that are not feasible for this sized system, we believe the relatively small spin contaminations, comparison to the hypothetical Rh complex, and bond elongation from the Co doublet to quartet state allow us to conclude that there is significant π-bonding between Co and the diphenylcarbene.

Table F.3. Comparison of Mulliken spin densities for **19** with different functionals and $\mathbf{19_{Rh}}$.

	19			$\mathbf{19_{Rh}}$		
	B3LYP	**OPBE**	**ωB97-XD**	**B3LYP**	**OPBE**	**ωB97-XD**
M spin	1.77	1.42	1.89	0.91	0.78	1.02
C spin	–0.68	–0.44	–0.82	–0.16	–0.07	–0.25
O spin	0.05	0.07	0.05	0.12	0.12	0.12
S^2	0.88	0.77	0.99	0.75	0.75	0.75

To further validate the electronic structure of **19**, we simulated the EPR parameters with ORCA.[110] A summary of the predicted hyperfine couplings may be found in **Table F.4**. The simulated spectra based on these values are shown in **Figure F.15**, and visualization of the directionality of the tensor components may be seen in **Figure F.16**. Inspection of **Table F.5** shows that the lowest 1-electron excitation corresponds to the promotion of a β, spin-down electron from the doubly-occupied dx^2-y^2 orbital to the singly-occupied d*xy* orbital. Interestingly, the two orbital states corresponding to the ground and first excited orbital states are mixed by the *z* component of the spin-orbit operator $\hat{H}_{SO} = \lambda \vec{\mathbf{L}} \cdot \vec{\mathbf{S}}$. Consequently, the largest orbital contributions to the g and A(^{59}Co) tensors are expected along the z-direction along the Co–C bond.

Table F.4. Simulated hyperfine coupling tensor components at the B3LYP/6-31G(d) level within the diphenylcarbene Co portion of the complex. FC = Fermi contact, SD = spin dipole. ^{1}H values for the ortho, para, and meta substituents are averaged over both phenyl rings.

	$\mathbf{A_{FC}}$	$\mathbf{A_{SD}}$			$\mathbf{A_{FC+SD}}$		
^{59}Co	+368	-108	-76	185	260	292	553
$^{13}C^{a}$	-144	-68	27	41	-212	27	41
$^{1}H_{ortho}$	8.3	-7.2	-1.8	9.0	1.1	6.5	17.3
$^{1}H_{para}$	8.1	-4.0	0.0	4.0	4.1	8.1	12.1
$^{1}H_{meta}$	-4.2	-1.6	0.3	1.3	-5.8	-3.9	-2.9

a. C in diphenylcarbene bound to Co.

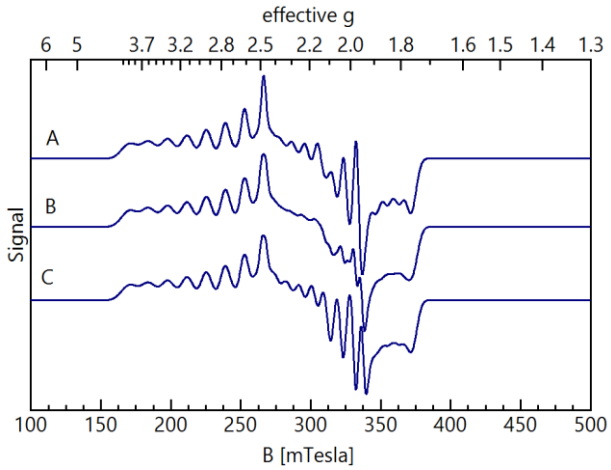

Figure F.15. (A) Simulation of the X-band spectrum shown in **Figure 62**; (B) Simulation of the X-band spectrum shown in **Figure 62** that also includes a I = 1/2, ^{13}C nuclei with an isotropic HFC tensor such that A_{iso} = -144 MHz i.e., the DFT-predicted value; (C) Simulation of the X-band spectrum shown in **Figure 62** that also includes a I = 1/2, ^{13}C nuclei with a HFC tensor such that A_x = -103 MHz, A_y = -212 MHz, and A_z = -103 MHz. These values were obtained from the sum of the DFT-predicted, B3LYP/6-31G(d), Fermi-contact and spin-dipolar contributions to the HFC tensor.

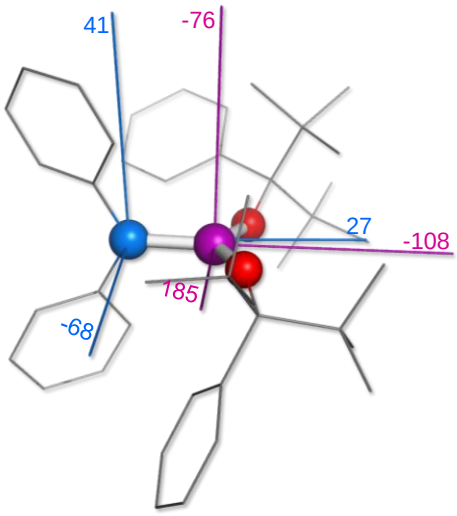

Figure F.16. Relative orientations of the spin-dipolar components of the HFC tensors of the ^{13}C shown in blue and ^{59}Co shown in purple predicted at B3LYP/6-31G(d) level. The predicted values of the principal tensor components are shown near their respective axis and are expressed in MHz. The Fermi-contact values of the HFC tensor predicted for the ^{13}C nucleus is -144 MHz and respectively, +368 MHz for the ^{59}Co nucleus, see **Table F.4**. Analysis of the TD-DFT excitations suggests that the g tensor is oriented such that its largest component, $g_{max} \sim 3$, is found along the Co-C axis and that the intermediate value, $g_{mid} \sim 2.2$, is perpendicular to the plane defined by the Co-O bonds, see **Table F.5**.

Table F.5. Isosurface plots (iso = 0.05 au) of the TD-DFT derived Natural Transition Donor (NTDO) and Acceptor (NTAO) orbitals[111] involved in the lowest three single-electron excitations. We define the z axis to contain the Co-C bond, the yz plane to contain the ipso carbons of diphenylcarbene, and the xy plane to contain the Co–$O_{alkoxide}$ bonds. These transitions are consistent with either an intermediate-spin Co^{III} ion $|d_{yz}^2 d_{x2-y2}^2 d_{xy}^1 d_{xz}^1 d_{z2}^0|$ or a low-spin Co^{IV} ion $|d_{yz}^2 d_{x2-y2}^2 d_{xy}^1 d_{xz}^0 d_{z2}^0|$.

Excitation Energy (eV)	NTDO	NTAO	Description
0.5570	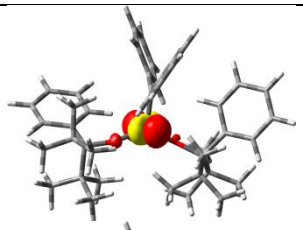	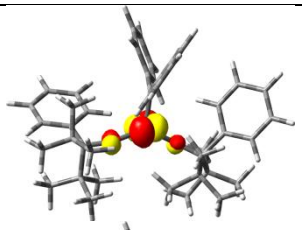	$d_{x2-y2} \rightarrow d_{xy}$ (β)
0.7439	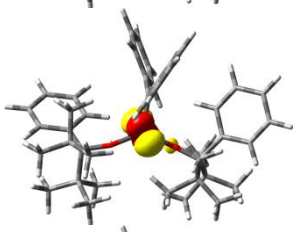	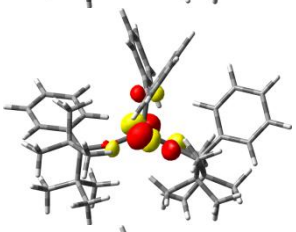	$d_{yz} \rightarrow d_{xy}$ (β)
1.0747	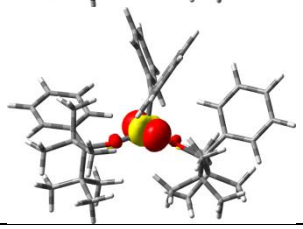	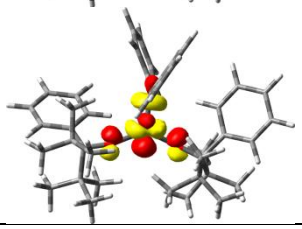	$d_{x2-y2} \rightarrow d_{z2}$ (β)

Table F.6. Energies (in E_h) for all species at the B3LYP/6-31G(d) level of theory (SDD for Rh). Some small (< 50 cm^{-1}) imaginary frequencies corresponding to methyl and/or phenyl rotations in the alkoxide ligand were ignored for the higher energy spin states of **19**.

Species	E(SCF)	H(gas)	G(gas)
19 doublet	–3205.335533	–3204.398353	–3204.528927
19 quartet	–3205.324277	–3204.390002	–3204.519235
19 sextet	–3205.315018	–3204.380249	–3204.511710
quartet @ **19** doublet	–3205.312649	-	-
$\mathbf{19_{Rh}}$ doublet	–1933.220962	–1932.284802	–1932.416418

REFERENCES

1. (a) Bräse, S.; Gil, C.; Knepper, K.; Zimmermann, V. *Angew. Chem. Int. Ed.* **2005**, *44*, 5188-5240. (b) Bräse, S.; Banert, K. *Organic Azides: Syntheses and Applications*; John Wiley & Sons, Ltd.: United Kingdom, 2010.

2. (a) Fulton, J. R.; Holland, A. W.; Fox, D. J.; Bergman, R. G. *Acc. Chem. Res.* **2002**, *35*, 44-56. (b) Eikey, R. A.; Abu-Omar, M. M. *Coord. Chem. Rev.* **2003**, *243*, 83-124. (b) Mehn, M. P.; Peters, J. C. *J. Inorg. Biochem.* **2006**, *100*, 634-643. (c) Ray, K.; Heims, F.; Pfaff, F. F. *Eur. J. Inorg. Chem.* **2013**, 3784-3807.

3. (a) Müller, P.; Fruit, C. *Chem. Rev.* **2003**, *103*, 2905-2919. (b) Cenini, S.; Gallo, E.; Caselli, A.; Ragaini, F.; Fantauzzi, S.; Piangiolino, C. *Coord. Chem. Rev.* **2006**, *250*, 1234-1253. (c) Hartwig, J. F. *Organotransition Metal Chemistry: From Bonding to Catalysis*; University Science Books: Mill Valley, CA, 2010. (d) Driver, T. G. *Org. Biomol. Chem.* **2010**, *8*, 3831-3846. (e) Abu-Omar, M. M. *Dalton Trans.* **2011**, *40*, 3435-3444. (f) Roizen, J. L.; Harvey, M. E.; Du Bois, J. *Acc. Chem. Res.* **2012**, *45*, 911-922. (g) Zhang, L.; Deng, L. *Chin. Sci. Bull.* **2012**, *57*, 2352-2360. (h) Intrieri, D.; Zardi, P.; Caselli, A.; Gallo, E. *Chem. Commun.* **2014**, *50*, 11440-11453.

4. (a) Laskowski, C. A.; Miller, A. J. M.; Hillhouse, G. L.; Cundari, T. R. *J. Am. Chem. Soc.* **2011**, *133*, 771-773. (b) King, E. R.; Hennessy, E. T.; Betley, T. A. *J. Am. Chem. Soc.* **2011**, *133*, 4917-4923. (c) King, E. R.; Sazama, G. T.; Betley, T. A. *J. Am. Chem. Soc.* **2012**, *134*, 17858-17861. (d) Jenkins, D. M. *Synlett* **2012**, 1267-1270. (e) Xiao, J.; Deng, L. *Dalton Trans.* **2013**, *52*, 5607-5610. (f) Zhang, L.; Liu, Y.; Deng, L. *J. Am. Chem. Soc.* **2014**, *136*, 15525-15528.

5. Dow Chemical. Dow Specialty Amines-Applications. http://www.dow.com/amines/apps/ (accessed Mar 23, 2016).

6. (a) Mindiola, D. J.; Hillhouse, G. L. *Chem. Commun.* **2002**, 1840-1841. (b) Baidiei, Y. M.; Krishnaswamy, A.; Melzer, M. M.; Warren, T. H. *J. Am. Chem. Soc.* **2006**, *128*, 15056-15057.

7. Centers for Disease Control and Prevention. Isocyanates. http://www.cdc.gov/niosh/topics/isocyanates/ (accessed Mar 23, 2016).

8. (a) Hansert, B.; Vahrenkamp, H. J. Organomet. Chem. **1993**, *459*, 265-269. (b) Ragaini, F.; Penoni, A.; Gallo, E.; Tollari, S.; Gotti, C. L.; Lapadula, M.; Mangioni, E.; Cenini, S. *Chem. Eur. J.* **2003**, *9*, 249-259. (c) Zarkesh, R. A.; Ziller, J. W.; Heyduk, A. F. *Angew. Chem., Int. Ed.* **2008**, *47*, 4715-4718. (d) Harrold, N. D.; Waterman, R.; Hillhouse, G. L.; Cundari, T. R. *J. Am. Chem. Soc.* **2009**, *131*, 12872-12873. (e) Mankad, N. P.; Müller, P., Peters, J. C. *J. Am. Chem. Soc.* **2010**, *132*, 4083-4085. (f) Heyduk, A. F.; Zarkesh, R. A.; Nguyen, A. I. *Inorg. Chem.* **2011**, *50*, 9849-9863. (g) Takaoka, A.; Moret, M.-E.; Peters, J. C. *J. Am. Chem. Soc.* **2012**, *134*, 6695-6706.

9. (a) Ashutosh, P. N. D.; Mehrotra, J. K. *Colourage* **1979**, *26*, 25. (b) Hunger, K. *Industrial Dyes: Chemistry, Properties, Applications*, 3rd ed.; Wiley-VCH: Weinheim, Germany, 2003.

10. Ikeda, T.; Tsutsumi, O. *Science* **1995**, *268*, 1873-1875.

11. Feringa, B. L.; Van Delden, R. A.; Koumura, N.; Geertsema, E. M. *Chem. Rev.* **2000**, *100*, 1789-1816.

12. Li, X. Y.; Wu, Y. Z.; Gu, D. D.; Gan, F. X. *Mater. Sci, Eng. B* **2009**, *158*, 53-57.

13. Roldo, M.; Barbu, E.; Brown, J. F.; Laight, D. W.; Smart, J. D.; Tsibouklis, J. *Expert Opin. Drug Delivery* **2007**, *4*, 547-560.

14. (a) Cowley, R. E.; Elhaik, J.; Eckert, N. A.; Brennessel, W. W.; Bill, E.; Holland, P. L. *J. Am. Chem. Soc.* **2008**, *130*, 6074-6075. (b) Bonyhady, S. J.; Green, S. P.; Jones, C.; Nembenna, S.; Stasch, A. *Angew. Chem. Int. Ed.* **2009**, *48*, 2973-2977. (c) Bonyhady, S. J.; Jones, C.; Nembenna, S.; Stasch, A.; Edwards, A. J.; McIntyre, G. J. *Chem. Eur. J.* **2010**, *16*, 938-955. (d) Gondzik, S.; Schulz, S.; Bläser, D.; Wölper, C.; Haack, R.; Jansen, G. *Chem. Commun.* **2014**, *50*, 927-929. (e) Fohlmeister, L.; Jones, C. *Aust. J. Chem.* **2014**, *67*, 1011-1016.

15. (a) Gondzik, S.; Wölper, C.; Haack. R.; Jansen, G.; Schulz, S. *Dalton Trans.* **2015**, *44*, 15703-15711. (b) Steinen, C.; Gondzik, S.; Gehlhaar, A.; Haack, R.; Wölper, C.; Jansen, S.; Schulz, S. *Organometallics* **2016**. *In press.*

16. (a) Cardin, D. J.; Cetinkaya, B.; Lappert, M. F. *Chem. Rev.* **1972**, *72*, 545-574. (b) Doyle, M. P.; Forbes, D. C. *Chem. Rev.* **1998**, *98*, 911-935. (c) Davies, H. M. L.; Beckwith, R. E. *J. Chem. Rev.* **2003**,

103, 2861-2903. (d) Lebel, H.; Marcoux, J. F.; Molinaro, C.; Charette, A. B. *Chem. Rev.* **2003**, *103*, 977-1050. (e) Doyle, M. P.; Duffy, R.; Ratnikov, M.; Zhou, L. *Chem. Rev.* **2010**, *110*, 704-724.

17. (a) Brookhart, M.; Studabaker, W. B. *Chem. Rev.* **1987**, *87*, 411-432. (b) Kirmse, W. *Angew. Chem., Int. Ed.* **2003**, *42*, 1088-1093. (c) Wee, A. G. H. *Curr. Org. Synth.* **2006**, *3*, 499-555. (d) Davies, H. M. L.; Hedley, S. J. *Chem. Soc. Rev.* **2007**, *36*, 1109-1119.

18. Kumar, A. *Int. J. Pharm. Pharm. Sci.* **2013**, *5*, 467-472.

19. Metcalf, R. L. *Ullmann's Encyclopedia of Industrial Chemistry*; Wiley-VCH: Weinheim, Germany, 2002.

20. (a) Doyle, M. P. *Acc. Chem. Res.* **1986**, *19*, 348-356. (b) Harvey, D. F.; Sigano, D. M. *Chem. Rev.* **1996**, *96*, 271-288. (c) James, O. O.; Chowdhury, B.; Mesubi, M. A.; Maity, S. *RSC Adv.* **2012**, *2*, 7347-7366.

21. (a) Schrock, R. R. *Polyhedron* **1995**, *14*, 3177-3195. (b) Schrock, R. R.; Hoveyda, A. H. *Angew. Chem. Int. Ed.* **2003**, *42*, 4592-4633.

22. Mol, J. C. *J. Mol. Cat. A.* **2004**, *213*, 39-45.

23. Gianetti, T. L.; Bergman, R. G.; Arnold, J. *Chem. Sci.* **2014**, *5*, 2517-2524.

24. Waterman, R.; Hillhouse, G. L. *J. Am. Chem. Soc.* **2003**, *125*, 13350-13351.

25. (a) Paulissen, R.; Reimlinger, H.; Hayez, E.; Hubert, A. J.; Teyssié, P. *Tetrahedron Lett.* **1973**, *14*, 2233-2236. (b) Lowenthal, R. E.; Abiko, A.; Masamune, S. *Tetrahedron Lett.* **1990**, *31*, 6005-6008. (c) Harvey, D. F.; Lund, K. P. *J. Am. Chem. Soc.* **1991**, *113*, 8916. (d) Doyle, M. P.; Peterson, C. S.; Zhou, Q.-L.; Nishiyama, H. *Chem. Commun.* **1997**, 211-212.

26. (a) Mindiola, D. J.; Hillhouse, G. L. *J. Am. Chem. Soc.* **2002**, *124*, 9976-9977. (b) Mankad, N. P.; Peters, J. C. *Chem. Commun.* **2008**, 1061-1063. (c) Cowley, R. E.; DeYonker, N. J.; Eckert, N. A.; Cundari, T. R.; DeBeer, S.; Bill, E.; Ottenwaelder, X.; Flaschenriem, C.; Holland, P. L. *Inorg. Chem.* **2010**, *49*, 6172-6187. (d) Marquard, S.; Bezpalko, M. W.; Foxman, B. M.; Thomas, C. M. *J. Am. Chem. Soc.* **2013**, *135*, 6018-6021. (e) Russell, S. K.; Hoyt, J. M.; Bart, S. C.; Milsmann, C.; Stieber, S. C. E.; Semproni, S. P.; DeBeer, S.; Chirik, P. C. *Chem. Sci.* **2014**, *5*, 1168-1174.

27. (a) Mehrotra, R. C. *Inorg. Chim. Acta Rev.* **1967**, *1*, 99-112. (b) Bradley, D. C.; Mehrotra, R. C.; Rothwell, I.; Singh, A. *Alkoxo and Aryloxo Derivatives of Metals*; Academic Press: London, 2001. (c) Turova, N. Y.; Turevskaya, E. P.; Kessler, V. G.; Yanovskaya, M. I. *The Chemistry of Metal Alkoxides*; Springer US: New York, 2002.

28. (a) Bradley, D. C.; Hillyer, M. J. *Trans. Faraday Soc.* **1966**, *62*, 2367. (b) Bradley, D. C.; Hillyer, M. J. *Trans. Faraday Soc.* **1966**, *62*, 2374.

29. (a) Wolczanksi, P. T. *Polyhedron* **1995**, *14*, 3335-3362. (b) Wolczanski, P. T. *Chem. Commun.* **2009**, 740-757.

30. (a) Bradley, D. C.; Mehta, M. L. *Can. J. Chem.* **1962**, *40*, 1710. (b) Ibers, J. A. *Nature* **1963**, *197*, 686-687. (c) Barraclough, C. G.; Martin, R. L.; Winter, G. *J. Chem. Soc.* **1964**, 758-762. (d) Adams, R. W.; Martin, R. L.; Winter, G. *Aust. J. Chem.* **1966**, *19*, 363-371. (e) Bradley, D. C.; Holloway, C. E. *J. Chem. Soc. A* **1968**, 219. (f) Horvath, B.; Moseler, R.; Horvath, E. G. *Z. Anorg. Allg. Chem.* **1979**, *449*, 41. (g) Chisholm, M. H.; Huffman, J. C.; Leonelli, J. *Chem. Commun.* **1981**, 270. (h) Day, V. W.; Eberspacher, T. A.; Klemperer, W. G.; Park, C. W.; Rosenberg, F. S. *J. Am. Chem. Soc.* **1991**, *113*, 8190-8192. (i) Schmid, R.; Mosset, A.; Galy, J. *J.Chem. Soc., Dalton Trans.* **1991**, 1999-2005. (j) Lv, Y.; Willkomm, J.; Leskes, M.; Steiner, A.; King, T. C.; Gan, L.; Reisner, E.; Wood, P. T.; Wright, D. S. *Chem. Eur. J.* **2012**, *18*, 11867-11870. (k) Chen, Y.; Trzop, E.; Makal, A.; Sokolow, J. D.; Coppens, P. *Inorg. Chem.* **2013**, *52*, 4750-4752.

31. (a) Kim, M.; Zakharov, L. N.; Rheingold, A. L.; Doerrer, L. H. *Polyhedron* **2005**, *44*, 1803-1812. (b) Zheng, B.; Miranda, M. O.; DiPasquale, A. G.; Golen, J. A.; Rheingold, A. L.; Doerrer, L. H. *Inorg. Chem.* **2009**, *48*, 4274-4276. (c) Cantalupo, S. A.; Lum, J. S.; Buzzeo, M. C.; Moore, C.; DiPasquale, A. G.; Rheingold, A. L.; Doerrer, L. H. *Dalton Trans.* **2010**, *39*, 374-383. (d) Cantalupo, S. A.; Ferreira, H. E.; Bataineh, E.; King, A. J.; Petersen, M. V.; Wojtasiewicz, T.; DiPasquale, A. G.; Rheingold, A. L.; Doerrer, L. H. *Inorg. Chem.* **2011**, *50*, 6584-6596. (e) Lum, J. S.; Tahsini, L.; Golen, J. A.; Moore, C.; Rheingold, A. L.; Doerrer, L. H. *Chem. Eur. J.* **2013**, *19*, 6374-6384. (f) Tahsini, L.; Specht, S. E.; Lum, J. S.; Nelson, J. J. M.; Long, A. F.; Golen, J. A.; Rheingold, A. L.; Doerrer, L. H. *Inorg. Chem.* **2013**, *52*,

14050-14063. (g) Petersen, M. V.; Iqbal, A. H.; Zakharov, L. N.; Rheingold, A. L.; Doerrer, L. H. *Polyhedron* **2013**, *52*, 276-283.

32. (a) Hvoslef, J.; Hope, H.; Murray, B. D.; Power, P. P. *J. Chem. Soc., Chem. Commun.* **1983**, 1438-1439. (b) Murray, B. D.; Power, P. P. *J. Am. Chem. Soc*. **1984**, *106*, 7011-7015. (c) Lubben, T. V.; Wolczanski, P. T.; Van Duyne, G. D. *Organometallics* **1984**, *3*, 977-983. (d) Murray, B. D.; Hope, H.; Power, P. P. *J. Am. Chem. Soc*. **1985**, *107*, 169-173. (e) Olmstead, M. M.; Power, P. P.; Sigel, G. *Inorg. Chem*. **1986**, *25*, 1027-1033. (f) Lubben, T. V.; Wolczanksi, P. T. *J. Am. Chem. Soc.* **1987**, *109*, 424-435.

33. (a) Sigel, G. A.; Bartlett, R. A.; Decker, D.; Olmstead, M. M.; Power, P. P. *Inorg. Chem*. **1987**, *26*, 1773-1780. (b) Stavropoulos, P.; Bryson, N.; Youinou, M.-T.; Osborn, J. A. *Inorg. Chem*. **1990**, *29*, 1807-1811. (c) Bartlett, R. A.; Ellison, J. J.; Power, P. P.; Shoner, S. C. *Inorg. Chem*. **1991**, *30*, 2888-2894. (d) Ohta, S.; Ohki, Y.; Hashimoto, T.; Cramer, R. E.; Tatsumi, K. *Inorg. Chem*. **2012**, *51*, 11217−11219.

34. (a) Bochmann, M.; Wilkinson, G.; Young, G. B.; Hursthouse, M. B.; Malik, K. M. A. *J. Chem. Soc., Dalton Trans.* **1980**, 1863-1871. (b) Nakahara, K.; Mitsui, C.; Okamoto, T.; Yamagishi, M.; Miwa, K.; Sato, H.; Yamano, A.; Uemura, T.; Takeya, J. *Chem. Lett*. **2013**, *42*, 654-656.

35. (a) Groysman, S.; Villagrán, D.; Nocera, D. G. *Inorg. Chem.* **2010**, *49*, 10759-10761. (b) Groysman, S.; Villagrán, D.; Freedman, D. E.; Nocera, D. G. *Chem. Commun.* **2011**, *47*, 10242-10244. (c) Chambers, M. B.; Groysman, S.; Villigran, D.; Nocera, D. G. *Inorg. Chem.* **2013**, *52*, 3159-3169.

36. (a) Bartlett, P. D.; Lefferts, E. B. *J. Am. Chem. Soc*. **1955**, *77*, 2804-2805. (b) Syper, L. *Rocz. Chem.* **1973**, *47*, 433-439.

37. Bestian, H.; Clauss, K. Organo-titanium compounds and a process to prepare them. US 3104249 (A), September 17, 1963.

38. (a) Jenkins, D. M.; Peters, J. C. *J. Am. Chem. Soc.* **2003**, *125*, 11162-11163. (b) Evans, D. J.; Hill, M. S.; Hitchcock, P. B. *Dalton Trans*. **2003**, 570–574.

39. Purdy, A. P.; George, C. F.; Callahan, J. H. *Inorg. Chem*. **1991**, *30*, 2812-2819.

40. (a) Ferguson, R.; Solari, E.; Floriani, C.; Osella, D.; Ravera, M; Re, N.; Chiesi-Villa, A.; Rizzoli, C. *J. Am. Chem. Soc.* **1997**, *119*, 10104-10115. (b) Kawaguchi, H.; Matsuo, T. *Angew. Chem., Int. Ed.* **2002**, *41*, 2792-2794.

41. (a) Shilov, A. E.; Denisov, N. T.; Efimov, O. N.; Shuvalov, V. F.; Shuvalova, N. I.; Shilova, A. K. *Nature*, **1971**, *231*, 460. (b) Shilov, A. E. In *New Trends in the Chemistry of Nitrogen Fixation*; Chatt, J.; da Camara Pina, L. M.; Richards, R. L.; Academic Press: London, 1980; p 130.

42. Winkler, J. R.; Gray, H. B. Electronic Structures of Oxo-Metal Ions. In *Molecular Electronic Structures of Transition Metal Complexes I*; Mingos, D. M. P.; Day, P.; Dahl, J. P.; Springer-Verlag: Berlin, 2012; Vol. 142; p 17-28.

43. (a) Gray, H. B.; Hare, C. R. *Inorg. Chem.* **1962**, *1*, 363. (b) Mahammed, A.; Gray, H. B.; Meier-Callahan, A. E.; Gross, Z. *J. Am. Chem. Soc.* **2003**, *125*, 1162-1163. (c) Gross, Z.; Gray, H. B. *Adv. Synth. Catal*. **2004**, *346*, 165. (d) Liu, S.; Mase, K.; Bougher, C.; Hicks, S. D.; Abu-Omar, M. M.; Fukuzumi, S. *Inorg. Chem.* **2014**, *53*, 7780-7788.

44. Somewhat related topologies are observed, but none replicates all of the structural features found in **3-6**. For selected examples, see: (a) Gun'ko, Y. K.; Cristmann, U.; Kessler, V. G. *Eur. J. Inorg. Chem.* **2002**, 1029-1031. (b) Anson, C. E.; Klopper, W.; Li, J.-S.; Ponikiewski, L.; Rothenberger, A. *Chem. Eur. J.* **2006**, *12*, 2032-2038. (c) Gallagher, D. J.; Henderson, K. W.; Kennedy, A. R.; O'Hara, C. T.; Mulvey, R. E; Rowlings, R. B. *Chem. Commun.* **2002**, 376-377. (d) Drewette, K. J.; Henderson, K. W.; Kennedy, A. R.; Mulvey, R. E.; O'Hara, C. T.; Rowlings, R. B. *Chem. Commun.* **2002**, 1176-1177. (e) Kennedy, A. R.; Klett, J.; Mulvey, R. E.; Newton, S.; Wright, D. S. *Chem. Commun.* **2013**, *42*, 6676-6693.

45. Eckert, N. A.; Smith, J. M.; Lachicotte, R. J.; Holland, P. L. *Inorg. Chem.* **2004**, *43*, 3306-3321.

46. Randall, C. R.; Shu, L.; Chiou, Y.-M.; Hagen, K. S.; Ito, M.; Kitajima, N.; Lachicotte, R. J.; Zang, Y.; Que, Jr., L. *Inorg. Chem.* **1995**, *34*, 1036-1039.

47. (a) Zabrodsky, H.; Peleg, S.; Avnir, D. *J. Am. Chem. Soc.* **1992**, *114*, 7843-7851. (b) Pinsky, M.; Avnir, D. *Inorg. Chem.* **1998**, *37*, 5575-5582.

48. Cicera, J.; Alemany, P.; Alvarez, S. *Chem. Eur. J.* **2004**, *10*, 190-207.

49. Evans, D. F. *J. Chem. Soc.* **1959**, 2003-2005.

50. Silvi, B.; Savin, A. *Nature* **1994**, *371*, 683-686.

51. (a) Johnson, E. R.; Keinan, S.; Mori-Sánchez, P.; Contrera-García, J.; Cohen, A. J.; Yang, W. *J. Am. Chem. Soc.* **2010**, *132*, 6498-6506. (b) Contreras-García, J.; Johnson, E. R.; Keinan, S.; Chaudret, R.; Piquemal, J.-P.; Beratan, D. N.; Yang, W. *J. Chem. Theory Comput.* **2011**, *7*, 625-632.

52. (a) Gillet, N.; Chaudret, R.; Contreras-García, J.; Yang, W.; Silvi, B.; Piquemal, J.-P. *J. Chem. Theory Comput.* **2012**, *8*, 3993-3997. (b) Fang, D.; Chaudret, R.; Piquemal, J.-P.; Cisneros, G. A. *J. Chem. Theory Comput.* **2013**, *9*, 2156-2160. (c) Fang, D.; Lord, R. L.; Cisneros, G. A. *J. Phys. Chem. B* **2013**, *117*, 6410-6420.

53. (a) Greiser, T.; Weiss, E. *Chem. Ber.* **1976**, *109*, 3142-3146. (b) Lopes, C.; Håkansson, M.; Jagner, S. *Inorg. Chem.* **1997**, *36*, 3232-3236. (c) Håkansson, M.; Lopes, C.; Jagner, S. *Inorg. Chim. Acta* **2000**, *304*, 178-183.

54. For selected studies on the *β*-scission of alkoxy radicals, see: (a) Richardson, W. H.; Yelvingtoan, B.; Andrist, H.; Ertlyer, W.; Smith, S.; Johnson, T. D. *J. Org. Chem.* **1973**, *38*, 4219-4225. (b) Weber, M.; Fischer, H. *J. Am. Chem. Soc.* **1999**, *121*, 7381-7388. (c) Buback, M.; Kling, M.; Schmatz, S. *Z. Phys. Chem.* **2005**, *219*, 1205-1222.

55. Bain, G. A.; Berry, J. F. *J. Chem. Educ.* **2008**, *85*, 532-536.

56. (a) Deacon, G. B.; Goh, L. Y.; Jackson, W. R.; Skelton, B. W.; Chen, W.; White, A. H. *Z. Anorg. Allg. Chem.* **2010**, *636*, 1478-1483. (b) Kondaveeti, S. K.; Vaddypally, S.; Lam, C.; Hirai, D.; Ni, N.; Cava, R. J.; Zdilla, M. J. *Inorg. Chem.* **2012**, *51*, 10095-10104.

57. For a discussion on the magnetic properties of two-coordinate complexes, see: Power, P. P. *Chem. Rev.* **2012**, *112*, 3482-3507.

58. (a) Ni, C.; Power, P. P. *Chem. Commun.* **2009**, 5543-5545. (b) Hatanaka, T.; Miyake, R.; Ishida, Y.; Kawaguchi, H. *J. Organomet. Chem.* **2011**, *696*, 4046-4050. (c) Bryan, A. M.; Long, G. J.; Grandjean, F.; Power, P. P. *Inorg. Chem.* **2014**, *53*, 2692-2698.

59. Buzzeo, M. C.; Iqbal, A. H.; Long, C. M.; Millar, D.; Patel, S.; Pellow, M. A.; Saddoughi, S. A.; Smenton, A. L.; Turner, J. F. C.; Wadhawan, J. D.; Compton, R. G.; Golen, J. A.; Rheingold, A. L.; Doerrer, L. H. *Inorg. Chem.* **2004**, *43*, 7709-7725.

60. (a) O'Keefe, B. J.; Monnier, S. M.; Hillmyer, M. A.; Tolman, W. B. *J. Am. Chem. Soc.* **2001**, *123*, 339-340. (b) O'Keefe, B. J.; Breyfogle, L. E.; Hillmyer, M. A.; Tolman, W. B. *J. Am. Chem. Soc.* **2002**, *124*, 4384-4393.

61. Gao, H.; Shreeve, J. M. *Chem. Rev.* **2011**, *111*, 7377-7436.

62. Optimizations were done at the B3LYP/LANL2DZ/6-31G(d, p) level of theory (2, 3) with a B3LYP/def2-TZVP(4) single-point energy refinement.

63. (a) Vosko, S. H.; Wilk, L.; Nusair, M. *Can. J. Phys.* **1980**, *58*, 1200-1211. (b) Lee, C.; Yang, W.; Parr, R. G. *Phys. Rev. B* **1988**, *37*, 785-789. (c) Becke, A. D. *J. Chem. Phys.* **1993**, *98*, 5648-5652. (d) Stephens, P. J.; Devlin, F. J.; Chabalowski, C. F.; Frisch, M. J. *J. Phys. Chem.* **1994**, *98*, 11623-11627.

64. (a) Hay, P. J.; Wadt, W. R. *J. Chem. Phys.* **1985**, *82*, 270-283. (b) Wadt, W. R.; Hay, P. J. *J. Chem. Phys.* **1985**, *82*, 284-298. (c) Hay, P. J.; Wadt, W. R. *J. Chem. Phys.* **1985**, *82*, 299-310.

65. Weigend, F.; Ahlrichs, R. *Phys. Chem. Chem. Phys.* **2005**, *7*, 3297-3305.

66. Legault, C. Y. *CYLview*, version 1.0b; Université de Sherbrooke: Sherbrooke, Quebec, Canada, 2009; http://www.cylview.org

67. These functional were chosen because they favor high- and low-spin states, respectively.

68. Lord, R. L.; Schultz, F. A.; Baik, M.-H. *J. Am. Chem. Soc.* **2009**, *131*, 6189-6197 and references cited therein.

69. (a) Swart, M.; Groenhof, A. R.; Ehlers, A. W.; Lammertsma, K. *J. Am. Chem. Soc.* **2004**, *108*, 5479-5483. (b) Wasbotten, I. H.; Ghosh, A. *Inorg. Chem.* **2007**, *46*, 7878-7890.

70. (a) Laitar, D. S.; Mathison, C. J. N.; Davis, W. M.; Sidighi, J. P. *Inorg. Chem.* **2003**, *42*, 7354-7356. (b) Barral, K.; Moorhouse, A. D.; Moses, J. E. *Org. Lett.* **2007**, *9*, 1809-1811. (c) Wiese, S.; Aguila, M. J. B.; Kogut, E.; Warren, T. H. *Organometallics* **2013**, *32*, 2300-2308.

71. (a) Clegg, W.; Sheldrick, G. M.; Stalke, D.; Bhaduri, S.; Khwaja, H. K. *Acta Crystallogr.* **1984**, *C40*, 2045-2047. (b) Link, H.; Decker, A.; Fenske, D. *Z. Anorg. Allg. Chem.* **2000**, *626*, 1567-1574. (c) Duncan, J. S.; Nazif, T. M.; Verma, A. K.; Lee, S. C. *Inorg. Chem.* **2003**, *42*, 1211-1224. (d) Takemoto, S.; Ogura, S.; Yo, H.; Hosokoshi, Y.; Kamikawa, K.; Matsuzaka, H. *Inorg. Chem.* **2006**, *45*, 4871-4873. (e) Duncan, J. S.; Zdilla, M. J.; Lee, S. C. *Inorg. Chem.* **2007**, *46*, 1071-1080. (f) Zdilla, M. J.; Verma, A. K.; Lee, S. C. *Inorg. Chem.* **2011**, *50*, 1551-1562. (g) Zhang, Q.; Xiang, L.; Deng, L. *Organometallics* **2012**, *31*, 4537-4543.

72. (a) Proulx, G.; Bergman, R. G. *J. Am. Chem. Soc.* **1995**, *117*, 6382-6383. (b) Fickes, M. G.; Davis, W. M.; Cummins, C. C. *J. Am. Chem. Soc.* **1995**, *117*, 6384-6385. (c) Barz, M.; Herdtweck, E.; Thiel, W. R. *Angew. Chem., Int. Ed.* **1998**, *37*, 2262-2265. (d) Albertin, G.; Antoniutti, S.; Baldan, D.; Castro, J.; Garcia-Fontan, S. *Inorg. Chem.* **2008**, *47*, 742-748. (e) Nieto, I.; Ding, F.; Bontchev, R. P.; Wang, H.; Smith, J. M. *J. Am. Chem. Soc.* **2008**, *130*, 2716-2717. (f) Ni, C.; Fettinger, J. C.; Long, G. J.; Brynda, M.; Power, P. P. *Chem. Commun.* **2008**, 6045-6047. (g) Scepaniak, J. J.; Young, J. A.; Bontchev, R. P.; Smith, J. M. *Angew. Chem., Int. Ed.* **2009**, *48*, 3158-3160. (h) Moret, M.-E.; Peters, J. C. *Angew. Chem., Int. Ed.* **2011**, *50*, 2063-2067. (i) Searles, K.; Fortier, S.; Khusniyarov, M. M.; Caroll, P. J.; Sutter, J.; Meyer, K.; Mindiola, D. J.; Caulton, K. G. *Angew. Chem., Int. Ed.* **2014**, *53*, 14139-14143.

73. Becke, A. D. *J. Chem. Phys.* **1993**, *98*, 1372-1377.

74. (a) Reiher, M.; Salomon, O.; Hess, B. A. *Theor. Chem. Acc.* **2001**, *107*, 48-55. (b) Salomon, O.; Reiher, M.; Hess, B. A. *J. Chem. Phys.* **2002**, *117*, 4729-4737. (c) Reiher, M. *Inorg. Chem.* **2002**, *41*, 6928-6945.

75. (a) Perdew, J. P.; Burke, K.; Ernzerhof, M. *Phys. Rev. Lett.* **1996**, *77*, 3865-3868. (b) Handy, N. C.; Cohen, A. J. *Mol. Phys.* **2001**, *99*, 403-412.

76. Swart, M. *J. Chem. Theory Comput.* **2008**, *4*, 2057-2066.

77. Hu, M.; Rong, J.; Miao, W.; Ni, C.; Han, Y.; Hu, J. *Org. Lett.* **2014**, *16*, 2030-2033.

78. (a) Bethell, D.; Eeles, M. F. *J. Chem. Soc., Perkin Trans. 2: Phys. Org. Chem.* **1974**, 704-710. (b) Crumrine, D. S.; Haberkamp, T. J.; Suther, D. J. *J. Org. Chem.* **1975**, *40*, 2274-2278. (c) Saha, A. K.;

Hossain, M. M.; Grubisha, D. S.; Bennett, D. W. *J. Chem. Cryst.* **1995**, *25*, 383-387. (d) Zhu, H.; Chai, J.; Stasch, A.; Roesky, H. W.; Blunk, T.; Vidovic, D.; Magull, J.; Schmidt, H.-G.; Noltemeyer, M. *Eur. J. Inorg. Chem.* **2004**, 4046-4051. (e) Bonyhady, S. J.; Goldberg, J. M.; Wedgwood, N.; Dugan, T. R.; Eklund, A. G.; Brennessel, W. W.; Holland, P. L. *Inorg. Chem.* **2015**, *54*, 5148-5150.

79. Parham, W. E.; Hasek, W. R. *J. Am. Chem. Soc.* **1954**, *76*, 935-936.

80. (a) Esposito, V.; Solari, E.; Floriani, C. *Inorg. Chem.* **2000**, *39*, 2604-2613. (b) Lindley, B. M.; Jacobs, B. P.; MacMillan, S. N.; Wolczanski, P. T. *Chem. Commun.* **2016**, *52*, 3891-3894.

81. (a) Kornecki, K. P.; Briones, J. F.; Boyarskikh, V.; Fullilove, F.; Autschbach, J.; Schrote, K. E.; Lancaster, K. M.; Davies, H. M. L.; Berry, J. F. *Science* **2013**, *342*, 351-354. (b) Werlé, C.; Goddard, R.; Fürstner, A. *Angew. Chem. Int. Ed.* **2015**, *54*, 15452-15456.

82. Harrison, D. J.; Gorelsky, S. I.; Lee, G. M.; Korobkov, I.; Baker, R. T. *Organometallics* **2013**, *32*, 12-15.

83. Lee, W.-T.; Jeon, I.-R.; Xu, S.; Dickie, D. A.; Smith, J. M. *Organometallics* **2014**, *33*, 5654-5659.

84. (a) Nakamura, A.; Konishi, A.; Tatsuno, Y.; Otsuka, S. *J. Am. Chem. Soc.* **1978**, *100*, 3443-3448. (b) Nakamura, A.; Konishi, A.; Tsujitani, R.; Kudo, M.; Otsuka, S. *J. Am. Chem. Soc.* **1978**, *100*, 3449-3461. (c) Niimi, T.; Uchida, T.; Irie, R.; Katsuki, T. *Tetrahedron Lett.* **2000**, *41*, 3647-3651. (d) Ikeno, T.; Sato, M.; Sekino, H.; Nishizuka, A.; Yamada, T. *Bull. Chem. Soc. Jpn.* **2001**, *74*, 2139-2150. (e) Niimi, T.; Uchida, T.; Irie, R.; Katsuki, T. *Adv. Synth. Catal.* **2001**, *33*, 79-88. (f) Huang, L.; Chen, Y.; Gao, G.-Y.; Zhang, X. P. *J. Org. Chem.* **2003**, *68*, 8179-8184. (g) Chen, Y.; Fields, K. B.; Zhang, X. P. *J. Am. Chem. Soc.* **2004**, *126*, 14718-14719. (h) Chen, Y.; Zhang, X. P. *J. Org. Chem.* **2007**, *72*, 5931-5934. (i) Chen, Y.; Ruppel, J. V.; Zhang, X. P. *J. Am. Soc. Chem.* **2007**, *129*, 12074-12075. (j) Zhu, S.; Ruppel, J. V.; Lu, H.; Wojtas, L.; Zhang, X. P. *J. Am. Chem. Soc.* **2008**, *130*, 5042-5043. (k) Zhu, S.; Perman, J. A.; Zhang, X. P. *Angew. Chem., Int. Ed.* **2008**, *7*, 8460-8463. (l) Fantauzzi, S.; Gallo, S.; Rose, E.; Raoul, N.; Caselli, A.; Issa, S.; Ragaini, F.; Cenini, S. *Organometallics* **2008**, *27*, 6143-6151. (m) Ruppel, J. V.; Gauthier, T. J.; Snyder, N. L.; Perman, J. A.; Zhang, X. P. *Org. Lett.* **2009**, *11*, 2273-2276. (n) Caselli, A.; Buonomenna, M. G.; de Baldironi, F.; Laera, L.; Fantauzzi, S.; Ragaini, F.; Gallo, E.; Golemme, G.;

Cenini, S.; Drioli, E. *J. Mol. Catal. A* **2010**, *317*, 72-80. (o) Morandi, B.; Mariampillai, B.; Carreira, E. M. *Angew. Chem. Int. Ed.* **2011**, *50*, 1101-1104.

85. (a) Dzik, W. I.; Xu, X.; Zhang, X. P.; Reek, J. N. H.; de Bruin, B. *J. Am. Chem. Soc.* **2010**, *132*, 10891-10902. (b) Belof, J. L.; Cioce, C. R.; Xu, X.; Zhang, X. P.; Space, B.; Woodcock, H. L. *Organometallics* **2011**, *30*, 2739-2746. (c) Lu, H.; Dzik, W. I.; Xu, X.; Wojtas, L.; de Bruin, B.; Zhang, X. P. *J. Am. Chem. Soc.* **2011**, *133*, 8518-8521.

86. (a) Carre, F.; Cerveau, G.; Colomer, E.; Corriu, R. J. P.; Young, J. C.; Ricard, L.; Weiss, R. *J. Organomet. Chem.* **1979**, *179*, 215-226. (b) Erker, G.; Lecht, R.; Petersen, J. L.; Boennemann, H. *Organometallics* **1987**, *6*, 1962-1967. (c) Filippou, A. C.; Herdtweck, E.; Alt, H. G. *J. Organomet. Chem.* **1988**, *355*, 437-447. (d) Harrison, D. J.; Lee, G. M.; Leclerc, M. C.; Korobkov, I.; Baker, R. T. *J. Am. Chem. Soc.* **2013**, *135*, 18296-18299.

87. Noodleman, L. *J. Chem. Phys.* **1981**, *74*, 5737-5743.

88. Neese, F. *J. Phys. Chem. Solids* **2004**, *65*, 781-785.

89. (a) Li, Y.; Huang,; J.-S.; Zhou, Z.-Y.; Che, C.-M.; You, X.-Z. *J. Am. Chem. Soc.* **2002**, *124*, 13185-13193. (b) Priya, S.; Balakrishna, M.-S.; Mobin, S.-M. McDonald, R. *J. Organomet. Chem.* **2003**, *688*, 227-235. (c) Dai, X.; Warren, T. H. *J. Am. Chem. Soc.* **2004**, *126*, 10085-10094. (d) Zarkesh, R. A.; Heyduk, A. F. *Organometallics* **2009**, *28*, 6629-6631. (e) Liu, H.; Wei, Y.; Cai, C. *New J. Chem.* **2016**, *40*, 674-678.

90. Scarrow, R. S.; Shearer, J. "EXAFS123 *v.* 0.3b: A general purpose K-edge data work and analysis software package." University of Nevada, Reno. 2013.

91. (a) Ankudinov, A. L.; Ravel, B.; Rehr, J. J.; Conradson, S. D. *Phys. Rev. B* **1998**, *58*, 7565. (b) Ankudinov, A. L.; Bouldin, C. E.; Rehr, J. J.; Sims, J.; Hung, H. *Phys. Rev. B* **2002**, *65*, 104107.

92. (a) Scarrow, R. C.; Brennan, B. A.; Cummings, J. G.; Jin, H.; Duong, D. J.; Kindt, J. T.; Nelson, M. *J. Biochemistry* **1996,** *35*, 10078-10088. (b) Scarrow, R. C.; Strickler, B. S.; Ellison, J. J.; Shoner, S. C.; Kovacs, J. A.; Cummings, J. G.; Nelson, M. J. *J. Am. Chem. Soc.* **1998,** *120*, 9237-9245.

93. Gaussian 09, Revision D.01, M. J. Frisch, G. W. Trucks, H. B. Schlegel, G. E. Scuseria, M. A. Robb, J. R. Cheeseman, G. Scalmani, V. Barone, B. Mennucci, G. A. Petersson, H. Nakatsuji, M. Caricato, X. Li, H. P. Hratchian, A. F. Izmaylov, J. Bloino, G. Zheng, J. L. Sonnenberg, M. Hada, M. Ehara, K. Toyota, R. Fukuda, J. Hasegawa, M. Ishida, T. Nakajima, Y. Honda, O. Kitao, H. Nakai, T. Vreven, J. A. Montgomery, Jr., J. E. Peralta, F. Ogliaro, M. Bearpark, J. J. Heyd, E. Brothers, K. N. Kudin, V. N. Staroverov, T. Keith, R. Kobayashi, J. Normand, K. Raghavachari, A. Rendell, J. C. Burant, S. S. Iyengar, J. Tomasi, M. Cossi, N. Rega, J. M. Millam, M. Klene, J. E. Knox, J. B. Cross, V. Bakken, C. Adamo, J. Jaramillo, R. Gomperts, R. E. Stratmann, O. Yazyev, A. J. Austin, R. Cammi, C. Pomelli, J. W. Ochterski, R. L. Martin, K. Morokuma, V. G. Zakrzewski, G. A. Voth, P. Salvador, J. J. Dannenberg, S. Dapprich, A. D. Daniels, O. Farkas, J. B. Foresman, J. V. Ortiz, J. Cioslowski, and D. J. Fox, Gaussian, Inc., Wallingford CT, 2010.

94. (a) Noury, S.; Krokidis, X.; Fuster, F.; Silvi, B. *Comput. Chem.* **1999**, *23*, 597-604. (b) Pilmé, J.; Piquemal, J.-P. *J. Comput. Chem.* **2008**, *29*, 1440-1449.

95. Becke, A. D.; Edgecombe, K. E. *J. Chem. Phys.* **1990**, *92*, 5397-5403.

96. Gillespie, R. J.; Robinson, E. A. *Chem. Soc. Rev.* **2005**, *34*, 396-407.

97. de Courcy, B.; Pedersen, L. G.; Parisel, O.; Gresh, N.; Silvi, B.; Pilmé, J.; Piquemal, J.-P. *J. Chem. Theory Comput.* **2010**, *6*, 1048-1063.

98. Parr, R. G.; Yang, W. *Density-Functional Theory of Atoms and Molecules*; Oxford University Press: New York, 1989.

99. Reed, B. R.; Stoian, S. A.; Lord, R. L.; Groysman, S. *Chem. Commun.* **2015**, *51*, 6496-6499.

100. (a) Schlegel, H. B.; McDouall, J.-J. In *Computational Advances in Organic Chemistry*; Oegretir, C.; Csizmadia, I. G., Eds.; Kluwer Academic: Amsterdam, The Netherlands, 1991. (b) Bauernschmitt, R.; Ahlrichs, R. *J. Chem. Phys.* **1996**, *104*, 9047-9052.

101. (a) Schlegel, H. B. *J. Comput. Chem.* **1982**, *3*, 214-218. (b) Schlegel, H. B. *WIREs Comput. Mol. Sci.* **2011**, *1*, 790-809.

102. Höfer, P.; Grupp, A.; Nebenführ, H.; Mehring, M. *Chem. Phys. Lett.*, **1986**, *132*, 279-282.

103. Gemperle, C.; Aebli, A.; Schweiger, A.; Ernst, R. R. *J. Magn. Res*. **1990**, *88*, 241-256.

104. This program can be downloaded from http://www.chem.cmu.edu/groups/hendrich/facilities/ and the spectral-simulation part of the software can be activated upon request.

105. (a) Stoll, S.; Schweiger, A. *J. Magn. Reson.* **2006**, *178*, 42. (b) Stoll, S.; Britt, R.D. *Phys. Chem. Chem. Phys.* **2009**, *11*, 6614.

106. Dogutan, D. K.; Stoian, S. A.; McGuire Jr, R.; Schwalbe, M.; Teets, T. S.; Nocera, D. G; *J. Am. Chem. Soc.* **2011**, *133*, 131-140.

107. Ozarowski, A.; Lee, H. M.; Balch, A. L. *J. Am. Chem. Soc.* **2003**, *125*, 12606-12614.

108. (a) Chai, J.-D.; Head-Gordon, M. *J. Chem. Phys.* **2008**, *128*, 084106. (b) Chai, J.-D.; Head-Gordon, M. *Phys. Chem. Chem. Phys.* **2008**, *10*, 6615.

109. (a) 6-31G(d) is not defined for Rh, so the Stuttgart basis including an ECP was employed for this atom only. (b) Bergner, A.; Dolg, M.; Küchle, W.; Stoll, H.; Preuß, H. *Mol. Phys.* **1993**, *80*, 1431.

110. (a) Neese, F. *ORCA – An ab initio, Density Functional, and Semiempirical Program Package*, Version 3.0.0. (b) Neese, F. *WIREs Comput. Mol. Sci.* **2012**, *2*, 73.

111. Martin, R. L. *J. Chem. Phys.* **2003**, *118*, 4775.

ABSTRACT

DESIGN OF FIRST-ROW TRANSITION METAL BIS(ALKOXIDE) COMPLEXES AND THEIR REACTIVITY TOWARD NITRENE AND CARBENE TRANSFER

by

JAMES A. BELLOW

August 2016

Advisor: Dr. Stanislav Groysman

Major: Chemistry (Inorganic)

Degree: Doctor of Philosophy

The novel alkoxide ligand [OC^{t}Bu$_2$Ph], or [OR], was synthesized in a single step as a lithium salt. It was then reacted with a series of first-row transition metal(II) halides, with widely varying results. Upon reaction with chromium, manganese, iron, or cobalt(II) chloride, dimeric complexes of the form $M_2(OR)_4Li_2Cl_2$ were formed, which displayed rare seesaw geometry at the metal. This unusual geometry was confirmed by various spectroscopic and computational studies. Computational studies also indicate that the steric bulk of the ligand, as well as the inclusion of lithium atoms in the molecules, are what lead to the seesaw geometry. Reaction of [OR] with nickel(II) halides generates monomeric species of the form $Ni(OR)_2XLi(THF)_2$ (X = Cl, Br), which display distorted trigonal planar geometry at three-coordinate nickel. Dimerization likely does not occur for nickel due to its smaller size. DFT studies support preference for nickel to form the monomer. Reaction of [OR] with copper(II) halides leads to reduction of the copper center by one electron, generating the tetramer $Cu_4(OR)_4$. Reduction of copper(II) by an alkoxide is a novel transformation. Spectroscopic studies to probe the mechanism suggest that $Cu(OR)_2XLi(THF)_2$ may be an intermediate prior to reduction. Observation by NMR of the ketone Ph(C=O)^{t}Bu and ROH suggest that alkoxide reduces the copper to give an alkoxide radical, which then decomposes via β-scission.

To form the desired bis(alkoxide) system, the halide-containing alkoxide complexes were reacted with thallium(I) hexafluorophosphate. For manganese, iron, and copper, complexes of the form

$M(OR)_2(THF)_2$ were isolated. The bis(alkoxide) complexes display distorted tetrahedral geometry at the metal, with large RO−M−OR angles. Cyclic voltammetry of these species show that the iron bis(alkoxide) is the most easily reduced of the three. Attempts to form the chromium bis(alkoxide) in a similar fashion led to the reduction of thallium(I) to thallium metal. Formation of the nickel bis(alkoxide) complex was also unsuccessful.

Reaction of the iron bis(alkoxide) complex with adamantyl azide led to reductive coupling of the azide moieties to give the bridging hexazene complex $(RO)_2Fe(\mu\text{-}\eta^2\text{:}\eta^2\text{-}AdN_6Ad)Fe(OR)_2$. This complex was confirmed to be stable to explosive decomposition. Computational studies suggest a dimerization mechanism, whereby azide initially coordinates to iron(II), and upon dimerization the iron centers reduce the azides before N−N bond formation occurs.

Stoichiometric reaction of the iron bis(alkoxide) complex with mesityl azide leads to nitrene formation followed by nitrene coupling to give the azoarene MesNNMes. Crystallization from a stoichiometric reaction afforded the azoarene and the iron tris(alkoxide) $Fe(OR)_3$. Catalytic azoarene formation with catalyst loading as low as 1 mol% cleanly generates azoarene at room temperature within a day or two for mesityl azide and 2,6-diethylphenyl azide. Asymmetric azoarene can also be formed by reacting mesityl azide and 2,6-diethylpheynyl azides together with the iron bis(alkoxide). This process is highly selective: azoarene is the only product formed, even if the reaction is performed in the presence of cyclohexadiene or isocyanide. Other azides (i.e. those not possessing groups in positions *ortho* to the azide on the ring) do not form azoarene upon reaction with the iron bis(alkoxide): instead they form bis(imido) complexes of the form $(RO)Fe(THF)(\mu\text{-}NAr)_2Fe(THF)(OR)$ (Ar = 4-(trifluoro)methyl, 3,5-dimethylphenyl, or phenyl). These are stable molecules that do not react with additional equivalents of aryl azide. A tentative mechanism is proposed, whereby the iron(III) imido radical $Fe(OR)_2(NAr)$ comproportionates with another equivalent of iron bis(alkoxide) to give the observed iron(III) tris(alkoxide), and the iron(III) bridging imido dimer. Nitrene coupling to give azoarene can occur from either the iron(III) imido radical complex, or from the bis(imido) dimer. For bulkier aryl azides, the bis(imido) dimer is disfavored to form due to sterics. This likely leads to preferential azoarene formation.

Reaction of the iron bis(alkoxide) with diphenyldiazomethane generates the azine $Ph_2CNNCPh_2$, suggesting that a reactive iron carbene complex is formed before reacting with another equivalent of the diazoalkane. A similar reaction with the cobalt bis(alkoxide) leads to isolation of the stable carbene complex, $Co(OR)_2(CPh_2)$. This molecule is the first example of an isolated, structurally characterized high-valent cobalt carbene complex. EPR and DFT studies confirm the electronics of the complex: it is likely that the cobalt oxidation state lies on a continuum between cobalt(III) and cobalt(IV) but that it displays significant alkylidene character. However, the high-valent cobalt carbene complex is surprisingly unreactive. Combination with both styrene and methyl acrylate at elevated temperatures failed to lead to any significant reactivity of the complex. This is likely due to the steric protection offered by both the bulky alkoxide ligands and the bulky carbene.

AUTOBIOGRAPHICAL STATEMENT

James A. Bellow

Education

Ph.D., Inorganic Chemistry, Wayne State University, Detroit MI
August 2011-June 2016; Advisor: Professor Stanislav Groysman

B.S., Chemistry with Departmental Honors, Wayne State University, Detroit, MI
August 2007- May 2011

Publications

1. **Bellow, J. A.**; Stoian, S. A.; van Toll, H.; Ozarowsky, A.; Lord, R. L.; Groysman, S. "Synthesis and Characterization of A Stable High-Valent Cobalt Carbene Complex" *J. Am. Chem. Soc.* **2016**, *138*, 5531-5534.
2. **Bellow, J. A.**; Yousif, M.; Groysman, S. "Discrete Complexes of 3d Metals with Monodentate Bulky Alkoxide Ligands and Their Reactivity in Bond Activation and Bond Formation Reactions" *Comments Inorg. Chem.* **2016**, *36*, 92-122.
3. **Bellow, J. A.**; Yousif, M.; Fang, D.; Cisneros, G. A.; Groysman, S. "Synthesis and Reactivity of 3d Metal Complexes with the Bulky Alkoxide Ligand [OC^{t}Bu$_2$Ph]" *Inorg. Chem.* **2015**, *54*, 5624-5633.
4. **Bellow, J. A.**; Yousif, M.; Cabelof, A. C.; Lord, R. L.; Groysman, S. "Reactivity Modes of an Iron Bis(alkoxide) Complex with Aryl Azides: Catalytic Nitrene Coupling vs. Formation of Iron(III) Imido Dimers" *Organometallics* **2015**, *34*, 2917-2923.
5. **Bellow, J. A.**; Martin, P. D.; Lord, R. L.; Groysman, S. "Reductive Coupling of Azides Mediated by an Iron(II) Bis(alkoxide) Complex" *Inorg. Chem.* **2013**, *52*, 12335-12337.
6. **Bellow, J. A.**; Fang, D.; Kovacevic, N.; Martin, P. D.; Shearer, J.; Cisneros, G. A.; Groysman, S. "Novel Cluster Topologies Featuring Rare Seesaw Geometry at Transition Metal Centers" *Chem. Eur. J.* **2013**, *19*, 12225-12228.

Selected Oral and Poster Presentations

1. **Bellow, J. A.**; Yousif, M.; Martin, P. D.; Groysman, S. "Synthesis of Low-Coordinate Bis(alkoxide) Metal Complexes and Their Reactivity in N-N Bond Formation Reactions" *Abstract of Papers*, Ohio Inorganic Weekend, University of Michigan, Ann Arbor, MI, November 15, 2014.
2. **Bellow, J. A.**; Yousif, M.; Martin, P. D.; Groysman, S. "Synthesis of Low-Coordinate Bis(alkoxide) Metal Complexes and Their Reactivity in N-N Bond Formation Reactions" *Abstract of Papers*, 35th Annual Michigan Catalysis Society Spring Symposium, Warren, MI, May 8, 2014.
3. **Bellow, J. A.**; Kovacevic, N.; Martin, P. D.; Shearer, J.; Cisneros, G. A.; Groysman, S. "Novel Cluster Topologies Featuring Rare Seesaw Geometry at Transition Metal Centers" *Abstract of Papers*, 246th National Meeting of the American Chemical Society, Indianapolis, IN, September 8-12, 2013; American Chemical Society: INOR 230.